Control of nanoparticle self-assembly

Von der Fakultät für Mathematik, Informatik und Naturwissenschaften der RWTH Aachen University zur Erlangung des akademischen Grades einer Doktorin der Naturwissenschaften genehmigte Dissertation

vorgelegt von

Vladislava Fokina, M.Sc.
aus
Tver, Russland

Berichter: Prof. Dr. Stephan Förster
Prof. Dr. Walter Richtering

Tag der mündlichen Prüfung*:* 08.05.2024

Diese Dissertation ist auf den Internetseiten der Universitätsbibliothek verfügbar.

Diese Arbeit wurde unter der wissenschaftlichen Leitung von Prof. Dr. Stephan Förster angefertigt. Die experimentellen Arbeiten wurden in der Zeit von Dezember 2019 bis März 2023 am Institut für Neutronenstreuung I (Jülich Centre for Neutron Science/ JCNS-1) des Forschungszentrums Jülich in Kollaboration mit Prof. Dr. Walter Richtering am Institut für Physikalische Chemie der RWTH Aachen Universität in der Arbeitsgruppe von Prof. Dr. Stephan Förster durchgeführt.

Eidesstattliche Erklärung

Ich, Vladislava Fokina, erkläre hiermit, dass diese Dissertation und die darin dargelegten Inhalte die eigenen sind und selbstständig, als Ergebnis der eigenen originären Forschung, generiert wurden.

Hiermit erkläre ich an Eides statt

1. Diese Arbeit wurde vollständig oder größtenteils in der Phase als Doktorand dieser Fakultät und Universität angefertigt;
2. Sofern irgendein Bestandteil dieser Dissertation zuvor für einen akademischen Abschluss oder eine andere Qualifikation an dieser oder einer anderen Institution verwendet wurde, wurde dies klar angezeigt;
3. Wenn immer andere eigene- oder Veröffentlichungen Dritter herangezogen wurden, wurden diese klar benannt;
4. Wenn aus anderen eigenen- oder Veröffentlichungen Dritter zitiert wurde, wurde stets die Quelle hierfür angegeben. Diese Dissertation ist vollständig meine eigene Arbeit, mit der Ausnahme solcher Zitate;
5. Alle wesentlichen Quellen von Unterstützung wurden benannt;
6. Wenn immer ein Teil dieser Dissertation auf der Zusammenarbeit mit anderen basiert, wurde von mir klar gekennzeichnet, was von anderen und was von mir selbst erarbeitet wurde;
7. Ein Teil dieser Arbeit wurde zuvor veröffentlicht und zwar in:

Vladislava Fokina, Manuel Wilke, Martin Dulle, Sascha Ehlert, and Stephan Förster
The Journal of Physical Chemistry C **2022** *126* (50), 21356-21367

_____ _____

Datum Unterschrift

Abstract

Core-shell nanoparticles are hybrid systems that self-assemble into complex structures with exceptional characteristics. Inorganic and polymeric core-shell nanoparticles are widely used for biomedical and industrial applications. The precise control of the nanoparticle assembly process is crucial for obtaining well-defined structures with desired properties and functions. For that, internal parameters of a system must be tuned, such as the core-shell ratio, the constituting materials, and the solvent type. Additionally, nanoparticle assembly can be impacted by external conditions, e.g. by shearing, magnetic fields, and temperature, which potentially leads to the formation of highly ordered structures.

The structural variability of core/shell particles allows to obtain a diversity of materials with specific structures. The challenge is to develop a fundamental understanding of the relation between the core/shell structure and the hierarchical structure of the obtained material. The general tendency of core-shell nanoparticle to assemble into specific structures can be described using phase diagrams. Depending on such parameters of spherical particles like core volume fraction and core-to-shell ratio, resultant self-assembly structures can thus be classified into a range of phases from the highly-symmetric face-centered cubic phase to low-symmetry quasicrystals.

In the current work, the solution self-assembly of hard- and soft-core core/shell nanoparticles are systematically investigated using small-angle X-ray scattering under shear, and transmission electron microscopy. The lyotropic liquid crystals and their lattices formed by self-assembly of the core/shell nanoparticles are then compared to predicted structures from molecular dynamic simulations and integrated into phase diagrams.
In the first part of the thesis, defined system parameters and external conditions for the formation and orientation of the A15 Frank-Kasper phase formed by micellar structures in water are presented. The role of polymer concentration and the size distribution of its hydrophobic part is highlighted.

In the second part, another type of soft-core nanoparticle, polyisoprene-polystyrene micelles in organic solvents, are investigated with respect to the formation of quasicrystal phases. Previous knowledge about the rheological behavior of the polymer system provided a starting point for a new cuette-type rheo-SAXS shearing device, which expanded the technical possibilities of shearing experiments and the studied materials. Besides,

measurements of PI-PS solutions revealed specific insights in FCC-BCC phase coexistence during temperature changes and at applied high strains.

In the third part of the thesis, hard-core nanoparticles are investigated. For hard core core/shell nanoparticles, core deformation during shearing as happens to soft matter systems is prevented. Synthesis conditions to control the core size of superparamagnetic magnetite nanoparticles (SPIONS) over a wide range are explored. SPIONs are synthesized using the thermal decomposition method that delivers spherical, uniform, monodisperse, and monocrystalline particles up to 24 nm diameter. Various paths of synthesis demonstrate the influence of the solvent type and the thermal pretreatment of precursor on resultant particles. Especially, their size, shape, and quality are essential for assembly in magnetic fields.

Shearing and magnetic external fields are powerful instruments for structure ordering and orientation, which enable phase transitions and the adjustment of lattice parameters. Polymer-grafted SPIONs are investigated as hard-core core/shell nanoparticles with respect to the formation of ordered FCC phases. It is found that shearing in combination with a permanent magnetic field leads to complex structural reorientation processes. For particular core-shell nanoparticles of 14 and 24 nm diameter, the influence of a permanent magnetic field during a long-time exposure causes well-defined disorder-BCC-FCC phase transitions. These studies conclude the investigations on the influence of core/shell-structure and external shear and magnetic fields on the self-assembly hard and soft core core/shell nanoparticles.

Kurzzusammenfassung

Kern-Schale-Nanopartikel sind Hybridsysteme, die sich selbst zu komplexen Strukturen mit außergewöhnlichen Eigenschaften organisieren. Anorganische und polymere Kern-Schale-Nanopartikel werden häufig für biomedizinische und industrielle Anwendungen verwendet. Die präzise Steuerung des Nanopartikel-Assemblierungsprozesses ist entscheidend für den Erhalt wohldefinierter Strukturen mit gewünschten Eigenschaften und Funktionen. Dazu müssen interne Parameter abgestimmt werden, wie das Kern-Schale-Verhältnis, die chemische Zusammensetzung, und die Art des Lösungsmittels. Darüber hinaus kann die Selbstorganisation von Nanopartikeln durch äußere Bedingungen beeinflusst werden, z.B. durch Scherung, externe Magnetfelder und Temperatur, was zur Bildung hochgeordneter Strukturen führt.

Die strukturelle Variabilität von Kern/Schale-Partikeln ermöglicht die Herstellung einer Vielzahl von Materialien mit spezifischen Strukturen. Die Herausforderung besteht darin, ein grundlegendes Verständnis für den Zusammenhang zwischen Kern/Schale-Struktur und der hierarchischen Struktur des gebildeten Materials zu entwickeln. Die allgemeine Tendenz von Kern-Schale-Nanopartikeln, sich zu spezifischen Strukturen zusammenzufügen, kann mithilfe eines Phasendiagramms beschrieben werden. Abhängig von Parametern sphärischer Partikel wie dem Kernvolumenanteil und dem Kern-zu-Schale-Verhältnis können die resultierenden Selbstorganisationsstrukturen in eine Reihe von Phasen eingeteilt werden, von der hochsymmetrischen kubisch-flächenzentrierten Phase bis hin zu Quasikristallen mit niedriger Symmetrie.

In der aktuellen Arbeit wird die Selbstorganisation von Kern/Schale-Nanopartikeln mit hartem und weichem Kern in Lösung systematisch mithilfe von Kleinwinkel-Röntgenstreuung unter Scherung und mithilfe der Transmissionselektronenmikroskopie untersucht. Die lyotropen Flüssigkristalle und ihre durch Selbstorganisation der Kern/Schale-Nanopartikel gebildeten Übergitter werden mit vorhergesagten Strukturen aus molekulardynamischen Simulationen verglichen und in Phasendiagrammen dargestellt.

Im ersten Teil der Arbeit werden definierte Systemparameter und äußere Bedingungen für die Bildung und Orientierung der durch mizellare Strukturen in Wasser gebildeten A15 Frank-Kasper-Phase vorgestellt. Die Rolle der Polymerkonzentration und der Größenverteilung des mizellaren hydrophoben Teils wird hervorgehoben.

Im zweiten Teil wird eine andere Art von Nanopartikeln mit weichem Kern, Polyisopren-Polystyrol-Mizellen (PS-PI) in organischen Lösungsmitteln, im Hinblick auf die Bildung quasikristalliner Phasen untersucht. Voruntersuchungen über das rheologische Verhalten des Polymersystems lieferten einen Ausgangspunkt für ein neues Rheo-SAXS-Schergerät, das die technischen Möglichkeiten von Scherexperimenten und den untersuchten Materialien erweiterte. Darüber hinaus ergeben Messungen von PI-PS-Lösungen spezifische Einblicke in die Koexistenz der FCC-BCC-Phase bei Temperaturänderungen und bei angelegten hohen Scherdeformationen.

Im dritten Teil der Arbeit werden Kern/Schale-Nanopartikel mit hartem Kern untersucht. Bei diesen Nanopartikeln wird eine Kernverformung während der Scherung, wie sie bei Systemen aus weichen Kernen auftritt, verhindert. Es werden Synthesebedingungen zur Steuerung der Kerngröße superparamagnetischer Magnetit-Nanopartikel (SPIONS) über einen weiten Bereich untersucht. SPIONs wurden mithilfe der thermischen Zersetzungsmethode synthetisiert, die kugelförmige, gleichmäßige, monodisperse und monokristalline Partikel mit einem Durchmesser von bis zu 24 nm liefert. Verschiedene Synthesewege zeigen den Einfluss des Lösungsmitteltyps und der thermischen Vorbehandlung des Precursors auf die resultierenden Partikel. Insbesondere ihre Größe, Form und Qualität sind für das Verhalten in Magnetfeldern von entscheidender Bedeutung.

Scherung und magnetische äußere Felder haben großen Einfluss auf Strukturordnung und -orientierung, welche Phasenübergänge und die Anpassung von Gitterparametern ermöglichen. Polymerbeschichtete SPIONs werden als Kern/Schale-Nanopartikel mit hartem Kern im Hinblick auf die Bildung geordneter FCC-Phasen untersucht. Es zeigt sich, dass Scherung in Kombination mit einem permanenten Magnetfeld zu komplexen strukturellen Umorientierungsprozessen führt. Bei bestimmten Kern-Schale-Nanopartikeln mit einem Durchmesser von 14 und 24 nm führt der Einfluss eines permanenten Magnetfelds während einer Langzeitexposition zu genau definierten Phasenübergängen zwischen ungeordneten Phasen und geordneten BCC- und FCC-Phasen. Diese Studien beschließen die Untersuchungen zum Einfluss der Kern/Schale-Struktur sowie externer Scher- und Magnetfelder auf die Selbstorganisation harter und weicher Kern/Schale-Nanopartikel.

Contributions of authors

The results of this thesis are presented in five chapters.

Results of the **chapter 2** are included to the "Quasicrystals Optimize Sphere Packing" paper, which recently submitted to Nature journal. I prepared polymer solutions in water, performed SAXS shearing measurements and data analysis myself. Lisa Fruhner and Jürgen Allgaier carried out the polymer synthesis of homemade $C_{16}E_{20}$ surfactant. Margarita Kruteva and Martin Dulle provided me with technical support for SAXS experiments and took part in discussions of results together with Stephan Förster.

For **chapter 3** I prepared polymer mixtures in the selective solvent, performed all SAXS experiments and DLS measurements, and corrected and analyzed the resulting data. Studied block copolymer was synthesized by Daniela Pirner. Martin Dulle provided me with technical support for SAXS experiments and took part in discussions of results together with Margarita Kruteva and Aakash Sharma.

The results of **chapter 4** were published in the *Journal of Physical Chemistry C* and the chapter is presented very similarly to the publication:
Vladislava Fokina, Manuel Wilke, Martin Dulle, Sascha Ehlert, and Stephan Förster Size Control of Iron Oxide Nanoparticles Synthesized by Thermal Decomposition Method; *The Journal of Physical Chemistry C* **2022** *126* (50), 21356-21367; DOI: 10.1021/acs.jpcc.2c05380
I synthesized and characterized all iron oxide nanoparticles using the TEM technique under the supervision of Sascha Ehlert. I performed SAXS capillary measurements and analyzed the results using the polydisperse core-shell spherical model. I suggested and prepared the reaction mixture for the *in situ* kinetics experiment and took part in measurement together with Manuel Wilke, Martin Dulle, and Sascha Ehlert. Manuel Wilke analyzed the particle growth and Stephan Förster performed corresponding simulations of the kinetics of iron oxide growth. I wrote the parts of the manuscript related to the various synthesis parameters influencing nanoparticle size distribution and shape and prepared it for publication.

For **chapter 5** I got the batch of 17 nm iron oxide nanoparticles from Lisa Fruhner. I carried out the nanoparticles polymer grafting using the ligand exchange method and performed TEM measurements under the supervision of Sascha Ehlert. I prepared samples, conducted

SAXS measurements, and analysed data. Technical support during SAXS measurements was provided by Andrei Chumakov and Stephan Roth (MINAX, DESY), Martin Dulle (Ganesha, JCNS), and Margarita Kruteva (Galaxi, JCNS).

Parts of the **chapter 6** are under preparation for publication.

I synthesized iron oxide nanoparticles of two different diameters and performed ligand exchange to graft polystyrene chains. Polymer synthesis and functionalization were carried out by Kuno Schwärzer and Jürgen Allgaier. I prepared and measured samples, and analyzed SAXS data. Stephan Förster made a part of structural calculations for FCC/BCC formation path. Margarita Kruteva and Martin Dulle took part in the discussion of the results and building a phase diagram.

Table of Content

Abstract VII

Kurzzusammenfassung IX

Contributions of authors XI

Introduction 1

References 4

1 Theoretical background 5

1.1 Polymers 5

1.1.1 General properties 5

1.1.2 Block copolymers self-assembly 7

1.2 Nanoparticles 12

1.2.1 Synthesis 12

1.2.2 Nucleation and growth mechanism 13

1.2.3 Aggregation and stabilization 15

1.2.4 Polymer ligands for nanoparticle stabilization 17

1.2.5 Self - assembly of nanoparticles 19

1.3 Magnetic interactions. Superparamagnetism 20

1.4 Experimental techniques 23

1.4.1 Small-angle X-ray scattering 23

1.4.2 Transmission electron microscopy 30

1.4.3 Rheology 32

1.5 References 36

2 Shearing-induced phase transitions in $C_{16}E_{20}$ polymer water solutions 41

2.1 Abstract 41

2.2 Introduction 41

2.3 Results and discussion 43

2.3.1 Complex micelles packings of the hydrated di-block oligomer in water 43

2.3.2 Shearing-induced phase transitions and A15 phase orientation 45

2.3.3 Comparison of homemade and commercial polymer 51
2.4 Materials and methods 55
2.4.1 Materials 55
2.4.2 SAXS measurements 55
2.5 Conclusion 56
2.6 Supporting Information 58
2.7 References 65
3 Shearing-induced PI-PS block copolymer micelle assembly in an organic solvent 67
3.1 Abstract 67
3.2 Introduction 67
3.3 Results and discussions 69
3.3.1 Structure stability 69
3.3.2 Structure reproducibility 74
3.3.3 Shearing and temperature initiated reorientation 76
3.4 Materials and methods 78
3.4.1 Materials 78
3.4.2 Synthesis 78
3.4.3 Rheology measurements 78
3.4.4 SAXS measurements 78
3.4.5 Shearing cell of cuette type 78
3.5 Conclusion 80
3.6 Supporting information 81
3.7 References 83
4 Size-control of iron oxide nanoparticles synthesized by thermal decomposition methods 85
4.1 Abstract 85
4.2 Introduction 85
4.3 Results and discussion 86

4.3.1 Time-resolved small-angle X-ray scattering experiments 86
4.3.2 Iron oleate precursor synthesis 90
4.3.3 Influence of the main synthesis parameters 93
4.3.4 The use of high-boiling point solvents 98
4.4 Materials and methods 103
4.4.1 Materials 103
4.4.2 Transmission electron microscopy (TEM) 103
4.4.3 Small angle X-ray scattering (SAXS) 103
4.4.4 SAXS data analysis 103
4.4.5 The thermal decomposition route 104
4.5 Conclusions 105
4.6 Supporting Information 106
4.7 References 110
Introduction to chapters 5 and 6: Nanocomposite self-assembly in external fields. 113
5 Phase transitions in nanocomposite solutions derived in a magnetic field 114
5.1 Abstract 114
5.2 Results and discussion 114
5.3 Materials and methods 121
5.3.1 Materials 121
5.3.2 Ligand exchange 121
5.3.3 Sample preparation 121
5.3.4 Transmission electron microscopy (TEM) 122
5.3.5 SAXS measurements 122
5.4 Conclusion 123
5.5 Supporting Information 124
5.6 References 127
6 Shearing and magnetic field-induced phase transition in SPIONs complexes 129
6.1 Abstract 129

6.2 The FCC-BCC transition and lattice orientation in external fields 129
6.3 Experimental results and discussions 139
6.3.1 Influence of shearing external field 140
6.4 Materials and methods 153
6.4.1 Materials 153
6.4.2 Sample preparation 153
6.4.3 Transmission electron microscopy (TEM) 153
6.4.4 SAXS measurements 153
6.5 Conclusion 155
6.6 Supporting Information 156
6.7 References 159
Conclusion and Outlook 160
6.8 References 164
Acknowledgements 165
Curriculum Vitae 167

Introduction

Nanomaterials are intensively studied during the last decades and actively used in everyday life. They enable the building of precise circuits for electronics, the development of new ways to obtain and store energy, help in agriculture, and allow more effective medicine[1]. Modern technologies and societal needs initiated a demand for more advanced materials. Here core-shell structures came into play. Thank to evolved material characterization and synthesis technologies, core-shell nanoparticles have many types of various shapes, compounds, and their combinations. They are very perspective for highly functional materials with modified properties[2]. The properties can be modified by changing either the constituting materials or the core-to-shell ratio[3]. For instance, shell coating may influence reactivity, dispersibility, thermal stability, control release of the core, and increase functionality. Therefore, core-shell nanoparticles are widely used in biomedical and pharmaceutical applications[4–6], such as bioimaging, controlled drug release, and targeted drug delivery. Also, they are common for catalysis [7,8], electronics[9], and enhancing photoluminescence[10].

For most of the applications, it is common to use not a single particle, but plenty of them in either bulk or solution. Due to interparticle interactions and external field influence, nanoparticles start aggregating into larger objects, which often have a crystalline structure. The resultant size and the order degree of aggregates strongly impact on the properties of functional systems. Thus, the self-assembly of core-shell nanostructures should be precisely controlled. In comparison to cubic particles, spherical core-shell nanoparticles are easier to order, which results in a variety of possible structures, e.g. simple cubic (SC), face-centered cubic (FCC), base-centered cubic (BCC), hexagonally-packed cylinders (HPC) and lamellar (LAM) lattices. Besides, the formation of more complex phases like Frank-Kasper (FK) and quasicrystal (QC) in soft matter is highly interesting for fundamental research and for industrial applications, where biocompatibility, low friction, and corrosion resistance are required[11].

There are two general ways to control nanosystem assembly. The first one is to emerge small or large structures, depending on the interaction forces between the building blocks and their kinetic pathways during the self-assembly. In other words, changing systems parameters such as core-shell ratio, core volume fraction, material and solvent types. The other one is applying external fields and their combinations, e.g. temperature, light, shearing, pressure, magnetic and electric fields[12,13]. Meanwhile, the assembly of

each core-shell system demands an individual approach and a proper study for a particular application case.

Gaining deep knowledge of nanosystems' self-assembly depending on their core-shell parameters and adjusting the formed structures in external fields is the main aim of this project. The combination of small-angle X-ray scattering (SAXS) and transmission electron microscopy (TEM) enables the characterization of obtained structures by defining their shape, dimension, and crystallographic pattern. Since we consider two types of core-shell systems, with either a soft or hard core and a soft polymer shell, the first part of the study is related to amphiphilic polymer solutions and the second one to superparamagnetic nanoparticles grafted with polymer chains.

Amphiphilic polymers in solutions tend to assemble into lyotropic liquid crystals (LLC), likewise, poly(ethylene-block-ethylene oxide) diblock oligomers form A15 FK phase at certain concentrations in water. The phase can be changed either by varying the sample's temperature or by applying shearing. The shearing method also enables the ordering of A15 FK phase domains, which highly depends on polymer quality. Thus, the main goal is to define system parameters and external conditions for a regular order-order phase transition and A15 domain orientation. Particular interest the A15 phase causes due to its neighborhood with QCs on a phase diagram. Meanwhile, it is very challenging to obtain a QC from the A15 phase and the other way around. As a step towards finding the solution, an expansion of shearing device capabilities is necessary. For this purpose, a cuvette-type device with two possible directions of structure observation and a high threshold of applied strain must be tested. As a model system for the new shearing device test, another well-studied amphiphilic polyisoprene-polystyrene polymer was chosen. PI_{210}-PS_{154}-OH block copolymer in diethyl phthalate (DEP) solvent forms mostly FCC, BCC, and Q12 LLCs. Phase transition can be initiated via shearing at high strains and changing temperature, which triggers the change of DEP solvent solubility and as a result the shell modification. Choosing shearing parameters based on the rheological behavior of the polymer gels, the test of the cuvette-type device is performed in radial and tangential directions.

For the second part of the study of the core-shell systems, spherical superparamagnetic iron oxide nanoparticles (SPIONs) were used as an inorganic hard core and grafted with polystyrene chains because of their high temperature resistance. Iron oxide particles such as magnetite (Fe_3O_4) or its oxidized form maghemite (Fe_2O_3) are the most commonly employed for biomedical applications, e.g. MRI contrast enhancement, tissue repair, drug delivery, and cell separation[1]. All of these require that SPIONs have a high

magnetization value, a size smaller than 100 nm, and a narrow particle size distribution[14]. Such properties of nanoparticles as blocking temperature, magnetic saturation and coercivity are size and shape-dependent. One of the most common and versatile techniques to synthesize iron oxide nanoparticles is the thermal decomposition method. For the reason of a rather complex nucleation and growth kinetics, it demands a systematic investigation of common variations of the iron oxide heat-up synthesis routes to understand and conclude which methods allow good and reproducible size control over a range of relevant nanoparticle diameters up to 24 nm. Particular attention is paid here to the type of solvent and the thermal pretreatment of precursor that input resultant particles the most.

Among all functional materials, a special place is given to magnetic nanoparticles which can be grafted with polymer chains[15] for preventing aggregation and for tuning system parameters such as interparticle distance and polymer shell density. In the scope of this project, the final aim was the study of the structural behavior of polystyrene grafted magnetite nanoparticles in external fields using synchrotron and laboratory X-ray sources. Experimental results of FCC and BCC crystals formation in organic solutions under shearing and permanent magnetic field were compared to calculated 2D scattering patterns and have revealed that the reorientation process does not progress along a reorientation path with a well-defined rotation axis and often includes twining effects. Overall, the study of nanoparticle self-assembly and its control in external fields give new insights into core-shell systems ordering, initiation of phase transitions, assembly restrictive parameters as well as into material and technique improvement.

References

[1] I. Khan, K. Saeed, I. Khan, *Arabian Journal of Chemistry* **2019**, *12*, 908–931.

[2] S. Kalele, S. Gosavi, J. Urban, S. Kulkarni, *Curr Sci* **2006**, *31*, 645–651.

[3] S. J. Oldenburg, R. D. Averitt, S. L. Westcott, N. J. Halas, *Chem Phys Lett* **1998**, *288*, 243–247.

[4] K. K. Jain, *Technol Cancer Res Treat* **2005**, *4*, 407–416.

[5] G. F. Paciotti, L. Myer, D. Weinreich, D. Goia, N. Pavel, R. E. McLaughlin, L. Tamarkin, *Drug Delivery: Journal of Delivery and Targeting of Therapeutic Agents* **2004**, *11*, 169–183.

[6] K. Sokolov, M. Follen, J. Aaron, I. Pavlova, A. Malpica, R. Lotan, R. Richards-Kortum, *AACR* **1999**, *63*.

[7] M.-C. Daniel, D. Astruc, **2004**, DOI 10.1021/CR030698.

[8] C. Li, Y. Jin, C. P. Li, Y. D. Jin, *Adv Funct Mater* **2021**, *31*, 2008031.

[9] C. Li, D. Cahen, P. Wang, H. Li, J. Zhang, Y. Jin, *iScience* **2018**, *8*, 213–221.

[10] Y. Yang, M. Nogami, J. Shi, H. Chen, G. Ma, S. Tang, *Journal of Physical Chemistry B* **2005**, *109*, 4865–4871.

[11] L. Fehrenbacher, *MRS Bull* **2011**, *36*, 581.

[12] Y. Min, M. Akbulut, K. Kristiansen, Y. Golan, J. Israelachvili, *Nature Materials 2008 7:7* **2008**, *7*, 527–538.

[13] H. Wang, H. Li, P. Gu, C. Huang, S. Chen, C. Hu, E. Lee, J. Xu, J. Zhu, *Nanoscale* **2023**, *15*, 2018–2035.

[14] S. Laurent, D. Forge, M. Port, A. Roch, C. Robic, L. Vander Elst, R. N. Muller, *Chem Rev* **2009**, *110*, 2574.

[15] S. Ehlert, S. M. Taheri, D. Pirner, M. Drechsler, H. W. Schmidt, S. Förster, *ACS Nano* **2014**, *8*, 6114–6122.

1 Theoretical background

1.1 Polymers

1.1.1 General properties

Polymers are macromolecules formed by the chemical bonding of large numbers of smaller molecules, or repeating units, called monomers. The number of monomers within the polymer molecule can vary greatly. Moreover, the degree to which regularity appears in the order, relative orientation and the presence of differing monomers within the same polymer molecule also can vary. In many synthetic and some natural polymers, the number of monomers (sometimes referred to as the degree of polymerization) can be determined precisely to tailor material properties[1]. Macromolecules can be either the typical organic carbon main chains or inorganic, hydridic (carbon-free main chain) or have natural compounds like DNA, cellulose etc. Besides their chemical constituents, macromolecules can also be classified due to their architectures as linear, branched, brushes, star-like, dendritic, cross-linked or hyperbranched [2]. The simplest form of a polymer is one that is made up of only one type of monomer (a homopolymer). Copolymers are composed of monomers that differ from each other. The degree to which they differ – either by structure or composition – and the quantities of each type of monomer relative to one another in the same polymer molecule ultimately determine the material's chemical and physical properties. An important class of copolymers are block copolymers which consist of two or more connected blocks each built of one monomer species.

Polymers can be synthesized by various polymerisation reactions. Generally, they are divided into two procedures: step-growth and chain-growth polymerisation. The difference between them is the distribution of reactive centres during the reaction [3]. For step-growth, each monomer has at least two reactive centres, allowing them to react with any other monomer or already assembled larger units. In contrast, chain growth relies on an initiator to produce one or more reactive centres which can then add one monomer at a time to one reactive centre while the reactive centre is passed to the end of the chain. The monomers cannot simply react with each other. Finally, the choice of the polymerisation technique depends on the thermodynamics and kinetics of the desired reactions.

Particularly living anionic polymerization is a powerful tool for the precise synthesis of polymers with extremely narrow size distribution. It can be applied to build up copolymers consisting of different monomers sequentially and in a controlled manner, therefore it is very suitable for the controlled synthesis of block copolymers[4]. For example,

after the complete polymerization of the first monomer A, the second monomer B is added and the propagation proceeds until the monomer molecules are consumed [5].

Since the properties of polymers are inherently size-dependent, another important characteristic of a polymer is its molecular weight. The term molecular weight is used here as a synonym for the molar mass of the polymer (typical unit: g/mol) as this is the common term in polymer chemistry. The molecular weight is connected to the number of monomer units, the so-called degree of polymerisation. As the product of polymerisation has a certain molecular weight distribution, the obtained number of molecular weight differs depending on the calculation method. The two most important quantities are the number-average molecular weight M_n and the weight-average molecular weight M_w.

By dividing the total weight of all molecules w by the number of molecules N_{total}, M_n can be calculated. Another approach is to measure the molecular weights of a certain number of molecules and sort them by their number of monomer units i. Summing the products of the corresponding numbers N and masses M of each unit i and dividing by the total amount of molecules again yields M_n:

$$M_n = \frac{w}{N_{total}} = \frac{\sum_i N_i M_i}{\sum_i N_i} \qquad 1.1$$

M_w is determined by summing over the products of the weight fraction w_i of molecules with molecular weight M_i and their number N_i:

$$M_w = \sum_i w_i N_i = \frac{\sum_i N_i M_i^2}{\sum_i N_i M_i} \qquad 1.2$$

The ratio of M_w and M_n is defined as the polydispersity $Đ$ and is a measure for the width of the molecular weight distribution:

$$Đ = \frac{M_w}{M_n} \qquad 1.3$$

Polymer molecular weight can be defined using nuclear magnetic resonance (NMR) spectroscopy, mass spectrometry and size exclusion chromatography (SEC) methods.

Noteworthy, copolymerization of different types of monomers leads to an extension of polymer architectures and properties. Usually, diblock copolymers designed of two

incompatible blocks show an amphiphilic character, which means the presence of both hydrophilic and hydrophobic properties. By reason of incompatibility and supplemental covalent linking, block copolymers have the ability to spontaneous self-assemble in solutions. Therefore, diblock copolymers are suitable candidates for fabrication of hierarchically ordered structures [6].

1.1.2 Block copolymers self-assembly

The self-assembly of polymers offers many potential applications in nanotechnological and nanobiotechnological fields. Copolymer is a type of polymer with two or more chemically distinct homopolymer blocks that are connected by a covalent bond. In Figure 1.1 the different typical structures of block copolymers containing two types of blocks (A and B) are illustrated: AB diblock, triblock, alternating and tapered blocks.

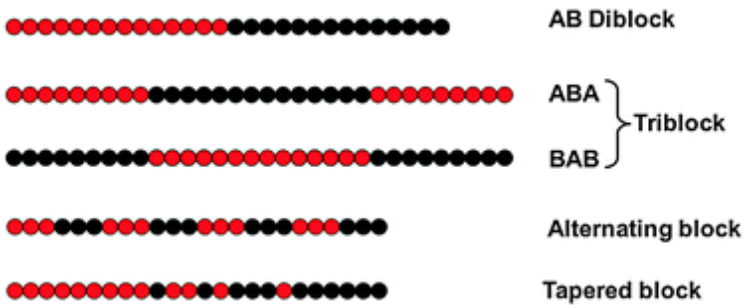

Figure 1.1 Typical structures of block copolymers containing two types of blocks, A and B. This figure originates from the reference [7]. *© The Royal Society of Chemistry 2012*

There are two main conditions for block copolymer assembly: short-range attractive forces coming from covalent bond or magnetic dipole interaction and long-range repulsive forces of chemical incompatibility [8]. Nature of morphologies and molecular architecture are determined by three independent parameters including Flory-Huggins interaction parameter χ, degree of polymerization N, and the block length ratio f [9].

The total degree of polymerization N of the block copolymer is obtained by summation of the degrees of polymerization of the individual blocks A and B. The block length ratio f is the geometric factor that affects the symmetry of the superstructure and has a major impact [8], it allows to control and predict the kind of ordered structure by varying the block lengths [9]. Furthermore, the strength of the repulsive interaction is represented by χ, which is the Flory-Huggins or χ-interaction parameter. The magnitude of the Flory-Huggins parameter is determined by the physical and chemical properties of the A-B pair and the temperature. With increasing temperature T the Flory-Huggins parameter χ decreases with $\chi \sim 1/T$.

Moreover, χ - parameter describes both the interaction between two blocks A and B of a copolymer as well as the respective interaction of a block with a selective solvent [7–10].

Figure 1.2 demonstrates the cone column mechanism for morphological transitions. When the diblocks are highly asymmetric the block with smaller volume fraction prefer to aggregate into spherical microdomains, leaving the larger B blocks to surround them as ‘‘corona’’. This way affords the system the lowest interfacial area and increased configurational entropy, which is in comparison to other morphologies energetically favourable. As f_A increases at a fixed temperature, the corona volume fraction decreases and less curved interfaces are formed, the polymer chains have to adopt new arrangements to reduce their stretching, leading to a morphological transition from spheres to cylinders and to lamellae [7].

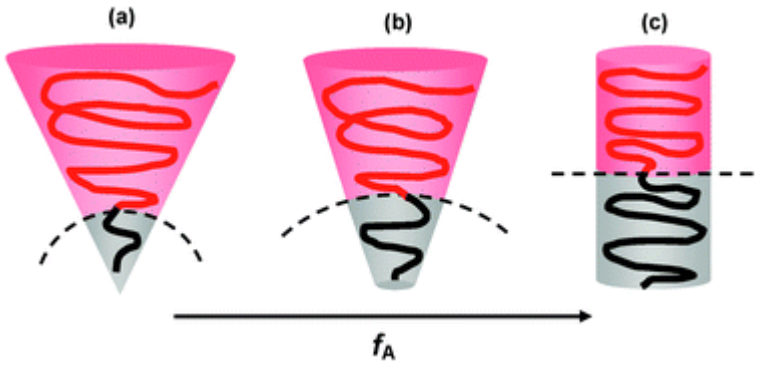

Figure 1.2 Schematic illustration of the possible polymer chain arrangements in different morphologies of AB diblocks changing from sphere (a) to cylinder (b) and to lamella (c), as the volume fraction (f_A) of the A block (black) increases to ~0.5. The dash curve in each morphology represents a part of the interface between A and B domains. This figure originates from the reference [7]. © The Royal Society of Chemistry 2012

As mentioned before two competing forces provide the formation of ordered domains on the mesoscale and as a consequence, block copolymers facilitate the preparation of various microstructure materials such as micelles and vesicles in solution or FCC and BCC packed spheres, hexagonally packed cylinders (HEX), and lamellae (LAM) in thin films and bulk [8]. Figure 1.3 a demonstrates a temperature phase diagram based on theoretical assumptions in terms of interaction and molecular weight**.** There various ordered domains with different geometries can be found. With the increase of the block molecular weight the tendency for segregation between the block also increases and decreases with decreasing temperature [6].

Self-assembly of block copolymers can be roughly divided into three areas of an increasing polymer concentration: dilute solutions, lyotropic phases and bulk phases [7,8]. At low concentrations micelles are isolated and have almost no spatial correlations. At higher concentrations the formation of lyotropic and/or thermotropic liquid crystalline phases is

induced, which displays similarities of both solution and bulk morphologies . Thus, besides the interesting morphologies obtained in bulk, block copolymers can self-assemble in selective solvents toward several ordered structures (*e.g.* spherical micelles, cylinders or vesicles) related to those found in neat block copolymers (Figure 1.3 b).

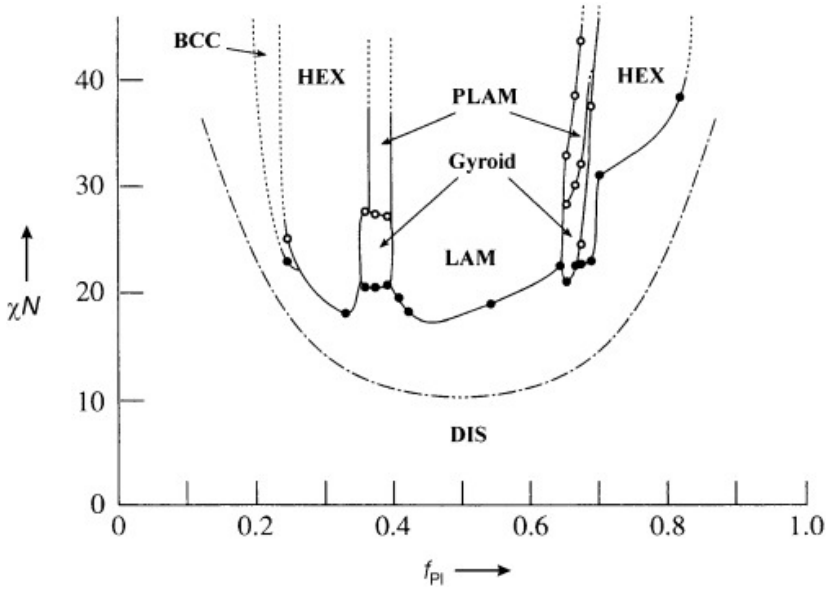

a)

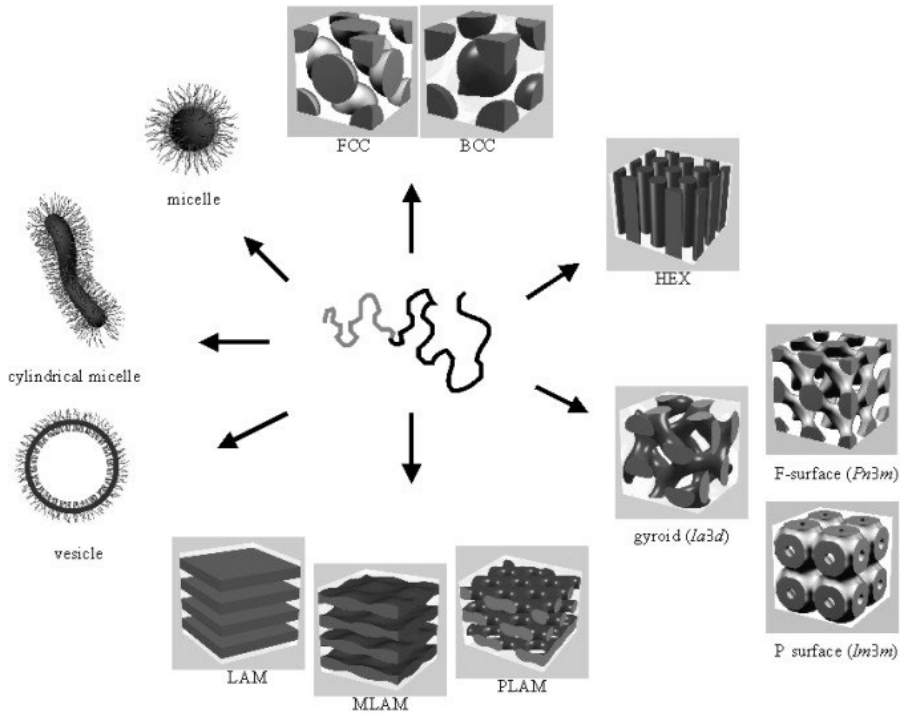

b)

Figure 1.3 a) Theoretical phase diagram of AB block copolymers with various ordered superlattices as a function of block length ratio f (CPS: close-packed spheres, DIS: disordered, BCC: bcc-packed spheres, HEX: hexagonally packed cylinders, LAM: lamellar) b) Self-organized structures of block copolymers: spherical micelles, cylindrical micelles, vesicles, fcc- and bcc-packed spheres (FCC, BCC), hexagonally packed cylinders (HEX), various minimal surfaces (gyroid, F surface, P surface), simple lamellae (LAM), as well as modulated and perforated lamellae (MLAM, PLAM). This figure originates from the reference [8] © 2002 WILEY-VCH Verlag GmbH, Weinheim, Fed. Rep. of Germany

Well-defined block copolymer amphiphiles undergo self-assembly in aqueous solution in order to minimize energetically unfavourable hydrophobic interactions. Specific self-assembled nanostructures can be targeted according to a dimensionless 'packing parameter' *p,* which is defined in Equation 1.4, where *v* is the volume of the hydrophobic chains, a_o is the optimal area of the head group, and l_c is the length of the hydrophobic tail. Thus, the packing parameter of a given molecule usually dictates its most likely self-assembled morphology. As a general rule, spherical micelles are favoured when $p \leq \frac{1}{3}$, cylindrical micelles when $\frac{1}{3} \leq p \leq \frac{1}{2}$, and enclosed membrane structures (vesicles) when $\frac{1}{2} \leq p \leq 1$ [11].

$$p = \frac{v}{a_o l_c} \qquad 1.4$$

In contrary to the melt behaviour, where the driving force is based on repulsive interaction between the different monomers, the situation changes using selective solvents. There one type of block is soluble and the other one is insoluble which leads to micellization (Figure 1.4) [6].

Essential parameters for the micelle formation are the critical micelle temperature (CMT) and the critical micelle concentration (CMC), which is well-described for surfactant molecules with polar head groups and a hydrocarbon chain (*e.g.* sodium dodecyl sulfate) [12]. The micellization has some limitations regarding the growth process. On the one hand, hydrophobic hydrocarbon chains want to minimize the contact to water and form micelles. On the other hand, repulsive forces between the head groups are present on short distances. At a certain size micelles stop growing even when more surfactant is added. Above the CMC further addition of surfactants only generates new micelles rather than a growing of existing micelles. However, micelles can vary their shape or size by changing the environmental conditions such as temperature, concentration, pH, and pressure [12].

Analogues to surfactant molecules block copolymers self-assemble in solution. In a selective solvent the obtained micelles are in a thermodynamic equilibrium with the unimers. The soluble polymer chain orients toward the solvent and forms the corona, whereas the insoluble blocks are shielded from the solvent and form the cores of the micelles. Consequently, self-assembly is based on the relative strength of the interactions, the composition and the architecture of the block copolymer [6,8,13]. The phase transition of a block copolymer to packed spheres in a selective solvent happens in a following way. First, at very low concentrations the block copolymers exist as unimer and then at a certain CMC the

amphiphilic polymer unimers self-assemble into spherical micelles. With increasing concentration the spherical micelles start to pack and overlap with each other and form an ordered, gel-like material [6]. The phase behaviour of packed block copolymer micelles can also be greatly affected by the concentration, and temperature [14,15].

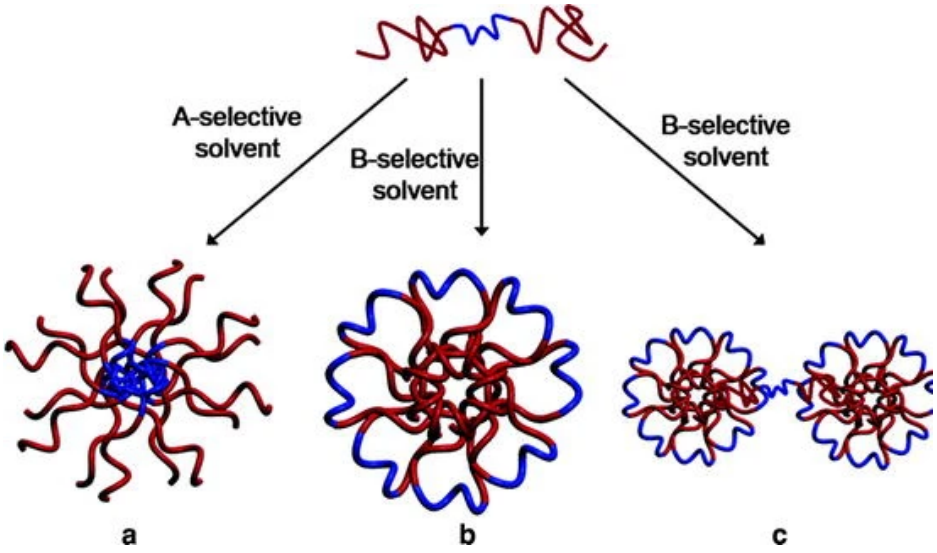

*Figure 1.4 Self-assembly of ABA triblock copolymers under different conditions. (**a**) Star-like micelle. (**b**) Flower-like micelle. (**c**) Micelle assembly This figure originates from the reference [16] Copyright © 2011, Springer-Verlag Berlin Heidelberg*

Block copolymers can be classified into ionic and non-ionic ones regarding the self-assembly process. In ionic block copolymer systems the electrostatic interactions between the free charges are the main influencing parameters. Apparently, in non-ionic block copolymer the driving force depends on the solvent. In aqueous solutions the self-assembly process is usually entropic driven, whereas in organic solvents the enthalpic contributions dominate [6]. Therefore in organic solvents the negative standard Gibbs energy ΔG_0 results from the standard enthalpy ΔH_0 and the standard entropy ΔS_0 values ($\Delta G_0 = \Delta H_0 - T\Delta S_0$). The entropy is negative which originates from the loss of combinatorial entropy caused by the less swollen polymer chains in the micelles compared to the polymer unimers in the non-associated state, and additionally, the loss of possible conformations due to the creation of a core/shell interface. The negative enthalpic values arise from the exothermic process of micellar core formation which is attributed to the balance of polymer/solvent and polymer/polymer interactions. The core-forming polymer block replaces the polymer/solvent interaction for one with the identical polymer block, whereas the shell-forming block remains interacting with the selective solvent [13,17,18].

The size of block-copolymer micelles is determined by the molecular weight of the polymer and thus the length of both blocks. The aggregation number Z describes the number of block copolymers in one micelle and is defined as given in Equation 1.5[8]:

$$Z = Z_0 N_A^{\alpha} N_B^{-\beta} \quad 1.5$$

Here, N_A and N_B are the degrees of polymerization for block A and block B, respectively. Z_0 is a constant, which is tabulated for many block copolymers and in many cases equals 1. Also α equals 2 and β equals 0.8.

1.2 Nanoparticles

1.2.1 Synthesis

Nanoparticles are tiny materials having a size range from 1 to 100 nm. They can be classified into different classes based on their properties, shapes, or sizes. Due to this, nanoparticles have properties that differ significantly from bulk materials, whether these are spheres, rods, disks, or self-assembled super crystals. Their optical properties are reported to be dependent on the size, which imparts different colors due to absorption in the visible region. The reactivity and toughness are also dependent on their unique size, shape, and structure[19]. Another advantageable effect coming with nanoparticles' small size is the quantum confinement effect. It is caused by the energy distribution of the electrons within the nanoparticle compared to the bulk. Moreover, the energy gap increases with the decrease in particle size. All these properties make nanoparticles suitable candidates for various commercial and domestic applications, which include catalysis, imaging, medical applications, energy-based research, and environmental applications[20–25].

There are two general methodologies for the fabrication of nanoparticles: the top-down and the bottom-up approaches [26–28]. The top-down approach involves the breaking down of large pieces of material to generate the required nanostructures from them. It employs mostly physical, high-energy procedures such as milling, thermal evaporation, and laser ablation, which provide large quantities of nanoparticles without precise control of over size, shape, and dispersity.

On contrary, the bottom-up approach implies assembling single atoms and molecules into larger nanostructures and guarantees more precise control of the structural parameters. This method is based on chemical processes such as solvothermal reactions and chemical precipitation, which are for nanoparticles starting from a precursor. During this chemical reaction, additional surfactants can be added to the reaction mixture for particle stabilization and therefore, preventing aggregation. The bottom-up approach also allows the achievement of even distribution of spherical, cubic nanoparticles, rods, disks, and higher-level architectures like nanowires and sheets.

Three main routes of bottom-up synthesis can be distinguished: sol-gel methods, reduction of metal salts, and thermal decomposition method. For the first method, a sol is formed from the precursors (inorganic metal salts or metal organic compounds), then it starts to link in a three-dimensional network – the gel [29]. With the sol-gel method, various metal oxide nanoparticles can be synthesized including Fe_3O_4, ZnO, and TiO_2 [30–32]. The second, reduction method is based on the reduction of metal salts in solution to form metal nanoparticles. The formation of all nanoparticles starts at the same moment when the reducing agent is injected into the metal salt solution. The most common nanoparticles obtained with this method are Au, Ag, Pt, Pd, Cu, and Co [33,34]. The third type of bottom-up route is a thermal decomposition method, where the formation of particles is based on the decomposition of an organometallic compound in solution. This method has high reproducibility and delivers monodisperse particles with easily tunable shapes and sizes depending on synthesis parameters. The formation of particles starts once a supersaturation is reached within the solution, which can be achieved in two ways. The first way is the 'hot-injection' of the precursor at high temperatures for the nucleation step and, meanwhile, the growth phase takes place at lower temperatures[35]. The other method is the 'heating-up' route, where nucleation and growth start after the homogeneous mixing of all components. Since the thermal decomposition method with the 'heating-up' route allows the synthesis of monodisperse spherical particles in large amounts [36], this type of synthesis is chosen for the current work.

1.2.2 Nucleation and growth mechanism

For the synthesis of uniform, monodisperse nanoparticles the separation of nucleation and growth phases is crucial, which was first introduced by LaMer and colleagues as the 'burst nucleation' concept [37]. It describes that all nuclei have the same growth history if they were formed at the same time. Afterward, nanoparticles continue to grow without further nucleation, therefore the size distribution of all nanoparticles as a whole can be controlled during growth. Nucleation can be heterogeneous so that the nuclei formation is started from impurities on surfaces. In contrast, the LaMer concept assumes homogenous nucleation, which means that nuclei are formed without any seeds. This involves a high energy barrier because the system changes from a one-phase to a two-phase system, which is visualized with the LaMer plot in Figure 1.5. The plot shows the development of monomer concentration over time and includes three stages. At the first stage (I) the system reaches supersaturated condition due to the increase of monomer concentration. The degree of supersaturation increases until at the second stage (II) it is

high enough to overcome the energy barrier, at this point nuclei start to form. The nucleation step demands the consumption of monomer, thus its concentration decreases. Once monomer concentration is below the level of critical supersaturation, nucleation will stop and at the third stage (III) already existing nuclei will grow until a further concentration drops. With the limited supply of monomer available, the monomer concentration approaches the lower solubility limit, and additional growth proceeds by Ostwald ripening[38][39].

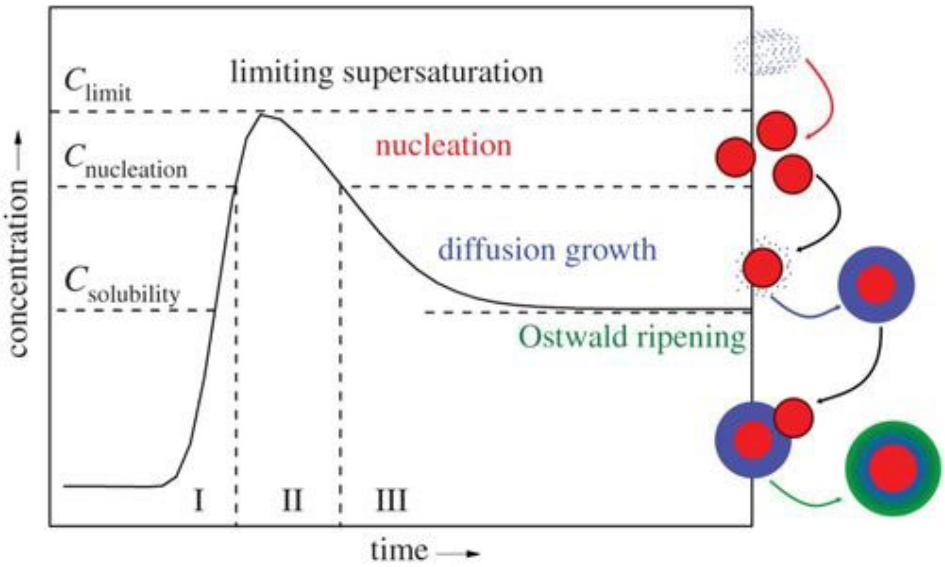

Figure 1.5 LaMer Plot of a solution concentration as a function of time. Phil. Trans. This figure originates from the reference [40] *Copyright © 2015 Dunne Peter W., Munn Alexis S., Starkey Chris L., Huddle Tom A., and Lester Published by the Royal Society, License Number_1327497-1*

Ostwald ripening is a phenomenon observed in solid solutions or liquid sols that describes the change of an inhomogeneous structure over time, i.e. small crystals dissolve and redeposit onto larger crystals. This thermodynamically-driven spontaneous process occurs because larger particles are more energetically favoured than smaller particles. This stems from the fact that molecules on the surface of a particle are energetically less stable than the ones in the interior[41].

At the stage of nucleation nuclei form and dissolve again before they reach a critical radius r_c, which can be determined by considering the Gibbs free energy for the formation of spherical crystals of radius r [42]

$$\Delta G = 4\pi r^2\gamma + \frac{4}{3}\pi r^3 \Delta G_v \qquad 1.6$$

where γ is the surface free energy per unit area and the change in free energy is defined as $\Delta G_v = \frac{-k_b T ln(S)}{V}$ with Boltzmann constant k_b, temperature T, the degree of supersaturation

S and molecular volume V . Hence, Gibbs energy ΔG at the critical radius r_c is maximal in supersaturated solutions, where the surface contributions (~r^2) are always positive and volume contributions (~r^3) are negative.

For a nucleus to be able to grow spontaneously and not dissolve again it needs to have a minimum radius value equal to the critical radius $r_c = \frac{2\gamma V}{k_b T ln(S)}$. Moreover, the degree of supersaturation needs to be high enough so that the critical radius is below the spontaneously forming nuclei. Thus, the critical degree of supersaturation is reached when the number of nuclei formed is higher than the number of nuclei dissolving.

Referring back the 'heating-up' thermal decomposition method[43] which is actively used for the synthesis of iron oxide nanoparticles and provides separated nucleation and growth stages. There iron oleate precursor in the mixture with an organic solvent is heated up at a constant rate and aged for a determined time. The supersaturation of the solution happens due to the combination of elevated temperature and the decomposition of the iron oleate, which leads to the formation of a monomer. The separation of nucleation and growth is possible by passing the temperature range in which nucleation occurs and then aging the particles at a growth temperature, which no longer allows the creation of new nuclei and leads to a narrow size distribution.

1.2.3 Aggregation and stabilization

Control of nanoparticle properties is crucial for their application, therefore their aggregation is a much-undesired event. There are several factors, which determine nanoparticle stability in solution.

Nanoparticles can be described as a colloidal dispersion if they don't have a surface modification. In this case, attractive and repulsive forces can be described quantitatively with the DLVO theory [44,45]. In this theory, two forces are considered to impact colloidal stability: Van der Waals forces and electrical double-layer forces. The attractive van der Waals forces are mainly caused by the attraction between the induced dipoles within the particles. The electron distribution within the particles undergoes fluctuation, which leads to the formation of a temporary dipole. This temporary dipole then induces a second temporary dipole in a neighboring particle, and they both can now interact with each other. When two particles of radii $R_1$and R_2 approach one another, their ionic atmospheres begin to overlap and a repulsion force is developed, it is caused by the repulsion of the electric double layers around the particle.

The double layer is formed when the surface charges of particles attract oppositely charged ions. Since the electrical potential decreases with increasing distance from the particle

surface, two particles can come close to each other up to the point at which the repulsion between the identical charges is too strong to be overcome.

The potential energy of attraction W_a equals to:

$$Wa = \frac{-A}{6s} \cdot \left(\frac{R_1 R_2}{R_1 + R_2}\right), \quad 1.7$$

where the Hamaker constant $A = \pi^2 C \rho_1 \rho_2$ and s<<R_1,R_2 is a distance between particles. Also, C is the coefficient in the atom-atom pair interaction, ρ_1 and ρ_2 are the number of atoms per unit volume.

Including the energy of repulsion W_r, which depends on the interaction constant Z, the total potential energy with the combination of the double layer repulsion is described in Equation 1.8:

$$Wt = \left(\frac{R_1 R_2}{R_1 + R_2}\right) \cdot \left(Ze^{-ks} - \frac{A}{6s}\right) \quad 1.8$$

where k^{-1} is Debye length.

Van der Waals force is stronger than the double layer force when interparticle distance is sufficiently small enough, which leads to particle aggregation. To prevent this there are various ways of surface stabilization during and after synthesis, and one of the most efficient is modifying the surface with ligands for steric stabilization[46,47].

Meanwhile, the quality of the solvent as well as the grafting density of a surfactant on the nanoparticle surface are important factors for the steric stabilization in colloids. In a proper solvent, the surfactants will repulse other coated particles due to the osmotic and elastic contributions. The osmotic repulsion is based on the unfavourable exclusion of solvent molecules when the shells of two particles start to overlap. The elastic repulsion is due to the compression of the surfactants when nanoparticles come closer.

The free energy ΔG within the interpenetration area of the shells is described in Equation 1.9:

$$\Delta G = 2k_b T \cdot \frac{\upsilon_s^2}{\upsilon_i}\left(\frac{1}{2} - \chi\right)\int_V \varphi_1 \varphi_2 dV \quad 1.9$$

Here $\upsilon_s$is the Kuhn segment volume, υ_i is the solvent molecular volume, χ is the Flory-Huggins chain-solvent interaction parameter and $\varphi_1$and φ_2 are the segment density distribution functions. For a poor solvent (χ > 0.5) the free energy is negative which leads to the aggregation of nanoparticles. In a good solvent (χ < 0.5) the free energy is positive,

then penetration of the shells is not favourable, which leads to the repulsion of the nanoparticles and thus to stabilization[46,48].

1.2.4 Polymer ligands for nanoparticle stabilization

Surfactants such as polymer ligands can be attached to the surface of the nanoparticle to create a shell-like layer of molecules. In this way instead of the electrostatic repulsion caused by the double layer, it is now the shell that opposes the van der Waals forces and prevents the aggregation[49].
Several types of surfactants and the ways of their attachment to the particle surface exist[50–53]. One of the most common approaches is to use low molecular weight hydrocarbons during the synthesis. They coordinate to the surface of the nanoparticle via a functional head group such as amine, thiol or carboxylic acid. However, for many applications this initial stabilization is not sufficient. It is often desirable to attach macromolecules such as polymers to the nanoparticle surface. This can be done either via covalently binding or coordinating.

For covalent binding either the ‘grafting-to’ (polymer growth is directly on the surface of particles covered with initiator) or the ‘grafting-from’ (using pre-synthesized polymer with functional end group, e. g. hydroxyl groups) approach can be used. As a disadvantage, it is very difficult to realize high grafting densities of the ligand on the nanoparticle surface using both methods[54].

For non-covalent binding the ligand exchange method is employed. In this case the low molecular weight ligands from the synthesis are exchanged for the polymeric ligands. To achieve this the polymer chains also carry a functional end group such as pentaethylene hexamine (PEHA) or diethylene triamine [55]. Furthermore, the binding strength of PEHA is sufficiently high without binding too strong to the nanoparticle. Thus, the surface coordination shows a certain reversibility, which allows a moderate mobility of the polymeric ligand on the nanoparticle surface (Figure 1.6). Because of the surface mobility of the end groups, bound polymer chains can relocalize on the surface to facilitate attachment of further polymer chains to yield very high brush densities.

The ligand exchange approach is very versatile and allows to precisely control the grafting density parameter. It is calculated using Equation 1.10

$$\sigma_{TGA} = \frac{\frac{wt\%_{shell}}{wt\%_{core}} \rho_{core} \frac{4}{3} \pi r_{core}^3 N_A}{M_w 4\pi r_{core}^2} \quad 1.10$$

where the relative mass of the polymer $wt\%_{shell}$ and the residual mass of the pure iron oxide nanocrystal $wt\%_{core}$ can be found from the experimental thermogravimetric analysis (TGA) data. Moreover, the method provides the controlled aggregation of nanoparticles, which is desirable for applications for e.g. an increased electrical or thermal conductivity[56].

In the current work nanocomposites of iron oxide nanoparticles stabilized with polystyrene polymer chains were studied, and grafting to the surface was performed using the ligand exchange approach.

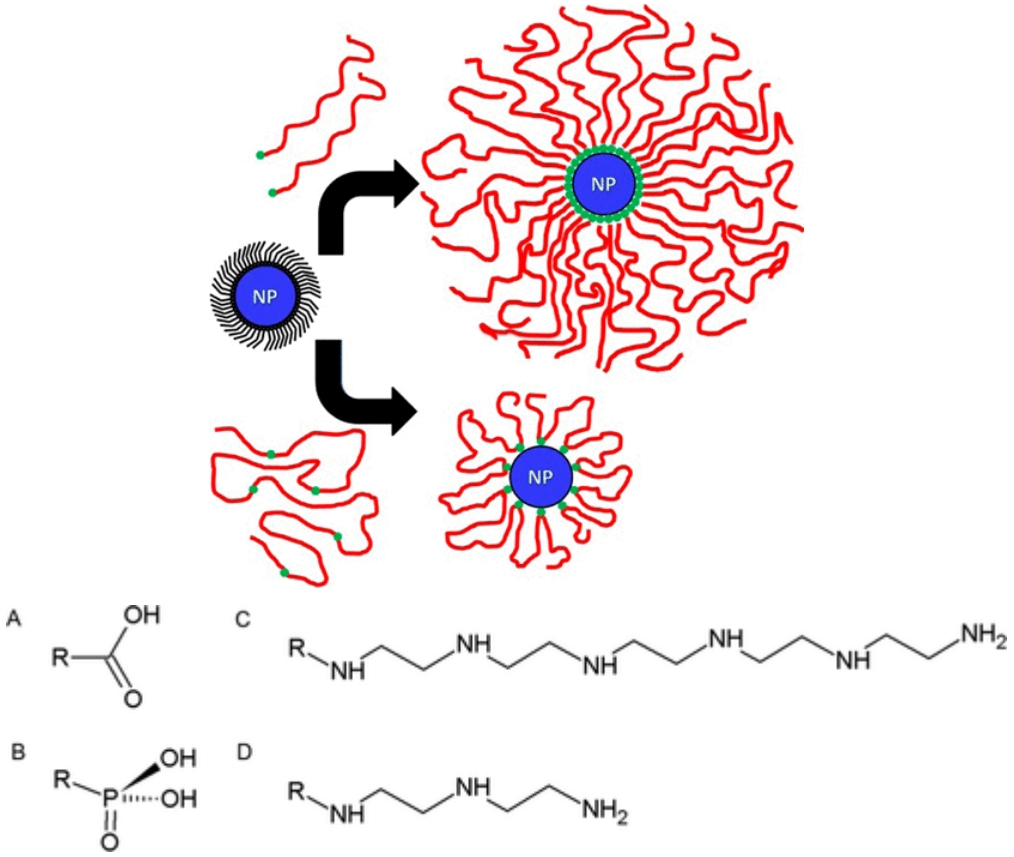

Figure 1.6 Nanocrystal coated with oleic acid (black), which is exchanged against a polymer (red) with a coordinating end-group (green) . Suitable coordinating groups for polymer ligand exchange: (A) carboxylic acid (-COOH), (B) phosphonic acid (-PO(OH)$_2$), (C) pentaethylenehexamine (-PEHA), and (D) diethylenetriamine (-DETA). R represents the polymer chain, which in the present study comprises polystyrene (PS), poly(methyl methacrylate) (PMMA), and polyisoprene (PI). Adapted with permission from Sascha Ehlert, Sara Mehdizadeh Taheri, Daniela Pirner, et al Polymer Ligand Exchange to Control Stabilization and Compatibilization of Nanocrystals Copyright © 2014, American Chemical Society

1.2.5 Self - assembly of nanoparticles

Self-assembly process occurs at all size scales, in the form of either static or dynamic self-assembly. Static self-assembly utilizes interactions amongst the nanoparticles to achieve a free-energy minimum. In solutions, it is an outcome of random motion of molecules and the affinity of their binding sites for one another. A dynamic system is forced to not reach equilibrium by supplying the system with a continuous, external source of energy to balance attractive and repulsive forces. Static self-assembly is significantly slower compared to dynamic self-assembly as it depends on the random chemical interactions between particles[57].

Self assembly can be directed in two ways. The first is by manipulating the intrinsic properties which includes changing the directionality of interactions or changing particle shapes. Self-assembly of nanoparticles in most cases refers to not covalently linked building blocks whose organization is driven by weak forces such as van der Waals forces or hard-particle interaction. The second is through external manipulation by applying and combining the effects of several kinds of fields such as temperature, shearing, electric, ultrasound, light or magnetic fields.

The controlled organization within a self-assembled material allows for interaction of the single components. Thus, these materials demonstrate outstanding, collective properties and are suitable for many applications where it is inappropriate to use individual building blocks[58–60]. Examples for the application of self-assembled structures are biosensors and digital memory devices. For that an extremely high level of direction and control is required and developing a simple, efficient method to organize molecules and molecular clusters into precise, predetermined structures is crucial[61].

Most molecules are far from spherical, and both their size and shape determine how they will pack in their different solid or liquid-crystalline phases. The sizes and shapes of large complex and asymmetric molecules such as surfactants, lipids, polymers, proteins, and other biological macromolecules, are particularly important in determining how they can pack together, ‘self-assemble’, or fold into structures such as micelles, membranes, and proteins in water, which in turn determines many of their properties. Packing mismatches are particularly important in the interactions of nano-, micro- and macroscopic particles. For example, a concentrated dispersion of spherical colloidal particles of uniform diameter can order into a solid-like lattice, but when a few larger spheres are present, these will tend to associate into clusters or collect at certain interfacial regions or grain boundaries rather than be randomly dispersed [46].

Considering a close-packed lattice of identical spherical molecules or particles the maximum volume fraction or density of close-packed spheres is $\pi/3\sqrt{2} = 0.74$ or 0.74% of the total volume, where each sphere has 12 nearest neighbors. This is known as close-packing (CP), and it occurs in the FCC and HCP lattices of many van der Waals solids, metals, C_{60} (bucky-balls), and spherical colloidal particles that form colloidal crystals in solution. There is also a noncrystalline but solid structure in which spherical molecules or particles are randomly ordered yet as close-packed as they can be. This is known as random close-packing (RCP), which occurs at a packing density of approximately 64% and where on average each sphere has about eight contact points with its neighbors. There will be no long-range crystalline order, but neither will the spheres be able to move collectively or flow, since the structure has become "frozen" into an amorphous solid. For bulk flow to occur, the spheres have to be able to move past each other. This requires some additional free volume that is not available in the random close-packing configuration. The density at which a collection of random hard spheres can flow is about 55% and is known as random loose packing (RLP). Clearly, when compacted molecules or particles are forced to flow or shear, they can do this only by expanding first, a phenomenon known as 'dilatency'. A sample of a material is called dilative if its volume increases with increasing shear and contractive if the volume decreases with increasing shear.

1.3 Magnetic interactions. Superparamagnetism

Magnetism arises from three sources such as electric current, spin magnetic moments of elementary particles or changing electric fields. The magnetic properties of materials are mainly due to the magnetic moments of their atoms' orbiting electrons. The magnetic moments of the nuclei of atoms are typically thousands of times smaller than the electrons' magnetic moments, so they are negligible in the context of the magnetization of materials. Nuclear magnetic moments are nevertheless important in other contexts, particularly in nuclear magnetic resonance (NMR) and magnetic resonance imaging (MRI).

In diamagnetism or paramagnetism for localized moments, the magnetic moments are independent and very weak magnetic interaction exist. However, some solids show long-range magnetic order (Figure 1.7). The group of materials is called ferromagnetic, when the orientation of the moments points in the same direction. When the ordering is alternating in opposite directions, it is known as antiferromagnetic. Finally, the material is ferrimagnetic when the ordering is in opposite directions but with different magnitudes of the sublattice moments. It means that an overall magnetisation is produced but not all the magnetic moments may give a positive contribution.

Superparamagnetism is a form of magnetism which appears in small ferromagnetic or ferrimagnetic nanoparticles. In sufficiently small nanoparticles, magnetization can randomly flip direction under the influence of temperature. The typical time between two flips is called the Neel relaxation time**.** In the absence of an external magnetic field, when the time used to measure the magnetization of the nanoparticles is much longer than the Neel relaxation time, their average value of magnetization appears to be zero: they are said to be in the superparamagnetic state. In this state, an external magnetic field is able to magnetize the nanoparticles, similar to a paramagnet. However, their magnetic susceptibility is much larger than that of paramagnets[62,63].

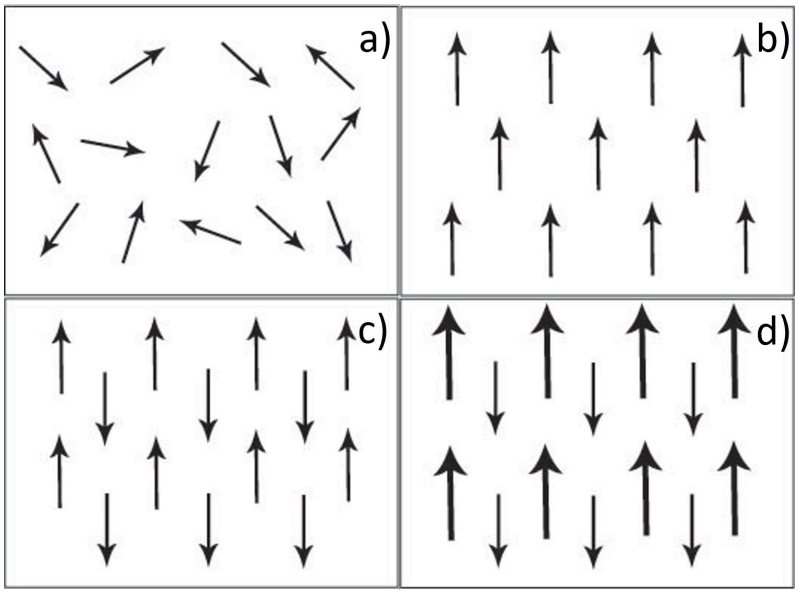

Figure 1.7 Types of the long-range magnetic order depending on the interactions between magnetic moments a) dipole moments randomly aligned in a paramagnetic sample b) aligned parallel in a ferromagnetic material c) adjacent magnetic dipole moments with equal magnitude aligned anti-parallel in an antiferromagnetic material d) magnetic moments of different magnitudes aligned anti-parallel in a ferrimagnetic material

Magnetic dipole–dipole interaction, also called dipolar coupling, refers to the direct interaction between two magnetic dipoles. Suppose $\overrightarrow{\mu_1}$ and $\overrightarrow{\mu_2}$ are two magnetic dipole moments that are far enough apart that they can be treated as point dipoles in calculating their interaction energy. Thus, potential energy of the interaction is given in Equation 1.11:

$$E_d = \frac{\mu_0}{4\pi r^3}\left[\overrightarrow{\mu_1}\cdot\overrightarrow{\mu_2} - \frac{3}{r^2}(\overrightarrow{\mu_1}\cdot\vec{r})(\overrightarrow{\mu_2}\cdot\vec{r})\right] \qquad 1.11$$

where where μ_0 is the magnetic constant, $\vec{r}$ is a unit vector parallel to the line joining the centers of the two dipoles, and r is the distance between the centers. The energy depends on the separation and the orientation of the moments.

For magnetic materials, after applying an external magnetic field $\vec{H}$, a magnetization (magnetic moment per volume) $\vec{M}$ is generally induced. In the simplest case

of a linear and isotropic response magnetization equals $\vec{M} = \chi\vec{H}$, where χ is the magnetic susceptibility. Depending on χ parameter all magnetic materials can roughly be distinguished in three classes: diamagnetic ($\chi < 0$), paramagnetic ($\chi > 0$), and ferromagnetic ($\chi \gg 1$).

An important energy contribution determines the direction of spontaneous magnetization in a magnetic material, which is known as the magnetic anisotropy. There are two directions in materials, one of them is called 'easy axis' and another one is 'hard axis'. Along the 'easy axis' the smaller magnetic field is required to magnetize a material. The overall anisotropy in a bulk material includes factors of magnetocrystalline anisotropy (dependance on the crystallographic direction) and magnetostatic demagnetization. Meanwhile, for nanostructures the shape, surface (unsaturated atoms) and strain anisotropy (e.g. due to the change of magnetization direction) are essential[64].

Referring back to superparamagnetic materials consisting of ferromagnetic or ferrimagnetic nanoparticles it is important to mention the formation of domain wall. It is determined by the competition between the energy cost for the wall formation E_{DW} and the energy reduction of the magnetostatic energy E_{MS}. For spherical particles of radius r the volume energy of magnetostatic energy is described in Equation 1.12:

$$E_{MS} = \frac{1}{2}\mu_0 N M_s^2 V \qquad 1.12$$

where N=4π/3 for sphere in demagnetizing factor, μ_0 is vacuum permeability, V is volume of the particle, Ms is the saturation magnetization. It means that magnetostatic energy is highly dependent on nanoparticles radius.

A single domain state is preferred in the particles, thus large values of magnetostatic energies are desirable. In Figure 1.8 various domain states are illustrated

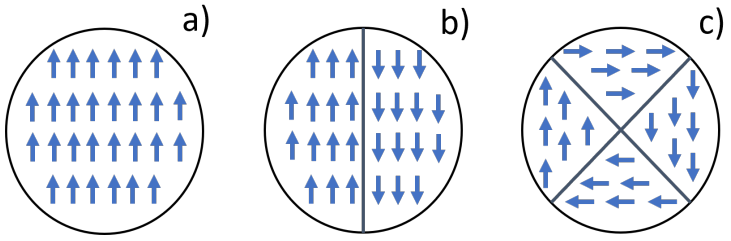

Figure 1.8 Schematic illustration of spherical particle in a) the single domain state and large magnetostatic energy b) two domain state with low magnetostatic energy and c) four domain state and $E_{MS} = 0$

The magnetic structure is divided into Weiss domains above a critical radius of particles. Decreasing the size leads to only a single remaining domain with the magnetisation along

a certain direction of the crystal. For smallest particles, the magnetisation becomes instable, it can flip by 180° due to thermal energy.

Ferromagnetic nanoparticles are magnetised uniformly along an applied magnetic field but lose this magnetisation due to thermal fluctuation without external field. The main contrast to classical paramagnets is the high magnetic moment of superparamagnetic particles in a magnetic field which leads to a high susceptibility. However, at low temperatures, the thermal energy is not sufficient to flip the magnetisation of the particles and therefore, they show the typical hysteresis of a ferromagnetic material. The temperature that divides these two states is called the blocking temperature T_B, which depends on the nanoparticle size, chemical composition and anisotropy.

Applying an alternating magnetic field to superparamagnetic nanoparticles can lead to two different responses of magnetic nanoparticles: above T_B the magnetic moment within the nanoparticle flips (Néel relaxation), below T_B the particle itself rotates with the field direction (Brown relaxation)[65–67].

One of the most popular types of magnetic nanoparticles is iron oxide. It found application in nanoelectronics and biophysics[68–71]. Out of all the variety of iron oxides there are four which are widely investigated and used: Wüstite, Hematite, Magnetite and Maghemite.

The most common mineral of all iron oxides is Fe_3O_4 magnetite, it has a spinel structure with the space group Fd3m with the lattice parameter 0.84 nm. This material also has the saturation of magnetization value equal 480 kA/m and magnetic moment of $4\mu_\beta$ and the critical radius of single domain nanoparticles $r_c = 50$ nm.

1.4 Experimental techniques

1.4.1 Small-angle X-ray scattering

Small-angle scattering (SAS) is a technique that can probe the structural organization of matter and its changes in external conditions. X-ray and neutron scattering profiles measured from bulk materials or materials deposited at surfaces arise from nanostructural inhomogeneities of electron or nuclear density. The technique allows to prepare and measure samples in situ, moreover, the measurements are performed at various external atmospheres such as temperatures, pressures, flows, shears or stresses, electric fields, and in a time-resolved fashion[72].

It is based on the measurement of the intensity *I*, of scattered X-rays or neutrons as a function of the scattering angle. The intensities are a summed convolution of the angle-

dependent interference of the squared scattering amplitudes of X-ray or neutron spherical waves arising from all atoms irradiated by the incident beam. The resulting intensity pattern $I(q)$ is expressed as a function of the magnitude of the momentum transfer vector q:

$$q = 4\pi sin\,\theta/\lambda \qquad 1.13$$

where 2θ is the scattering angle and λ is the radiation wavelength. The reciprocal relationship between the scattering angle and the length scales probed in the sample equals $d = 2\pi/q$. As a result, the scattering intensities relate to the structures and the distribution of subcomponents either within the occupied volume elements of bulk materials or deposited at surfaces.

In this thesis, the focus on the use SAXS technique for the characterization of nanoparticle systems was chosen. Comparable to electron microscopy X-ray scattering makes use of the variation of a sample's electron density to generate contrast. Concerning the probing capability the electron microscopy allows to "look" at very specific areas, while SAS technique probes large volumes containing billions of objects. Both techniques provide the same information; however, the former yields real space images while the latter provides reciprocal space data. As "reciprocal" implies, a spatial variation of electron density at nanometer length scales will scatter an X-ray beam to low angles while that in the atomic scale will scatter to high angles. Small-angle X-ray scattering (SAXS) is therefore a technique to study material structures at large distances, or small angles. Conversely, wide-angle X-ray scattering (WAXS) is used to measure the scattering intensity at large angles, or small distances.

When X-ray beam heats material a fraction of it will be absorbed and transformed to another form of energy (e.g. heat or fluorescence), and the other fraction will be scattered into other directions of propagation. In order to obtain qualitive SAXS data a sample should have an optimal thickness, which depends on the linear absorption coefficient μ. This parameter can be calculated from mass-absorption coefficient $\frac{\mu}{\rho_m}$, which tabulated and related to atomic species of material, material density ρ_m and wavelength.

There are two types of scattering concerning beam interaction with a substance: elastic and inelastic. The elastic scattering of X-ray photons may be viewed as occurring from the interaction between the incident X-ray field and individual electrons, without an associated change in energy. A free electron has a defined scattering length determined by the classical electron radius known as the Thomson scattering length. The elastic or coherent scattering length of atoms scales to the atomic number, thus the more electrons present in an atomic shell the higher is the probability of a scattering event. Electrons also

have an associated inelastic cross section, where both a change in the energy and direction of a scattered X-ray photon occurs (Compton scattering). Inelastic X-ray scattering is typically orders of magnitude smaller than elastic scattering and is linked to electron bonding and orbital/valence occupancy states. Meanwhile, the contributions of incoherent inelastic X-ray scattering to a SAXS profile are small.

Each atom has a certain probability of scattering or absorbing an incident X-ray photon or neutron at a particular energy, which is described by its scattering factor. The probability of producing a scattering event is known as the differential scattering cross section, which has units of square centimeters or barns (1×10^{-24} cm^2). The scattering cross section describes the magnitude of the interaction that yields a particular type of scattering event, taking into account the flux (the number of photons or neutrons delivered per unit of time) and energy. The differential scattering cross section $\frac{d\sigma}{d\Omega} = b^2$ is quantified by the scattering length b, which is a measure of how much a neutron/X-ray interacts with a nucleus/electrons (expressed in centimeters). So the scattering length of a single electron b_e is defined as

$$b_e = r_e \sqrt{\frac{1 + cos^2 2\theta}{2}} \tag{1.14}$$

Since one is usually interested in the distribution of scattering centers in a volume, the density of scattering length per unit volume is

$$\rho(r) = \frac{b_e(r)}{V} \tag{1.15}$$

When X-ray beam scatters at atoms they emit spherical waves, which produce interference patterns at the detector's position. The interferences can be constructive (in phase), destructive (out of phase) or somewhere in-between depending on the observation angle, the orientation and the distance of the light-emitting atoms from each other. In the first case, the interference causes a bright spot at the detector and in a destructive constellation the waves extinguish each other, thus producing a dark spot at the detector. It results in a 2D interference pattern, where the intensity varies with position in the detection plane (usually measured in terms of scattering angle 2θ and azimuthal angle φ). The interference pattern of material is characteristic to the orientation and distances of the atoms relative to

each other. Every distance is measured relative to the wavelength of the applied radiation as shown in Equation 1.13 [73].

The schematic experimental set-up for a classical SAS experiment is represented in Figure 1.9. It consists of a source of radiation and a set of optical devices that define the beam energy and shape the beam geometry and direction (slits/collimation system). This collimation system is typical for synchrotron instruments, which differ from laboratory source machines. As the source is much farther from the sample all optical paths are much longer and due to the much much higher intensity more precise optics can be used. But the principles to shape the beam before it hits the sample are the same in both types of setup. A sample is placed in the incident beam and the scattering profile is recorded on a 2D detector. The 2D area detector is used to collect the angle-resolved SAXS signal that is elastically scattered (without any change in wavelength) by the sample. The beam monitor m_1 is used to correct for any variation of incoming flux, while the monitor m_2 is typically mounted on the beamstop and is used to normalize the transmittance of the sample. Standard calibrants should be measured each time the setup is changed, for example, silver behenate to determine the sample-to-detector distance, and glassy carbon or water to determine the absolute intensity[74].

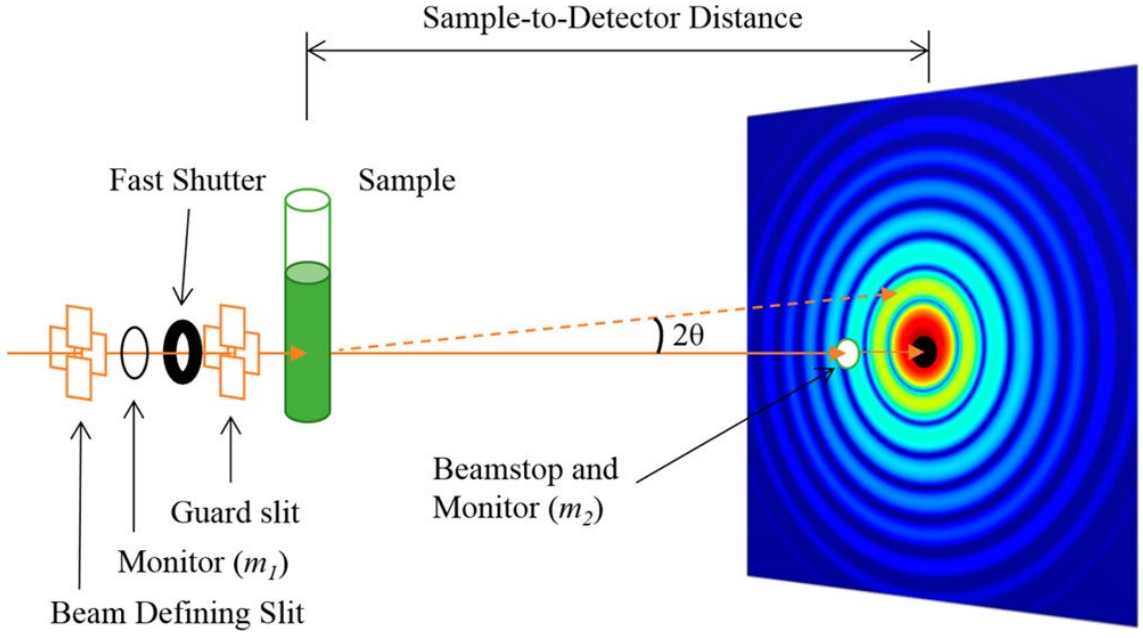

Figure 1.9 Schematic representation of the SAS experiment. Reprinted with permission from reference[74] Copyright © 2016, American Chemical Society

The measurement of elastic and coherent scattering phenomena provides structural information relating to preserved spatial correlations between scattering centers embedded within, and between, contiguous regions of different average scattering length density ρ in a material. So for a homogeneous mixture of nanoparticles in a solvent, the contrast value can be calculated as the averaged difference between the summed contributions of all

correlated distance and time-preserved atomic positions within the particle volume and the scattering length density of the solvent. Thus, it defines the magnitude of the scattering signal[72].

$$\Delta\rho(\boldsymbol{r}) = \rho(\boldsymbol{r}) - \rho_{bgr} \quad 1.16$$

After the subtracting background scattering contributions, an isotropic scattering profile can be described by the absolute square of the Fourier transform of $\Delta\rho(\boldsymbol{r})$ taken over the coherently scattering volume V:

$$I(q) = \frac{1}{V}\left|\int_V \Delta\rho(\boldsymbol{r}) exp\,(i\boldsymbol{q}\cdot\boldsymbol{r})d\boldsymbol{r}\right|^2 \quad 1.17$$

Scattering of a single particle results in the interference pattern (square of wave amplitudes' sum), which oscillates in a fashion that is characteristic for the shape of the particle. In the real experiment situations many particles are illuminated at the same time and the observed scattering pattern corresponds to the form factor of one particle only, if the particles are uniform and monodisperse, and they are far away from each other (i.e., dilute sample). For chaotically tumbling systems of identical particles, the intensity depends only on the magnitude of **q**:

$$I(q) = n\Delta\rho^2 V^2 P(q) S(q) \quad 1.18$$

where n is the number density of particles, V is the volume of a single particle and the rotationally averaged scattering form factor of the particle $P(q)$ is:

$$P(q) = \frac{1}{V^2}\left\langle\left|\int_V exp(i\boldsymbol{q}\cdot\boldsymbol{r})d\boldsymbol{r}\right|^2\right\rangle \quad 1.19$$

The term $S(q)$ is the scattering structure factor, which describes the interference of scattering waves from between different neighbouring particles in the sample and should not be confused with structure factors in crystallography that refer to diffraction amplitudes arising from preserved atomic positions between crystal lattice planes.

Interpretation of results is individual for each system and type of experiment. Generally, small-angle scattering curves can be divided into several regions (forward scattering, Guinier regime, Debye regime, and Porod regime), which give various information about studied structures. For instance, the spherical form factor of particles and various structural factors are presented in Figure 1.10.

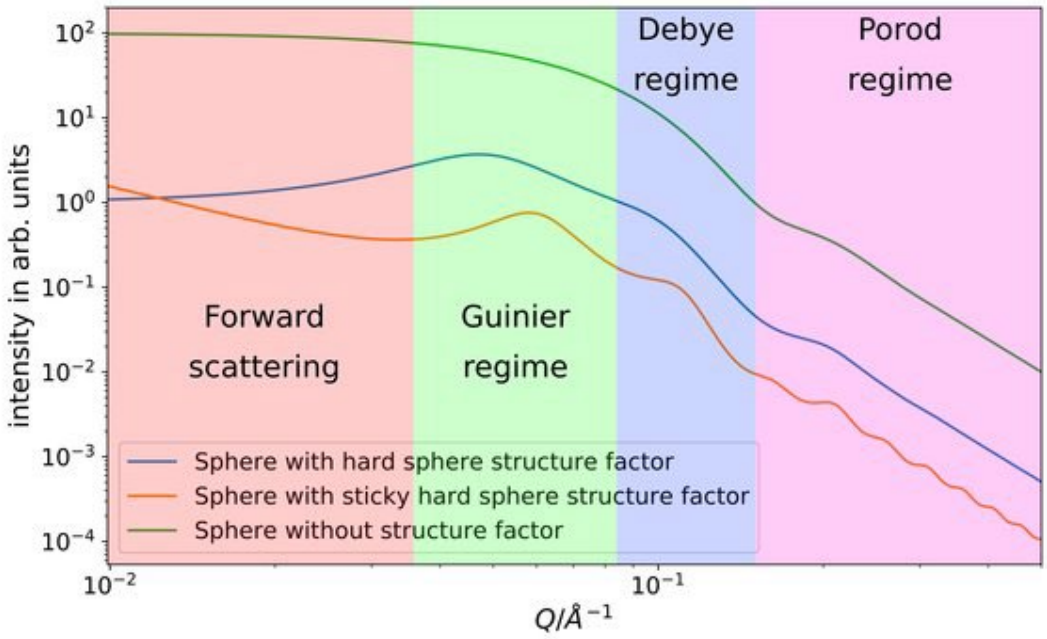

Figure 1.10 Diverse scattering curves from identical spherical form factors and different structure factors. The image originates from the reference [75]

A steep increase of scattering intensity at low q region of forward scattering indicates larger aggregates. In addition, two types of sphere interaction can be distinguished in this region: strongly repulsive interaction of hard spheres and attractive interaction of sticky spheres. For dilute solutions or a weak potential between the particles only the structure factor of a single particle is visible. In the Guinier region, the forward scattering isn't dominant and the slope of the scattering curve changes to the scattering intensity of the form factor, so the overall particle size can be determined using Guinier law:

$$I(q) = \rho_0 v^2 exp\left(\frac{-q^2 R_g^2}{3}\right) \qquad 1.20$$

The gyration radius $R_g = \frac{1}{V}\int_V r^2 \rho_0 dr$ provides information about nanoparticle dimension depending on it's shape, and for solid spheres of radius R it equals $R_g = \sqrt{\frac{3}{5}}R$, for the rod of length L $R_g = \frac{1}{\sqrt{12}}L$, and for a circular disk $R_g = \frac{1}{\sqrt{2}}R$.

In the Debye regime, the scattering can be scaled with $I(q)\, q^{-D}$, where D is the dimensionality of the scattering object (for spheres D = 3). Here the scattering from fractal objects is possible, so the slope of scattering curves can have also non-integer values and refer to the surface and mass fractals. In the Porod regime, the interface between the particle

and the solvent dominates the scattered intensity. The higher order terms don't present at large q but only the characteristic behavior of the scattered intensity Q^{-4}. The complete amount of the surface in the sample can be determined from the absolute intensity of the Porod regime[75].

Real scattering systems don't have ideal size and shape distribution, therefore the scattered intensity should be convoluted with the size distribution function *f(r)*. It gives the effect of convolution, so the minima of scattering curves are smeared out or vanished completely. The magnitude of polydispersity is polydispersity index $PDI = \sigma\big(f(r)\big)/\mu\big(f(r)\big)$, where $\sigma\big(f(r)\big)$ is the standard deviation of the size distribution function and $\mu\big(f(r)\big)$ is the mean of the size distribution function.

At high concentrations, the nanoparticles can form periodic lattices for which the structure factor can be described as:

$$S(q) = 1 + \beta(q)(Z(q) - 1)G(q) \qquad 1.21$$

where $\beta(q)$ is the diffuse scattering due to particle polydispersity leading to an intensity increase at high q, $Z(\mathrm{q})$ the lattice factor, and $G(\mathrm{q})$ the isotropic Debye-Waller factor. The lattice factor $Z(Q)$ determines the shape of the function and can be calculated for an ideal lattice by:

$$Z(q) = \frac{(2\pi)^{d-1} c}{n V_d \Omega_d q^{d-1}} \sum_{\{hkl\}} m_{hkl} f_{hkl}^2 L_{hkl}(q) \qquad 1.22$$

Here, d denotes the dimension of the unit cell, c the Porod constant, n the number of particles per unit cell, V_d the volume of the unit cell, Ω_d the solid angle. The Miller indices describe lattice planes in the crystal leading to a Bragg reflex and depend on the crystal symmetry. The intensity and locations of the peaks are defined by peak multiplicity m_{hkl} and symmetry factor f_{hkl}, the shape is characterized by the function L_{hkl} (q) for which e.g. either a Lorentzian or Gaussian functions can be used. The sum is then made over all reflections.

In the scattering patterns, a decrease in intensity can be found for the peaks at higher q values. The most prominent reason for this is the Debye-Waller factor which arises from the thermal displacement of the particles around their lattice positions $G(q) = e^{-\sigma_D^2 q^2 d_p^2}$. Here d_p is the nearest neighbor distance, $\sigma_D^2$is the mean squared displacement. When a sample has a crystalline structure the scattering curve gets narrow peaks of a lattice

structure factor, and the 2D image turns to be anisotropic. The scattered beam leaves a diffraction pattern which is varied depending on the direction in which the structure is observed. Reducing the domain size leads to a significant drop in the peak intensity and broader peaks.

1.4.2 Transmission electron microscopy

In a transmission electron microscope (TEM), electrons penetrate a thin specimen and are then imaged by the appropriate lenses, in a broad analogy with the biological light microscope (Figure 1.11). Transmission electron microscopes are capable of imaging at a significantly higher resolution than light microscopes, owing to the smaller de Broglie wavelength of electrons. Recent electron microscopes can achieve resolutions well below 1 Å.

When the electron beam hits the specimen three types of interactions can be distinguished: the electrons pass through the sample, and they are scattered in an elastic or inelastic way. In the first case electrons have no interaction with any part of the sample and therefore a TEM image has the brightest parts. In the case of elastic scattering, almost no energy is transferred as the incoming electron interacts with the atom core. The positive charge of the nucleus deflects the electron and due to the big difference in mass, almost no energy is exchanged. However, the scattering angle and thus the deviation from the primary beam can be up to 180°. Thus, elastic scattering is responsible for the majority of contrast in TEM images. Finally, inelastic scattering occurs because the beam electrons interact with the electrons in the atomic shell, which results in a considerable loss of energy, while the scattering angle remains relatively small.

The contrast in a TEM image is generated by several different contributions. The significant influence comes from the areas with larger thicknesses and higher atomic numbers or vice versa. The first type appears darker because fewer electrons reach the detector. On the other hand, lighter elements and thinner areas appear brighter.

TEM instruments have multiple operating modes including conventional imaging, scanning TEM imaging (STEM), diffraction, spectroscopy, and combinations of these. Each mechanism tells the user a different kind of information, depending not only on the contrast mechanism but on how the microscope is used—the settings of lenses, apertures, and detectors. Contrast can arise from position-to-position differences in the thickness or density, atomic number, crystal structure or orientation, the slight quantum-mechanical phase shifts that individual atoms produce in electrons that pass through them (‘phase

contrast'), the energy lost by electrons on passing through the sample ("spectrum imaging") and more.

This overall flexibility is achieved with an electron-optical system containing an electron gun (which produces the beam of electrons) and several magnetic lenses, stacked vertically to form a lens column. It is convenient to divide the instrument into three sections: the illumination system, the specimen stage, and the imaging system.

The illumination system comprises the electron gun, together with two or more condenser lenses that focus the electrons onto the specimen. Its design and operation determine the diameter of the electron beam at the specimen and the intensity level in the final TEM image. The specimen stage allows specimens to be held stationary, or else intentionally moved, its mechanical stability is an important factor in determining the spatial resolution of the TEM image. The imaging system contains at least three lenses that together produce a magnified image (or a diffraction pattern) of the specimen on a fluorescent screen, for immediate viewing or recording by an electronic camera system. How the imaging lenses are operated determines the magnification of the TEM image, while their design specifications largely determine the spatial resolution that can be obtained from the microscope[76,77].

For nanomaterial analysis, the wavelength of the used radiation needs to be in a suitable range, which can be achieved by using high-energy accelerated electrons. The wavelength of an electron is defined by the de Broglie wavelength λ as given in Equation 1.23:

$$\lambda = \frac{h}{p} = \frac{h}{m_e v} = \frac{h}{\sqrt{2m_0 E_k \left(1 + \frac{E_k}{2m_e}\right) c^2}} \qquad 1.23$$

where the kinetic energies $E_k = eU$, h is the Planck constant, p is the momentum, m_e is the mass of the electron and v is the velocity of the electron (determined by the electron gun accelerating voltage U), e is the elementary charge and c is the speed of light[78].

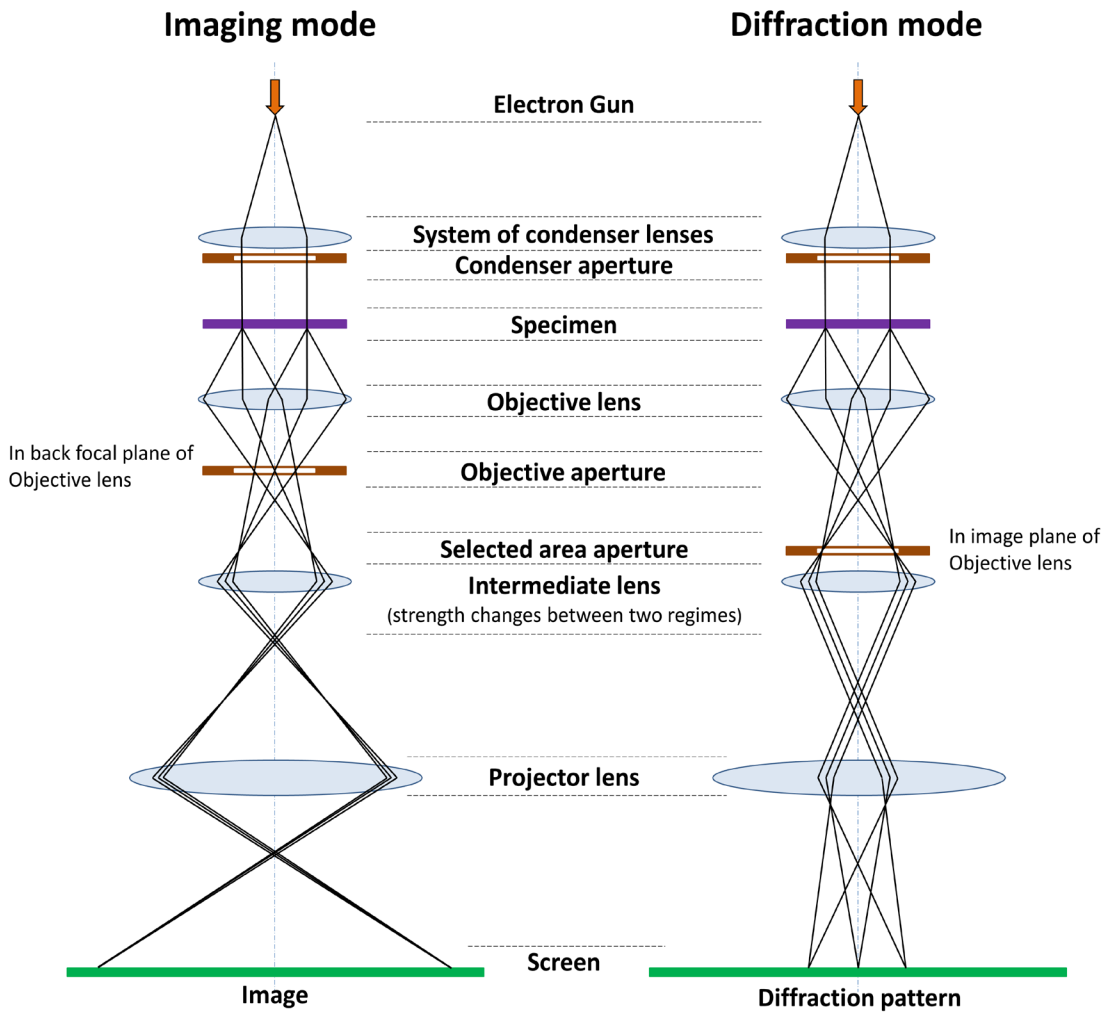

Figure 1.11 Schematic view of imaging and diffraction modes in TEM. Attribution: Eric Kvaalen, CC BY-SA 4.0 via Wikimedia Commons.

1.4.3 Rheology

Rheology is the science of the flow and deformation of matter, and the relationship between stress and deformation is a property of the material. Of special interest are the materials which do not follow Newton's law of viscosity. Newtonian fluids can be characterized by a single coefficient of viscosity for a specific temperature. Although this viscosity will change with temperature, it does not change with the strain rate. The large class of fluids whose viscosity changes with the strain rate (the relative flow velocity) is called non-Newtonian fluids. Research of non-Newtonian fluids is carried out in the paint and lacquer industry, oil drilling, food industry, pharmacology, and polymer processing. Polymers consist of long-chain macromolecules, which significantly impact their non-Newtonian flow behavior, thus polymers are defined as viscoelastic materials. The reasons for non-Newtonian behavior can be found in the molecular structure: polymers consist of long

molecules that entangle with each other, forming several flexible, reversible "joints". These enable different conformations of the molecules by a rotation along the backbone and cause the elastic behavior of polymer melts. The chains can also move with respect to each other by a crawling kind of movement called reptation. These rotation and reptation occurring above the glass transition temperature of the polymer are called Brownian motions, and they tend to return the molecules towards the equilibrium, i.e., to the energetically most preferable state, after being oriented by applying deforming stress[79,80].

The deformation of a matter can be described using a two-plate model of shear rheometry. Shear is in this case applied to a sample sandwiched between the two plates where the lower plate act as the stationary plate that will not move around, while the upper plate will move with the presence of shear force *F (*Figure 1.12*)*. The external force takes the form of a shear stress σ which is defined as the force F acting over a unit area A, thus $\sigma = \frac{F}{A}$. In response to this force, the upper layer will move to a given distance Δx, while the bottom layer remains constant and parallel with the gap h. The displacement gradient across the sample is shear strain $\gamma = \Delta x h$. For a solid material, the strain will be limited for applied stress where flow behavior is impossible. Contrarily, the shear strain will continue to increase for the period of applied stress for a liquid material where the constituent components can move relative to one another and creates the shear rate $\dot{\gamma} = \Delta\gamma\Delta t$, which is the rate of change of shear strain with time.

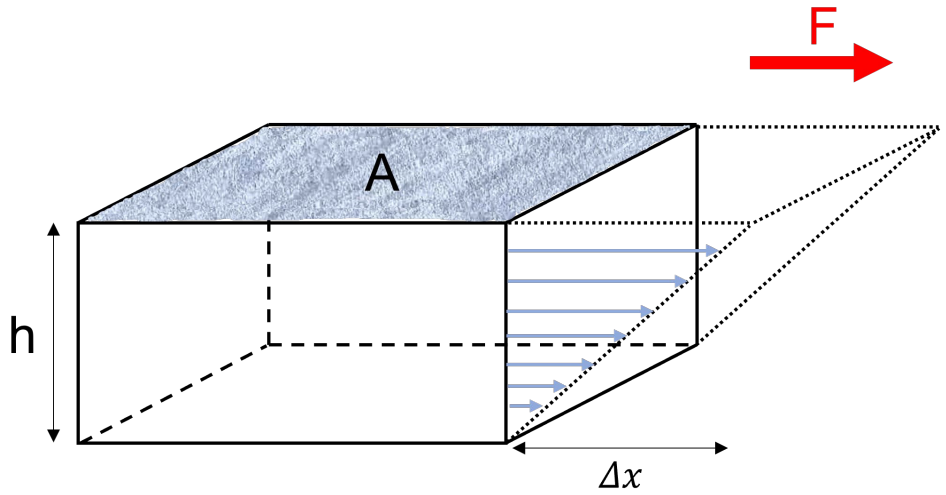

Figure 1.12 Schematic representation of a sheared object for a two-plate model

Shear modulus is a property of viscoelastic materials that equals the ratio of stress to strain $G = \frac{\sigma}{\gamma}$. Other important viscoelastic parameters are the storage G′ and the loss modulus G′′. The Elastic (Storage) Modulus is the ability of the material to store energy. The Viscous (Loss) Modulus is the ability to dissipate energy through heat. When shear

modulus G is independent of the magnitude of strain γ, the response of the material is linear, which means that stress $\gamma \to 0$. The linear viscoelastic region of a material is determined in an oscillatory measurement at a constant frequency with increasing stress or strain amplitude. The measured moduli remain constant as long as the critical strain has not been reached. The end of the linear region is given by a decrease in viscosity or elastic modulus and an increase in the phase shift. The ratio of the moduli G´´/ G´ is defined as $tan\delta$, and indicates the relative degree of energy dissipation or damping of the material[81].

Rheology allows us to characterize the flow of materials that exhibit a combination of elastic, viscous, and plastic behavior by properly combining elasticity and fluid mechanics. The relationship between elastic shear stress r_e and strain γ for fully elastic materials, such as metals, is determined by Hooke's law: $r_e = G\gamma$. For pure viscous liquids deformation is time-dependent, and the relationship between the viscous shear stress r_v and strain rate $\dot{\gamma}$ is determined by Newton's law: $r_v = \eta\dot{\gamma}$. The Newtonian and Hookean laws represent two extremes. Most materials however show some characteristics of both elastic and viscous behavior and can be described by combining springs and dashpots parallel or in series. Maxwell and Kelvin models are schematically shown in Figure 1.13. The Maxwell model is a spring and dashpot assembled in series. In this model, the applied stress is the same for each element, the strain is additive. If a constant strain is applied to this model, the stress increases instantly to a maximum value determined by the elastic modulus of the spring and then relaxes exponentially to zero. How fast the stress relaxes is given by the relaxation time $t = G/h$.

$$\gamma = \gamma_{spring} + \gamma_{dashpot} = \frac{\sigma}{G} + \int \frac{\sigma}{\eta} dt \qquad 1.24$$

The Kelvin model consists of a spring and dashpot in parallel. The strain for this model is the same for both elements whereas the stress is additive. If constant stress is applied, the dashpot will initially take the entire load and the model deforms at a maximum rate. As the deformation increases, the spring contribution to the total stress increases and the deformation rate exponentially slows down to zero (deformation reaches its maximum value). At this point, the spring supports the total stress applied to the model. How fast the deformation reaches the maximum is given by the retardation time $\tau = \frac{G}{\eta}$.

$$\sigma = \sigma_{spring} + \sigma_{dashpot} = G \cdot \gamma + \eta \cdot \frac{d\gamma}{dt}\gamma \qquad 1.25$$

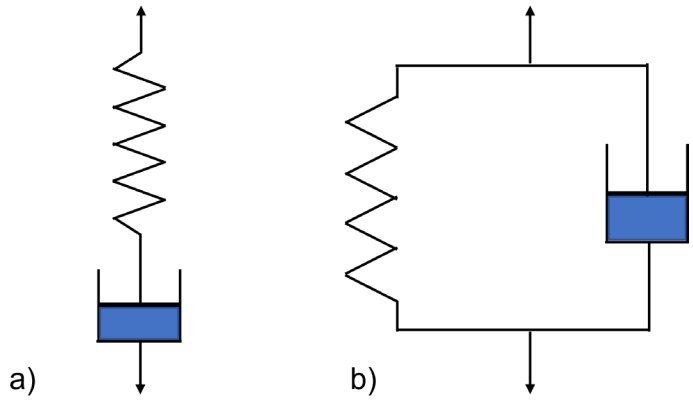

Figure 1.13 Maxwell and Kelvin models of viscoelastic behavior

In an oscillatory measurement the material is subjected to a sinusoidal stress or strain and the strain or stress response is measured. The general rheological behavior in an oscillation experiment can be described with the Maxwell model. At the application of a sinusoidal stress, the spring will expand instantaneously. The dashpot however retards the deformation of the overall system. Therefore, a phase shift δ between strain and stress is present. For a pure elastic material, for example steel, the maximum stress occurs at the maximum strain and both stress and strain are in phase, δ = 0°. Whereas for a pure viscous material for example water, the maximum stress occurs when the strain rate is maximum and the stress and strain are said to be out of phase by 90°. On the other hand, most samples show viscoelastic behaviour where the phase difference between stress and strain occur between the two extremes, *i.e.,* 0° < δ < 90°. The phase angle shall not exceed 90° as the upper plate would turn in the opposite direction once the rotation angle exceeds 90°.

The ratio of the applied strain/stress to the measured stress/strain yields the complex modulus, G^*=G'+iG'' which describes the resistance of the sample to deform (viscoelastic behaviour). The $G'= G^*cos\delta$ represents the elastic component of the viscoelastic behaviour, also known as the real part of G^*. On the other hand, the $G''=sin\delta$ represents the viscous component, also known as imaginary part of G^*. Phase angle, δ is also expressed as the loss tangent, defined as $tan\frac{G''}{G'}$

All oscillatory experiments have to be carried out at small strain or stress amplitude to remain within the so-called linear viscoelastic region. Inside this region, which is limited by the critical stress (or strain), the material's structure is in equilibrium and the relation between the applied stress and the measured quantities is linear; this means they are only a function of time or frequency at a constant temperature. Dynamic mechanical analysis processes both elastic and viscous material response simultaneously. In this type of experiment, a motor is used to either apply a sinusoidal strain or stress to a material and the

resulting stress is measured with a force transducer. The rheological material behavior can be measured as a function of time, temperature, strain, or stress amplitude and frequency. The results obtained provide information about the sample structural properties such as molecular weight and its distribution, concentration, crosslinking density for polymers or particle/domain size, shape, interface properties, and more.

A typical viscoelastic spectrum of a polymer spanning from low to high frequencies consists of a terminal, plateau, transition, and glassy zones. In the terminal zone, G′′> G′ is observed which indicates liquid-like behavior (flowing behavior). For a Maxwell fluid, the G′ and G′′ curves in the lower frequency range show a slope of 2 and 1, respectively. Furthermore, the time scale is associated with long-range relaxations in which the relaxation of the polymer chain happens faster than the deformation.

On the contrary, in the plateau zone, G′ > G′′ is observed which indicates solid-like behavior where the sample is not flowable. The time scale in the plateau zone is associated with short-range relaxation where it involves local segmental relaxation. Meanwhile, in the transition to the glassy zone, the response of the polymer chains is less dependent on the frequency applied. The high frequency applied is too high and the configurational rearrangements of the chains do not have enough time to take place. Finally, the glassy zone designates a glassy state, where the polymer chains have low mobility and thermodynamically a non-equilibrium state. However, in most cases, it is only possible to observe a fragment of this spectrum using a standard rheometer which depends on the sensitivity of the rheometer as well as the relaxation behavior of the material. A widely used principle used to extend the relaxation spectrum is the time-temperature superposition principle which uses the concept of time and temperature[79,81].

1.5 References

[1] S. E. Gad, *Encyclopedia of Toxicology: Third Edition* **2014**, 1045–1050.

[2] D. Braun, H. Cherdron, M. Rehahn, H. Ritter, B. Voit, *Polymer Synthesis: Theory and Practice: Fundamentals, Methods, Experiments* **2005**, 1–385.

[3] G. Odian, *Principles of Polymerization* **2004**, DOI 10.1002/047147875X.

[4] K. Matyjaszewski, *Controlled and living polymerizations : methods and materials; from mechanisms to applications* **2009**, XXI, 612 S.

[5] N. Hadjichristidis, S. Pispas, G. Floudas, *Block Copolymers: Synthetic Strategies, Physical Properties, and Applications* **2003**, 419.

[6] B. Lindman, Paschalis. Alexandridis, *Amphiphilic block copolymers : self-assembly and applications* **2000**, 435.

[7] Y. Mai, A. Eisenberg, *Chem Soc Rev* **2012**, *41*, 5969–5985.

[8] Förster Stephan, Plantenberg Thomas, "From Self-Organizing Polymers to Nanohybrid and Biomaterials," **2002**.

[9] M. W. Matsen, F. S. Bates, *Macromolecules* **1996**, *29*, 1091–1098.

[10] K. E. B. Doncom, L. D. Blackman, D. B. Wright, M. I. Gibson, R. K. O'Reilly, *Chem Soc Rev* **2017**, *46*, 4119–4134.

[11] A. Blanazs, S. P. Armes, A. J. Ryan, *Macromol Rapid Commun* **2009**, *30*, 267–277.

[12] H. W. D. F. Evans, *Chemistry, Biology, and Technology meet* **1999**, 424.

[13] J. Rodríguez-Hernández, F. Chécot, Y. Gnanou, S. Lecommandoux, *Prog Polym Sci* **2005**, *30*, 691–724.

[14] J. A. Pople, I. W. Hamley, J. P. A. Fairclough, A. J. Ryan, B. U. Komanschek, A. J. Gleeson, G. E. Yu, C. Booth, *Macromolecules* **1997**, *30*, 5721–5728.

[15] I. W. Hamley, J. A. Pople, C. Booth, Y. W. Yang, S. M. King, *Langmuir* **1998**, *14*, 3182–3186.

[16] D. Quémener, A. Deratani, S. Lecommandoux, *Top Curr Chem* **2012**, *322*, 165–192.

[17] P. Somasundaran, *Encyclopedia of Surface and Colloid Science, Third Edition* **2015**, DOI 10.1081/E-ESCS3.

[18] G. Riess, *Prog Polym Sci* **2003**, *28*, 1107–1170.

[19] N. Toropov, T. Vartanyan, *Comprehensive Nanoscience and Nanotechnology* **2019**, *1–5*, 61–88.

[20] I. Khan, K. Saeed, I. Khan, *Arabian Journal of Chemistry* **2019**, *12*, 908–931.

[21] D. D. Evanoff, G. Chumanov, *ChemPhysChem* **2005**, *6*, 1221–1231.

[22] S. Prabhu, E. K. Poulose, *International Nano Letters 2012 2:1* **2012**, *2*, 1–10.

[23] D. D. Evanoff, G. Chumanov, *ChemPhysChem* **2005**, *6*, 1221–1231.

[24] S. B. Rizvi, S. Ghaderi, M. Keshtgar, A. M. Seifalian *Semiconductor quantum dots as fluorescent probes for in vitro and in vivo bio-molecular and cellular imaging*, **2010**, *1*, 5161.

[25] Q. Guo, G. M. Ford, W. C. Yang, B. C. Walker, E. A. Stach, H. W. Hillhouse, R. Agrawal, *J Am Chem Soc* **2010**, *132*, 17384–17386.

[26] P. Iqbal, J. A. Preece, P. M. Mendes, *Supramol Chem* **2012**

[27] J. Park, J. Joo, G. K. Soon, Y. Jang, T. Hyeon, *Angewandte Chemie International Edition* **2007**, *46*, 4630–4660.

[28] N. Abid, A. M. Khan, S. Shujait, K. Chaudhary, M. Ikram, M. Imran, J. Haider, M. Khan, Q. Khan, M. Maqbool, *Adv Colloid Interface Sci* **2022**, *300*, 102597.

[29] R. Ghosh Chaudhuri, S. Paria, *Chem Rev* **2012**, *112*, 2373–2433.

[30] J. Wang, J. Polleux, J. Lim, B. Dunn, *Journal of Physical Chemistry C* **2007**, *111*, 14925–14931.

[31] I. Bilecka, M. Niederberger, *Electrochim Acta* **2010**, *55*, 7717–7725.

[32] B. Saif, C. Wang, D. Chuan, S. Shuang, B. Saif, C. Wang, D. Chuan, S. Shuang, *J Biomater Nanobiotechnol* **2015**, *6*, 267–275.

[33] S. Panigrahi, S. Kundu, S. Ghosh, S. Nath, T. Pal, *Journal of Nanoparticle Research 2004 6:4* **2004**, *6*, 411–414.

[34] K. S. Tan, K. Y. Cheong, *Journal of Nanoparticle Research 2013 15:4* **2013**, *15*, 1–29.

[35] X. Chun, S. C. Cheng, X. Lin, V. P. Dravid, Y. W. Chung, Y. Zhu, J. P. Hare, C. L. Reeves, A. K. Cheetham, M. Rühle, H. W. Kroto, D. R. M Walton, H. Chen, H. S. Yang, G. T. Wu, M. Wang, F. M. Deng, X. B. Zhang, J. C. Peng, W. Z. Li, B. A. Margaret Hines, G. D. Scholes, G. D. Scholes, M. A. Hines, *Advanced Materials* **2003**, *15*, 1844–1849.

[36] J. Park, J. Joo, G. K. Soon, Y. Jang, T. Hyeon, *Angewandte Chemie - International Edition* **2007**, *46*, 4630–4660.

[37] V. K. Lamer, R. H. Dinegar, *J Am Chem Soc* **1950**, *72*, 4847–4854.

[38] R. J. Deltete, *Found Chem* **2007**, *9*, 265–316.

[39] C. B. Whitehead, S. Özkar, R. G. Finke, *Mater Adv* **2021**, *2*, 186–235.

[40] P. W. Dunne, A. S. Munn, C. L. Starkey, T. A. Huddle, E. H. Lester, *Philosophical Transactions of the Royal Society A: Mathematical, Physical and Engineering Sciences* **2015**, *373*

[41] L. Ratke, P. W. Voorhees, *Growth and Coarsening: Ostwald Ripening in Materials Processing.* Springer-Verlag, **2002**.

[42] J. W. Mullin, *Crystallization: Chpater 5- Nucleation*, **2001**.

[43] J. Park, K. An, Y. Hwang, J. E. G. Park, H. J. Noh, J. Y. Kim, J. H. Park, N. M. Hwang, T. Hyeon, *Nat Mater* **2004**, *3*, 891–895.

[44] Jacob N. Israelachvili, "Intermolecular and Surface Forces ," **2011**.

[45] G. Lagaly, *Berichte der Bunsengesellschaft für physikalische Chemie* **1988**, *92*, 1058–1058.

[46] J. Israelachvili, *Intermolecular and Surface Forces* **2011**

[47] G. Brezesinski, H.-J. Mögel, *Grenzflächen und Kolloide: physikalisch-chemische Grundlagen* **1993**, 269.

[48] M. A. Boles, M. Engel, D. V. Talapin, *Chem Rev* **2016**, *116*, 11220–11289.

[49] I. G. Barnes G, *Interfacial Science: An Introduction* **2005**, 131, 215.

[50] Z. Sun, X. Yan, Y. Xiao, L. Hu, M. Eggersdorfer, D. Chen, Z. Yang, D. A. Weitz, *Particuology* **2022**, *64*, 153–163.

[51] J. Prabhuram, X. Wang, C. L. Hui, I. M. Hsing, *Journal of Physical Chemistry B* **2003**, *107*, 11057–11064.

[52] L. Shen, P. E. Laibinis, T. Alan Hatton, *Langmuir* **1999**, *15*, 447–453.

[53] Y. K. Takahara, S. Ikeda, S. Ishino, K. Tachi, K. Ikeue, T. Sakata, T. Hasegawa, H. Mori, M. Matsumura, B. Ohtani, *J Am Chem Soc* **2005**, *127*, 6271–6275.

[54] S. Minko, *Polymer Surfaces and Interfaces: Characterization, Modification and Applications* **2008**, 215–234.

[55] S. Ehlert, S. M. Taheri, D. Pirner, M. Drechsler, H. W. Schmidt, S. Förster, *ACS Nano* **2014**, *8*, 6114–6122.

[56] D. N. Benoit, H. Zhu, M. H. Lilierose, R. A. Verm, N. Ali, A. N. Morrison, J. D. Fortner, C. Avendano, V. L. Colvin, *Anal Chem* **2012**, *84*, 9238.

[57] B. Wang, Y. Zhang, Z. Guo, L. Zhang, *Materials Today* **2019**, *25*, 112–113.

[58] K. J. M. Bishop, C. E. Wilmer, S. Soh, B. A. Grzybowski, *Small* **2009**, *5*, 1600–1630.

[59] Z. Nie, A. Petukhova, E. Kumacheva, *Nat Nanotechnol* **2010**, *5*, 15–25.

[60] H. Aldewachi, T. Chalati, M. N. Woodroofe, N. Bricklebank, B. Sharrack, P. Gardiner, *Nanoscale* **2017**, *10*, 18–33.

[61] E. Shinn, A. Hübler, D. Lyon, M. G. Perdekamp, A. Bezryadin, A. Belkin, *Complexity* **2013**, *18*, 24–27.

[62] V. Marghussian, *Nano-Glass Ceramics* **2015**, 181–223.

[63] D. E. Laughlin, K. Hono, *Physical Metallurgy* **2014**, 1–2899.

[64] S. Bedanta, O. Petracic, W. Kleemann, *Handbook of Magnetic Materials* **2015**, *23*, 1–83.

[65] X. C. Sun *Microstructure characterization and magnetic properties of nanomaterials* **2009**, *100*, 3059–3063.

[66] M. Naitō, T. Yokoyama, K. Hosokawa, K. Nogi, Nanoparticle Technology Handbook **2018**

[67] O. Petracic, *Superlattices Microstruct* **2010**, *47*, 569–578.

[68] A. S. Kamzin, I. M. Obaidat, V. S. Kozlov, E. V. Voronina, V. Narayanaswamy, I. A. Al-Omari, *Physics of the Solid State 2021* **2021**, *2021*, 1–10.

[69] X. Guan, S. Yan, Q. Zeng, Z. Xu, Y. Chen, H. Fan, *Fibers and Polymers 2016 17:8* **2016**, *17*, 1131–1139.

[70] Ş. Yılmaz, A. Zengin, Y. Akbulut, T. Şahan, *Environmental Science and Pollution Research* **2019**, *26*, 20454–20468.

[71] J. Yan, S. Li, F. Cartieri, Z. Wang, T. K. Hitchens, J. Leonardo, S. E. Averick, K. Matyjaszewski, *ACS Appl Mater Interfaces* **2018**, *10*, 21901–21908.

[72] C. M. Jeffries, J. Ilavsky, A. Martel, S. Hinrichs, A. Meyer, J. S. Pedersen, A. V. Sokolova, D. I. Svergun, *Nature Reviews Methods Primers 2021 1:1* **2021**, *1*, 1–39.

[73] Heimo Schnablegger, Yashveer Singh, “The SAXS Guide. Getting acquainted with the principles,”, **2011**.

[74] T. Li, A. J. Senesi, B. Lee, *Chem Rev* **2016**, *116*, 11128–11180.

[75] “Scattering! Soft, functional and quantum materials : lecture notes of the 50th IFF Spring School 2019 - RWTH Publications

[76] D. B. Williams, C. B. Carter, *Transmission Electron Microscopy: A Textbook for Materials Science* **2009**, 1–760.

[77] G. H. Michler, W. Lebek, *Polymer Morphology: Principles, Characterization, and Processing* **2016**, 37–53.

[78] R. F. Egerton, *Physical Principles of Electron Microscopy: An Introduction to TEM, SEM, and AEM, Second Edition* **2016**, 1–196.

[79] H. Ramli, N. F. A. Zainal, M. Hess, C. H. Chan, *Chemistry Teacher International* **2022**, *4*, 307–326.

[80] J. Aho, *Rheological characterization of polymer melts in shear and extension : measurement reliability and data for practical processing* **2011**, *12*.

[81] T. P. Lodge, P. C. Hiemenz *Polymer Chemistry*, **2020**

2 Shearing-induced phase transitions in $C_{16}E_{20}$ polymer water solutions

2.1 Abstract

Low-symmetry Frank-Kasper phases, which are more typical for metals and their alloys were found in diblock copolymer melts a decade ago[1]. Since the hydrated diblock oligomer, $C_{16}E_{20}$ (Brij 58) forms the A15 phase at high concentrations > 49 wt% of surfactant, it is an attractive model for studying Frank-Kasper phases formation and related quasicrystal phases. In this work, we report the ordering of the A15 phase in 111 direction using a Small-angle scattering with a shearing technique and compare it to molecular dynamic simulations of the A15 order. We suggest several ways to achieve this long-range order with oscillating shearing at a constant 8 Hz frequency and either constant low 1.2% strain, high 100 % strain, or gradually increased up to 100% strain. In addition, it is shown that the influence of a slight temperature increase by 10 °C improves the order of the Frank-Kasper phase and ruins it when the value of temperature is close to 40°C. Finally, we demonstrate the difference between Lyotropic Liquid Crystals formed in commercial and homemade hydrated $C_{16}E_{20}$ polymer. Improved molecular weight distribution of the surfactant's hydrophobic part leads to the anisotropic pattern of the BCC phase, which transfers to the non-oriented A15, HPC, and Lamellar phases with shearing.

2.2 Introduction

Amphiphilic polymers are widely studied systems that tend to assemble in lyotropic liquid crystals (LLC)[2–5], for instance, face-centered cubic (FCC), body-centered cubic (BCC), hexagonally closest-packed (HCP), and lamellar phases. However, along with high-symmetry phases, soft materials also form Frank-Kasper (FK) phases, wherein multiple classes of symmetry-equivalent particles pack into large unit cells with ≥ 7 particles[6–10]. FK phases were reported in both metal alloys[11] and soft matter systems such as giant shape amphiphiles, block polymers, and functional nanoparticles[12–15]. The origin of these complex phases comes from the balance between the preferred local spherical particle symmetry and filling the space at a constant density to maximize interparticle Van der Waals interaction[16–18].

In comparison to metallic crystals, LLC phases of packed micelles can be easily tuned in several ways. The first one is changing starting parameters of the system like micelle size, and selectivity of the solvent for different blocks. The other way is applying

external forces, e.g. shearing and temperature, so that a lattice parameter, grain size, and the size of a resulting feature can be manipulated. Furthermore, the shearing technique often induces a long-range structural interaction, which is enabled by grain orientation alignment[19].

Earlier studies of concentration-dependent LLC phases formed by poly(ethylene-block-ethylene oxide) diblock oligomers in water reported the existence of both high-symmetry spherical micelles packings as well as FK phases[18,20–22]. Originally, commercial C_iE_j surfactants found an application in the synthesis of nanofiltration membranes with hydrophilic properties for the filtration of dye aqueous solution[23–29]. Built on flat and transparent thin chromium films, Brij and PEO mixed systems have been proven to be promising coatings for electrochemical biosensor applications such as stabilizing a partially tethered supported biomimetic membrane[30]. Also, Brij 58 was effectively used for the creation of chemical conversion coatings on zinc surfaces[31].

Previous research by Jayaraman et al.[18] showed aqueous LLC phases formation with $C_{16}E_{20}$ diblock oligomer and its concentration-dependent phase sequence FCC→BCC→A15→ hexagonal H1 at 25 °C. Moreover, the authors properly studied temperature-induced phase transitions A15→BCC→H1 and the reversible transition through the σ phase to A15 during quenching samples at room temperature. A later research work by Valentine and colleagues[19]introduced the difference in the temperature-initiated H1→A15 transition between quenching and shearing. Nevertheless, the ordering of the A15 phase on the long-range scale wasn't reported so far to the best of our knowledge.

In this chapter the small angle X-ray scattering analyses of aqueous systems with the commercial Brij 58 and homemade polymer at 49-58 wt% $C_{16}E_{20}$ concentration is presented. We aim to achieve the long-range ordering of the Frank-Kasper A15 phase under the shearing conditions, compare the influence of hydrophobic block size distribution on structural properties of the system and define the temperature and shearing conditions at which order-order phase transition is regular.

2.3 Results and discussion

2.3.1 Complex micelles packings of the hydrated di-block oligomer in water

Poly(ethylene-block-ethylene oxide) diblock oligomers ($C_{16}E_{20}$) form core-shell micelles in water solutions that pack into various lyotropic liquid crystals (LLCs). With an increase in polymer concentration, the core-shell ratio varies as well as the type of an ordered phase[20–22]. Generally, alkane chains are located in the core of radius R_c = 1.9 nm, while the PEO blocks are inside the shell together with water at a thickness of Rs = 3.13 nm. Micelle size parameters were determined from the core-shell fit of SAXS data (Supporting Information, Figure 2.11 a).

One of the most attractive phases, which is formed in highly concentrated surfactant/water mixtures is the Frank-Kasper A15 phase (Figure 2.1 a). It is a low-symmetry phase that belongs to the Pm3n space group and appears at certain values of the core volume fraction ϕ_{core} and λ parameter, where $\lambda = \frac{R_{core}+R_{shell}}{R_{core}}$. The phase diagram in Figure 2.1 c presents the dependence of a formed structure on ϕ_{core} and λ parameters. It was constructed based on molecular dynamic simulations (Figure 2.1 b) and corresponds to experimental results of core-shell systems with both hard and soft shell types. The theoretical calculations are based on the Dauod-Cotton star polymers model and the Witten-Pincus potential, which is derived from that model[32].

Noteworthy, the A15 phase has a place in between BCC and Quasicrystal regions. We aim to obtain this particular Frank-Kasper phase from $C_{16}E_{20}$ polymer gels in water solutions and fit its parameters to the phase diagram.

The sample preparation and the concentration range were chosen as suggested in Jayaraman and colleagues' work[18]. Nevertheless, phase occurrence differs at the same system parameters. For instance, authors report the presence of the A15 phase for 57.9 wt % of $C_{16}E_{20}$ in water at 25 °C instead of the HPC phase (Figure 2.2 c). It appears that the system is very sensitive to shearing, which causes a phase transition during the sample preparation step. In particular, the polymer mixture was centrifuged additionally in borosilicate capillaries for SAXS measurements and led to the packing, which typically appears either at higher concentrations or at higher temperatures.

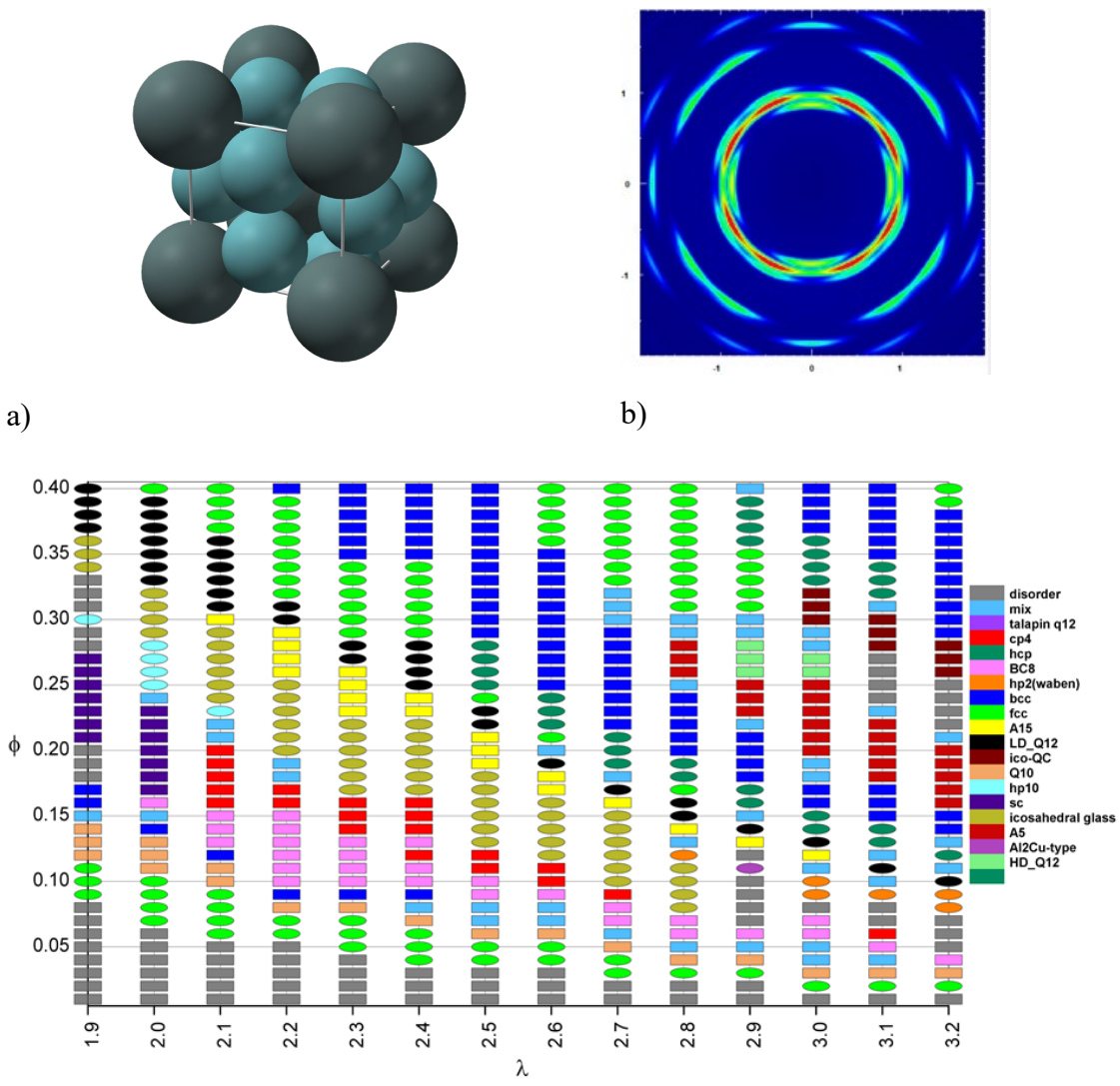

Figure 2.1 a) Space-filling model of the A15 phase unit cell of the crystal structure of niobium-tin, Nb_3Sn. from J. Less-Common Metals (1991). 172-174, 358-365. Copyright © 1991 Published by Elsevier B.V. b) MD simulation of A15 phase in 100 direction c) Phase diagram

Figure 2.2 demonstrates a phase transition for 49.5 wt%, 53.7 wt%, and 57.9 wt% polymer concentrations caused by the increase in temperature. The main common peculiarity of this kind of transition is a change of A15 phase to HPC while heating from 25 to 55 °C, it stays in good agreement with Jayaraman and colleagues [18] experimental results. Moreover, the lattice parameter value decreases with the increase in temperature as evidence of closer HPC packing (Supporting Information, Table 2-1).

Authors also report a stable HPC phase at higher temperatures up to 100 °C at 45-54 wt% $C_{16}E_{20}$ concentrations. In complete opposite to this, we observe an order-disorder transition above 55 °C to 75 °C for all sample concentrations between 49 wt% and 58 wt% (Figure 2.2 a). In most cases cooling down the system to 25 °C leads to the formation of either the Lamellar phase, which is typical for higher concentrations[33] or HPC. This kind of irreversible transition could be caused by water evaporation during the heating.

Following experimental results of SAXS temperature-dependent measurements for highly concentrated Brij58 system in water and taking into account the role of the shearing field in phase transitions, we intend to study micelles packings of the hydrated diblock oligomer under various shearing conditions and temperatures. Considering LLC phase formation depended on temperature and concentration, as presented in the work of colleagues[18], we choose $C_{16}E_{20}$ concentrations in water between 54 wt% and 59 wt%. This range promises a rich variety of A15, BCC, HPC, and A15+HPC phases.

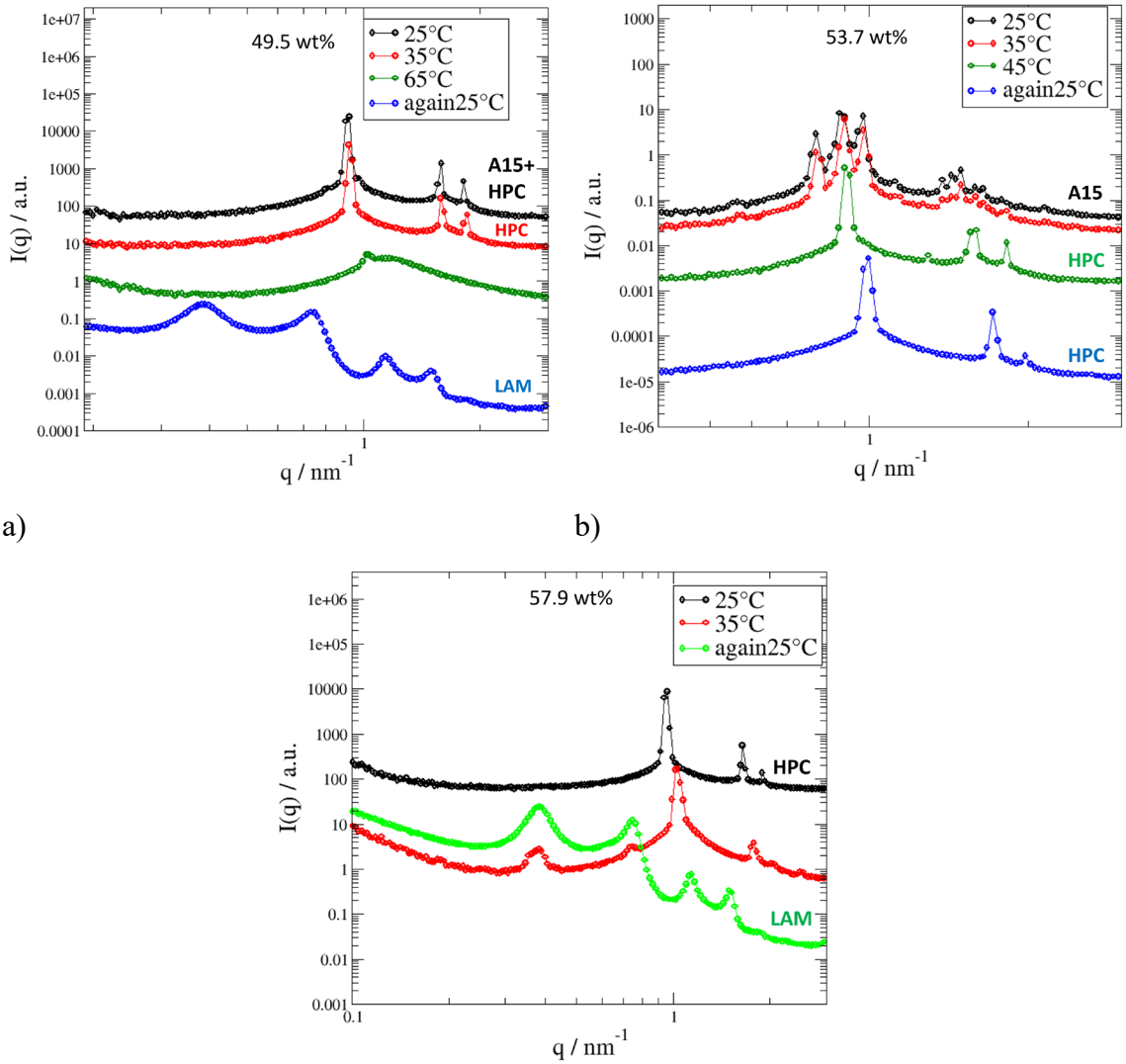

Figure 2.2 Scattering curves represent temperature-dependent structural changes for Brij 58 polymer at a) 49.5 wt%, b) 53.7 wt%, and c) 57.9 wt% concentration in water

2.3.2 Shearing-induced phase transitions and A15 phase orientation

The study of Valentine and colleagues[19] is related to the stabilization of metastable BCC phase and an accelerated A15 phase formation using shearing at low 0.1 Hz and high 9.9 Hz frequencies, and at constant 177 %, 354 %, and 1770 % strain. The authors suggest an efficient combination of shearing parameters to obtain the A15 phase, which includes a

high frequency and a high strain. On contrary, we aim to follow the phase transition during shearing starting directly with the A15 phase, to prove its stability and to achieve the Frank-Kasper phase order on a long-range scale. For that, we chose a high 8 Hz constant frequency oscillation and various strain parameters, for instance, the shearing at gradually increased strain, low 1.2 % constant strain, and higher 80 %, 100 % strains

Amplitude sweep shearing procedure was applied to 54.8 wt% $C_{16}E_{20}$ polymer solution in water. SAXS scattering patterns of the sample, which was measured during logarithmically increasing strain from 0 to 103 % are shown in Figure 2.3. Scattering curves have three peaks of high intensity, which are typical for the A15 phase. Noteworthy, the A15 phase is formed at the chosen concentration and stays stable at the gradually increasing shearing. In addition, the lattice parameter equals a = 14.5 nm at 60 % strain and decreases with further shearing. 2D SAXS images demonstrate a change in the diffraction pattern, which indicates the ordering of the A15 phase after a continuous shearing with increasing strain up to 59 % (Figure 2.3 b). Applying of significantly higher 103 % strain leads to the worsening of the order and the appearance of the fourth, additional peak of the A15 phase with a = 14.8 nm. A shearing result also highly depends on the way of the sample loading to the shearing cell, since the pre-shearing process often influences the reproducibility and a resultant phase formation (Supporting Information, Figure 2.10).

As a next step, we apply a constant 1.2 % strain for 250 minutes to a freshly loaded sample. As a result, there is no ordering of the A15 phase during continuous shearing at low strain. The phase stays stable during one hour of shearing and has a constant lattice parameter a = 14.58 nm (Figure 2.4). After 80 minutes micelles form a mixed phase of A15 and HPC, which turns to Lamellar after 250 minutes.

The Lamellar phase is seemingly formed due to the drying of the sample after a continuous shearing. To avoid evaporation we changed water to the widely used solvent $C_4H_{10}O_3$ diethylene glycol (DEG). Since DEG is miscible in H_2O and has a boiling point above 245 °C, we would expect a longer drying time for the sample. Meanwhile, polymer micelles with DEG solvent form only the Lamellar phase in the whole concentration range between 30 wt% and 50 wt% (Supporting Information, Figure 2.12).

Since the frequency of shearing is the inversely proportional parameter of time, we set it to be as high as possible to obtain LLC phases faster, due to the fast drying time of the sample.

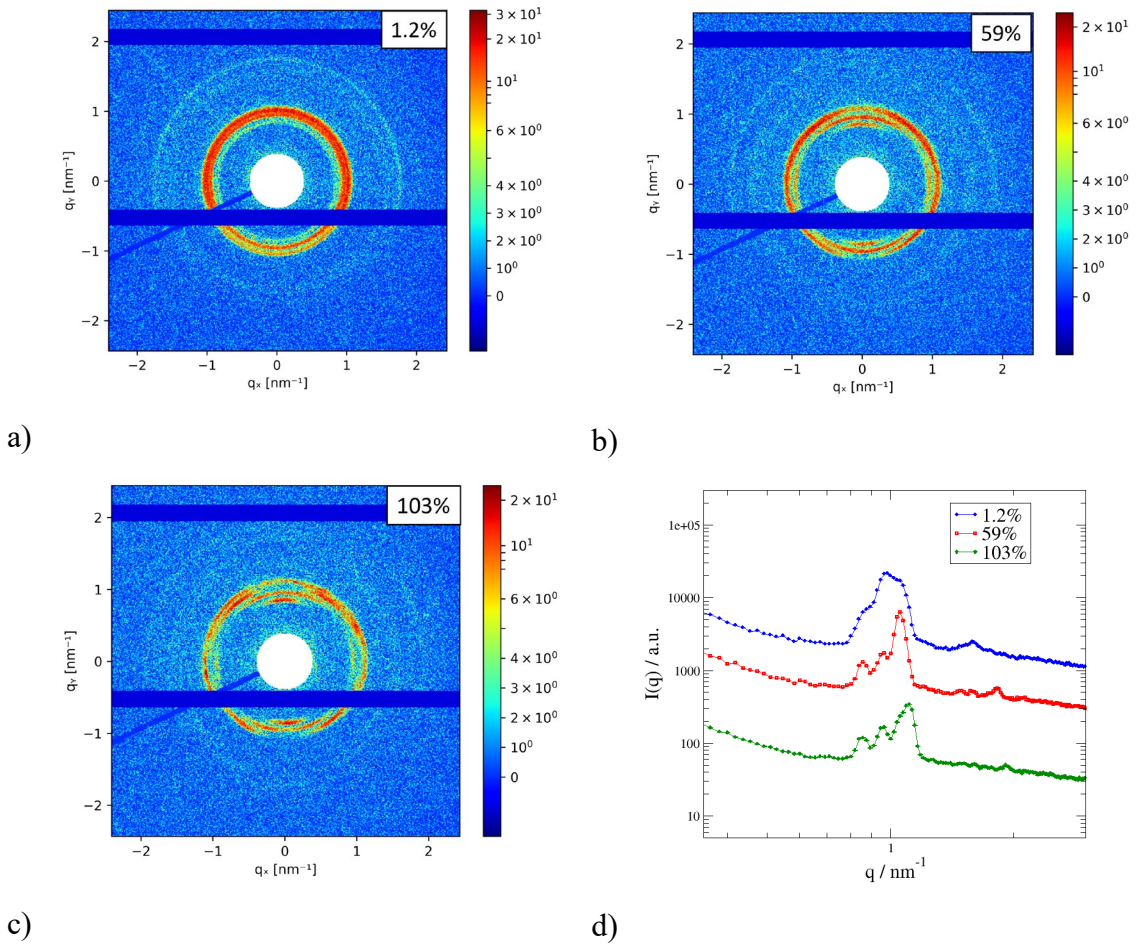

Figure 2.3 SAXS 2D scattering patterns of 54.8 wt% $C_{16}E_{20}$ concentration in H_2O after shearing for 5 minutes at gradually increased a) 1.2% strain, b) 59 % strain, c) 103% strain, and d) corresponding them radially averaged scattering curves of A15 phase

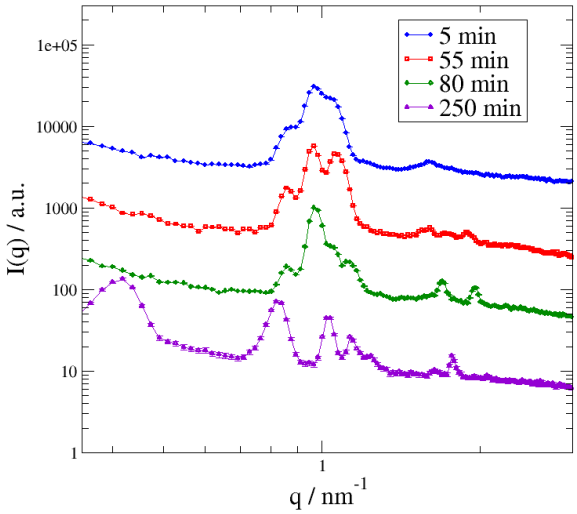

*Figure 2.4 SAXS curves of 54.8 wt% $C_{16}E_{20}$ polymer solution in H_2O during shearing at low 1.2 % constant strain for **5 min**, **55 min**, **80 min**, and **250 min***

A similar result of A15 phase transformation can be achieved at a significantly higher 100% strain for a shorter time. In Figure 2.5 d the broad triple peak (blue curve) separates into three independent peaks with the increase of shearing time at a constant 100% strain. Later the structure gets diffraction peaks of the HPC phase at the high q range (red curve) and the fourth peak at the low q range (purple curve). In contrast to the previous example, the ordering of the A15 phase can be observed. The diffraction pattern of the polymer sample shows the starting order in the 011 direction, but not a complete one as the third diffraction ring is still even.

Therefore, we slightly change the shearing parameters and decrease the shearing rate to 80 % for a better A15 phase orientation as shown in Figure 2.6. After 10 minutes of shearing with constant 80 % strain, the phase ordering (red curve) starts, and in 25 minutes the scattering pattern of the ordered A15 phase becomes more pronounced, meanwhile, HPC reflections disappear (green curve). Shearing time at 80 % strain is comparable to shearing time at 100 % strain for the A15 phase orientation (30 minutes). Nevertheless, at 80% strain, the A15 phase is evenly ordered as shown in Figure 2.6 c.

Figure 2.6 e and f prove that slight heating of the sample improves the A15 phase orientation. With an increase of temperature to 35 °C the diffraction pattern gets a squire-like shape and becomes sharper. Further increase of temperature to 45 °C destroys the obtained order irreversibly.

Shearing experiments for sample concentrations between 49 and 56 wt% revealed that at the beginning A15 phase forms in $C_{16}E_{20}$ polymer water mixtures, then it changes with shearing to BCC, HPC, and later to the Lamellar phase. It is previously reported that the system demonstrates a similar behavior at 58.7 wt% while heating the sample. It results in a phase transition sequence A15 (25 °C) → A15 + BCC (37 °C) → H_1 (60 °C) with increasing temperature[18].

For the 53.7 wt% concentrated sample, which was sheared at 160% strain and formed the HPC phase, lattice parameter a = 6.77 nm is lower than after the increase of sample's temperature without shearing (Supporting Information, Table 2-1). It means that the lattice parameter of the system can be desirably tuned in the following way. For obtaining a structure with a large lattice parameter the lower concentration of polymer in water can be chosen. Further decrease of the lattice can be done with a slight increase of polymer concentration or temperature. For even smaller lattices a shearing force of various strains could be applied. The higher strain or shearing time, the smaller lattice.

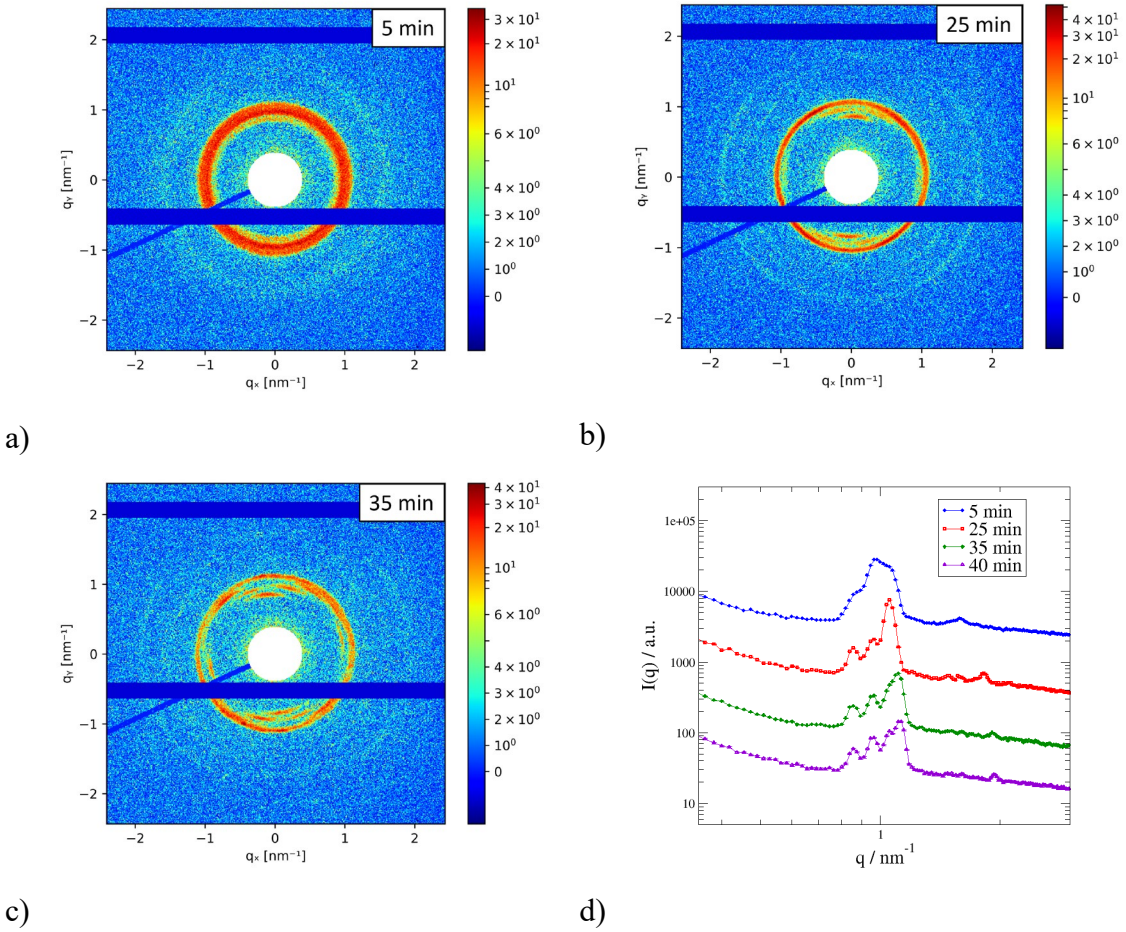

*Figure 2.5 SAXS 2D patterns and radially averaged scattering curves for 54.8 wt% $C_{16}E_{20}$ polymer solution in H_2O during shearing at high constant 100% strain for **5 min**, **25 min**, **35 min**, and **40 min***

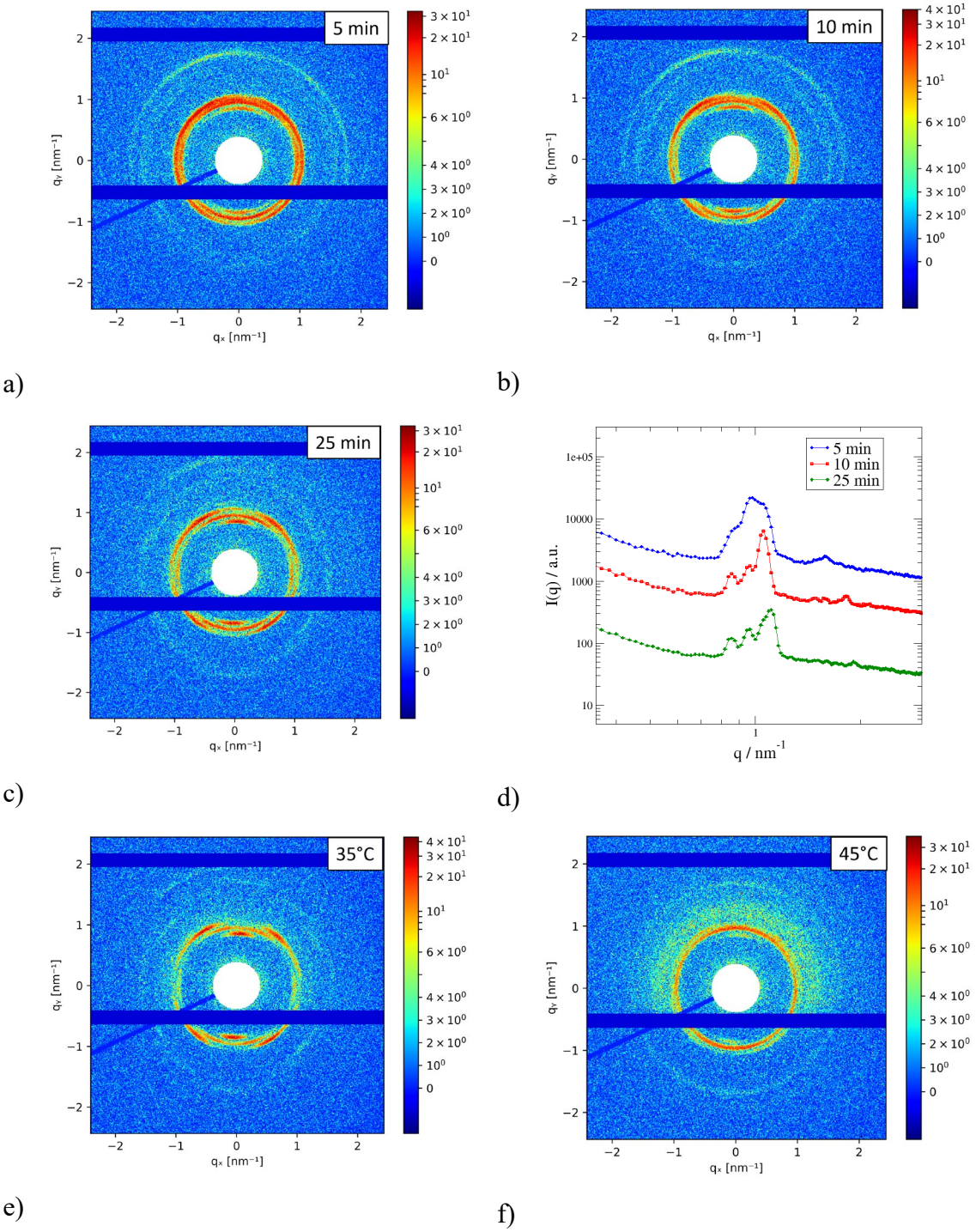

*Figure 2.6 a) - c) SAXS 2D patterns of the ordering A15 phase, d) radially averaged scattering curves for 54.8 wt% $C_{16}E_{20}$ polymer solution in H_2O during shearing at high constant 80% strain for **5 min**, **10 min**, **25 min**, e)-f) influence of temperature on A15 phase order*

2.3.3 Comparison of homemade and commercial polymer

Earlier we showed studies of water solutions with commercially produced Brij 58 polymer. To improve the purity and size distribution of the hydrophobic part, $C_{16}E_{20}$ was synthesized and characterized using the NMR technique (Supporting Information, Figure 2.13 - Figure 2.15).

The homemade polymer directly shows diffraction spots after the sample loading to the shearing cell and the transition from BCC to the A15 phase, which is achieved with shearing. The example of shearing 52.2 wt% concentration laboratory synthesized polymer in water is shown in Figure 2.7. At 40 % strain, the BCC phase has a closer packing than the initial BCC phase before shearing (lattice parameter changes from a = 9.34 nm to a = 9.29 nm) and appears to be ordered, which is well-observed in the azimuthal plot (Figure 2.7 c). At 100% the transition to the A15 phase occurs (Figure 2.7 d, green curve, a = 14.48 nm), which is followed by HPC phase formation after the decrease of shearing rate to 20% (purple curve, a = 6.77 nm). After 10 minutes of further shearing HPC turns to Lamellar (black curve, a = 16.29 nm).

A slight increase of concentration to 55.5 wt% delivers the A15 phase, which is stable when the shearing strain is gradually increased up to 120 % (Figure 2.8 a). With the rapid increase of shearing strain to 80 %, the A15 phase with lattice parameter a = 14.78 nm (Figure 2.8 b, blue curve) changes to HPC after 15 minutes of constant oscillation at 80 % (red curve, a = 7.17 nm) and after 25 minutes further to Lamellar (green curve, a = 16.29 nm).

As well as for the commercial polymer samples, the A15 phase is obtained for homemade surfactant, when the sample is sheared with a slowly increasing strain or directly at a high 100 % strain. Therefore, a phase transition can be achieved with a rapid high strain applied or by continuous shearing with a gradually increasing strain, if the A15 phase is already formed.

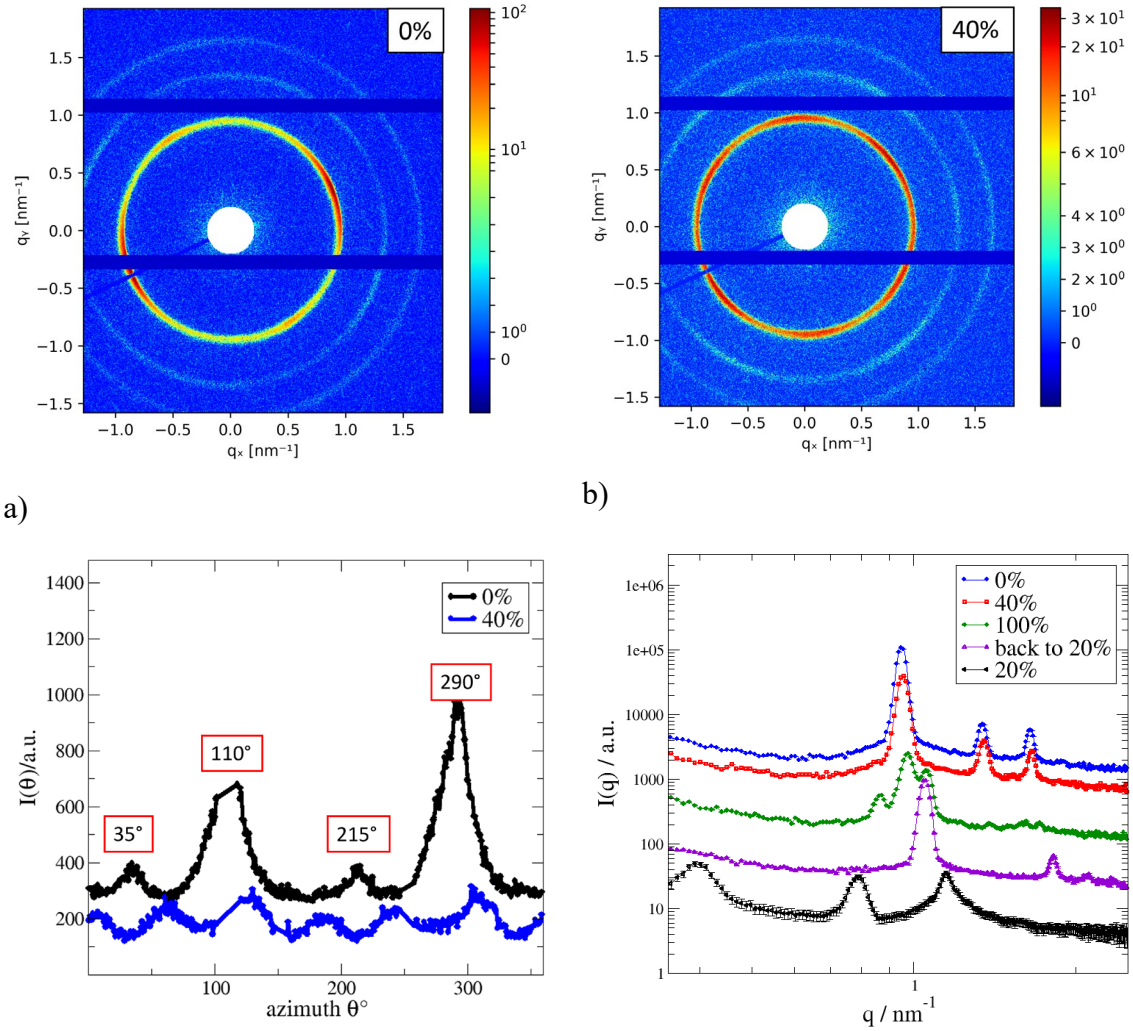

*Figure 2.7 SAXS 2D pattern for 52.2wt% homemade $C_{16}E_{20}$ in H_2O a) without shearing b) during 40% strain c) azimuthal plot of the sample **before shearing** and **after shearing** at 40% strain d) radially averaged scattering curves of **BCC**, **A15**, **HPC**, and **Lamellar** phases*

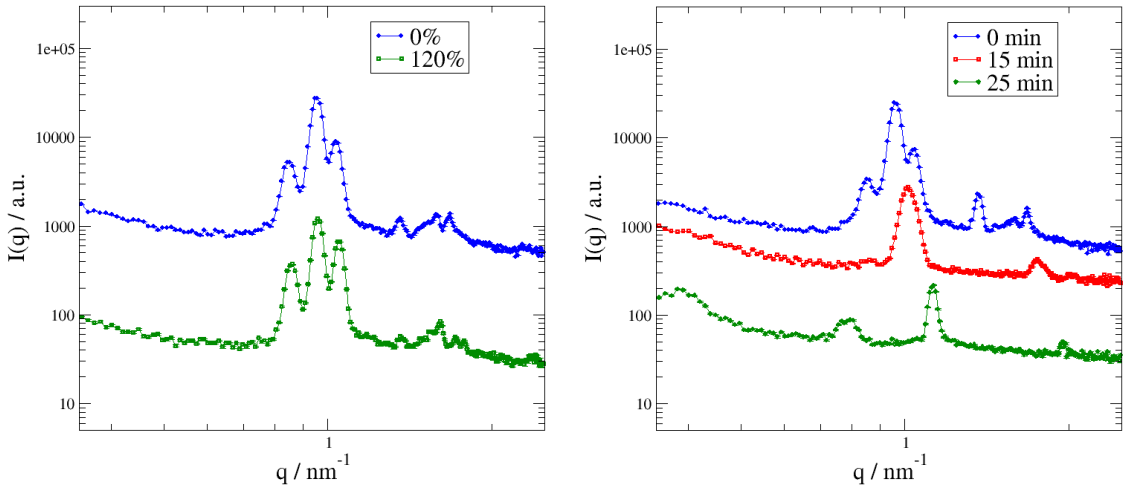

a) b)

Figure 2.8 SAXS curves for 55.5 wt% $C_{16}E_{20}$ concentration in H_2O, which a) has stable A15 phase with a gradually increased shearing and b) A15 phase changes to HPC at high constant 80 % strain, applied at the beginning of shearing

Above all, the difference in the phase behavior of water solutions with commercial and laboratory synthesized polymer is observed. Even though the phase transition paths within shearing are similar and include A15 → HPC → Lamellar transition, laboratory-synthesized polymer shows often an ordered BCC phase instead of the A15. Another common behavior both polymers have is the formation of a stable A15 phase as shown in Figure 2.9 c.

In the contrast to the industrial Brij 58, the A15 phase could not be oriented for the laboratory synthesized sample. Additionally, a peculiar difference commercial polymer water solutions have is the sample aging. After six months laboratory synthesized sample creates the same BCC structure at the same 52 wt% concentration value and shearing conditions as before (Figure 2.9 a). However, the industrial Brij 58 solution changes over time and forms the expected A15 phase, but already with additional diffraction spots representing disordered domains (Figure 2.9 b). An effect of sample aging was previously reported by Jayaraman and colleagues[18], who demonstrated the phase transition from the H1 phase to σ and A15 phase on the time scale of 6 months.

To conclude, the better size distribution of the hydrophobic part of homemade surfactant influences the type of a resultant structure and provides a BCC phase, which is ordered on a long-range scale.

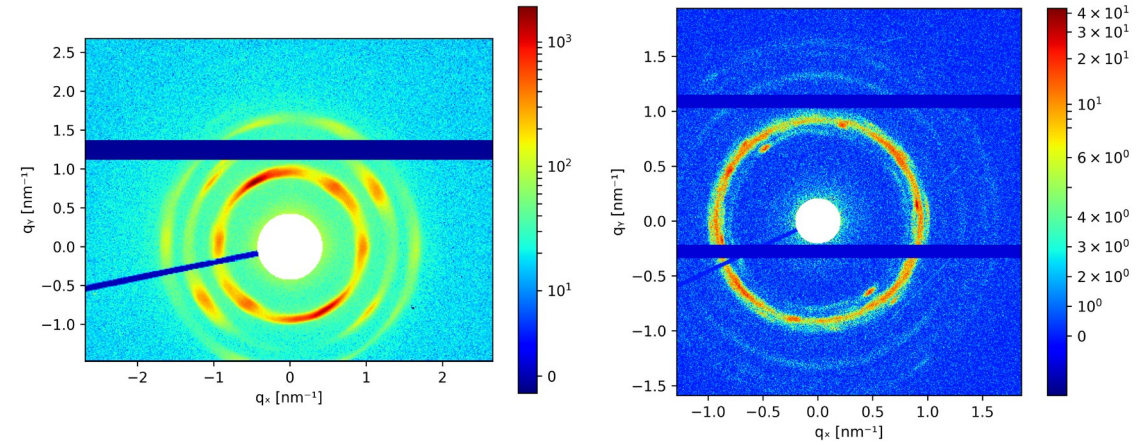

a) b)

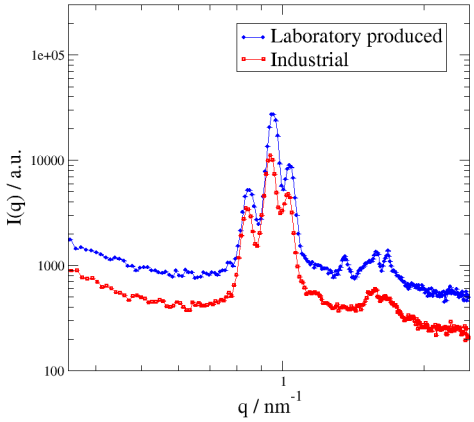

c)

Figure 2.9 SAXS 2D pattern of a) 52 wt% homemade polymer in H_2O sheared at 20% strain for 5 minute,, b) 51 wt% commercial polymer in H_2O, and c) radially averaged scattering curves of A15 phases for ***laboratory produced*** *and* ***commercial*** *samples for 54.8 wt% $C_{16}E_{20}$ concentration in H_2O*

2.4 Materials and methods

2.4.1 Materials

Brij 58, Sigma Aldrich (M_n~1124 g) was used as received. Di-block polymer ($C_{56}H_{114}O_{21}$) contains an alkyl hydrophobic tail and polyoxyethylenic hydrophilic head.

The home-made Brij 58 ($C_{16}EG_{20}$) was synthesized by ethoxylation of 1-hexadecanol with 20 units of ethylene oxide. First, the alcohol was metalated with 0.15 equivalents of potassium tert-butoxide in dry DMSO. After the removal of tert-butanol under reduced pressure, ethylene oxide was added and polymerized at 50 °C for 5 days. The reaction mixture was then neutralized with the ion exchange resin Amberlite IR 120 and the solvent was removed under reduced pressure.

Sample preparation procedure includes a mixing of Brij58 polymer with deionized water, manual stirring and centrifugation for 30 minutes at 3000*g. Stirring and centrifugation steps were repeated 3 times until complete dissolution of polymer in water.

2.4.2 SAXS measurements

SAXS experiments of Brij industrial sample in borosilicate capillaries were performed at the Gallium Anode Low-Angle X-ray Instrument (GALAXI), Forschungszentrum Jülich[34]. The incident beam wavelength was 1.34 Å and the detector distance 1.4 m. Samples with 49 to 58 wt% polymer concentrations were sealed in 2 mm diameter capillaries during centrifugation at 800*g for 10 minutes. Measurement was done while heating from 25 °C to 75 °C with the step of ten degrees. Exposure time was set to be 30 min for each sample.

SAXS shearing experiments were performed at Ganesha-Air using the shearing device Linkam CSS450. The X-ray source is D2-Metalljet (Excillium) with a liquid metal anode operating at 70 kV and 3.57 mA with Ga-Kα radiation (λ = 0.1314 nm) providing a thick beam (< 100 μm) of high brilliance. A typical measurement includes a 5 minute shearing with constant 8 Hz frequency at 25 °C temperature. After long time shearing the sample is changed to a fresh one due to water evaporation.

The data analysis was held using the Python based project Jscatter [35]. Measured data was corrected and calibrated to absolute intensities.

2.5 Conclusion

Highly-concentrated water solutions of $C_{16}E_{20}$ diblock oligomer at 49-58 wt% concentrations were studied using the SAXS method in the shearing atmosphere. Commercial Brij 58 at 52.4 wt% concentration in water forms A15 Frank-Kasper phase with an average lattice parameter a = 15 nm, which is oriented on a long-range scale at various shearing conditions. In particular, during constant shearing with 1.2 % strain for 55 minutes, with 80 % strain for 10 minutes, and with 100 % strain for 35 minutes A 15 phase was oriented. Additionally, a gradually increased strain to 103 % also results in the A15 phase orientation. This system has volume fraction $\varphi = 0.06$ and lambda parameter = 2.65, which correspond to the A15 phase in the phase diagram and agree with MD simulations results.

The time of A15 phase orientation is comparable for the shearing both at constant 80 % strain and 100 % strain and equals 30 minutes. The even scattering pattern of oriented A15 is achieved at 80 % strain, structural defects are reduced with an increase of temperature by 10 °C.

The sample preparation method suggested by Jayaraman and colleagues [18] was used for obtaining homogeneous polymer mixtures. Sample transferring to a capillary and its centrifugation lead to the additional shearing and therefore, to the formation of close-packed phases, which are usually observed either at higher concentrations of the polymer or at higher temperatures. Meanwhile, a transition of the A15 phase to HPC while heating from 25 to 55 °C stays in good agreement with colleagues' [18] experimental results.

A15 phase in Brij 58 water solutions showed high stability during shearing for a long time up to 80 minutes at strains up to 120 %. Nevertheless, strains above 120% or a longer shearing ruin the ordering and form the Lamellar phase.

To improve the purity and size distribution of the hydrophobic part, $C_{16}E_{20}$ was synthesized and studied at the same concentration range as the commercial sample. Monodisperse hydrophobic tails of homemade surfactant significantly influence the resultant structure. Thus, the oriented BCC phase is observed at the same concentrations, where the A15 phase is expected based on experimental results with the commercial Brij 58 polymer.

The phase transition caused by shearing is similar to the transition for industrial polymer solutions and includes BCC, H1, and Lamellar phases. In addition, the homemade polymer didn’t show any changes connected to sample aging, whereas the commercial sample showed additional diffraction spots after the annealing at room temperature for 6 months.

To conclude, in this work we suggested several shearing procedures to orient the A15 phase in water solutions with $C_{16}E_{20}$ polymer, proved its stability, and showed the influence of polymer distribution on the formation of LLC phases.

2.6 Supporting Information

1. **Lattice parameters of ordered structures from commercial sample Brij 58**
2. **Influence of a preliminary shear on the formed structure**
3. **Core-shell sphere model**
4. **Aggregates in solutions with reduced concentration**
5. **Polymer mixtures in diethylene glycol**
6. **NMR spectra of homemade surfactant**

Lattice parameters of ordered structures from commercial sample Brij 58

Polymer mixtures of high concentrations were measured at the laboratory SAXS machine while increasing the sample temperature. Table 2-1 shows a decrease of lattice parameter value with heating.

Table 2-1 Temperature-induced phase transition for the commercial polymer water solutions and lattice parameter corresponding to each phase

Concentration, wt%	Temperature, °C	Phase	a, nm
49.5	25	A15+HPC	7.98
	35	HPC	7.89
	65	liquid-like packing state LLP	-
	again 25	Lamellar	16.8
53.7	25	A15	16
	35	A15	15.8
	45	HPC	8
	again 25	HPC	7.35
57.9	25	HPC	7.65
	35	Lamellar +HPC	7
	again 25	Lamellar	17

Influence of a preliminary shearing on the formed structure

Influence of a preliminary shearing on the structure, while loading a sample into the shearing cell (Figure 2.10). Here the same procedure of logarithmically increasing strain as shown in Figure 2.3 was used for shearing the same sample of 54.8 wt% concentration.

Already at a low 2 % strain A15 phase becomes a mix of A15 and HPC phases and at 6 % strain turns to HPC. The effect of pre-shearing is brightly demonstrated by the comparison of lattice parameters for both amplitude sweep measurements. In the first case, the A15 phase has lattice parameter a = 14.84 nm at 1.2 % strain, and in the second case, the lattice parameter a = 14.26 nm is lower.

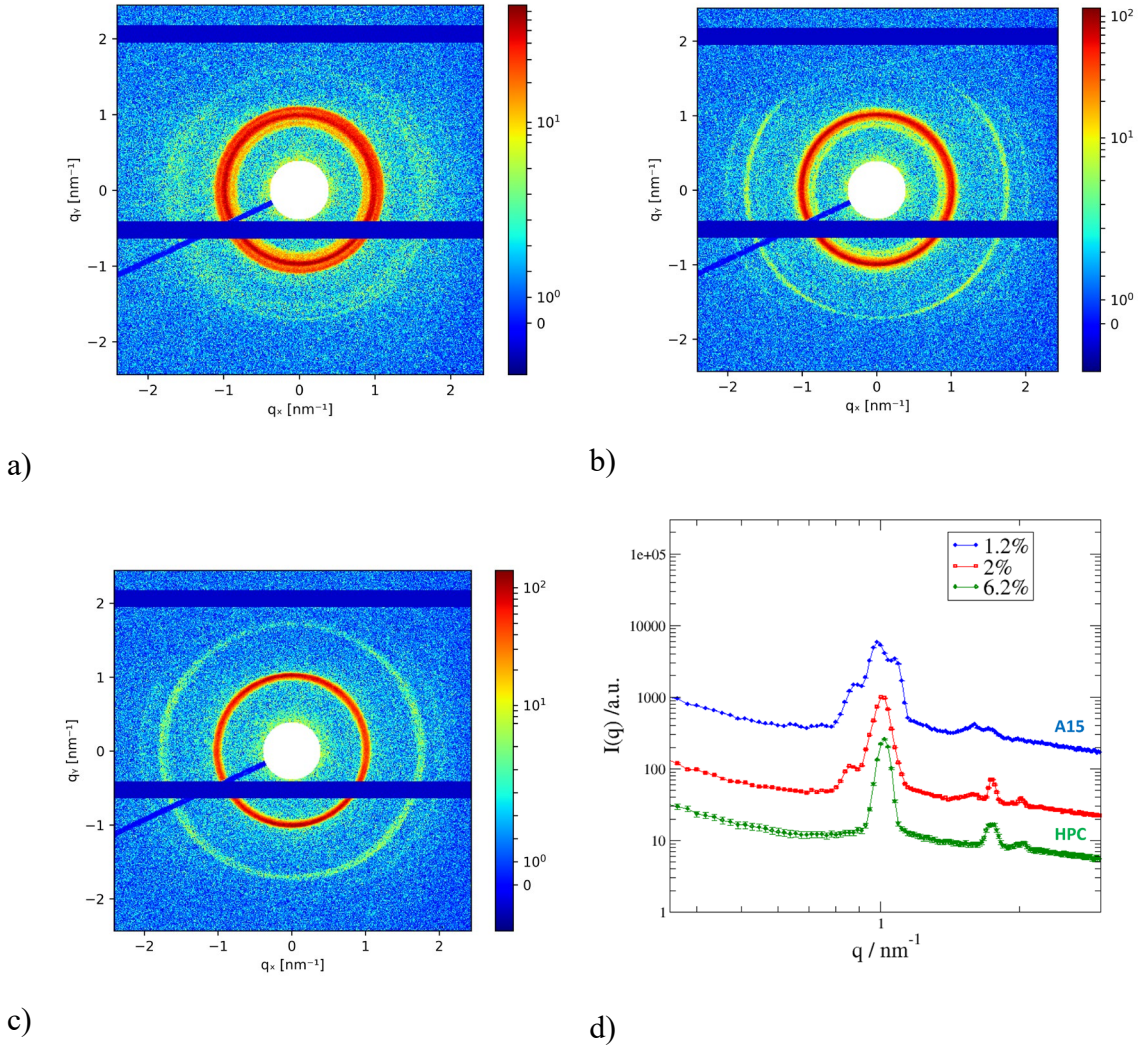

*Figure 2.10 SAXS 2D patterns for the shearing of 54.8 wt% $C_{16}E_{20}$ in H_2O with logarithmically changed strain value a) **1.2%** b) **2%** c) **6.2%** d) corresponding scattering curves of **A15 (a=14.26 nm)**, **mixed** and **HPC** (a=7.2 nm) phases*

Core-shell sphere model

Core-shell model fit using Jscatter software[36] gives slightly different parameters for micelles size than in the work of Fall and colleagues[33]. These parameters for 5.1 wt% Brij 58 in water are equal to R_c = 1.7 nm, and R_s = 2.66 nm. Our model provides higher values Rc = 1.9, Rs = 3.13 for 2 wt% concentration (Figure 2.11), where micelles size was expected to be lower.

The core-shell model provides high-quality fits because of included polydispersity parameter and the shell parameter.

The form factor of the core-shell sphere is described in the following way[37]

$$F(q) = \frac{3}{V_s}\left[V_c(\rho_c - \rho_s)\frac{sin(qr_c) - qr_c\,cos(qr_c)}{(qr_c)^3} + V_s(\rho_s - \rho_{solv})\frac{sin(qr_s) - qr_s\,cos(qr_s)}{(qr_s)^3}\right] \quad 2.1$$

where V_s is the volume of the whole particle, V_c is the volume of the core, r_s is the radius of the particle, r_c is the radius of the core, ρ_c , ρ_s and ρ_{solv} are the scattering length density of the core, shell, and solvent.

Aggregates in solutions with reduced concentration

Form-factor of the Brij 58 sample at 2 wt% concentration in H_2O and core-shell fit of D = 6.3 nm micelles are shown in Figure 2.11 a. In comparison to that low-concentrated samples of 1 wt%, 5 wt%, and 10 wt%, which were obtained from 54.8 wt% Brij 58 water solution, have a structure factor at the low q range. It means that the reduction of the concentration of $C_{16}E_{20}$ polymer in water demands additional manipulations with samples for preventing aggregation. The lower q range of SAXS curves (Figure 2.11 b) has significant raise in intensity. It means that even though samples with reduced concentration look homogeneous, it doesn't exclude a possible aggregation. Therefore, an additional step of sonification is necessary for breaking the micelles' confinement.

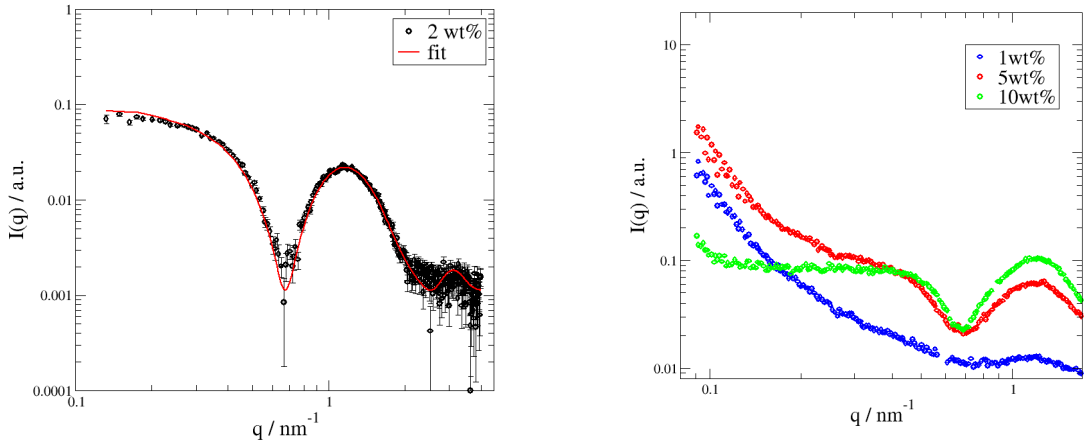

a) b)

*Figure 2.11 SAXS curves of a) Brij 58 sample at **2 wt%** concentration in H_2O and b) polymer mixture diluted from 54.8 wt% sample to **1 wt%**, **5 wt%**, and **10 wt%***

Polymer mixtures in diethylene glycol

$C_{16}E_{20}$ polymer mixtures in diethylene glycol (DEG) were prepared to reduce the impact of solvent evaporation on the structure formation during a shearing process. SAXS measurements reveal that in this case, micelles form only Lamellar structures at concentrations from 30 wt% to 50 wt%. At 50 wt% lattice parameter equals a=18 nm, which corresponds to the size of the Lamellar lattice, which is usually formed in Brij water systems at high concentrations.

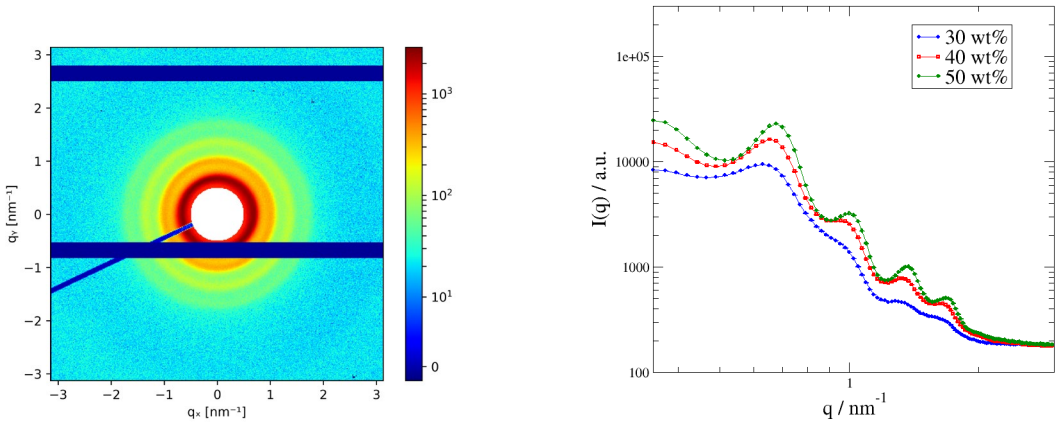

a) b)

*Figure 2.12 a) 2D SAXS pattern for **50 wt%** Brij58 in DEG representing lamellar structure with lattice parameter a = 18 nm and b) scattering curves for **30 wt%**, **40 wt%** and **50 wt%** of Brij 58 in DEG*

NMR spectrum for the commercial and homemade Brij 58

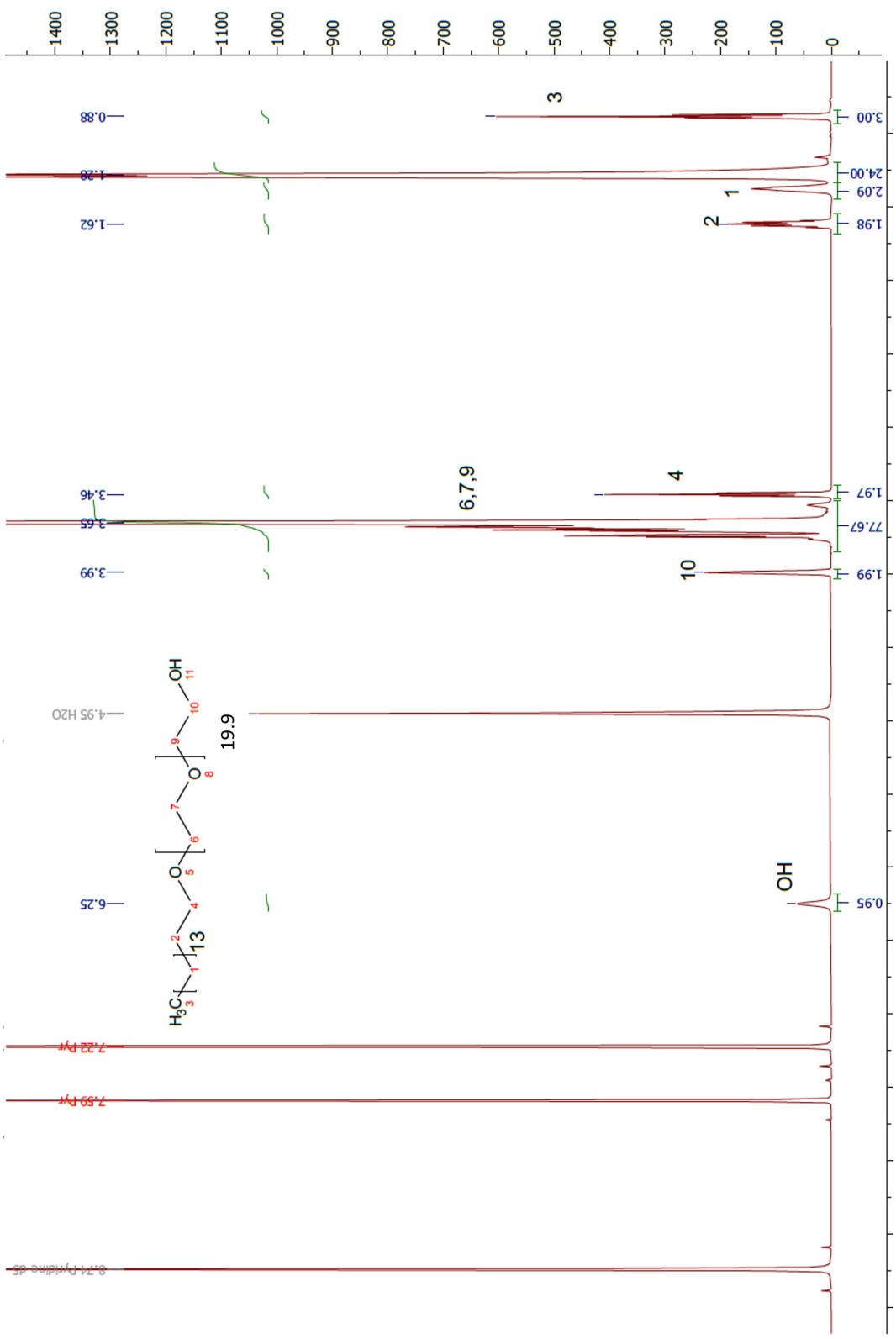

Figure 2.13 NMR spectra of homemade $C_{16}EG_{20}$ in pyridine d5

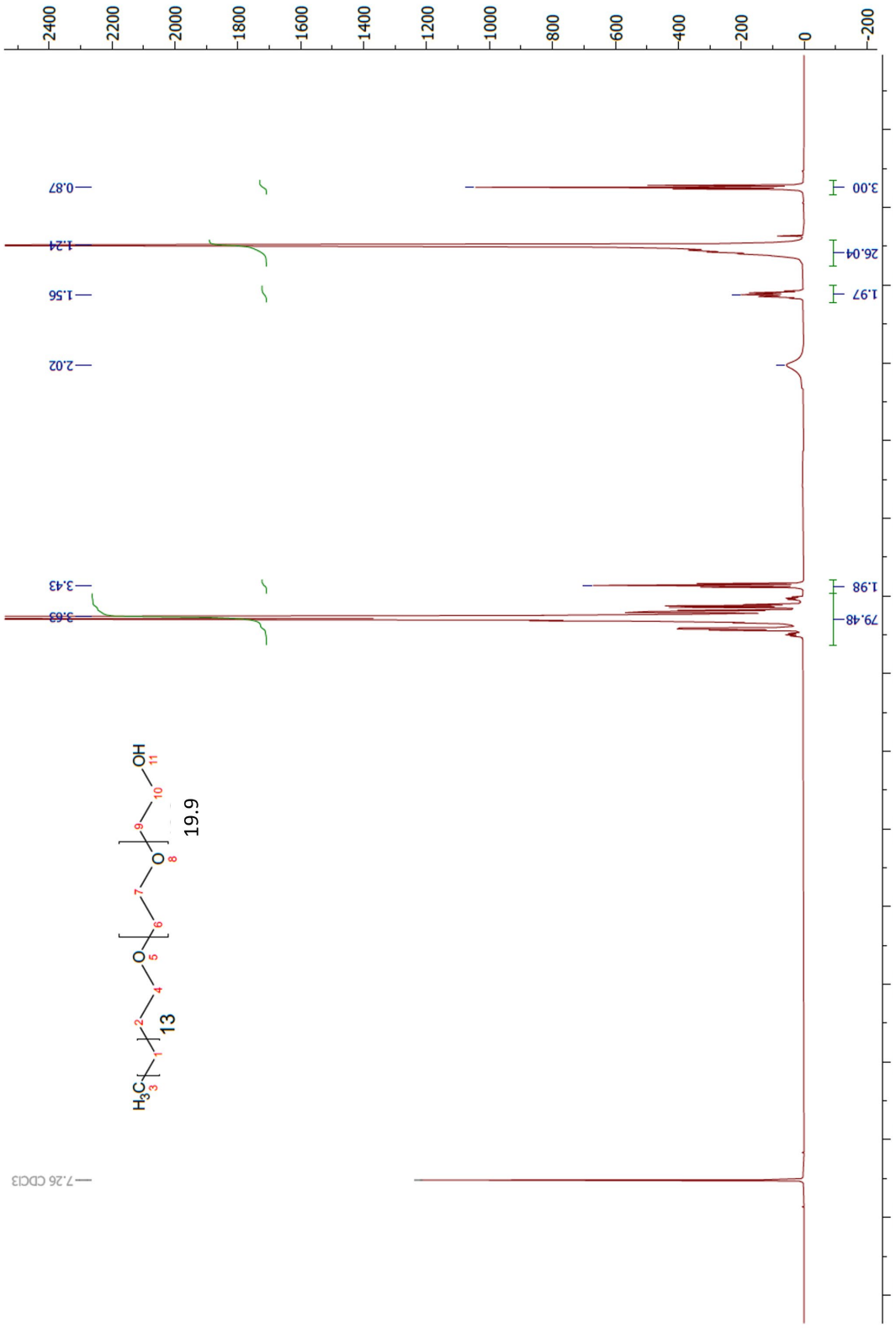

Figure 2.14 NMR spectra of homemade $C_{16}EG_{20}$ in chloroform $CDCl_3$

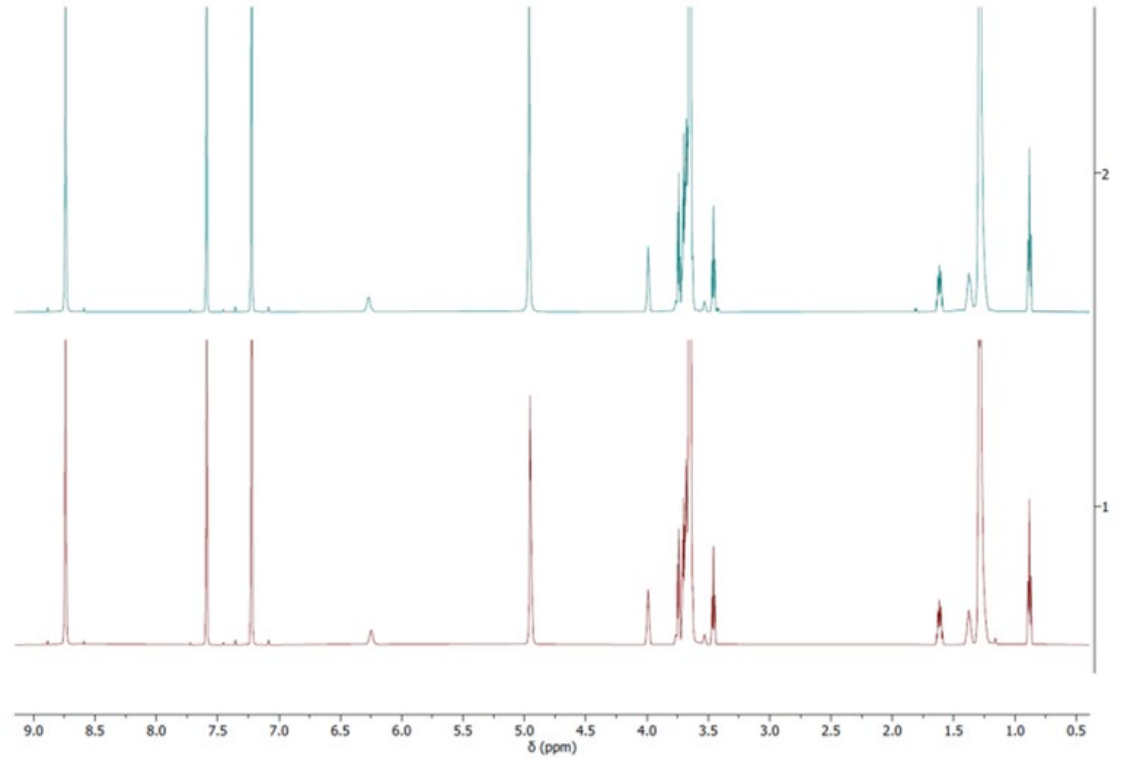

a)

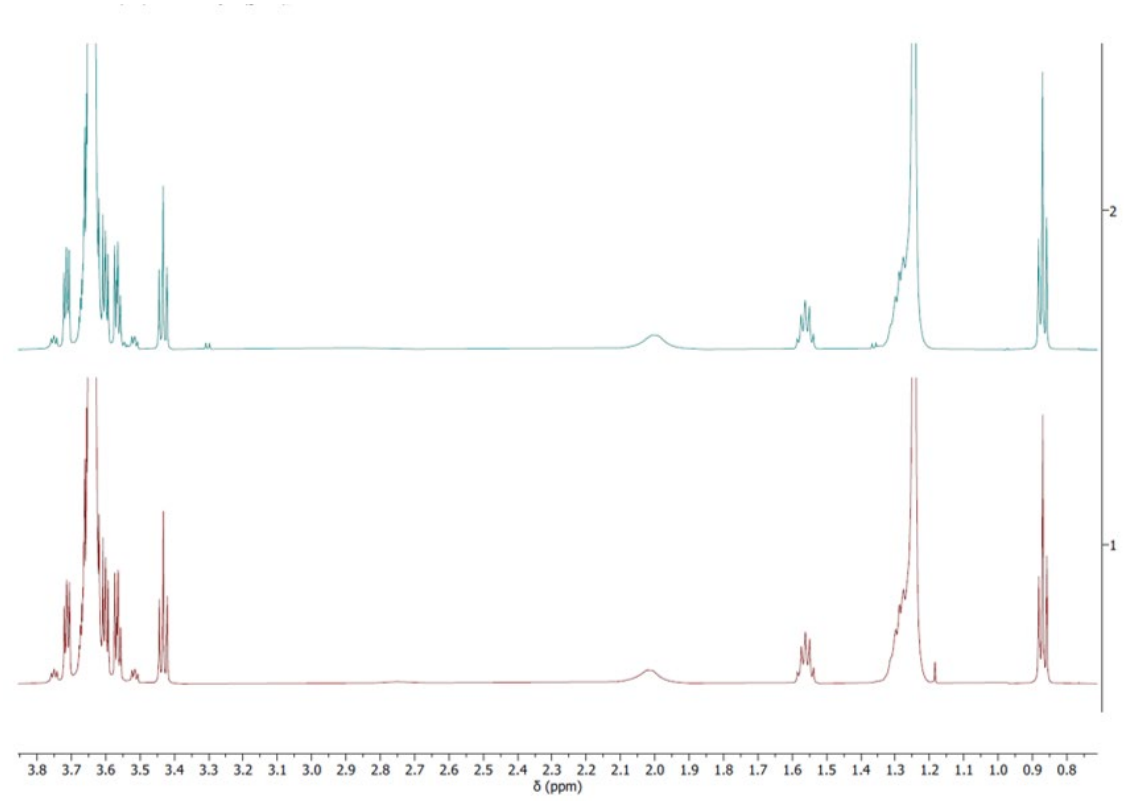

b)

Figure 2.15 Comparison of NMR spectra of homemade (red) and commercial (green) $C_{16}EG_{20}$ in a) pyridine d5 and b) chloroform $CDCl_3$

2.7 References

[1] S. Lee, M. J. Bluemle, F. S. Bates, *Science (1979)* **2010**, *330*, 349–353.

[2] M. J. Park, K. Char, J. Bang, T. P. Lodge, *Macromolecules* **2005**, *38*, 2449–2459.

[3] G. C. Shearman, A. I. I. Tyler, N. J. Brooks, R. H. Templer, O. Ces, R. v. Law, J. M. Seddon, **2010**, *37*, 679–694.

[4] R. Mezzenga, J. M. Seddon, C. J. Drummond, B. J. Boyd, G. E. Schröder-Turk, L. Sagalowicz, R. Mezzenga, M. Seddon, C. J. Drummond, B. J. Boyd, G. E. Schröder-Turk, L. Sagalowicz, *Advanced Materials* **2019**, *31*, 1900818.

[5] S. Förster, M. Antonietti, *Adv.Mater* **1998**, *10*

[6] K. K. Lachmayr, L. R. Sita, *Angewandte Chemie International Edition* **2020**, *59*, 3563–3567.

[7] G. Ungar, X. Zeng, *Soft Matter* **2005**, *1*, 95–106.

[8] A. Travesset, *Phys Rev Lett* **2017**, *119*, 115701.

[9] K. D. Dorfman, *Macromolecules* **2021**, *54*, 10251–10270.

[10] S. Lee, M. J. Bluemle, F. S. Bates, *Science (1979)* **2010**, *330*, 349–353.

[11] A. C. Lawson, C. E. Olsen, J. W. Richardson, M. H. Mueller, G. H. Lander, *urn:issn:0108-7681* **1988**, *44*, 89–96.

[12] M. Huang, C. H. Hsu, J. Wang, S. Mei, X. Dong, Y. Li, M. Li, H. Liu, W. Zhang, T. Aida, W. bin Zhang, K. Yue, S. Z. D. Cheng, *Science (1979)* **2015**, *348*, 424–428.

[13] K. Kim, M. W. Schulze, A. Arora, R. M. Lewis, M. A. Hillmyer, K. D. Dorfman, F. S. Bates, *Science (1979)* **2017**, *356*, 520–523.

[14] G. Ungar, Y. Liu, X. Zeng, V. Percec, W. D. Cho, *Science (1979)* **2003**, *299*, 1208–1211.

[15] S. Lee, M. J. Bluemle, F. S. Bates, *Science* **2010**, *330*, 349–353.

[16] M. Rappolt, F. Cacho-Nerin, C. Morello, A. Yaghmur, *Soft Matter* **2013**, *9*, 6291–6300.

[17] S. Lee, C. Leighton, F. S. Bates, *Proc Natl Acad Sci U S A* **2014**, *111*, 17723–17731.

[18] A. Jayaraman, D. Y. Zhang, B. L. Dewing, M. K. Mahanthappa, *ACS Cent Sci* **2019**, *5*, 619–628.

[19] C. S. Valentine, A. Jayaraman, M. K. Mahanthappa, L. M. Walker, *ACS Macro Lett* **2021**, *10*, 538–544.

[20] H. Kunieda, K. Shigeta, K. Ozawa, M. Suzuki, *Journal of Physical Chemistry B* **1997**, *101*, 7952–7957.

[21] M. Imai, I. Yoshida, T. Iwaki, K. Nakaya, *J Chem Phys* **2005**, *122*, 044906.

[22] P. Sakya, J. M. Seddon, R. H. Templer, R. J. Mirkin, G. J. T. Tiddy, *Langmuir* **1997**, *13*, 3706–3714.

[23] B. Rastegar, E. Saljoughi, S. M. Mousavi, S. Kiani, *Korean Journal of Chemical Engineering* **2022**, *39*, 2465–2473.

[24] P. Liu, W. Gao, Q. Zhang, K. Chen, J. Zhang, L. Chen, X. Zhang, K. Wang, *React Funct Polym* **2015**, *89*, 1–8.

[25] W. Gao, Q. Zhang, P. Liu, S. Zhang, J. Zhang, L. Chen, *RSC Adv* **2014**, *4*, 34460–34469.

[26] N. Nikooe, E. Saljoughi, *Appl Surf Sci* **2017**, *413*, 41–49.

[27] Y. Liu, L. Xing, Q. Zhang, Q. Mu, P. Liu, K. Chen, L. Chen, X. Zhang, K. Wang, Y. Wei, *Colloid Polym Sci* **2016**, *294*, 617–628.

[28] J. Choma, A. Żubrowska, J. Górka, M. Jaroniec, *Adsorption* **2010**, *16*, 377–383.

[29] F. Johansson, M. Olbe, M. Sommarin, C. Larsson, *The Plant Journal* **1995**, *7*, 165–173.

[30] O. Squillace, C. Esnault, J. F. Pilard, G. Brotons, *ACS Appl Mater Interfaces* **2017**, *9*, 42313–42326.

[31] S. Jacques, E. Rocca, M. J. Stebe, J. Steinmetz, *Surf Coat Technol* **2008**, *202*, 3878–3885.

[32] T. A. Witten, P. A. Pincus, P. A. Pincus, *Macromolecules* **1986**, *19*, 2509–2513.

[33] S. Fall, B. Pattier, L. Benyayia, A. Gibaud, *Acta Phys Pol A* **2012**, *121*, 388–396.

[34] E. Kentzinger, M. Krutyeva, U. Rücker, *Journal of large-scale research facilities JLSRF* **2016**, *2*, A61–A61.

[35] R. Biehlid, **2019**, DOI 10.1371/journal.pone.0218789.

[36] R. Biehl, *PLoS One* **2019**, *14*, DOI 10.1371/JOURNAL.PONE.0218789.

[37] A. Guinier, *Small-Angle Scattering of X-Rays*, Wiley, New York, **1955**.

3 Shearing-induced PI-PS block copolymer micelle assembly in an organic solvent

3.1 Abstract

For decades block copolymer liquid crystals are used for the building of functional nanostructures, nanodevices, and drug delivery. We investigate PI_{210}-PS_{154}-OH block copolymer in a selective solvent that served as a model for self-assembly and perform SAXS experiments under shear with the parameters obtained from rheological measurements. A new cuvette for the shearing device was tested. The block copolymers demonstrate structural stability and reproducibility of the self-assembly properties. It has been shown that changing temperature along with the shearing leads to the reduction of structural defects and building or destruction of well-ordered FCC lattices. In addition, the new cuvette-type cup for the shearing device made it possible to perform measurements of both liquid and stiff samples, having an access to strains up to 500 % and studying structures from two directions (radial and tangential).

3.2 Introduction

Block copolymers tend to self-assemble in solutions into a variety of well-ordered nanostructures on a nanometer scale[1], these structures may have various morphologies, e.g. spheres, cylinders, bi-continuous structures and lamellae depending on block lengths ratio [2]. We are focusing on studying block copolymers forming micelles in selective solvents, which show the thermodynamic preference of the diluent for one of the two blocks. In concentrated solutions, block copolymer micelles organize further into ordered lyotropic or thermotropic liquid crystalline phases[3], e.g. FCC (face-centered-cubic) and BCC (body-centered-cubic) phases as well as quasicrystalline phases[4].

Block copolymer-assembled structures have found their application as templates to generate functional nanostructures and nanodevices[5–7]. Advanced nanoscale systems created by the self-assembly of polymers were used for drug delivery over the last decade[8]. Therefore, it demands precise control of large-domain, oriented, high-resolution assemble and the microdomain pattern orientation, which can be achieved in several ways.

An application of external fields on block copolymer melts and concentrated solutions in bulk state causes a long-range domain orientation. As an example, shear field and electric fields, elongation or compression fields, and temperature gradients effectively induce single-crystal-like oriented microdomain textures[9–14].

In the current work one of the block copolymer assembly approaches is applied to obtain high-resolution scattering patterns, combining temperature gradient and shearing methods. PI_{210}-PS_{154}-OH block copolymer in diethyl phthalate (DEP) solvent forms micelles of hydrodynamic radius R_H = 18 nm, which self-organize in a lyotropic crystals phase (LCP) when an external force is applied. We aim to compare lyotropic phase SAXS diffraction patterns and rheological behavior of the system at the same shearing parameters, to test a new shearing device of cuvette type for temperature measurements up to 70 °C and to prove the stability of the studying system at high shearing rates.

3.3 Results and discussions

3.3.1 Structure stability

The polymer solution was studied at several concentrations using the rheological measurement technique. Amplitude sweep measurement for 25 wt% concentrated samples (Figure 3.1) shows the linear region ending at 1.2 % strain and a change of viscoelastic behavior after the cross point at 10% strain. Structural changes are shown on SAXS images (Figure 3.3, Figure 3.5), which were obtained in situ using a shearing device and following the same rheological procedure: various oscillation strains applied at the constant frequency (w = 8 Hz or 50 rad/s). Since evaporation is very low, no influences of concentration changes during rheology and X-ray measurements are observed.

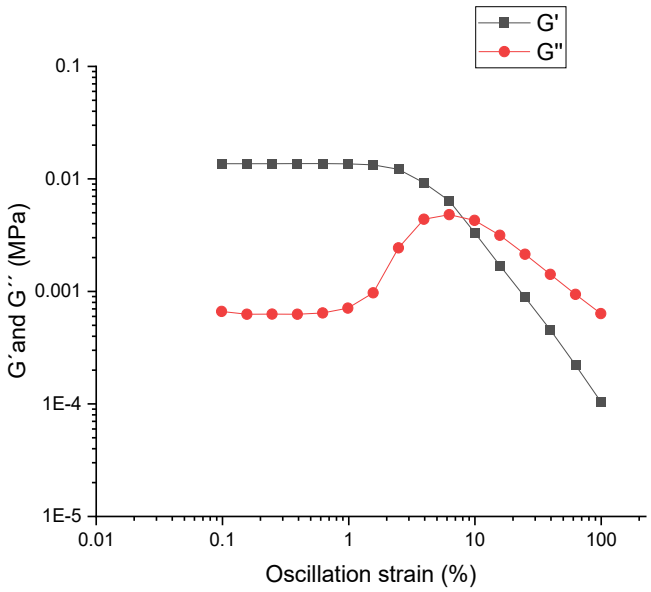

Figure 3.1 Storage and loss modulus with a respect to the strain y for 25wt% PI-PS micelles solution

Frequency sweep at 1% strain (Figure 3.2) reveals a rubbery plateau region with a three times higher storage modulus value for a more viscous sample. Here we can fix the frequency parameter at 8 Hz as it doesn't contribute significantly to structural changes of the polymer system. The strain value was chosen from amplitude sweep measurement (Figure 3.1) to focus on the linear region, where viscoelastic behavior is strain independent.

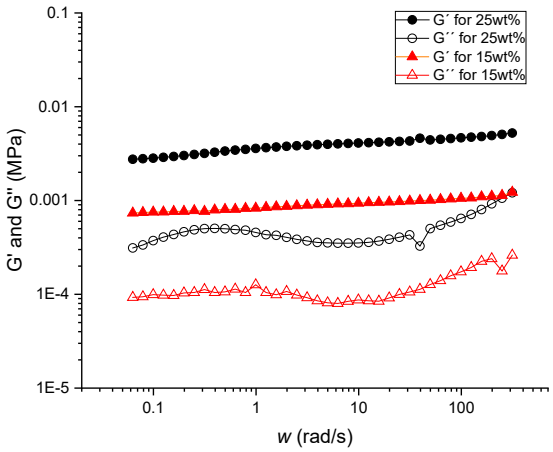

*Figure 3.2 Storage and loss modulus with a respect to frequency for 15 wt % and **25 wt %** PI-PS block copolymer in DEP at 1% oscillation strain*

Figure 3.3 shows SAXS diffraction patterns of 25 wt% concentrated sample, sheared continuously at 1 % strain. Already in the linear viscoelastic region one can see the formation of a hexagonal structure after 10 minutes of shearing. This scattering pattern becomes more pronounced with the increase of shearing time to 60 minutes. Azimuthally averaged scattering curve shows 60 degrees angle between diffraction spots and proves the presence of FCC phase. The drop of intensity values in the azimuthal plot (d in Figure 3.3) is coming from gaps in between the detector stripes and should be neglected.

FCC lattice in block copolymer micelles concentrated solutions have been identified in several cases [15–17], where interactions between the polymer and selective solvent in the shell layer play an important role in micelle ordering. The lattice structures were found to correlate with the ratio of shell thickness to the core radius, where a thinner shell favored the formation of an FCC lattice. Structural parameters of polymer micelles in the diluted regime were obtained by colleagues [18] using scattering measurements and core-shell sizes were determined with the corresponding model [19] data fit. Meanwhile, a phase diagram presented by Hanley et al [20] for PI-*b*-PS dissolved in diethyl phthalate (DEP) proves the existence of FCC phase volume fraction $0.2 < \phi < 0.3$ and temperature range between 0 °C and 100 °C.

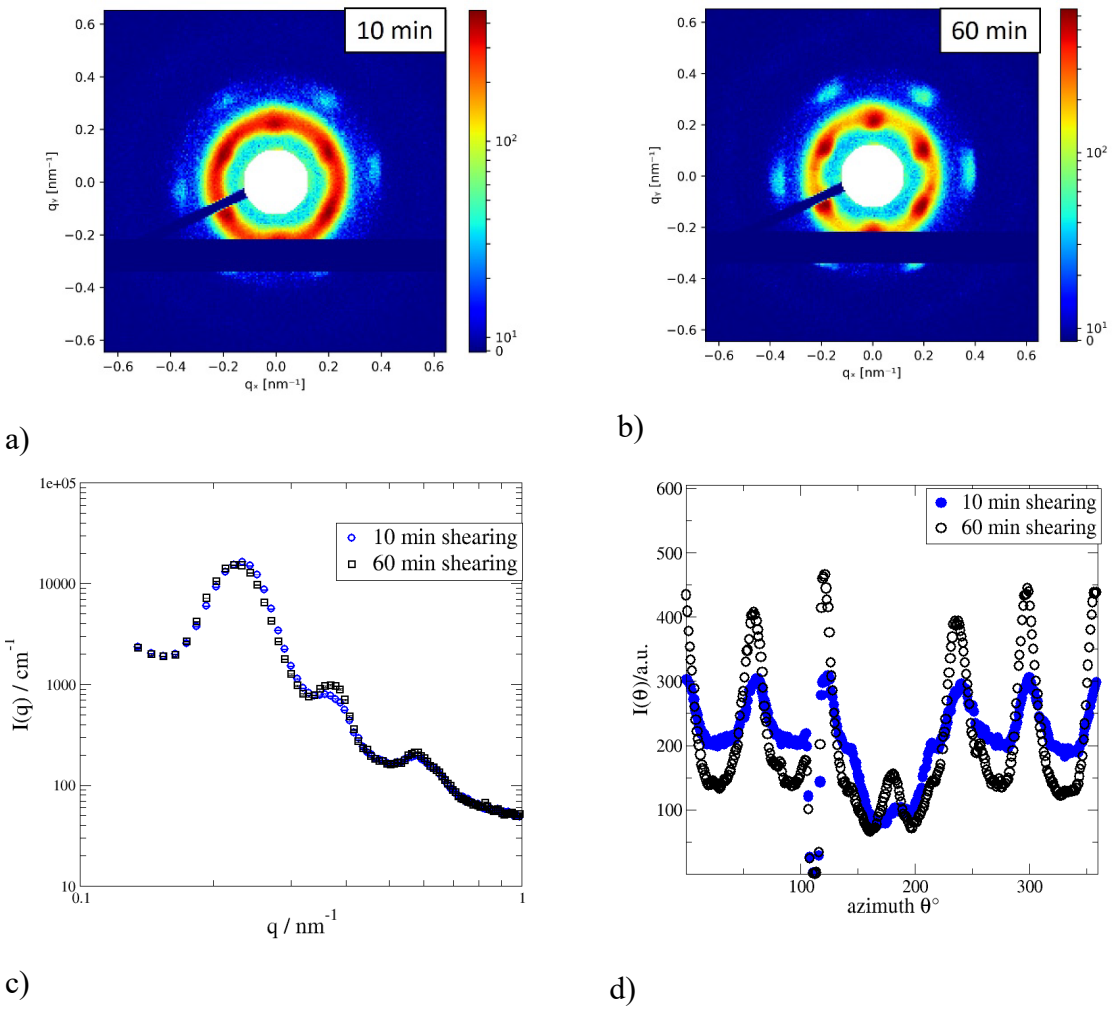

*Figure 3.3 25wt% PI-PS micelles in DEP at constant 1% Strain: a) after **10 min** of shearing b) after **60 min** #0024528 c) SAXS curves radial average d) SAXS curves azimuthal average in the range 0.18<q<0.26 nm^{-1} for 10 min shearing (blue curve) and 60 min shearing (black curve)*

We observe that the PI-PS micelles at 17 wt% concentration in DEP form weakly ordered FCC phase mixtures (Figure 3.4 a, b) at up to 80 % strain and then order to FCC lattice with a sharp diffraction pattern at high 160 % strain (Figure 3.4 c), which is disordered at 200 % strain (Figure 3.4 d). It demonstrates the common behavior of the system: FCC structure is weakly ordered at lower strain conditions, well-ordered at the intermediate strain, and completely disordered at the highest strain conditions. The fact that micelles form the stable FCC structure at determined strain conditions considers that the same sample can be reused for a new micelle assembly.

Since the storage modulus increases with the concentration of solutions (Figure 3.2), higher strain values are expected for disordering a formed structure in polymer mixtures with φ > 0.17.

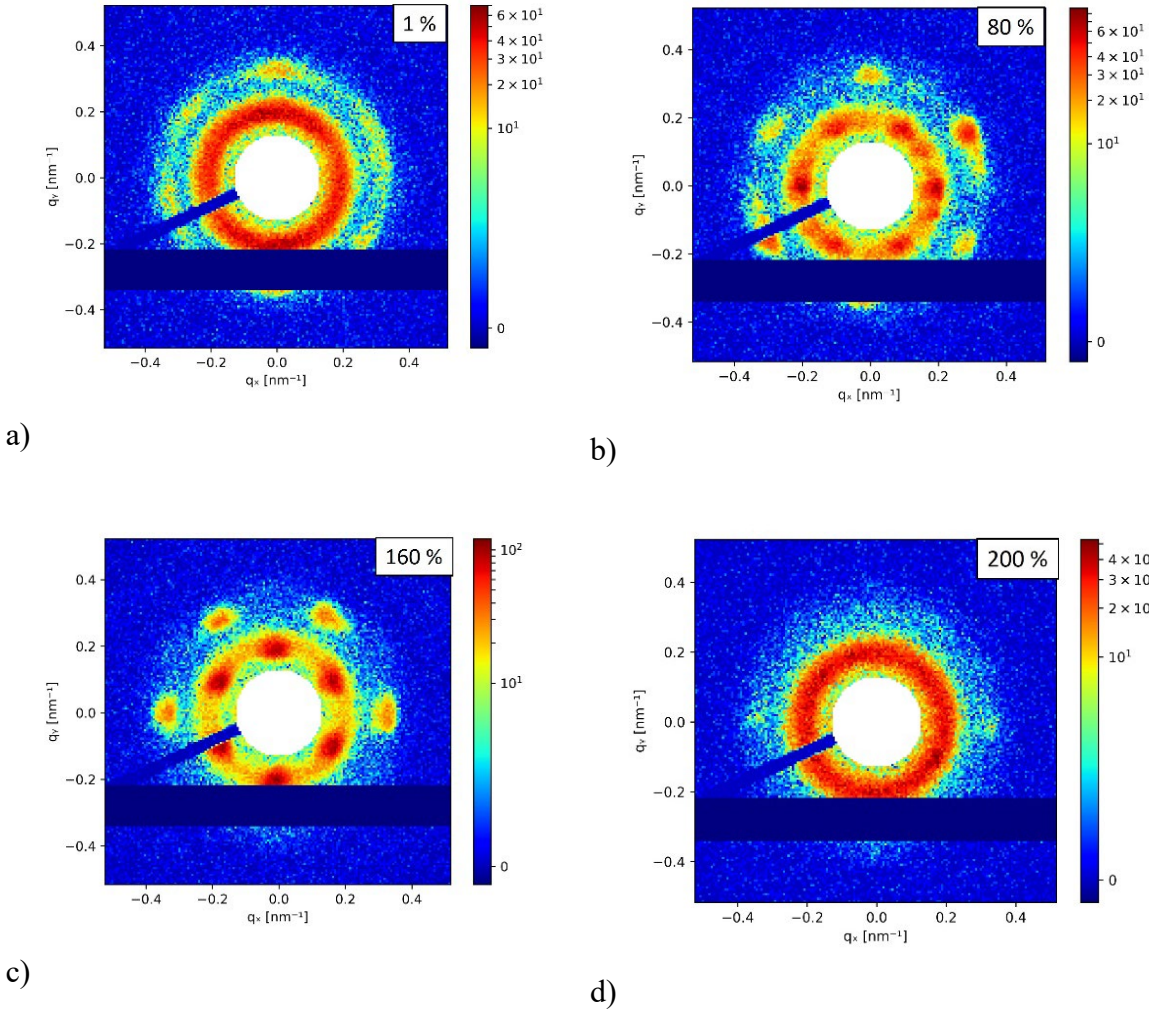

Figure 3.4 Phase transition for PI-PS in DEP at 17wt% concentration form a) weakly ordered fcc phase at 1% strain b) to a mixture of phases at 80% strain c) well-ordered fcc lattice at 160% strain d) and destroyed structure at 200% strain

As for lower concentrations, an increased polymer concentration up to 25 wt% also shows a weakly ordered FCC phase at lower strain, which appears already in the linear viscoelastic region (Figure 3.5). An increase in the shearing rate towards the region behind the cross-point of viscous and elastic compounds leads to the appearance of a mixed phase with a prevalent FCC structure. Noteworthy, shearing at an extremally high 240 % strain doesn't ruin a previously created lattice (Figure 3.5 d). Instead, the applied shearing (240 %) induces a lattice displacement, which is well-observed in the second order of the diffraction pattern (Figure 3.5 e). Shearing does not only create LCPs, but also causes various defects in the lattice, which was previously reported [21].

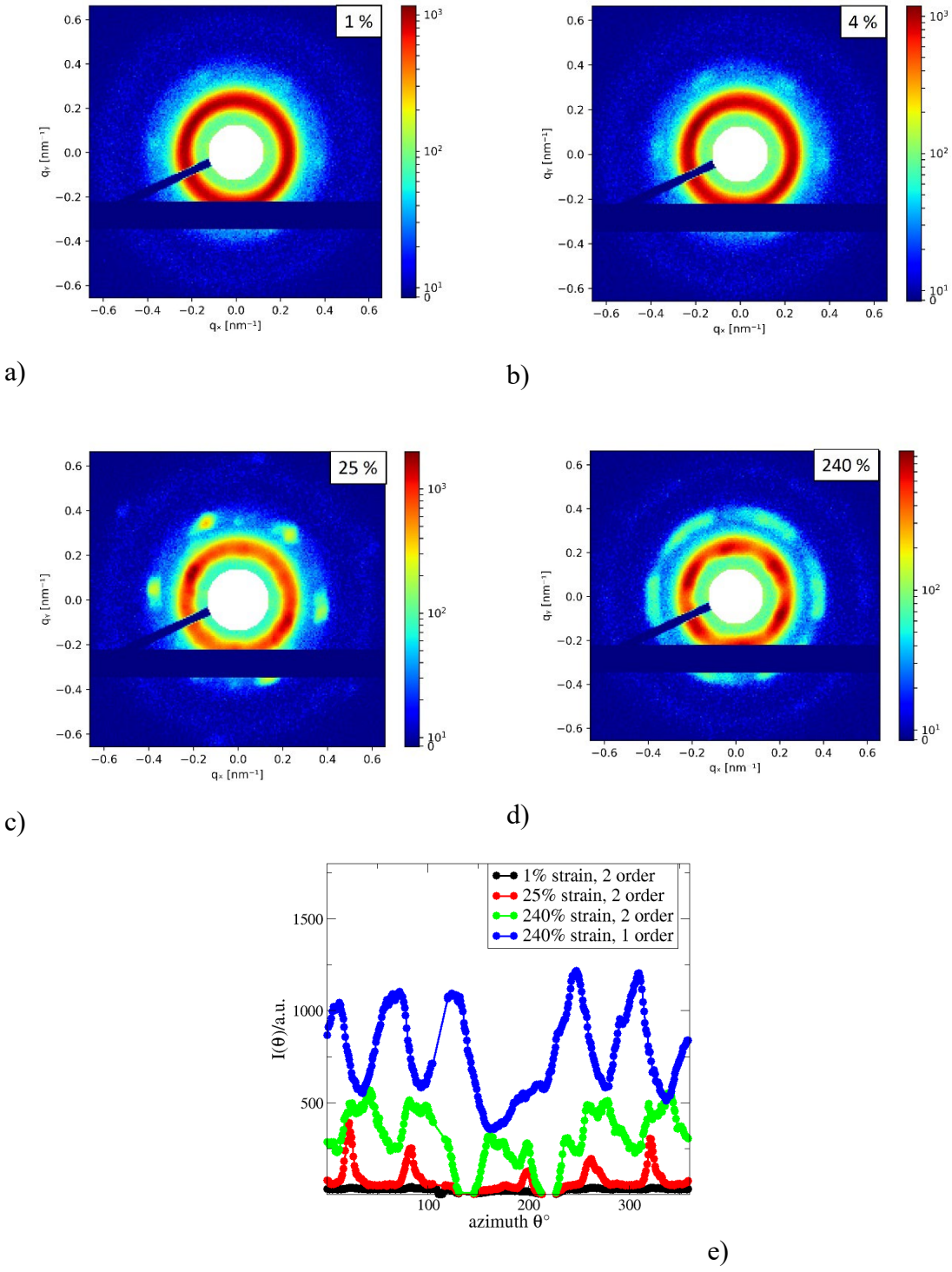

Figure 3.5 SAXS diffraction pattern for PI-PS solution at 25wt% concentration corresponding to the amplitude sweep: a) ***1% strain*** *in linear viscoelastic region b) 4% strain after linear region c) 25% strain after the cross point d) 240% strain far from cross point e) SAXS azimuthal average in the range* $0.32<q<0.42\ nm^{-1}$ *for* ***1% strain*** *(black curve),* ***25% (red)****,* ***240% (green)*** *and in the range* $0.18<q<0.26\ nm^{-1}$ *for* ***240% strain*** *(blue curve)*

3.3.2 Structure reproducibility

In the previous paragraph, we showed that a structure that is induced by the shearing of PI-PS block copolymer solution can be destroyed by applying a high strain to the system. This raises the question: could any structure appear again after decreasing the shearing strain to the value, at which a micelles order was already observed? To find out if the process of micelle's packing is reversible, we chose a 20 wt% concentration of PI_{210}-PS_{154}-OH block copolymer in DEP because the time of shearing correlates with concentration (the smaller volume fraction of micelles the faster they order). The initial value of strain (40%) was chosen based on amplitude sweep measurement (Figure 3.6) since well-ordered lattices appear behind the viscoelastic linear region and cross-point.

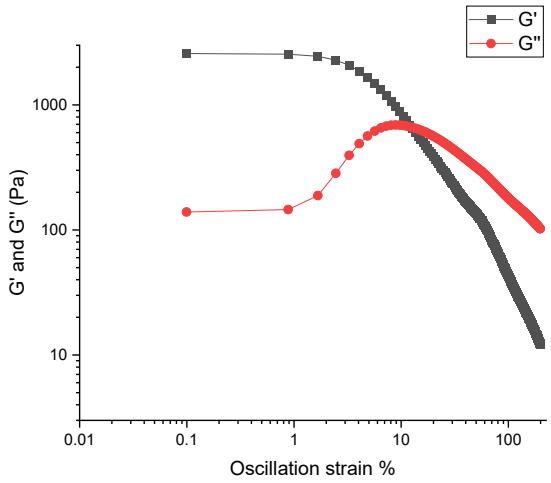

Figure 3.6 Amplitude sweep rheological procedure for 20wt% PI-PS micelles in DEP

Figure 3.7 illustrates a reversible process that turns a disordered phase into a mixed phase with predominant FCC. This experiment shows the FCC phase formed at 40 % strain, which was completely disordered at high strain and appeared again at the same shearing parameters (40 % strain). The azimuthal average shows an overlap of the first-order peaks with an equal distance of 60° angle, proving the reproducibility of the structure. The second order has additional diffraction spots, which are less intense, and indicates the imperfection of ordering and requires longer shearing.

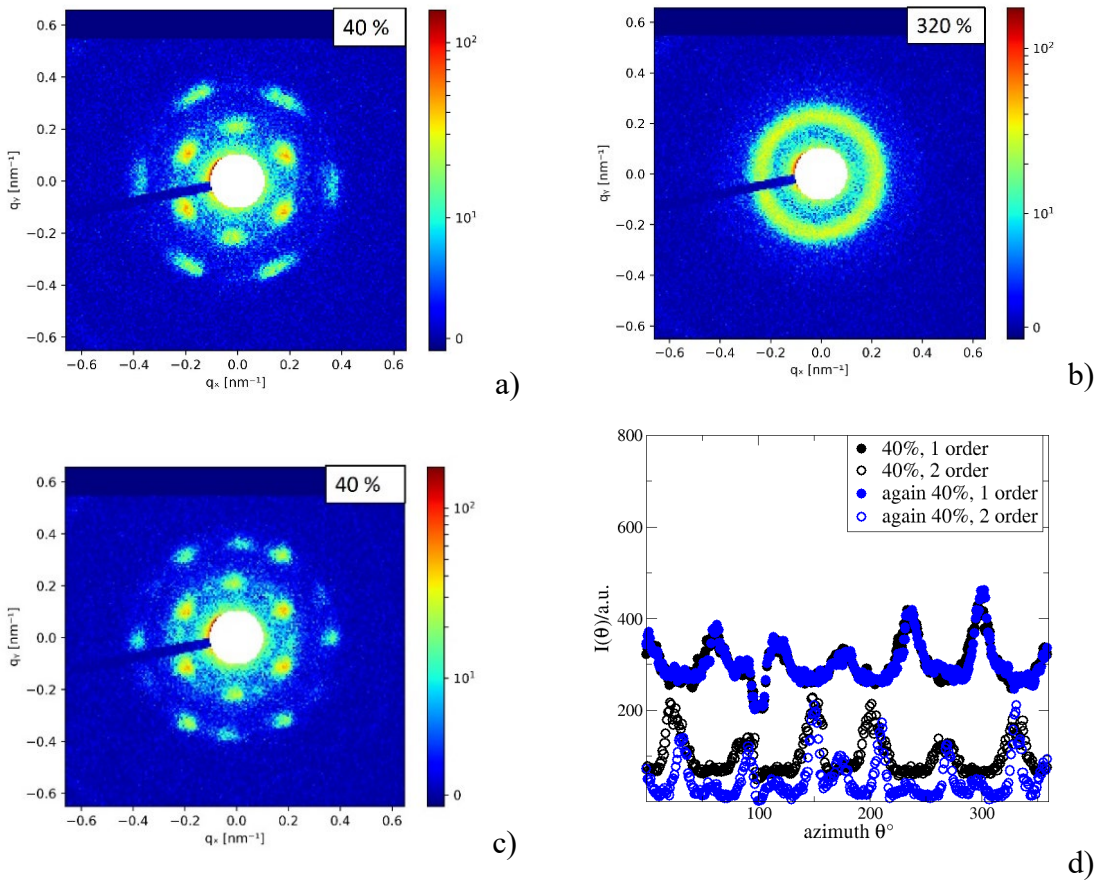

*Figure 3.7 PI PS 20wt% after applying a) 40% strain b) 320% strain c) again 40% strain d) SAXS azimuthal average in the range 0.18<q<0.26 nm^{-1} for **40% strain** (black solid dot), **again 40%** (blue solid dot) and in the range 0.32<q<0.42 nm^{-1} for **40% strain** (black hollow dot), **again 40%** (blue hollow dot)*

Another way to change a formed structure is to increase the temperature of the system [22–24]. Figure 3.8 demonstrates a mixed FCC phase of PI-PS micelles formed at 25 °C under 40 % strain shearing. Heating the sample to 70 °C under 40% strain shearing smears the diffraction pattern indicating a partial disordering of the structure. Further cooling down the system to 25 ºC under 40 % strain leads to the recovery of the FCC mixture phase.

Characteristic diffraction pattern of the second order has been already observed in Figure 3.7 c at the same conditions (25 °C and 40 % shearing). These 6 doubled peaks appear again after a significant change of temperature back to 25 °C (Figure 3.8 c) mirroring the reproducibility of micelles assembly after the temperature variation. This, in particular, indicates that the temperature increase disturbs a long-range order but leaves a local packing unchanged.

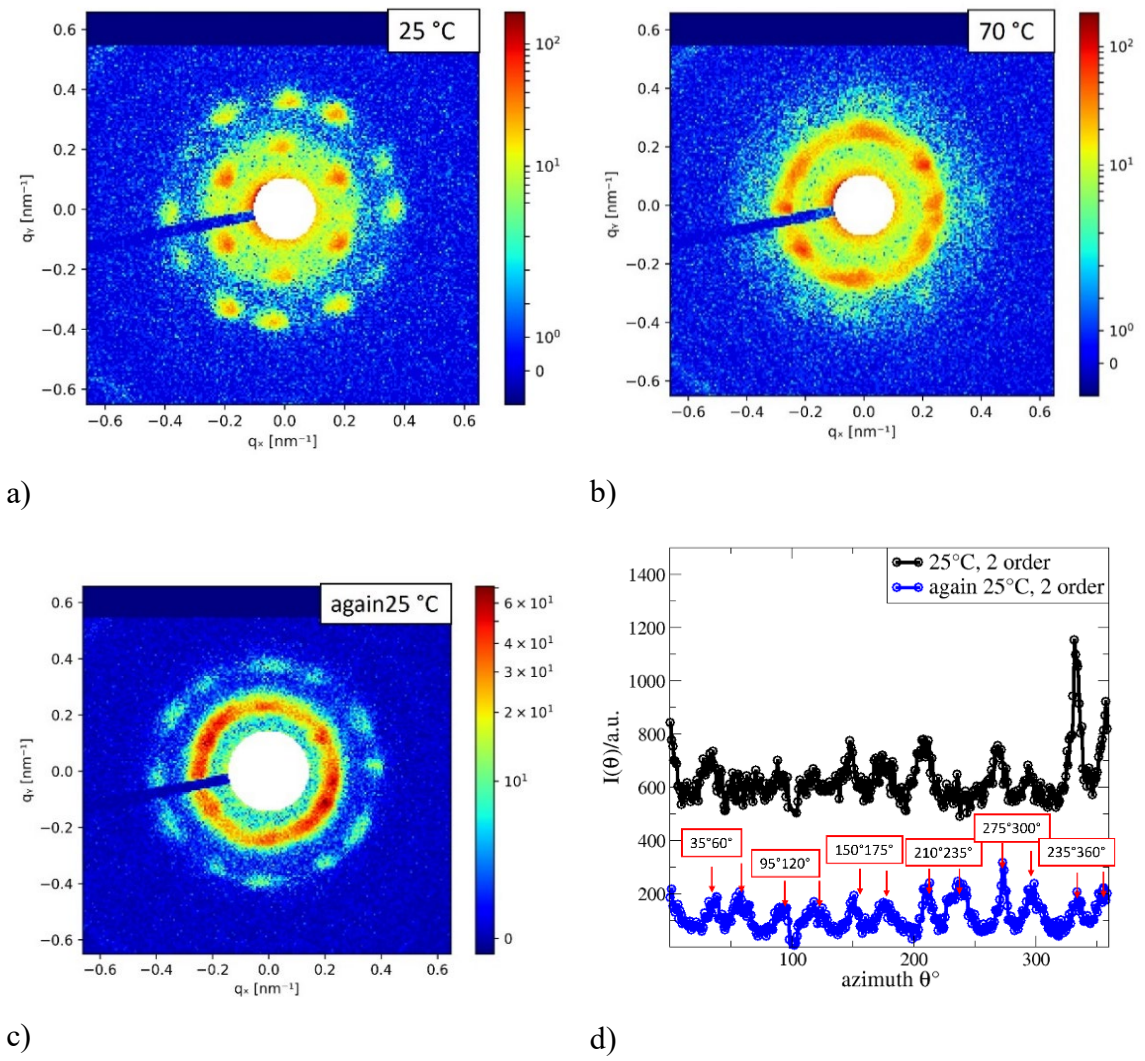

Figure 3.8 PI-PS 20wt% in DEP system shearing at 40% strain and temperatures a) 25 °C b) 70°C c) again 25 °C d) Azimuthally averaged SAXS curve for the ***second order at 25°C*** *and after cooling the sample* ***back to 25°C*** *in the range 0.32<q<0.42 nm^{-1}*

3.3.3 Shearing and temperature initiated reorientation

The combination of temperature and shearing methods helps to get assembled lattices for highly concentrated samples which usually demand longer shearing time. Even more, the combination of methods can induce a transition of LCP. As an example, we consider the phase transition from weakly-ordered FCC to a mixed phase and the rotated FCC for the PI-PS block copolymer system at 25 wt% concentration (Figure 3.9). Continuous shearing at the constant 60 % strain and an increase of temperature with the step 5/10 °C reveals a weakly ordered FCC phase at room temperature, rotated FCC at 70 °C, and in between a mixture of these two phases at 50 °C while heating. After the sample temperature is turned back to 25 °C the rotated FCC pattern doesn't change significantly but gets some additional reflections. Azimuthal plots (Figure 3.9 f) clearly show the presence of two phases at 50 °C (marked in red). It can be seen that both strain and temperature assist in removing or at

least reducing lattice defects. Moreover, upon the temperature is reduced to 25 °C the micellar structure has fewer defects: diffraction spots of FCC lattice have a sharp 60° angle in between.

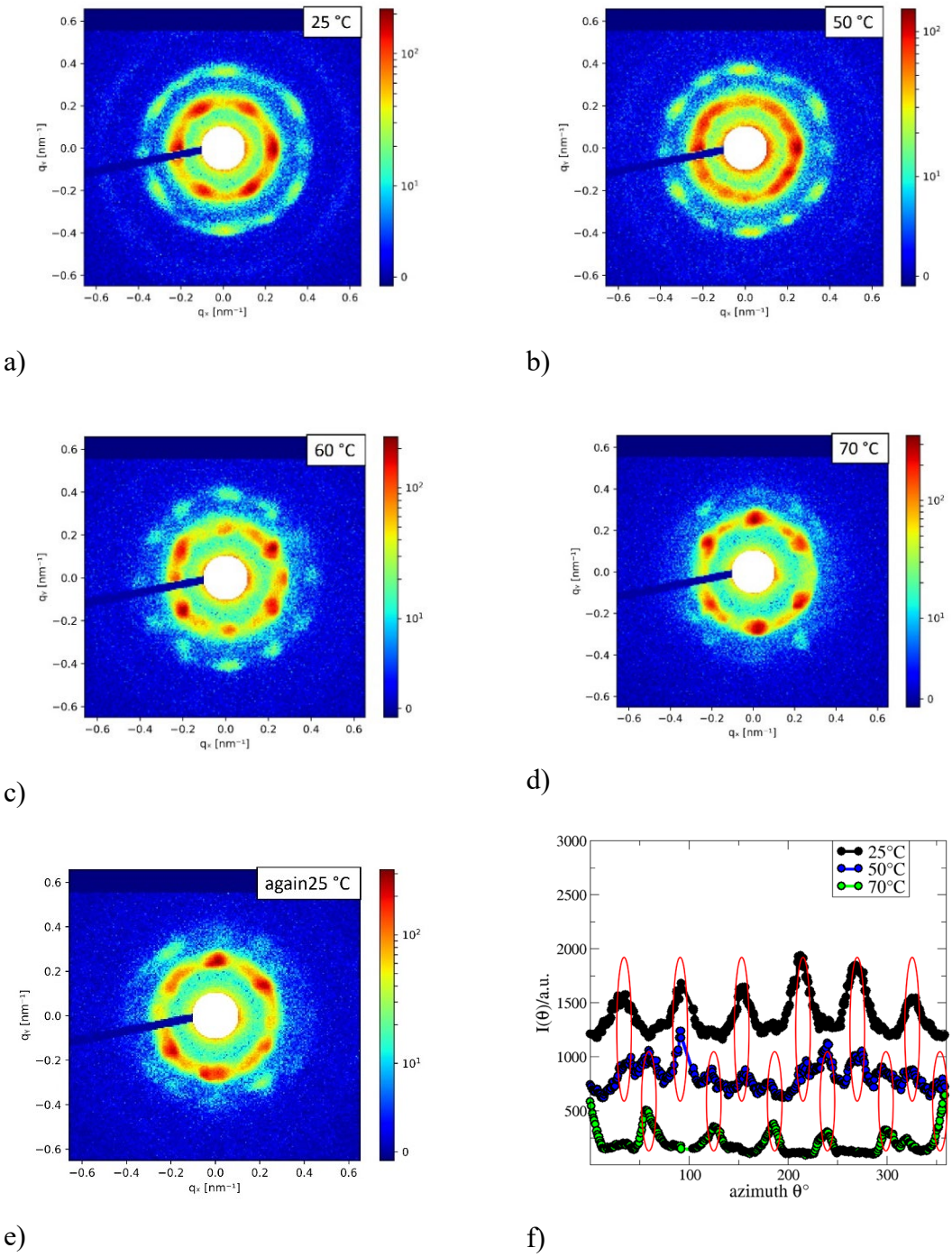

*Figure 3.9 Continuous shearing at 60% strain of 25wt% concentrated sample leads to the formation of a) FCC at **25 °C** (black curve) b) mixed phase at **50 °C** (blue curve) c) transitional mixed phase at 60 °C d) rotated FCC at **70°C** (green curve) e) rotated FCC at 25°C f) azimuthally averaged scattering curves for **25 °C**, **50 °C** and **70 °C***

3.4 Materials and methods

3.4.1 Materials

Diethyl phthalate (Sigma-Aldrich, 99.5 %), laboratory synthesized PI_{210}-PS_{154}-OH block copolymer.

3.4.2 Synthesis

Poly(isoprene-b-styrene) was synthesized via sequential living anionic polymerization, the whole procedure is described in detail by Pirner and colleagues [25].

Sample preparation was carried out in the following way: PI-PS polymer powder was directly mixed with the DEP solvent at concentrations 15 to 25wt %, the resulting mixture was left overnight in a shaker to let micelles form and later centrifuged for 30 min at 2200*g till homogeneous state.

The hydrodynamic radii of the micelles were determined by dynamic light scattering (DLS) and were carried out with a Malvern Instruments Zetasizer.

3.4.3 Rheology measurements

Rheological properties of the concentrated micellar solutions (ϕ >0.15) were studied by using a strain-controlled Ares-G2 rheometer with a 25 mm stainless steel parallel cone–plate setup, the gap width of 400 µm and at the room temperature T=24 °C.

3.4.4 SAXS measurements

SAXS experiments were held with the system “Ganesha-Air”. The X-ray source is D2-Metalljet (Excillium) with a liquid metal anode operating at 70 kV and 3.57 mA with Ga-Kα radiation (λ = 0.1314 nm) providing a thick beam (< 100 µm) of high brilliance. X-ray optics (Xenocs) provides small and intense beam at the sample position, the beam size is adjusted with two pairs of slits depending on the detector distance. Samples were measured in the cuette-type shear cell. Data was radially averaged and normalized to measurement time without background substruction.

3.4.5 Shearing cell of cuette type

A new shearing cell was constructed in FZ Jülich and tested with PI_{210}-PS_{154}-OH block copolymer system in DEP solvent (Figure 3.10). It represents itself a motor-rotated cylinder that is loaded to the cuette with the sample. Both the rotating cylinder and sample cup have tape-glued windows for SAXS measurements, furthermore, the sample cuette has one

additional window for measurements in the tangential direction. The presence of radial position means that the sample is perpendicular to the X-ray beam, tangential – sample is at an angle to the beam (Figure 3.13). After a series of tests, we found the need for proper gap setting and further improvement of measurement techniques in the tangential direction.

The brightest advantage of this particular shearing cell is its upper limit of strain, which reaches 500%. In comparison to Linkam CSS450, it is five times higher and allows measurements of highly-viscous samples. Meanwhile, the new shearing device has a water cooling/heating system, that provides a temperature range between 5 °C and 90 °C for the sample environment.

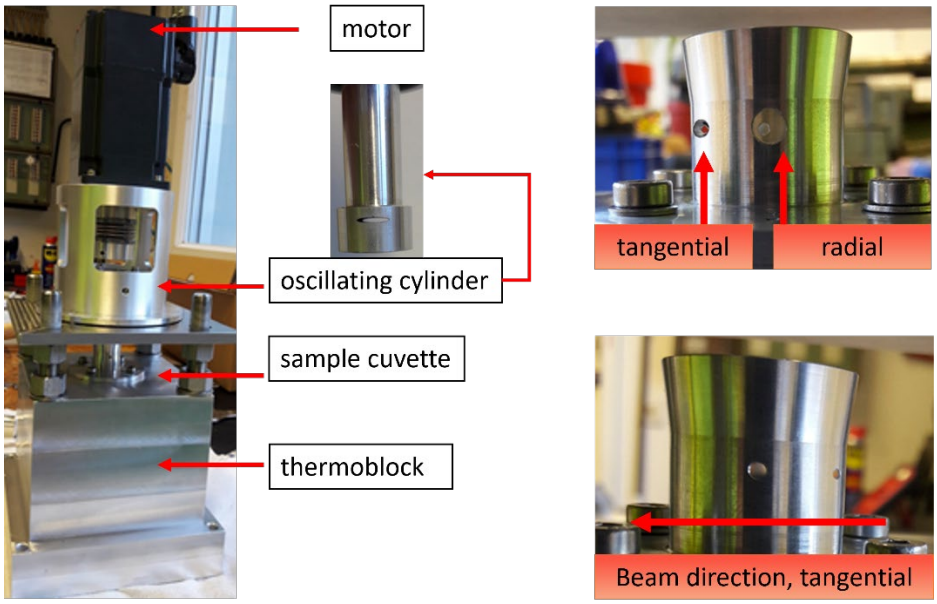

Figure 3.10 Shear cell of cuette type and sample cup with holes for measuring sample in radial and tangential positions

3.5 Conclusion

The results presented in this chapter confirm the importance of shearing parameters tuning for the formation of well-ordered assembled structures in polymer micellar systems. Using PI-PS block-copolymer in DEP we have demonstrated that in the linear viscoelastic region, only the formation of FCC lattice in the mixture with the other structural formations is possible, in agreement with the literature data. Moreover, FCC structure becomes well-ordered either with an increase of shearing time or shearing strain value. Well-ordered FCC appears at the strain values, which are slightly or far behind the cross-point of viscous and elastic components. Meanwhile, the application of significantly high strains up to 200 % doesn't lead to an improvement of the order, but on contrary it disorders the FCC structure. The appropriate shearing parameters depend on the rheological properties of the system: a higher micellar concentration requires a higher shearing rate to get a well-ordered structure as well as to disorder it completely. Here the role of concentration is emphasized as a way to construct a stable and robust system at higher shear rates.

Applying extremely high oscillation strains doesn't only disturb the assembly of the system, but also makes it possible to reuse the material. In comparison to the influence of high temperature, an ordered structure appears completely again after its disassembly by very high shearing rates. If the structure is disordered under shearing by a high temperature it irreversibly loses the long-range order. Furthermore, a combination of shearing and temperature can induce the formation of an intermediate phase indicated by diffraction spots of both, poorly- and well-ordered FCC lattices.

A successful test of the new shearing device of cuette type was carried out. In comparison to the commercial types of shearing instruments, it allows an application of strains up to 500% and measurement even of highly concentrated stiff gels. Additionally, a sample load to the cuette allows the shearing of more liquid mixtures. All performed experiments helped us find issues and will lead to a big improvement for the next iteration of the device. This includes the development of the procedure for a proper setup of the gap between the shearing rode and cuette. Finally, the presence of both radial and tangential positions makes possible a comprehensive study of soft matter systems using the laboratory X-ray source and the combination of temperature with the shearing field.

3.6 Supporting information

The average size of PI_{210}-PS_{154}-OH block copolymer micelles formed in DEP is 36 nm. Hydrodynamic radius is obtained via DLS measurements (Figure 3.11).

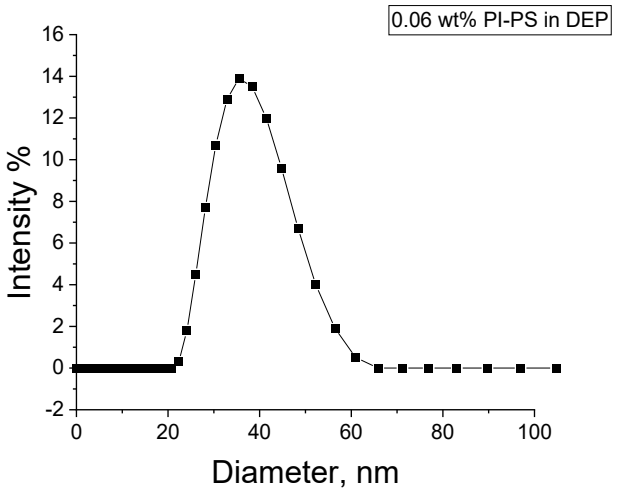

Figure 3.11 Size distribution of PI-PS micelles at 0.06 wt% concentration

In addition to Figure 3.8 azimuthally averaged SAXS curves for the first order are provided in Figure 3.12. Peak positions have the 60° distance revealing FCC lattice for 20 wt% concentration of PI-PS block copolymer in DEP after continuous shearing at 40 % strain.

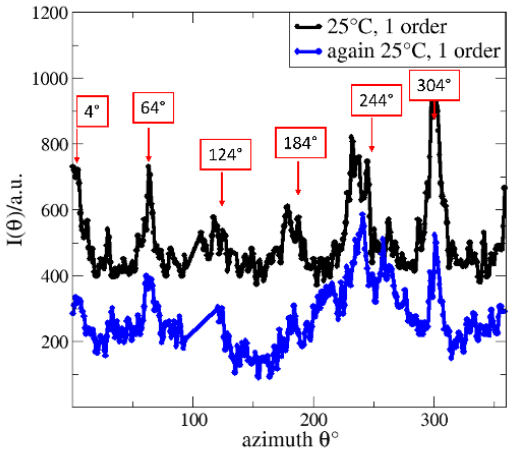

*Figure 3.12 Azimuthal average of SAXS data for the sample at **25°C** and cooled to **again 25°C** at the first order*

Figure 3.13 illustrates a comparison of measurements in radial and tangential positions for a 25 wt% concentrated polymer mixture in DEP. After shearing the sample at high strains (up to 80 %) well-ordered FCC structure is measured from both directions.

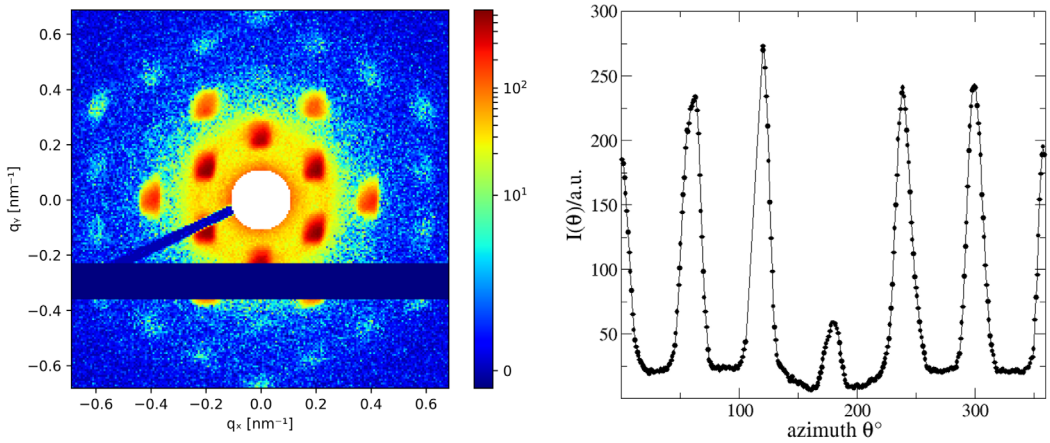

a)

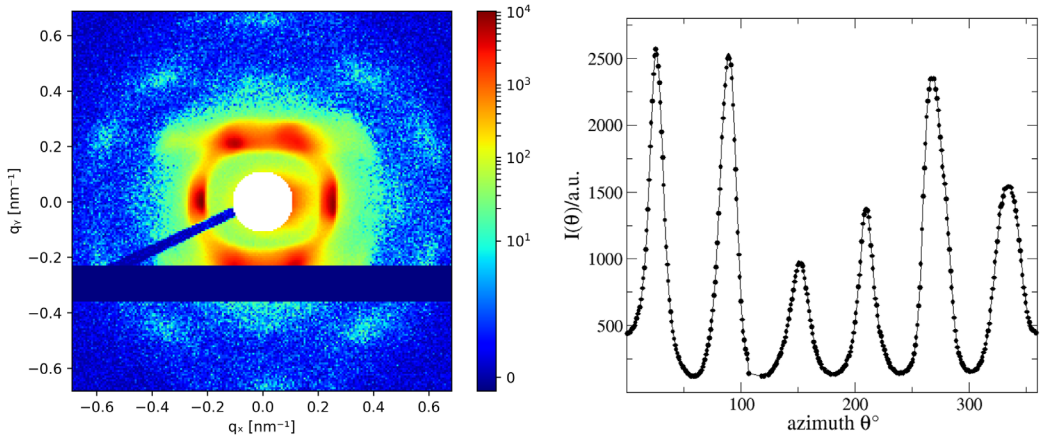

b)

Figure 3.13 SAXS measurements of PI-PS polymer at 25wt% concentration in DEP in a) radial position and b) tangential position

3.7 References

[1] I. W. Hamley, J. A. Pople, A. J. Gleeson, B. U. Komanschek, E. Towns-Andrews, *J. Appl. Cryst.* **1998**, *31*, 881–889.

[2] H. Feng, X. Lu, W. Wang, N. G. Kang, J. W. Mays, *Polymers 2017, Vol. 9, Page 494* **2017**, *9*, 494.

[3] S. Förster, M. Antonietti, *Adv.Mater* **1998**, *10*, DOI 10.1002/(SICI)1521-4095(199802)10:3.

[4] S. Fischer, A. Exner, K. Zielske, J. Perlich, S. Deloudi, W. Steurer, P. Lindner, S. Förstere, *Proc Natl Acad Sci U S A* **2011**, *108*, 1810–1814.

[5] T. Thurn-Albrecht, J. Schotter, G. A. Kastle, N. Emley, T. Shibauchi, L. Krusin-Elbaum, K. Guarini, C. T. Black, M. T. Tuominen, T. P. Russell, *Science (1979)* **2000**, *290*, 2126–2129.

[6] J. Y. Cheng, C. A. Ross, H. I. Smith, E. L. Thomas, *Advanced Materials* **2006**, *18*, 2505–2521.

[7] M. Stefik, S. Guldin, S. Vignolini, U. Wiesner, U. Steiner, *Chem Soc Rev* **2015**, *44*, 5076–5091.

[8] A. Rösler, G. W. M. Vandermeulen, H. A. Klok, *Adv Drug Deliv Rev* **2012**, *64*, 270–279.

[9] T. Hashimoto, K. Fukunaga, *NanoScience and Technology* **2007**, 45–97.

[10] T. Hashimoto, J. Bodycomb, Y. Funaki, K. Kimishima, *Macromolecules* **1999**, *32*, 952–954.

[11] A. C. Arsenault, D. A. Rider, N. Tétreault, J. I. L. Chen, N. Coombs, G. A. Ozin, I. Manners, *J Am Chem Soc* **2005**, *127*, 9954–9955.

[12] A. Böker, A. Knoll, H. Elbs, V. Abetz, A. H. E. Müller, G. Krausch, *Macromolecules* **2002**, *35*, 1319–1325.

[13] C. Y. Chao, X. Li, C. K. Ober, *Pure and Applied Chemistry* **2004**, *76*, 1337–1343.

[14] Z. R. Chen, J. A. Kornfield, S. D. Smith, J. T. Grothaus, M. M. Satkowski, *Science (1979)* **1997**, *277*, 1248–1253.

[15] Kenneth J. Hanley, Timothy P. Lodge and Ching-I Huang, *Macromolecules* **2000**, *33*, 5918–5931.

[16] J. A. Pople, I. W. Hamley, J. P. A. Fairclough, A. J. Ryan, B. U. Komanschek, A. J. Gleeson, G. E. Yu, C. Booth, *Macromolecules* **1997**, *30*, 5721–5728.

[17] Y. Y. Huang, H. L. Chen, T. Hashimoto, *Macromolecules* **2003**, *36*, 764–770.

[18] T. Jurczyk, S. F. Förster, W. Richtering, **2021**, DOI 10.18154/RWTH-2021-11518.

[19] A. Guinier, *Small-Angle Scattering of X-Rays*, Wiley, New York, **1955**.

[20] K. J. Hanley, T. P. Lodge, C. I. Huang, *Macromolecules* **2000**, *33*, 5918–5931.

[21] S. M. Taheri, S. Rosenfeldt, S. Fischer, P. Bösecke, T. Narayanan, P. Lindner, S. Förster, *Soft Matter* **2013**, *9*, 8464–8475.

[22] E. di Cola, C. Lefebvre, A. Deffieux, T. Narayanan, R. Borsali, *Soft Matter* **2009**, *5*, 1081–1090.

[23] A. Ianiro, M. M. R. M. Hendrix, P. J. Hurst, J. P. Patterson, M. Vis, M. Sztucki, A. C. C. Esteves, R. Tuinier, *Macromolecules* **2021**, *54*, 2912–2920.

[24] A. Matsushita, S. Okamoto, *Polymer Journal 2015 47:5* **2015**, *47*, 385–390.

[25] D. Pirner, M. Dulle, M. E. J. Mauer, S. Förster, *RSC Adv* **2016**, *6*, 42730–42738.

4 Size-control of iron oxide nanoparticles synthesized by thermal decomposition methods

4.1 Abstract

The controlled synthesis of superparamagnetic iron oxide nanoparticles is crucial for a variety of biomedical applications. Among different synthesis routes thermal precursor decomposition methods are the most versatile, yielding monodisperse nanoparticles on the multi-gram scale. Recent *in situ* kinetic studies of the nucleation and growth processes during thermal decomposition routes revealed non-classical nucleation and growth paths involving amorphous precursor phases and aggregative growth steps. With the knowledge of this kinetic mechanism we systematically examined a range of different iron oxide heat-up synthesis routes to understand and conclude which methods allow good and reproducible size control over a range of relevant nanoparticle diameters. Using transmission electron microscopy (TEM) and small-angle X-ray scattering (SAXS) for the characterization of the nanoparticle size distribution we find that a set of solvents (1-octadecene, trioctylamine, docosane) provides access to a temperature range between 300 – 370°C allowing to synthesize monodisperse nanoparticles in a size range of 5 – 24 nm on large scale. We confirm that a thermal pretreatment of the iron oxide precursor is essential to achieve reproducible size control. We find that each solvent provides access to a certain temperature range, within which the variation of temperature, heating rate or precursor concentration allows to reproducibly control the nanoparticle size.

4.2 Introduction

Magnetic nanoparticles have received increasing attention in fundamental research as well as in a range of applications, particularly in medical diagnostics and therapy. Of great interest are superparamagnetic iron oxide nanoparticles (SPIONs) that are used as contrast agents in magnetic resonance imaging (MRI), in magnetic hyperthermia, for targeted drug delivery, and for bio separation[1].

SPIONs can be synthesized by different synthesis routes, among which thermal precursor decomposition methods are the most versatile, yielding monodisperse nanoparticles on the multi-gram scale. Following the pioneering work of Park *et al.* [2], different variations of the thermal decomposition route have since then been developed. [2,3,4] They utilize ligand-assisted control over the nucleation and growth process to tailor nanoparticle size, shape and crystallinity. Thermal decomposition methods such as the heat-

up method aim to separate the nucleation phase from the subsequent growth phase. If this is achieved, the variation of synthesis parameters such as temperatures, heating rate, precursor and ligand concentrations allows a size-controlled synthesis of monodisperse nanoparticles.

Recent investigations by time-resolved in situ X-ray scattering and electron microscopy of the nucleation and growth of nanoparticles [5,6] in the heat-up synthesis method showed that the nucleation and growth kinetics is rather complex, involving an amorphous precursor phase and aggregative growth, presumably by oriented attachment, until subsequent growth by monomer consumption yields the final nanoparticles. With the knowledge of this kinetic mechanism we here systematically examined a range of common variations of the iron oxide heat-up synthesis routes to understand and conclude which methods allow good and reproducible size control over a range of relevant nanoparticle diameters between 5 and 24 nm. Using transmission electron microscopy (TEM) and small-angle X-ray scattering (SAXS) for the characterization of the nanoparticle size distribution we find that a set of solvents (1-octadecene, trioctylamine, docosane), which provide access over a temperature range between 300 – 370°C, allows to synthesize monodisperse nanoparticles in a size range of 8 – 24 nm on large scale. We confirm that a thermal pretreatment of the iron oxide precursor is essential to achieve reproducible size control.

4.3 Results and discussion

4.3.1 Time-resolved small-angle X-ray scattering experiments

Small-angle X-ray scattering (SAXS) was used to characterize the size and size distribution of the obtained nanoparticles in solution, and in one case during the synthesis. Figure 4.1 a-d show typical measured SAXS-curves for iron oxide nanoparticles. The scattering curves show a well-defined Guinier plateau at small values of the scattering vector q, followed by the q^{-4} Porod regime featuring several formfactor oscillations. These allow to determine the mean particle diameter and polydispersity with good accuracy.

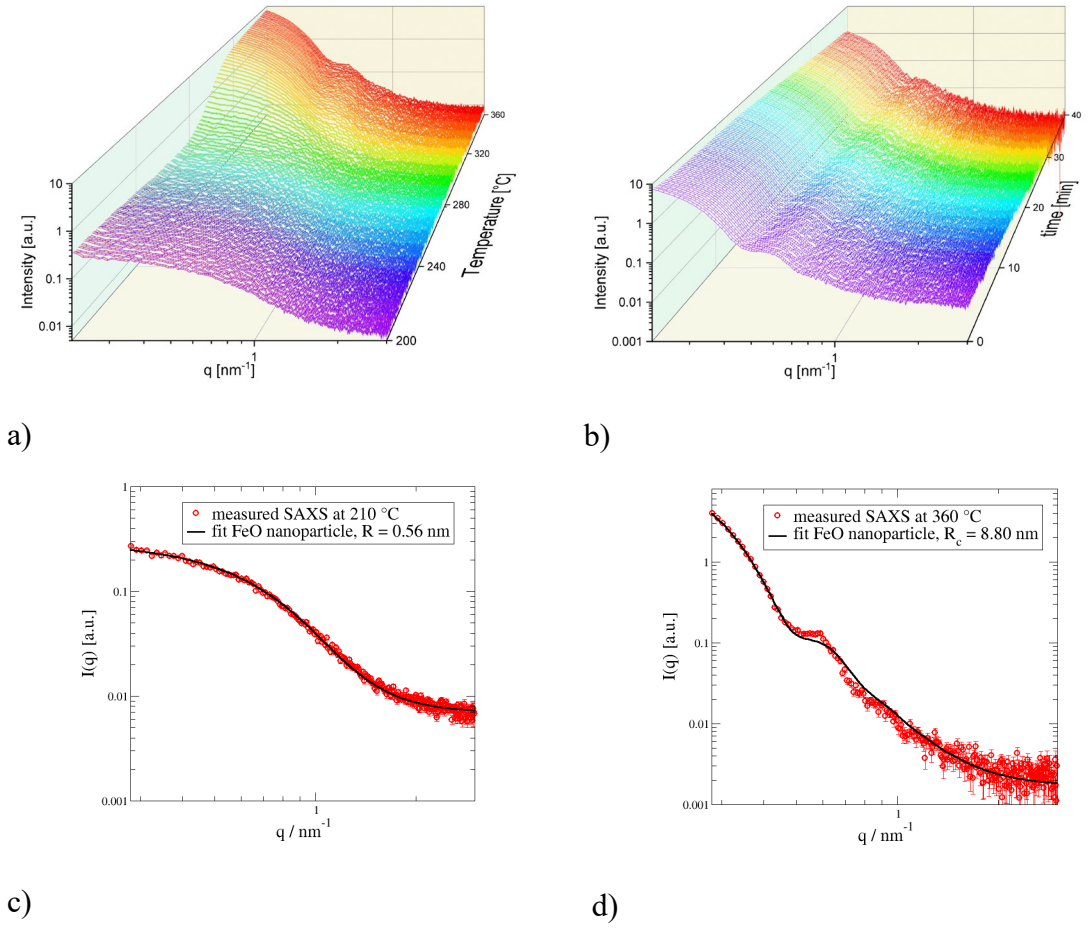

Figure 4.1 a) SAXS curves during heating of the reaction mixture in trioctylamine from 200 °C to 360 °C, b) SAXS curves for subsequent annealing phase at 360 °C for 40 min. c, d) SAXS curves at 210 °C and 360°C with fits to Eqs. (2, 3) (solid lines)

For a quantitative analysis we use an analytical description of the scattering curve. The scattering intensity $I(q)$ is given by

$$I(q) = I_0[P](\Delta b)^2 V^2 P(q) \qquad 4.2$$

where I_0 is the primary X-ray beam intensity, [P] the particle concentration, Δb the scattering contrast between particle and solvent, and V the volume of the particle. $P(q)$ is the formfactor of the particle, for which we assume a core/shell structure, where the iron oxide nanoparticle forms the core and the ligand forms the shell. In the limit $q \to 0$ the formfactor approaches $P(q) \to 1$. This allows to calculate a relative particle concentration $N_{rel} = I(0)/V^2$ from Eq. 4.2, which during the nucleation process first increases and later decreases due to aggregative growth (See Supporting Information, Figure 4.13).

The formfactor for polydisperse homogeneous spherical particles is given by

$$P(q) = \frac{9}{(qR)^6}(sin(qR) - qR\,cos(qR))^2 \qquad 4.3$$

where R is the particle radius. To take into account polydispersity, the formfactor $P(q)$ is averaged over a size as outlined in ref. [5]. This formfactor is used to describe the scattering curves in the initial phase of the heat-up synthesis as shown in Figure 4.1 c.

In the subsequent phase the scattering curves are described by the formfactor of spherical core/shell particles with homogeneous core and shell. The formfactor is given by

$$P(q) = \frac{3}{V_s}\left[V_c(\rho_c - \rho_s)\frac{sin(qR_c) - qR_c\,cos(qR_c)}{(qR_c)^3} + V_s(\rho_s - \rho_{solv})\frac{sin(qR_s) - qR_s\,cos(qR_s)}{(qR_s)^3}\right] \quad 4.4$$

where V_s is the volume of the whole particle, V_c is the volume of the core, R_s is the radius of the particle, R_c is the radius of the core, ρ_c , ρ_s and ρ_{solv} are the scattering length density of the core, shell and solvent. The ligand shell contributes significantly to the scattering intensity at high q. The shell thickness between 1.7 and 3 nm is in good agreement with the expected thickness of ligand monolayers.

During the development of a new *in situ* SAXS high-temperature reactor we were able to perform a first experiment using a high-boiling solvent trioctylamine. For the *in situ* experiment the reaction mixture was preheated to 200 °C. Below a temperature of 200°C we did not observe any changes of the reaction mixture or indications for particle formation. The measured SAXS curves for the heating process from 200 °C to 360 °C (Figure 4.1 a) show a typical Guinier region and a high-q decay typical for very small particles. Fig. 1 c shows the SAXS curve measured at 210 °C. We could fit this curve with a model of polydisperse spheres. The obtained radius is 0.56 nm, suggesting the presence of small stable iron-ligand species. All data until 280 °C give the same radius when fitted. Above 280°C growth of monodisperse particles can be observed. After the heating ramp from 200 – 360°C the reaction mixture was stirred for 40 min at 360 °C as shown in Figure 4.1 b, where a slight decay of the scattering intensity with time is observed. Figure 1 d shows the SAXS curve measured at 360 °C. We clearly observe the shift of the first minimum of the scattering curve to lower q-values during the second phase above 280°C, indicating the growth of the narrow disperse iron oxide nanoparticles.

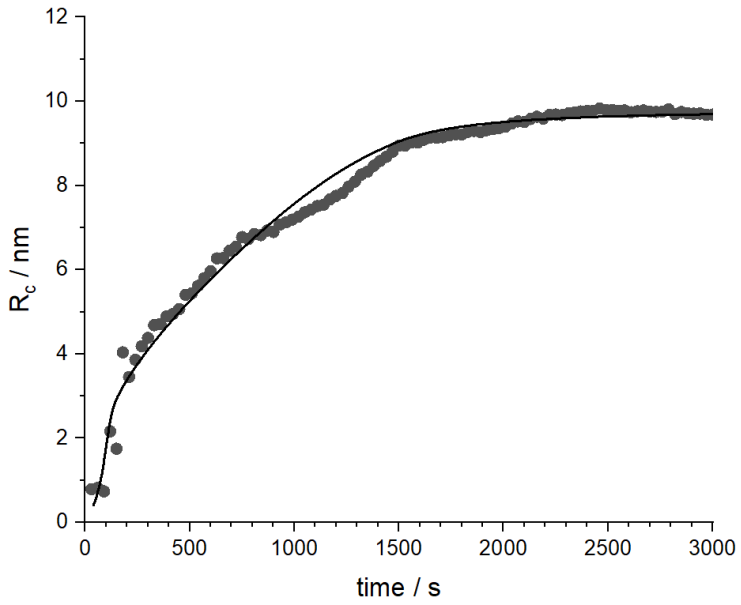

Figure 4.2 Measured core radii for the kinetic experiment shown in Fig. 1 together with a model calculation (solid line) using the kinetic scheme from Eq. (4). The time is set to zero when the temperature reached 280 °C and a growing of the particle radius could be observed. The calculated curve well describes the main features of the growth curve including the induction time, the time period for the burst nucleation, the subsequent growth phase and the final plateau value of the particle radius.

Figure 4.2 shows the measured core radii as a function of time as determined from the scattering curves in Figure 4.1 a and b. We observe the onset of nucleation to occur after 100 s, followed by a sharp initial increase of the radii to 4 nm during the next 100 seconds. Subsequently the particles grow at lower growth rates to finally reach a radius of 9.8 nm after 2000 seconds.

The main features of the growth curve including the induction time of 100 seconds, the nucleation phase in the subsequent 100 seconds and the following growth and saturation phase can be well described by a nucleation and growth model as shown by the solid line in Figure 4.2. The corresponding kinetic considers (i) the $Fe(OA)_3$ iron oleate precursor decomposition with a rate constant k_1, (ii) a classical nucleation step with the rate constant k_{nuc}, (iii) particle growth by consumption of precursor with a growth rate k_{gr}, and (iv) aggregative growth steps, e.g. by oriented attachment, with a rate constant k_{agg}

$$Fe(OA)_3 \xrightarrow{k_1} Fe(OA)_m$$

$$Fe(OA)_m \xrightarrow{k_{nuc}} (FeO_x)_{nuc}$$

$$P_J \xleftrightarrow{k_{gr,J}} P_{J+1} \qquad 4.5$$

$$P_J + P_{J'} \xrightarrow{k_{agg}} P_{J+J'}$$

The model is described in detail in reference [6] and the main parameters are summarized in the Supporting Information. For the present study we note that the model captures the main features of the iron oleate heat-up synthesis kinetics as shown in Figure 4.1 a, b, using the exact same thermodynamic and kinetic parameters used in the previous kinetic study [6], which themselves well compare to studies reported earlier in literature. In the previous study we used 1-octadecence as a solvent, whereas in Figure 4.1 and Figure 4.2 trioctylamine was the solvent. The only difference in parameters compared to the study in 1-octadecene is that for trioctylamine we used a smaller precursor decomposition rate constant of $k_{1,0}$ =6.0·10^2 mol/m^3·s compared to $k_{1,0}$ =3.0·10^5 mol/m^3·s for 1-octadecene, and a growth rate constant of $k_{gr,0}$ = 3.3·10^5 m/s which is slightly larger than for 1-octadence where the values were in a range of $k_{gr,0}$ = 5.8 - 17·10^4 m/s depending on temperature. In the Supporting Information we also consider the temporal evolution of the relative particle numbers N_{rel} which decreases during the reaction due to aggregative growth steps. The measured shell radius R_s varies between 1.7 nm and 3 nm when R_c reaches a size bigger than 4.5 nm. This is in good agreement with the thickness of a ligand shell.

The knowledge that the nucleation and growth kinetics at higher temperatures up to 360°C in the high-boiling solvent trioctylamine is the same as for 1-octadence at lower temperatures of 280 – 320°C allows us to better rationalize the influence of different experimental parameters to conclude on the most favorable experimental conditions to synthesis monodisperse iron oxide nanoparticles over a wide range of diameters.

4.3.2 Iron oleate precursor synthesis

We found that one essential parameter for a reproducible synthesis of superparamagnetic iron oxide nanoparticles (SPIONs) is the final treatment of the synthesized iron oleate complex. It can be synthesized via the reaction of iron chloride and sodium oleate 1, 2 or using iron oxides dissolved in oleic acid [8,9]. In the present work the synthesis of the iron-oleate precursor was performed using reaction of iron (III) chloride and sodium oleate.
Since the synthetic procedure is important, we here describe the synthesis steps with the relevant details. In a typical procedure 32.4 g of iron chloride ($FeCl_3 \cdot 6H_2O$) and 109.5 g of sodium oleate were mixed and dissolved in a mixture of 120mL of distilled water, 160 mL of ethanol and 280 mL of heptane. The solution was stirred at 70 °C for 4 hours. Afterwards the brownish organic phase was washed 3 times with distilled water in a separatory funnel. Subsequently, heptane was removed in a rotary evaporator, followed by drying the resultant

iron oleate at 60 °C for 3 days, until the substance became highly viscous. The iron oleate complex was further stored in a vacuum oven.

Systematic studies of the dependence of SPION size-control on the iron oleate drying time were reported earlier[10]. An increase of the particle size with increasing precursor drying time was observed. Using FTIR-spectroscopy and DSC-analysis, the authors detected a decreasing amount of weakly ligand-bound Fe centers with increasing drying time. Therefore, we investigated the influence of iron oleate drying time on the size, size distribution, and shape of the obtained SPIONs for our iron oleate precursors as well.

One type of synthesis was performed with a “fresh” precursor which was only dried in a rotary evaporator. The second type of reaction was done with iron oleate dried for 3 days at 60 °C. Afterwards both precursors were stored in a vacuum oven at room temperature. We observed that nanoparticles synthesized with the “fresh” iron oleate in 1-octadecene (ODE) as a solvent had a radius of 3.6 nm (Figure 4.3 a). The same synthesis was repeated after one and two weeks, where nanoparticles with radii of 4.3 and 5.5 nm were obtained, respectively (Figure 4.3b, c). The analysis of the SAXS curves with a polydisperse core/shell-sphere model (Figure 4.3 d) similarly showed that the average nanoparticle diameters increased with the second and the third synthesis, and that the polydispersity decreased in the same order. Although the quality of the nanoparticles is excellent, there is the disadvantage of the low reproducibility of synthesis because the particle diameter can only be varied rather uncontrollably.

To achieve a more reproducible synthesis and larger particle diameters, we used the second type of synthesis route, i.e. with the iron oleate precursor dried in a water bath at 60 °C. As shown in Figure 4.4 a, the nanoparticles reached a radius of 6.6 nm. A synthesis repeated after two months from the same iron oleate gave particles with a radius of 7.0 nm. (Figure 4.4 b), which indicates good reproducibility of the synthesis, if well-dried iron oleate precursor is used. In light of the investigations reported in ref. [10] we conclude that weakly bound iron centers form weakly stabilized nuclei that are nucleated at higher supersaturation and thus in a larger number, resulting in smaller nanoparticles after growth. In all following investigations we therefore used iron oleate prepared with the additional drying process at 60 °C for a well reproducible synthesis.

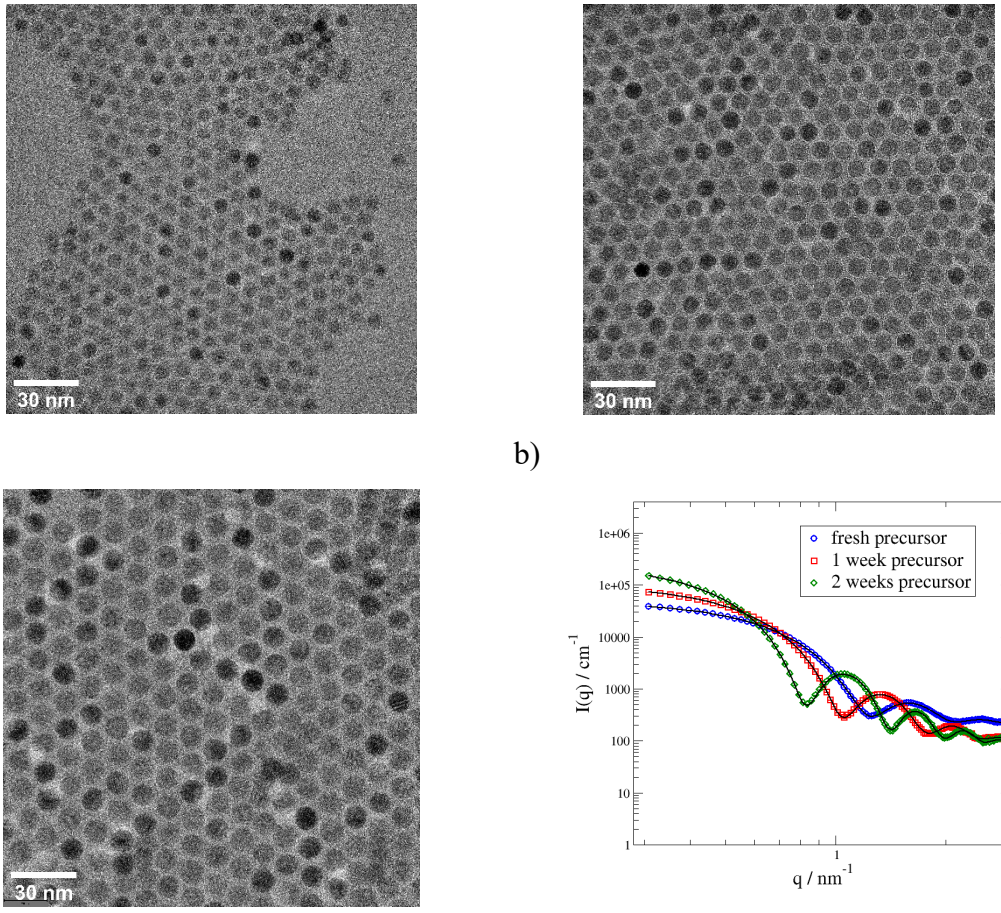

a) b)

c) d)

Figure 4.3 TEM images of SPIONs synthesized from iron oleate precursor which was a) dried only in a rotary evaporator, b) dried additionally for 1 week in the vacuum oven, c) dried additionally for 2 weeks in the vacuum oven, d) core-shell sphere model fits SAXS curves for nanoparticles with radiuses R = 5.5 nm (green curve), 4.3 nm (red curve) and 3.6 nm (blue curve) respectively

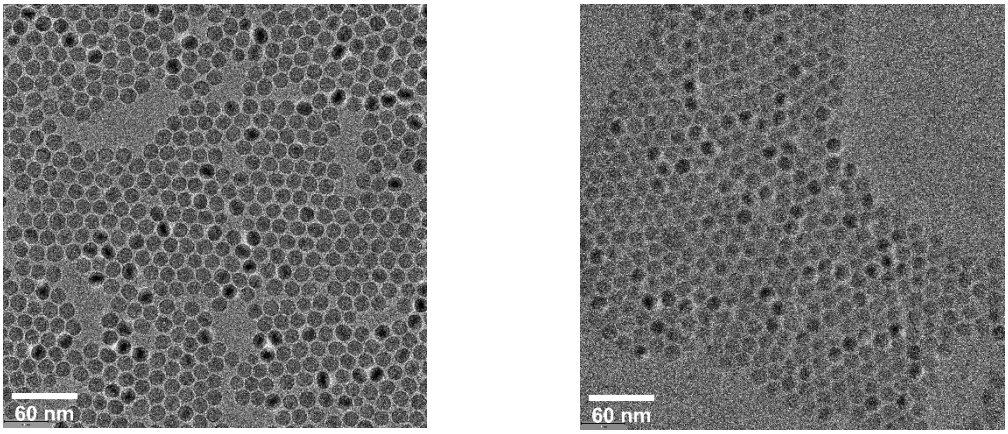

a) b)

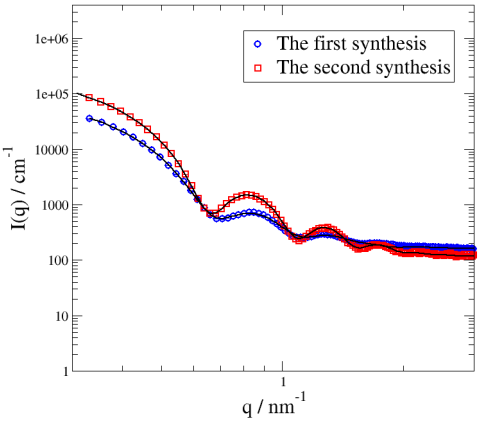

c)

Figure 4.4 SPIONs formed from iron oleate precursor dried in a water bath at 60 °C: a) the first synthesis, b) the second synthesis, repeated after one month, c) core-shell sphere model fits SAXS curves for nanoparticles with R = 6.6 nm (blue curve) and 7.0 nm (red curve), respectively

4.3.3 Influence of the main synthesis parameters

A) Heating rate

Having an adequate iron oleate precursor synthesis established, we changed the heating rate as the first parameter for varying the nanoparticle radius. We changed the heating rate of the reaction solution from the standard (3.3 °C /min) to a slower (1.6 °C /min) and a higher heating rate (10 °C /min), leaving all other standard parameters fixed. We observe that using the standard heating rate of 3.3°C/min leads to highly monodisperse particles with radii of 4.3 nm (Figure 4.5 a). A lower heating rate increases the radius slightly to 4.4 nm with an increased polydispersity (Figure 4.5 b). The higher heating rate broadens the size distribution (Figure 4.5 c).

Generally, lower heating rates lead to larger particles. According to the nucleation and growth kinetic scheme [6] this is due to the lower number of nuclei formed, which upon

consumption of the precursor grow to larger particles. The lower number of nuclei is related to the fact that nucleation for lower heating rates occurs already at lower temperatures, where the nucleation rates are smaller.

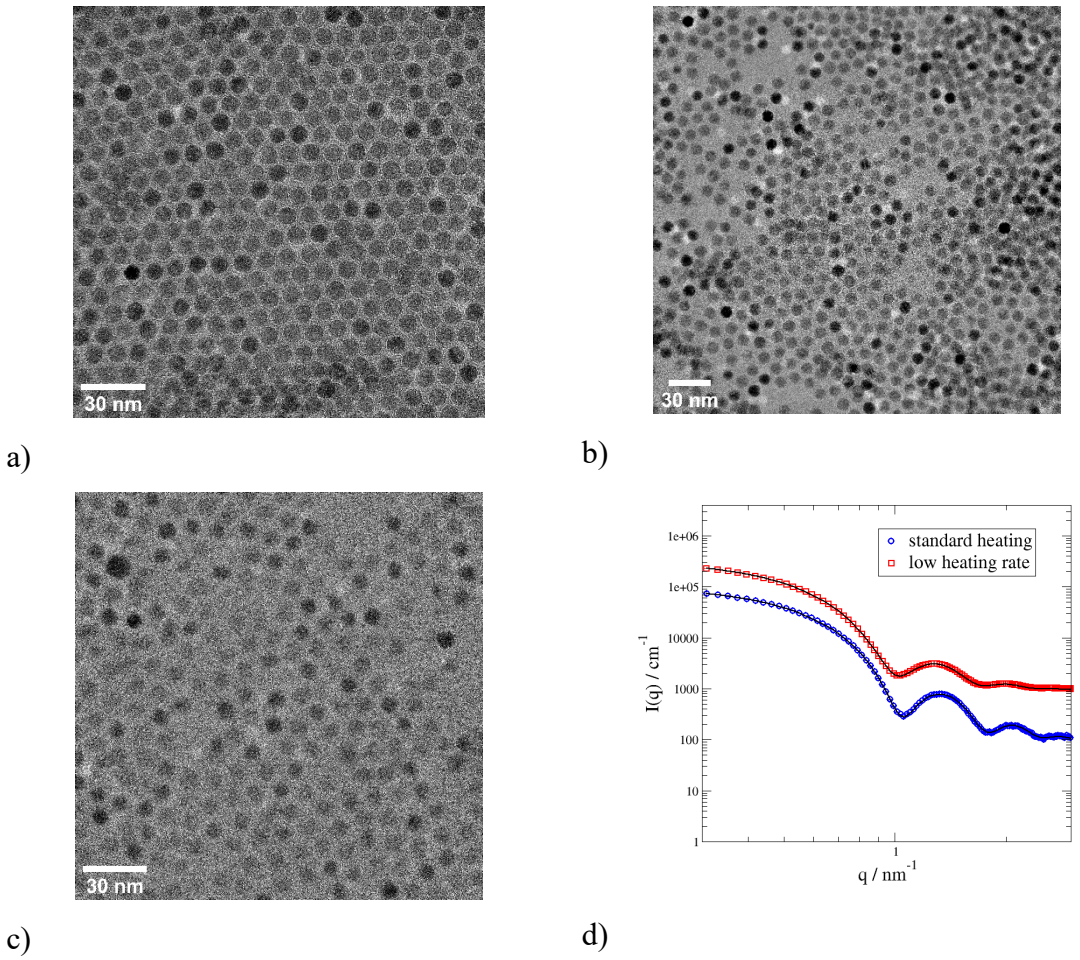

Figure 4.5 SPIONs formed with a) standard 3.3 °C /min rat, b) lower 1.6 °C /min rate, c) and higher 10 °C /min rate. d) Core-shell sphere model fits SAXS curves for nanoparticles with R = 4.3 nm for standard heating rate (blue curve) and 4.4 nm for lower rate (red curve).

B) Annealing time

The annealing time at the final plateau temperature is a parameter that also plays a role in the nanoparticle synthesis. We observe that 30 min of annealing yields monodisperse nanoparticles with a radius of 4.3 nm (Figure 4.6 a). After 60 min the size distribution broadens. Although at first sight the particles look monodisperse, in fact there is a small fraction of small nanoparticles with radii of 2 nm and large nanoparticles with radii of 6.5 nm. An annealing time of 0 minutes, i.e. immediate termination of the reaction right after reaching the final temperature of 320 °C, results in nanoparticles with broader size distributions between 2 to 4 nm radius, because the growth process is not yet completed (Figure 4.6 c). In all cases we obtain spherical nanoparticles. As will be outlined below, SPIONs synthesized in a high boiling solvent (docosane) become spherical and

monodisperse already after 3 min of annealing[11], because the growth rates are sufficiently high. Therefore, we conclude that the annealing time should be just long enough to complete growth.

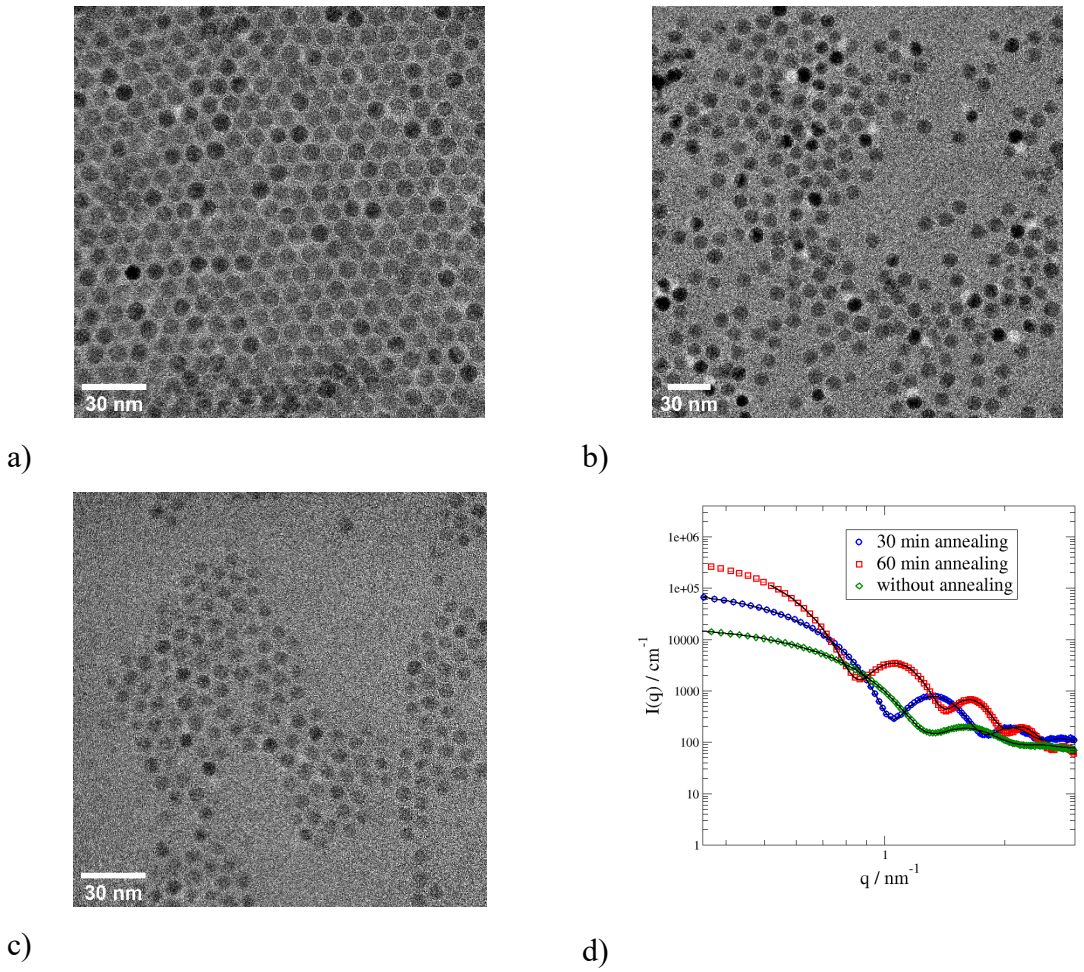

Figure 4.6 Nanoparticles are synthesized at 320 °C during different growth time: a) 30 min, b) 60 min, c) 0 min. d) Core-shell sphere model fits SAXS curves for nanoparticles with R = 4.3 nm (blue curve), 5.3 (red curve) nm and 3.4 nm (green curve), respectively.

C) Ligand type

Oleic acid is the most common ligand for SPIONs surface stabilization [4,7,10,12] . Usually, the variation of the ligands is used to control the shape of SPIONs, mainly via the variation of ratio of sodium/potassium oleate and oleic acid ligands[12,13]. In our case we only focus on the synthesis of spherical nanoparticles.

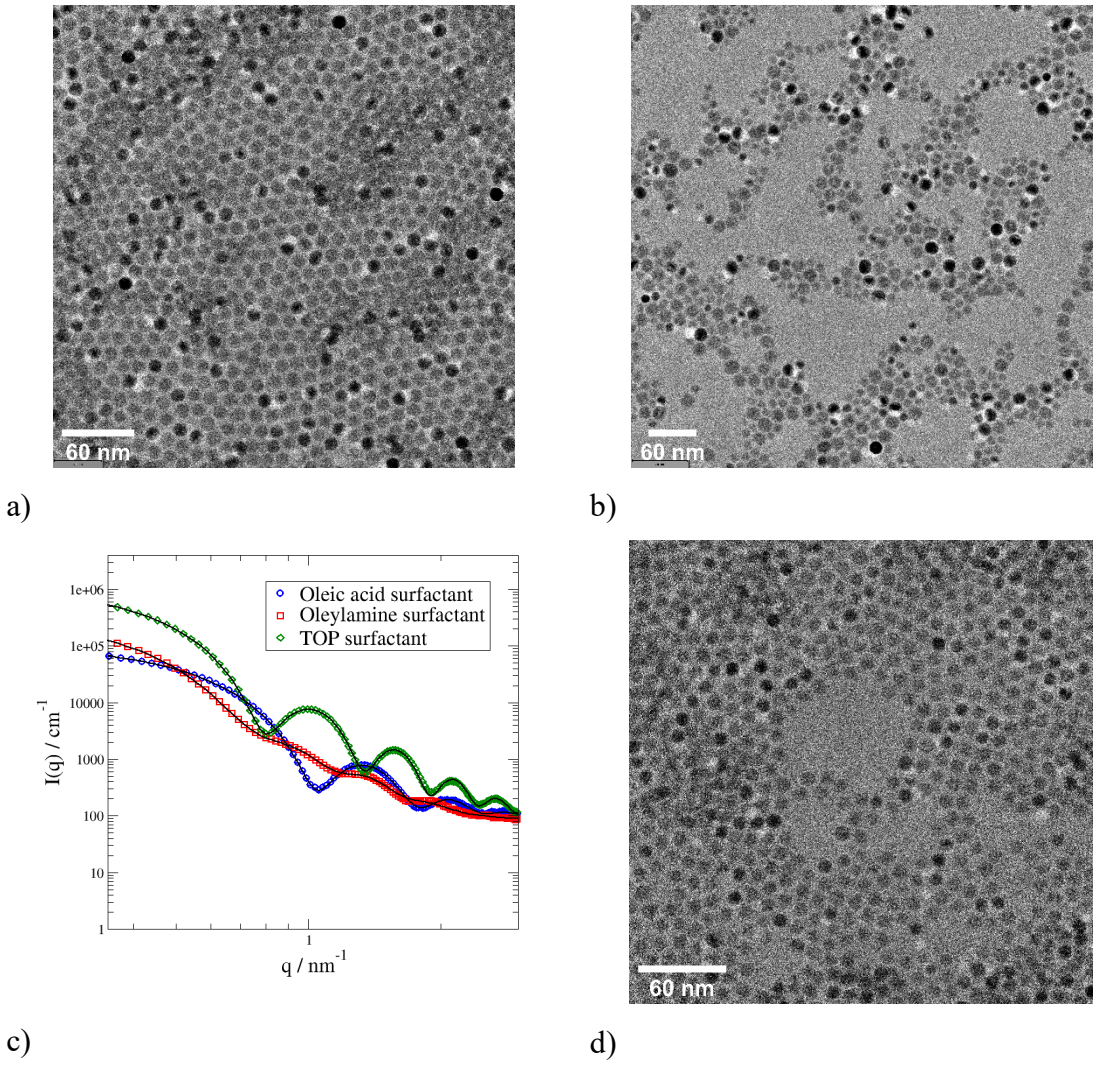

Figure 4.7 TEM pictures of iron oxide particles stabilized with a) trioctylphosphine, b) oleylamine, c) Core-shell sphere model fits SAXS curves for nanoparticles with R = 5.7 nm (green curve), 5.5 nm (red curve) and 4.3 nm (blue curve) respectively d) particles without extra surfactant.

We therefore investigated trioctylphosphine (TOP) as another possible ligand. As shown in Figure 4.7 a we obtained monodisperse spherical nanoparticles with radii of 5.7 nm. This is larger compared to oleic acid as a ligand, where particle radii of 4.4 nm are obtained for the standard procedure. When using oleylamine as a ligand (Figure 4.7b), polydisperse nanoparticles with different shapes were obtained. A complete absence of extra surfactant (Figure 4.7 d) leads to nanoparticles with increased polydispersity with an average radius of around 4.5 nm.

The role of the ligand is to stabilize the nuclei during their formation and to stabilize the growing nanoparticles. Different ligands have different binding strengths to the nanoparticle surface. Usually, there is an optimum binding strength where nuclei are sufficiently stabilized by the ligand, but not to a degree that the ligand shell subsequently

acts as a barrier that retards particle growth. Oleic acid interacts with iron oxide via hydrogen bounds Fe-O···H ··· O=C-. TOP, which is a weak base in the HSAB-sense, interacts with the hard acid Fe^{3+} at the iron oxide surface via intermediately strong Fe···P-C- bonds. Oleylamine, is a hard base in the HSAB-sense which has stronger binding via Fe···N-R-bridges and therefore leads to smaller and more polydisperse nanoparticles. Therefore, oleic acid and TOP are excellent ligands. TOP can be used to obtain larger nanoparticles compared to oleic acid as the ligand, both with good and reproducible control of the particle radius and narrow size distributions.

D) Iron/ligand ratio

There usually is an optimum Fe/ligand ratio for which large monodisperse nanoparticles are obtained. For the standard synthesis an Fe/ligand ratio 2:1 is used. Demortiere and co-workers[14] and also Hufschmid and colleagues[9] studied the influence of the oleic acid ratio in detail. They report that an increase of the oleic acid ratio increases the reaction time to several hours, leading to the formation of larger particles with broader distribution. We observe that the addition of a large excess oleic acid (62.5 mL instead of 3.2 mL) simultaneously with the reduction of 1-octadecene amount (62.5 mL instead of 125 mL) even prevents the formation of nanoparticles at all.

The Fe/OA-ratio has two competing effects on the particle size. A low excess of oleic acid leads to less nuclei stabilization corresponding to high oversaturation, which leads to higher particle numbers and therefore smaller radii of the final particles [14]. A large excess of ligand can form a steric barrier at the nanoparticle surface thereby limiting precursor diffusion to the surface and therefore growth.[5] Therefore, there is an optimum Fe/ligand ratio where the nuclei are sufficiently stabilized and the chosen excess of oleic acid does not yet limit precursor diffusion to the nanoparticle surface.

E) Variation of precursor concentration

We also investigated large variations of the iron oleate precursor concentration. Keeping the Fe/ligand ratio constant at 2:1, we used a 3-times reduced amount of iron oleate (6g) and a 9-times increased amount of iron oleate (54 g) in the same volume of solvent (125 ml). With the 3-fold reduction of the iron oleate precursor concentration polydisperse nanoparticles with an average radius of 4.7 nm are obtained (Figure 4.8 a). The 9-fold increased iron oleate concentration leads to nanoparticles with an average radius of 7.0 nm (Figure 4.8 b). We observe that reducing the concentration decreases the growth rate to a degree such that growth is slow leading to smaller and more polydisperse nanoparticles.

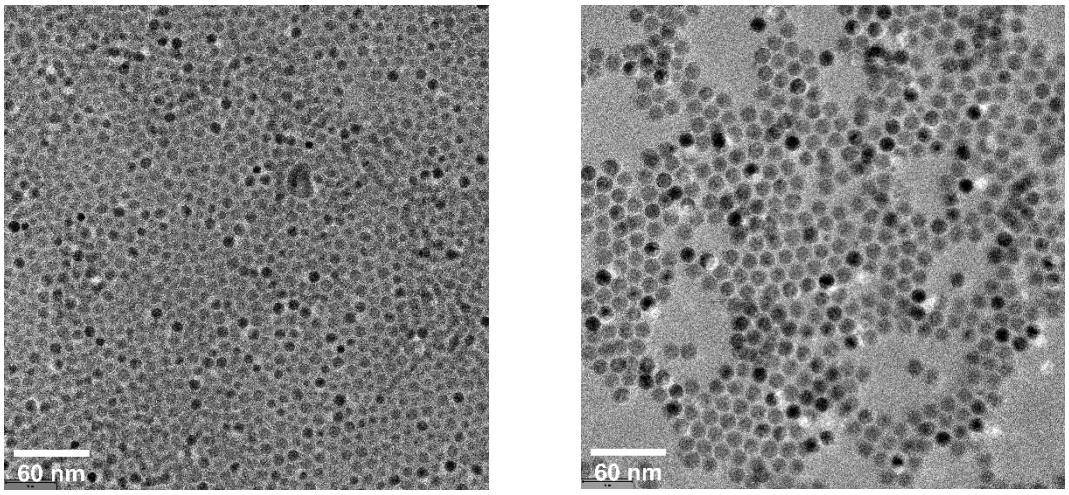

a) b)

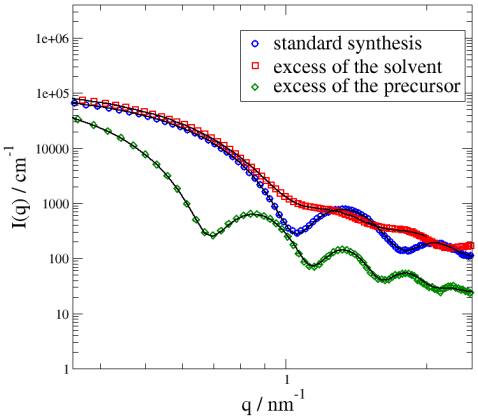

c)

Figure 4.8 SPIONs synthesized from a solution with a) excess of solvent, b) excess of precursor, c) Core-shell sphere model fits SAXS curves for nanoparticles with R = 4.7 nm (red curve), 6.7 nm (green curve) and 4.3 nm (blue curve), respectively.

4.3.4 The use of high-boiling point solvents

The variation of the standard synthesis parameters provides an opportunity for a fine control of spherical nanoparticles sizes. The main way to significantly increase nanoparticle diameters is by the use of higher temperatures in high boiling point solvents for the nanoparticle synthesis[4,9,11]. This change requires to adjust other parameters such as the end temperature, annealing time or the amount of compounds and demands some alterations of the synthesis set up depending on each solvent.

The standard solvent 1- octadecene (bp = 315 °C), which was used for the previous set of experiments, allows to synthesize nanoparticles with diameters of up to 14 nm diameter in case of well-dried iron oleate precursors at an end temperature 320 °C. These nanoparticles have a magnetite phase and a monocrystalline structure (Figure 4.9).

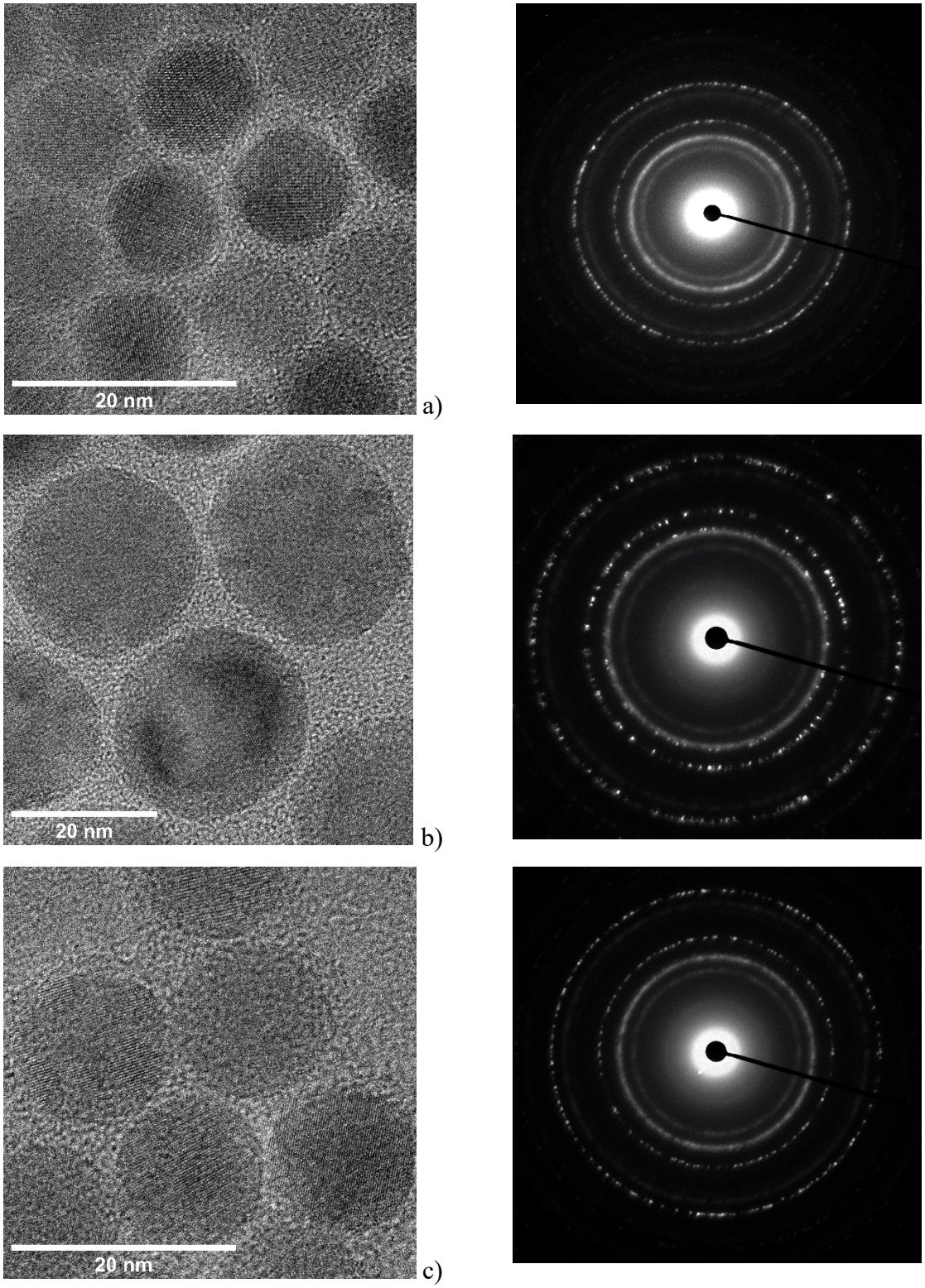

Figure 4.9 TEM image at high magnification and diffraction pattern of particles formed in a) 1-Octadecene, b) Docosane, and c) Trioctylamine.

Docosane

Using docosane as a higher boiling point solvent (bp = 368.6 °C) and following the procedure described by Bronstein and co-workers[11], it is possible to reach a nanoparticle radius of 10.5 nm (Figure 4.10 a). The diameters can be varied by changing the amount of

solvent in the precursor solution. Increasing the concentration 3-fold (10mL instead of 30mL solvent) reduces the radius to 9.8 nm (Figure 4.10 b). We note that the purification step is tricky for particles which were synthesized in docosane. In a usual purification procedure the resulting particles are precipitated by adding acetone to the mixture. Afterwards the solvents are removed by decantation and the particles are redispersed in THF.

This procedure is repeated at least two times with ethanol until the supernatant is transparent. For particles, which were synthesised in docosane, two additional precipitation steps with ethanol at 60°C are necessary, because docosane (m.p. > 60°C) is solid at room temperature and causes SPIONs aggregation, when the mixture is not purified enough.

One of the main peculiarities of the synthesis with docosane is that the nucleation step is shifted to high temperatures. There is hardly any difference in the resultant particle size distribution if the starting reaction temperature is either 60 °C, 100 °C or even 300 °C. The starting amount of material for synthesis also does not influence the SPIONs size: upscaling of the amount of all compounds by factor of 4 for the procedure described by authors[11] allows to get the same size range with a radius of 12.1 nm. (Figure 4.10 c). Therefore, the use of docosane as a solvent provides a highly reproducible synthesis of monodisperse nanoparticles, where the particle size can be controlled by the precursor concentration. We observe from the TEM-images that the particle shape slightly deviates from a spherical shape, which also influences the quality of SAXS fit.

The presence of several iron oxide phases was reported for particles synthesized at high temperatures. XRD measurements show a co-existence of Wüstite (FeO) and Spinel (most likely Fe_3O_4)[11]. It was argued that the Wüstite phase in iron oxide core-shell structures is more pronounced in larger particles because of longer diffusion path for the oxidation process[15]. The field dependent magnetisation measurements prove superparamagnetic behaviour of FeO-Fe_3O_4[10] particles and even better magnetic properties in comparison to one-component SPIONs [16].

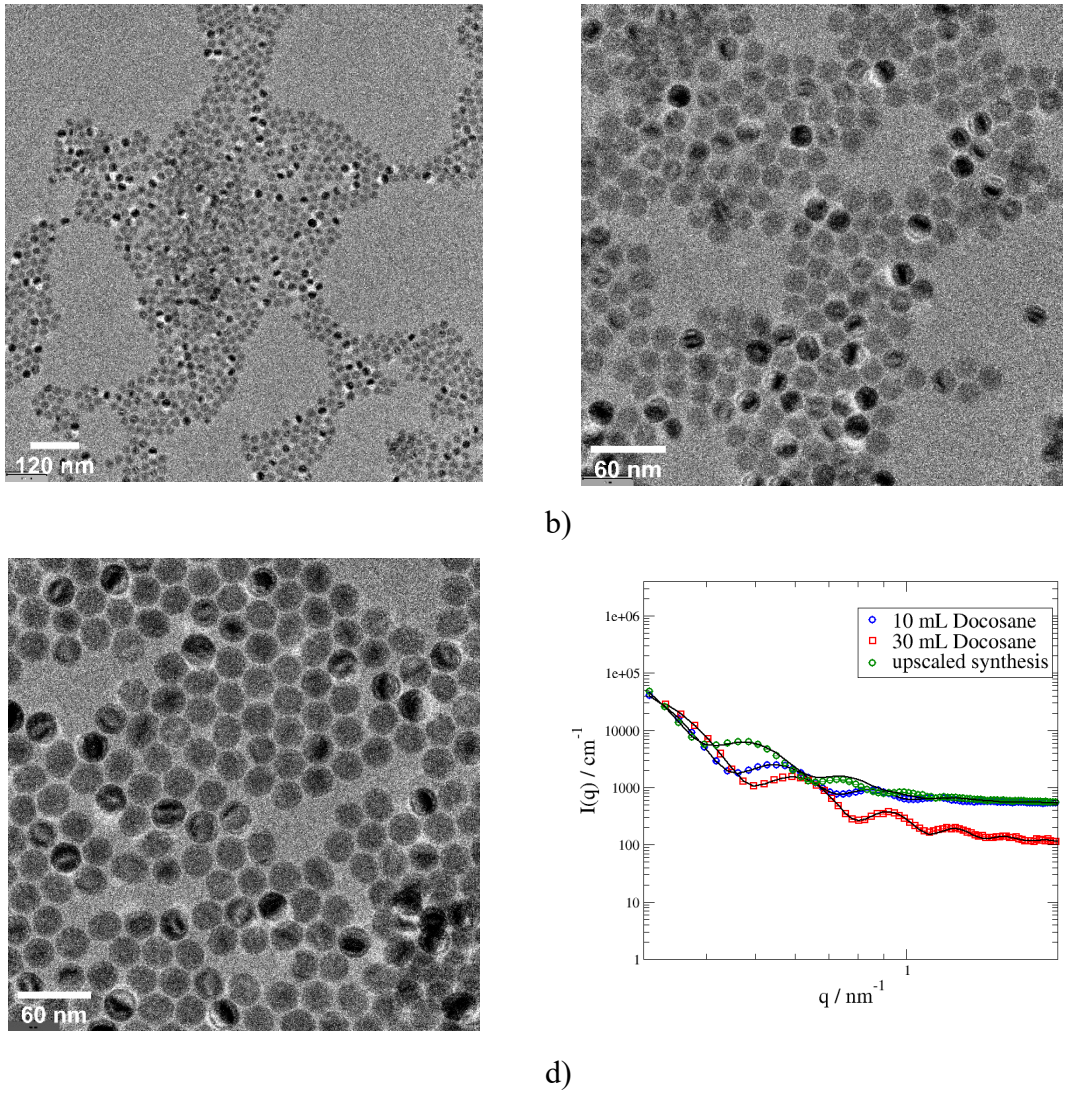

Figure 4.10 SPIONs formed in a) 30 mL docosane, b) 10 mL docosane, c) in 3 times more amount of synthesis solution d) SAXS curves show influence of the docosane solvent amount on the final nanoparticle size; core-shell sphere model fits R = 10.5 nm (blue curve), 9.8 nm (red curve) and 12.1 nm (green curve) respectively.

Trioctylamine

It is possible to obtain > 20 nm diameter SPIONs with a major fraction of magnetite by using trioctylamine as a high boiling point solvent (TOA, bp = 366 °C). It was mentioned as one of the possibilities to synthesize larger nanoparticles[4,17,18] , but we found that all suggested procedures mostly lead to formation of either cubic or extremely polydisperse SPIONs. We checked several reaction temperatures to find out the optimal one to obtain spherical iron oxide nanoparticles. At the standard reaction end temperature (320 °C) only SPIONs with broad size distribution (6.3 nm average radius) can be obtained (Figure 4.11 a). Changing the end temperature to 340 °C makes particles more monodisperse, yielding nanoparticles of 7.0 nm radius (Figure 4.11 b). Further raising the temperature up to 370 °C, allows to obtain SPIONs with 10.0 nm radius (Figure 4.11 c).

It shows that the final plateau temperature of the reaction is a crucial parameter for size tuning and can be varied to obtain nanoparticles with good size control. A similar result was achieved by Ahmadpoor and collegues[19] who performed the synthesis at 360 °C and obtained 18 nm diameter spherical iron oxide particles, which fits our results very well. The increased size at a temperature of 370°C likely is due to an increased growth rate. The synthesis procedure with trioctylamine as a solvent can provide a variety of monodisperse spherical particles in a size range 11-20 nm and provides an easier purification step in comparison to nanoparticles synthesized in docosane.

A notable effect for nanoparticle synthesis at temperatures at or above the boiling point of the solvent is that nanoparticles with lower size distribution are obtained. This effect is described in detail by Lynch and colleagues [20], who report that either gas bubbles appearing during solvent boiling or the Ar-gas flow can be used to tailor the kinetics of the nucleation and growth.

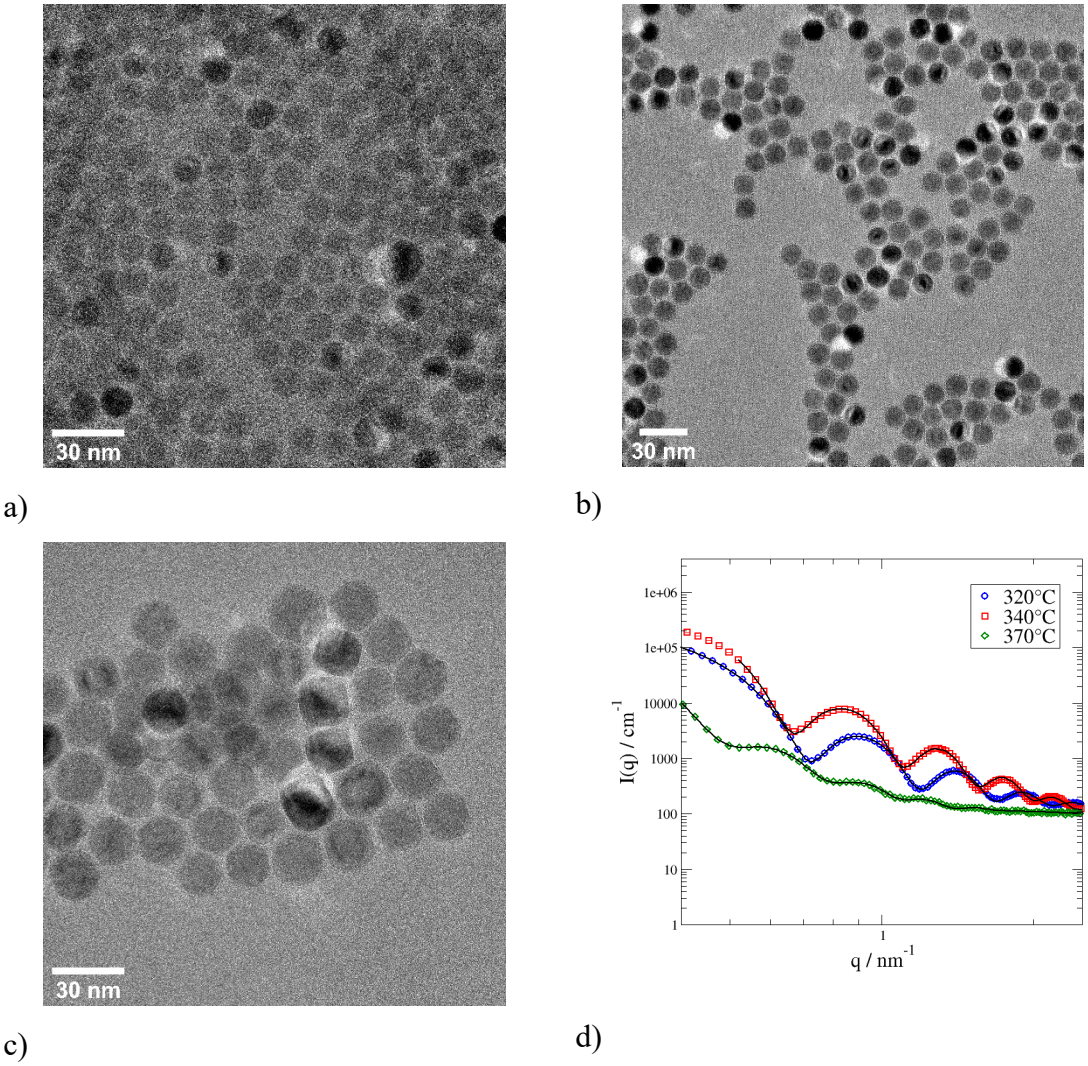

Figure 4.11 Iron oxide nanoparticles formed in trioctylamine at the end temperature a) 320 °C, b) 340 °C, c) 360 °C. d) Core-shell sphere model fits SAXS curves for nanoparticles with R = 6.4 nm (blue curve), 7.0 nm (red curve) and 10.0 nm (green curve), respectively.

4.4 Materials and methods

4.4.1 Materials

Iron oxide precursor synthesis: Iron (III) chloride hexahydrate (Merck, ≥ 99.0%), sodium oleate (TCI, ≥ 97.0%), potassium oleate (TCI, >98.0%), n-heptane (Merck, ≥ 91.0%), ethanol (Merck, 96%), deionized water.
Particle surfactants: oleic acid (Aldrich, 90%; b.p. 360°C), oleylamine (Aldrich, 70%; b.p. 364°C), trioctilphosphine (Aldrich, 90%; b.p. 294°C)
Organic solvents for nanoparticle synthesis: 1-octadecene (Merck, ≥ 91.0%; b.p. 315°C), n-docosane (TCI, 99%; b.p. 369°C), trioctylamine (Aldrich, ≥92.5%; b.p. 365°C)
Purification step: tetrahydrofuran (Merck, ≥ 99.0%), ethanol (Merck, 96%) and acetone (Merck, ≥ 99.5%)
All components were used as received.

4.4.2 Transmission electron microscopy (TEM)

TEM measurements were performed using JEOL-F200 Multipurpose Electron Microscope. The standard procedure for sample preparation includes partial drying of diluted nanocrystal solution on a carbon-coated copper grid with following removal of excess solution. Data evaluation was done in ImageJ software for the determination of average particles radii and size distribution.

4.4.3 Small angle X-ray scattering (SAXS)

SAXS experiments were held with the system "Ganesha-Air". The X-ray source is D2-Metalljet (Excillium) with a liquid metal anode operating at 70 kV and 3.57 mA with Ga-K_α radiation (λ = 0.1314 nm) providing a thick beam (< 100 µm) of high brilliance. X-ray optics (Xenocs) provides small and intense beam at the sample position, the beam size is adjusted with two pairs of slits depending on the detector distance. Samples were measures in borosilicate capillaries (d = 2 mm) at room temperature (T = 24 °C). If not stated otherwise data was radial averaged, normalized with respect to measurement time and transmission and the solvent as background subtracted.

4.4.4 SAXS data analysis

Small angle scattering curves were fitted with "polydisperse core-shell sphere" model using Jscatter software [3]. The model allows to increase quality of fits not only because of

included polydispersity parameter, also because of the shell parameter as iron oxide particles are stabilized with surfactant, which contributes overall scattering.

4.4.5 The thermal decomposition route

The synthesis of SPIONs was carried out by thermal decomposition of iron oleate as in the previously reported procedure by Park *et al*. [4]. The general procedure uses a mixture of precursor, organic solvent and ligand. In the standard procedure iron oleate is used as the precursor, oleic acid as the ligand, and 1-octadence as the solvent. A typical reaction mixture consists of 125 ml of 1-octadecene, 3.2 ml oleic acid (10 mmol), and 18 g of Fe(III)-oleate (20 mmol, 2:1 molar ratio to oleic acid). Thermal decomposition is performed under Argon atmosphere at a starting temperature of 100°C, a heating rate of 3.3 °C/min, an end temperature of 320°C, and rapid cooling down to room temperature after an annealing time of 30 minutes. Heating rates are varied between 1 – 10 °C/min.

4.5 Conclusions

We provided an overview over suitable methods and conditions to control the size of iron oxide (SPION) nanoparticles via the variation of the main synthesis parameters. We find that a set of solvents, 1-octadecene, trioctylamine, and docosane, provides access over temperature ranges from start-temperatures of 100°C to end-temperatures of up to 370°C, allowing to synthesize monodisperse nanoparticles in a diameter range of 6 – 24 nm on large scale. We observe that each solvent provides access to a certain temperature range (see Figure 4.12), within which the variation of temperature, heating rate, type of ligand (oleic acid, TOP) or precursor concentration allows to reproducibly vary and fine-control the nanoparticle size to ±0.5 nm as shown in Figure 4.12.

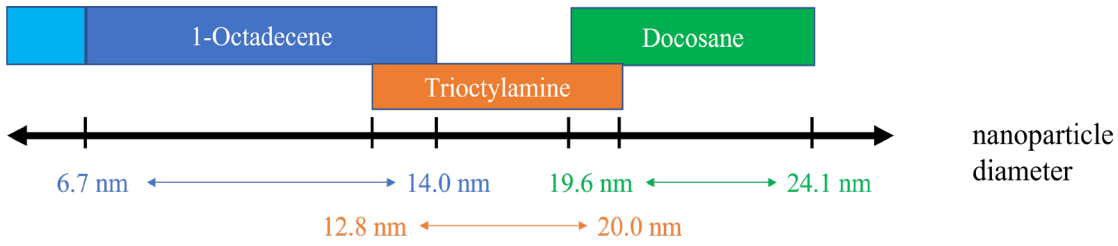

Figure 4.12 Chart of suitable solvents to access a broad range of iron oxide nanoparticle diameters with narrow size distribution, high crystallinity and a reproducible size control of ±0.5 nm. The light blue area for 1-octadecene shows the range accessible with pristine iron oleate precursor, where the reproducibility is reduced.

With knowledge of the nucleation and growth kinetics it is possible to better rationalize the effects of the variation of the synthesis parameters. An increase of the reaction temperature or precursor concentration increases the growth rate, such that larger nanoparticles are obtained. Lower heating rates lead to larger nanoparticles, because nucleation starts at lower temperatures, where the nucleation rate and thus the number of formed nuclei is smaller. Ligands should have intermediate binding strength to the nuclei and nanoparticles to sufficiently stabilize the nuclei during their formation process and not to not act as a too stable barrier preventing growth. The same arguments rationalize an optimal Fe/ligand ratio. We confirm that a thermal pretreatment of the iron oxide precursor is essential to achieve reproducible size control. The annealing time should be just long enough to complete nanoparticle growth. Our investigations thus provide an understanding and a guideline to choose the best synthesis procedure for reproducible size control of monodisperse iron oxide nanoparticles in a size range of 6 – 24 nm.

4.6 Supporting Information

1. Nucleation and Growth model

2. Influence of potassium oleate on iron oleate quality and resultant particle size

Nucleation and growth model

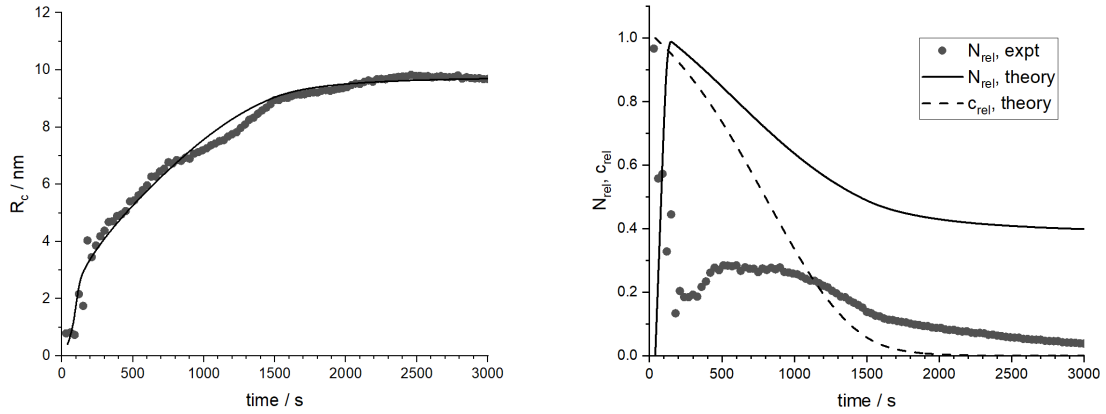

a) b)

Figure 4.13 (a) Measured growth curve R(t) for iron oxide nanoparticles during the heat-up synthesis. (b) Measured relative particle numbers N_{rel} and relative precursor concentration c_{rel} during the heat-up synthesis. The solid and dashed lines are calculated from the nucleation and growth model.

Figure 4.13 a shows the measured growth curve together with the calculated growth curve using the non-classical nucleation and growth model as discussed in the main text. Figure 4.13 b shows the measured relative particle number N_{rel} as a function of time during the heat-up synthesis. The initial sharp decrease is likely due to the dissociation of an amorphous precursor phase. The subsequent reduction of the particle number after 500 seconds is due to aggregative growth and can be qualitatively captured by the nucleation and growth model. For a more detailed comparison and a further refinement of the model a distinction between the number of precursor particles and the number of iron oxide nanoparticles would be required, which is unfortunately not possible from the SAXS-data alone.

Table 4-1 List of parameters used for the calculations of the growth curve.

Parameter	Value	Comment
Molar Mass *M*	M(Fe_3O_4): 233.55 g/mol M($FeO_{x=4/3}$) = M(Fe_3O_4)/3 = 77.85 g/mol	Lit.
Density ρ	5.18 g/cm^3	Lit.
Viscosity η	1 mPas	Lit.
Diffusion coefficient *D*	$2 \cdot 10^{-9}$ m^2/s	Calculated
Temperature *T*	200 – 360 °C	varied during heat-up synthesis
Saturation concentration $[Fe(OA)_m]_{sat}$	$[Fe(OA)_m]_{sat,0}$= $1 \cdot 10^{-7}$ mol/m^3 ΔE_{sol} =20 kJ/mol $[Fe(OA)_m]_{sat}$ = $1.3 \cdot 10^{-9}$ mol/ m^3 @ 280°C	prefitted, then fixed prefitted, then fixed
Interfacial tension γ	γ = 450 mN/m	prefitted, then fixed
Reaction rate constant k_1	$k_{1,0}$ =$6.0 \cdot 10^2$ mol/m^3·s ΔE_1 = 95 kJ/mol	prefitted, then fixed from TGA
Growth rate constant k_{gr}	$k_{gr,0}$ = $2.4 \cdot 10^5$ m/s ΔE_{gr} = 110 kJ/mol	Fitted individually
Aggregation rate constant k_{agg}	$k_{agg,0}$ =$1.0 \cdot 10^{12}$ mol/m^3·s ΔE_{agg} = 110 kJ/mol	prefitted / fixed estimate from Lit.

Influence of potassium oleate on iron oleate quality and resultant particle size

It is known that at high temperature alkaline (Na, K) metal oleates decompose in the reaction mixture which plays an important role on the shape control[13,21]. We therefore investigated whether the replacement of Na-oleate by K-oleate in the synthesis of the iron oleate precursor had effects on the nanoparticle size and shape. We observe that a 5% surplus of K-oleate with respect to iron resulted in nanoparticles (Figure 4.14 a) that are 0.24 nm smaller in diameter than ones formed from the standard (115.3 g of K oleate) precursor (Figure 4.14 b). Using 5% less potassium oleate leads to the formation of large polydisperse nanoparticles with irregular shape (Figure 4.14 c). Thus, even small changes in iron oleate precursor composition have strong effects on nanoparticle growth and allow

to control resultant particles size on sub-nanometre scale as well as influence shape and magnetic properties.

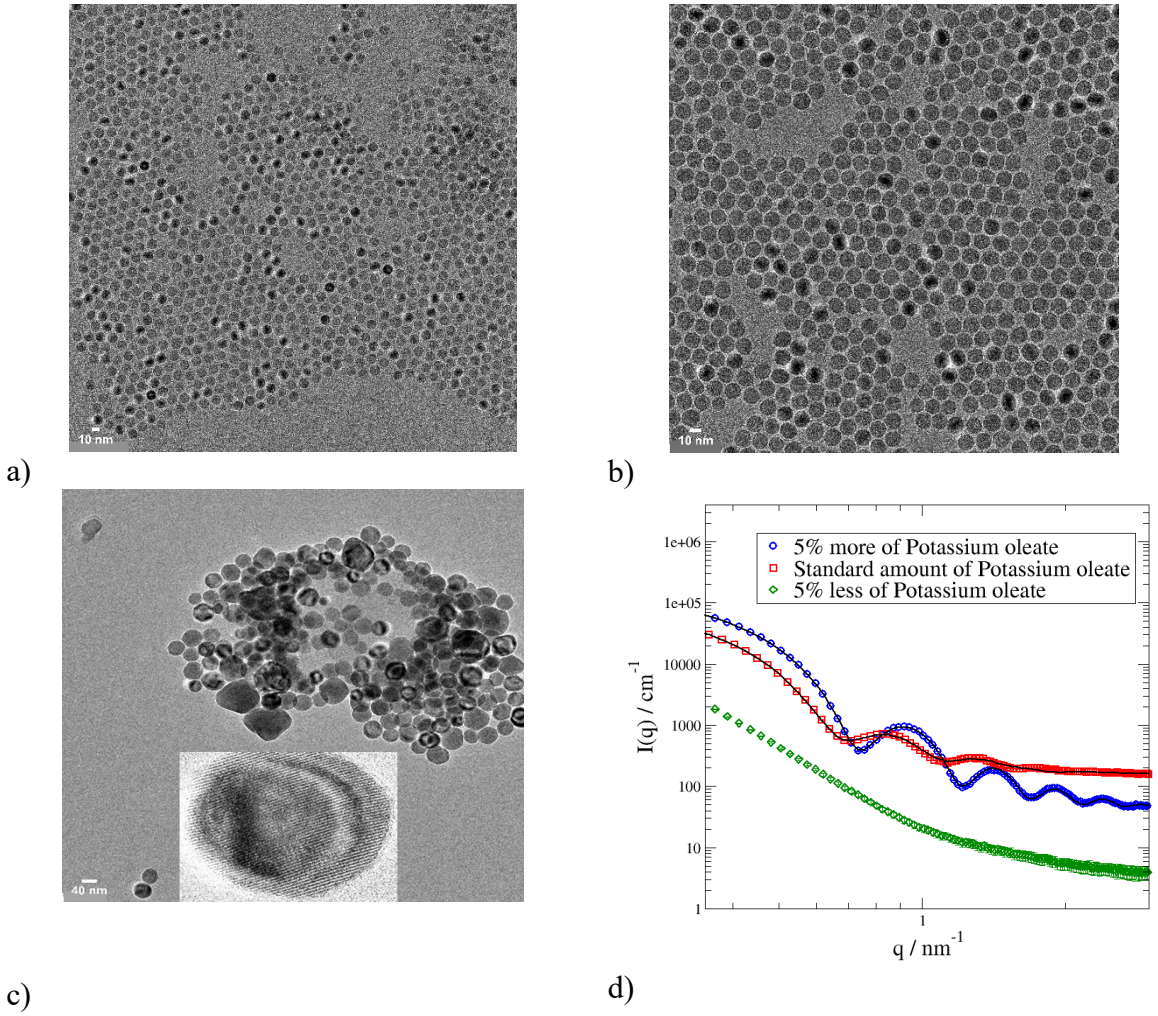

Figure 4.14 Iron oxide nanocrystals formed from a precursor with a) 5% more amount of potassium oleate b) standard amount of potassium oleate c) 5% less amount of potassium oleate d) Core-shell sphere model fits SAXS curves for nanoparticles with R= 6.41 nm (blue curve) and 6.58 nm (red curve) respectively. Green curve shows scattering for highly polydisperse particles with R = 12.5 - 60 nm (determined from TEM).

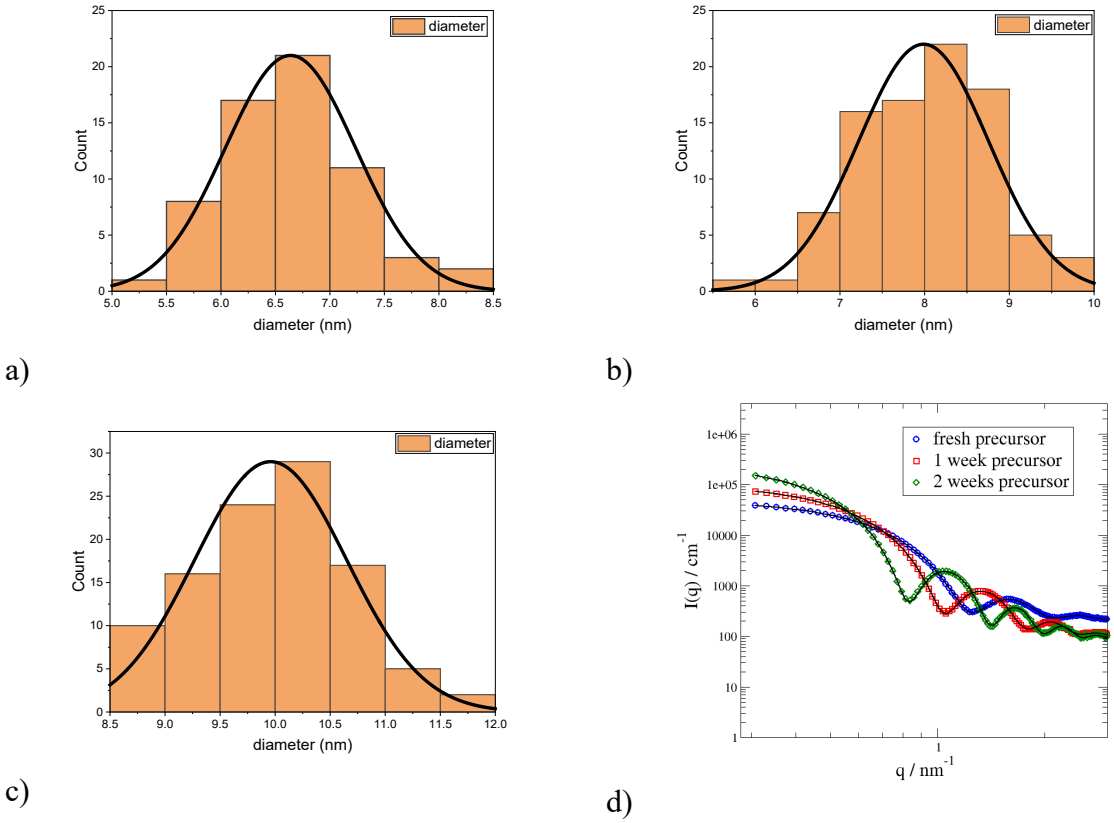

Figure 4.15 Size distribution diagrams are obtained from TEM images for SPIONs synthesized from iron oleate precursor which was a) dried only in a rotary evaporator (R = 3.3 nm), b) dried additionally for 1 week in the vacuum oven (R = 4 nm), c) dried additionally for 2 weeks in the vacuum oven (R = 5 nm) d) core-shell sphere model fits SAXS curves for nanoparticles with radiuses R = 5.5 nm (green curve), 4.3 nm (red curve) and 3.6 nm (blue curve) respectively

4.7 References

[1] A. Ali, T. Shah, R. Ullah, P. Zhou, M. Guo, M. Ovais, Z. Tan, Y. K. Rui, *Front Chem* **2021**, *9*, 548.

[2] J. Park, K. An, Y. Hwang, J. E. G. Park, H. J. Noh, J. Y. Kim, J. H. Park, N. M. Hwang, T. Hyeon, *Nat Mater* **2004**, *3*, 891–895.

[3] R. Biehl, *PLoS One* **2019**, *14*

[4] J. Park, K. An, Y. Hwang, J. E. G. Park, H. J. Noh, J. Y. Kim, J. H. Park, N. M. Hwang, T. Hyeon, *Nature Materials 2004 3:12* **2004**, *3*, 891–895.

[5] A. Guinier, *Small-Angle Scattering of X-Rays*, Wiley, New York, **1955**.

[6] V. Leffler, S. Ehlert, B. Förster, M. Dulle, S. Förster, *ACS Nano* **2021**, *15*, 840–856.

[7] A. G. Roca, M. P. Morales, C. J. Serna, *IEEE Trans Magn* **2006**, *42*, 3025–3029.

[8] W. W. Yu, J. C. Falkner, C. T. Yavuz, V. L. Colvin, **n.d.**, DOI 10.1039/b409601k.

[9] R. Hufschmid, H. Arami, R. M. Ferguson, M. Gonzales, E. Teeman, L. N. Brush, N. D. Browning, K. M. Krishnan, *Nanoscale* **2015**, *7*, 11142–11154.

[10] T. Balakrishnan, M.-J. Lee, S.-M. Choi, **2019**, *21*, 4063.

[11] L. M. Bronstein, X. Huang, J. Retrum, A. Schmucker, M. Pink, B. D. Stein, B. Dragnea, *Chemistry of Materials* **2007**, *19*, 3624–3632.

[12] G. Cotin, F. Perton, C. Petit, S. Sall, C. Kiefer, V. Begin, B. Pichon, C. Lefevre, D. Mertz, J. M. Greneche, S. Begin-Colin, *Chemistry of Materials* **2020**, *32*, 9245–9259.

[13] Alexey Shavel and Luis M. Liz-Marzán, *Physical Chemistry Chemical Physics* **2009**, *11*, 3762–3766.

[14] A. Demortière, P. Panissod, B. P. Pichon, G. Pourroy, D. Guillon, B. Donnio, S. Bégin-Colin, *Nanoscale* **2011**, *3*, 225–232.

[15] A. Lak, M. Kraken, F. Ludwig, A. Kornowski, D. Eberbeck, S. Sievers, F. J. Litterst, H. Weller, M. Schilling, *Nanoscale* **2013**, *5*, 12286–12295.

[16] P. Tancredi, P. C. R. Rojas, O. Moscoso-Londoño, U. Wolff, V. Neu, C. Damm, B. Rellinghaus, M. Knobel, L. M. Socolovsky, *New Journal of Chemistry* **2017**, *41*, 15033–15041.

[17] W. Glasgow, B. Fellows, B. Qi, T. Darroudi, C. Kitchens, L. Ye, T. M. Crawford, O. T. Mefford, *Particuology* **2016**, *26*, 47–53.

[18] D. Kumar, H. Singh, S. Jouen, B. Hannoyer, S. Banerjee, *RSC Adv* **2015**, *5*, 7138–7150.

[19] F. Ahmadpoor, A. Masood, N. Feliu, W. J. Parak, S. A. Shojaosadati, *Frontiers in Nanotechnology* **2021**, *3*, 13.

[20] J. Lynch, J. Zhuang, T. Wang, D. Lamontagne, H. Wu, Y. C. Cao, *J Am Chem Soc* **2011**, *133*, 12664–12674.

[21] E. Wetterskog, M. Agthe, A. Mayence, J. Grins, D. Wang, S. Rana, A. Ahniyaz, G. Salazar-Alvarez, L. Bergström, **2014**, *15*, DOI 10.1088/1468-6996/15/5/055010.

Introduction to chapters 5 and 6: Nanocomposite self-assembly in external fields.

Functional materials are specially designed to have a determined function and particular physicochemical properties, for example, polymers, molecular crystals, or nanoparticles. They possess remarkable properties and functions such as ferroelectricity, piezoelectricity, magnetism, or energy storage functions. Nanocomposite-based functional materials are hybrid materials consisting of both organic and inorganic ingredients. The research on their synthesis and their characterization is crucial for future applications[1].

Functional materials are extensively used in energy storage technologies[2], in biomedicine[3,4], and especially cancer therapy[5], in semiconductor technologies[6] and generally electronics[7,8], for development of microwave hydrothermal methods[9], for sorption-based atmospheric water generation[10], for biocompatible food packages[11] and in a variety of other fields[12].

Among all materials, a special place is given to magnetic nanoparticles which can be functionalized with polymer chains[13]. Polymer ligands not only stabilize particles to prevent aggregation but also allow tuning the system parameters such as interparticle distance and polymer shell density. The microstructure and superparamagnetic properties of magnetic nanoparticles are widely studied because of their perspective application[14]. Magnetic particles can serve as building blocks for data storage media and photonic[15]. Also thermally crosslinked superparamagnetic iron oxide nanoparticles (SPIONs) are highly effective for tumor detection in vivo by dual imaging.[16]

In the current work, we focus on the study of magnetite nanoparticles functionalized with polystyrene chains in organic solvents. As well as the polymer chain length and its grafting density the concentration of particles in the solvent is an additional way to control the interparticle distance and overall assembly[17].

Chapter 5 demonstrates the lyotropic crystalline phases formed in the nanocomposite system with Diethyl phthalate solvent and the phase transitions appearing in presence of a permanent magnetic field (0.7 Tesla). Iron oxide nanoparticles of diameter equal to 17 nm were grafted with short polystyrene chains (M_w = 6600 g/mol) and studied using a small angle X-ray scattering technique (SAXS) at P03-MiNaXS synchrotron beamline, DESY.

In addition, Chapter 6 shows the influence of magnetization time on the resultant long-range order for two nanocomposite systems: 13.7 nm particles with 6600 g/mol polystyrene and 21 nm particles with 2600 g/mol polymer in Xylene as organic solvent.

Both systems were studied under 0.1 Tesla magnetic field at the laboratory SAXS machine. Finally, the influence of the magnetic field was compared to the shearing and temperature combined fields. Thus, all observed phase transitions were summarized in one diagram, which includes parameters of the nanocomposite mixtures and external field parameters. The results described in the next two chapters provide a reproducible stable model of the functional nanocomposite, which is highly desirable for nanoelectronics and biomedicine applications. Moreover, cubic lattices with a defined long range order which are formed under external fields have a tunable lattice parameter.

5 Phase transitions in nanocomposite solutions derived in a magnetic field

5.1 Abstract

Polymer-functionalized superparamagnetic nanoparticles are widely used in medicine and nanoelectronics, therefore it is highly demanded to have precise control over the structural properties of nanocomposites. We suggest the way of nanocomposite self-assembly in the organic solvent Diethyl phthalate for a model system with fixed parameters of magnetite nanoparticle core and polystyrene shell. To assemble highly-concentrated systems into cubic structures the external magnetic field of 0.7 Tesla was applied. The disorder-order transition takes place for 30-50 wt% concentrated systems and BCC to FCC transition for 60 wt% nanocomposite in the organic solvent. Finally, we demonstrate the advantage of solutions for the grafted superparamagnetic nanoparticles assembly in the magnetic field. In comparison to the bulk samples the nanocomposite in solution is more ordered due to decreased attractive forces.

5.2 Results and discussion

We demonstrate the study of polymer-stabilized magnetite nanoparticles' behavior in an organic solvent Diethyl phthalate (DEP) under a permanent magnetic field. Iron oxide nanoparticles of 17 nm diameter were synthesized using the thermal decomposition method[18] and functionalized with 6600 g/mol polystyrene chains. Figure 5.1 shows spherical single-domain nanocrystals, which were characterized using transmission electron microscopy (TEM) and SAXS techniques. The scattering curve signalizes monodisperse particles due to its deep minima.

Mixtures of functionalized SPIONs at 20-70 wt% concentrations in DEP solvent were prepared in borosilicate capillaries and measured at a long detector distancen of the

SAXS synchrotron beamline detector (5.6 m). High-brilliance synchrotron beam has a small diameter of around 20 x 40 μm^2 and allows to proper scan of an obtained crystal structure in the nanocomposite system. Depending on the concentration SAXS curves show sharp peaks, which are analyzed via a comparison of the peak positions and a fitting lattice structure factor.

Afterward, the capillaries were placed into the 0.7 Tesla permanent magnet for 48 hours (Figure 5.2). After 2 days in the magnetic field, the capillaries were placed in the sample holder at the beamline and scanned again along the long axis of the capillary. This type of measurement allows checking the level of homogeneity of the initial structure and its changes caused by magnetic field. It is worth mentioning that structural changes don't happen immediately and demand longer "annealing" time in the magnet.

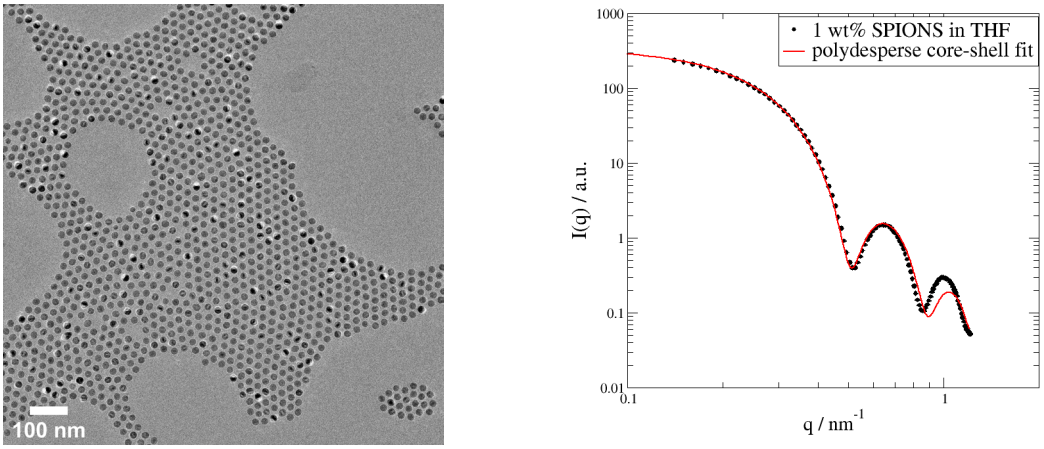

a) b)

*Figure 5.1 a) TEM image of iron oxide nanoparticles grafted with 6600 g/mol polystyrene polymer chains b) SAXS scattering curve of 1 wt% SPIONs in tetrahydrofuran (THF) solvent (**black dots**) and polydisperse core-shell fit (**red line**) calculating averaged particles size equal to 17 nm*

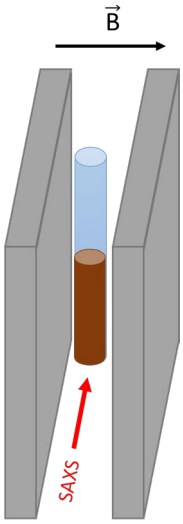

*Figure 5.2 Schematic representation of the sample placed to the 0.7 Tesla permanent magnet (**grey**). The SAXS beam direction (**red vector**) is perpendicular to the direction of the magnetic field (**black vector**)*

The experimental results are presented in Figure 5.3. The diagram shows the type of formed structures without the presence of a magnetic field (0 Tesla) and after storing samples for 2 days in the magnet (0.7 Tesla), depending on the concentration of the nanocomposite in DEP organic solvent. The structures were defined during the analysis of SAXS curves and the comparison of homogeneous and inhomogeneous diffraction patterns.

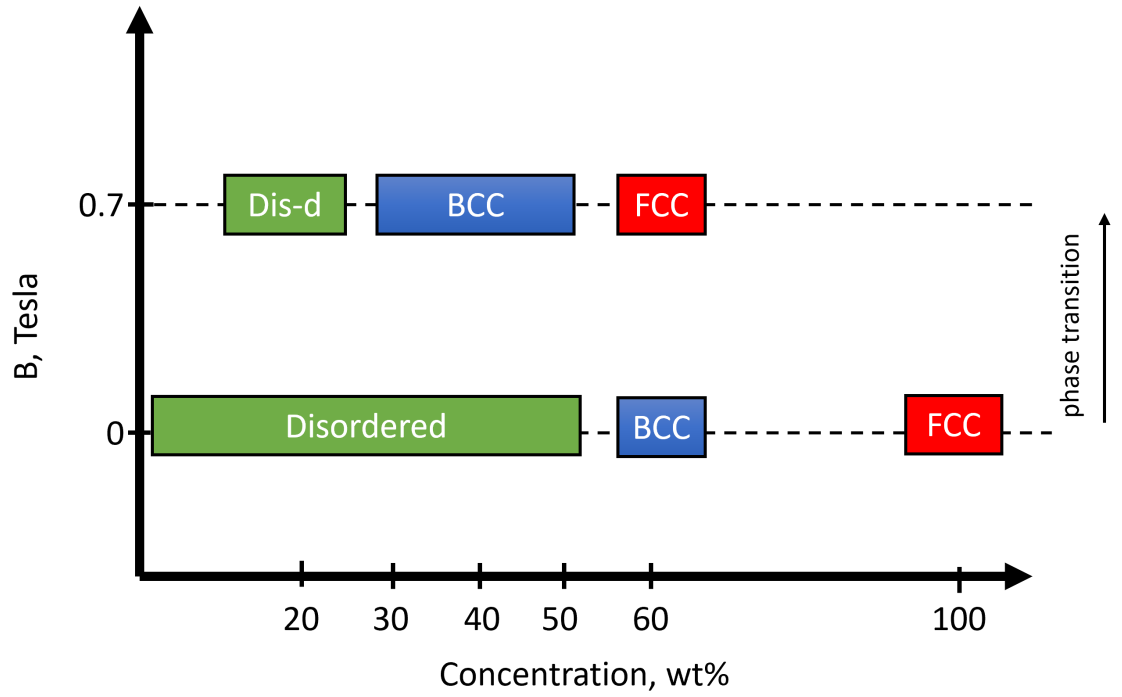

Figure 5.3 Diagram of structural changes of SPIONs nanocomposite solutions before and after 48 hours in the magnetic field

At low concentrations of polymer-grafted particles in the solvent (under 50 wt%) SAXS scattering curves have the structure factor of hard sphere interaction at a low q range, but no crystalline structure is observed (Figure 5.4). No significant change happens in the magnetic field, thus the system stays disordered.

Meanwhile, the 30 wt% and 40 wt% concentrated samples under the influence of the magnetic field change their scattering pattern, which shows how the broad peaks of a cubic lattice overlapping with the form factor of a sphere (Supporting Information, Figure 5.8 and Figure 5.9). It signalizes the phase change called disorder-order transition. The more significant effect of structural changes in the nanocomposite solution was achieved for a 50 wt% sample, with the obtained BCC lattice structure factor in a magnetic field (Figure 5.5). In this case, the 2D diffraction pattern becomes inhomogeneous and gets a "texture", which comes from many disordered domains of BCC lattices. It means that magnetization in the external magnetic field has led to the decrease of interparticle distance in the solvent and to the increase in their local concentration.

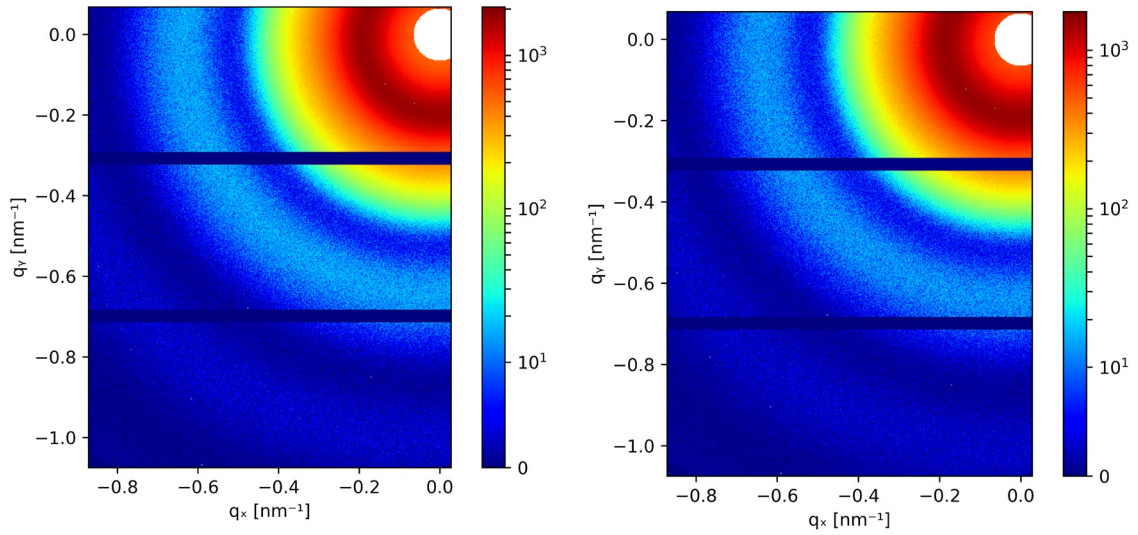

a) b)

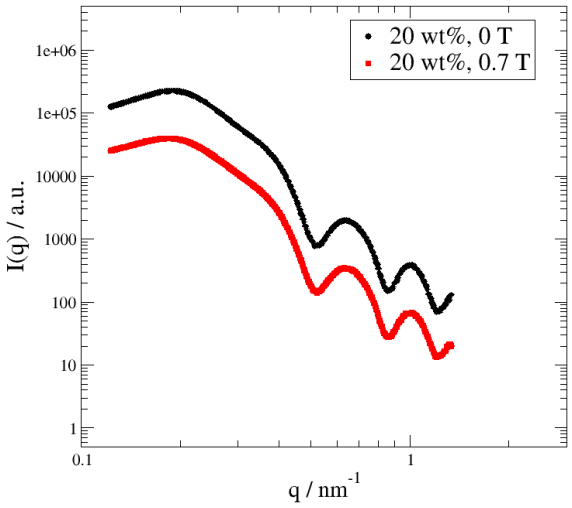

c)

*Figure 5.4 a) 2D SAXS pattern of the nanocomposite at 20 wt% concentration in DEP solvent before the magnetic field b) after the magnetic field and c) the corresponding SAXS curves before (**black curve**) and after (**red curve**) 2 days in the 0.7 Tesla magnet*

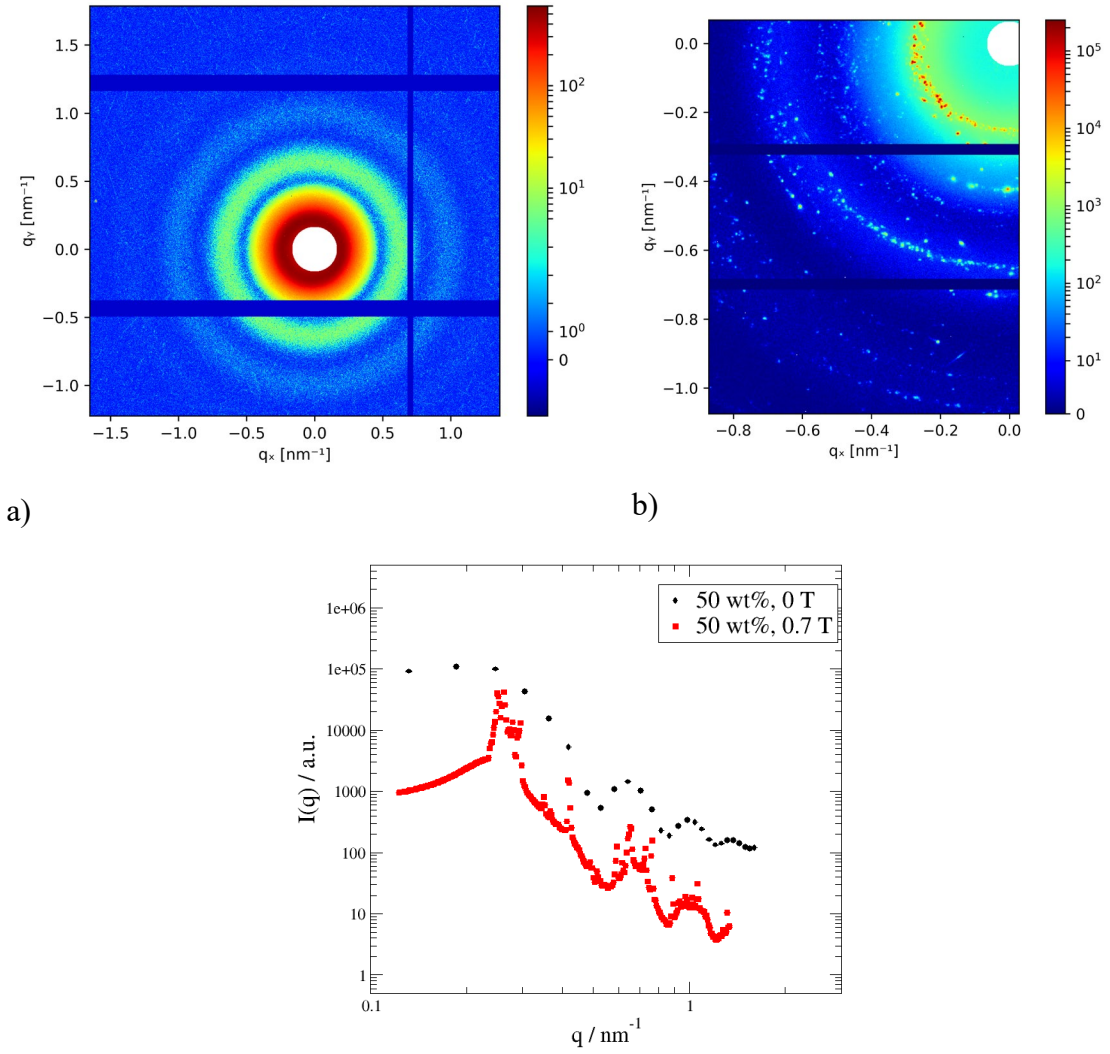

*Figure 5.5 a) 2D SAXS pattern of the nanocomposite at 50 wt% concentration in DEP solvent before the magnetic field b) after the magnetic field and c) the corresponding SAXS curves before (**black curve**) and after (**red curve**) 2 days in the 0.7 Tesla magnet*

With the increase of the concentration the lattice parameter is decreasing, thus particles obtain a closer packing in the magnetic field. Therefore, concentration is the important parameter for precise tuning of the resultant structure and it should be considered for creating a predetermined system for a certain application. Particularly at 60 wt% concentration the nanocomposite already forms the well-defined BCC lattice with the lattice parameter a = 33.94 nm even without an influence of the magnetic field (Figure 5.6). After "annealing" in the magnetic field the BCC lattice gets structural defects and in some parts of the sample, it turns to the FCC lattice with the lattice parameter a = 28.8 nm. Exactly the measurement procedure of scanning the samples along the Y-axe with a thin X-ray beam made it possible to catch the phase transition initiated by a magnetic field. Under the influence of the magnetic field ordered lattices reconstruct themselves into more dense FCC lattice, which causes the shift of the scattering curve towards the high q range.

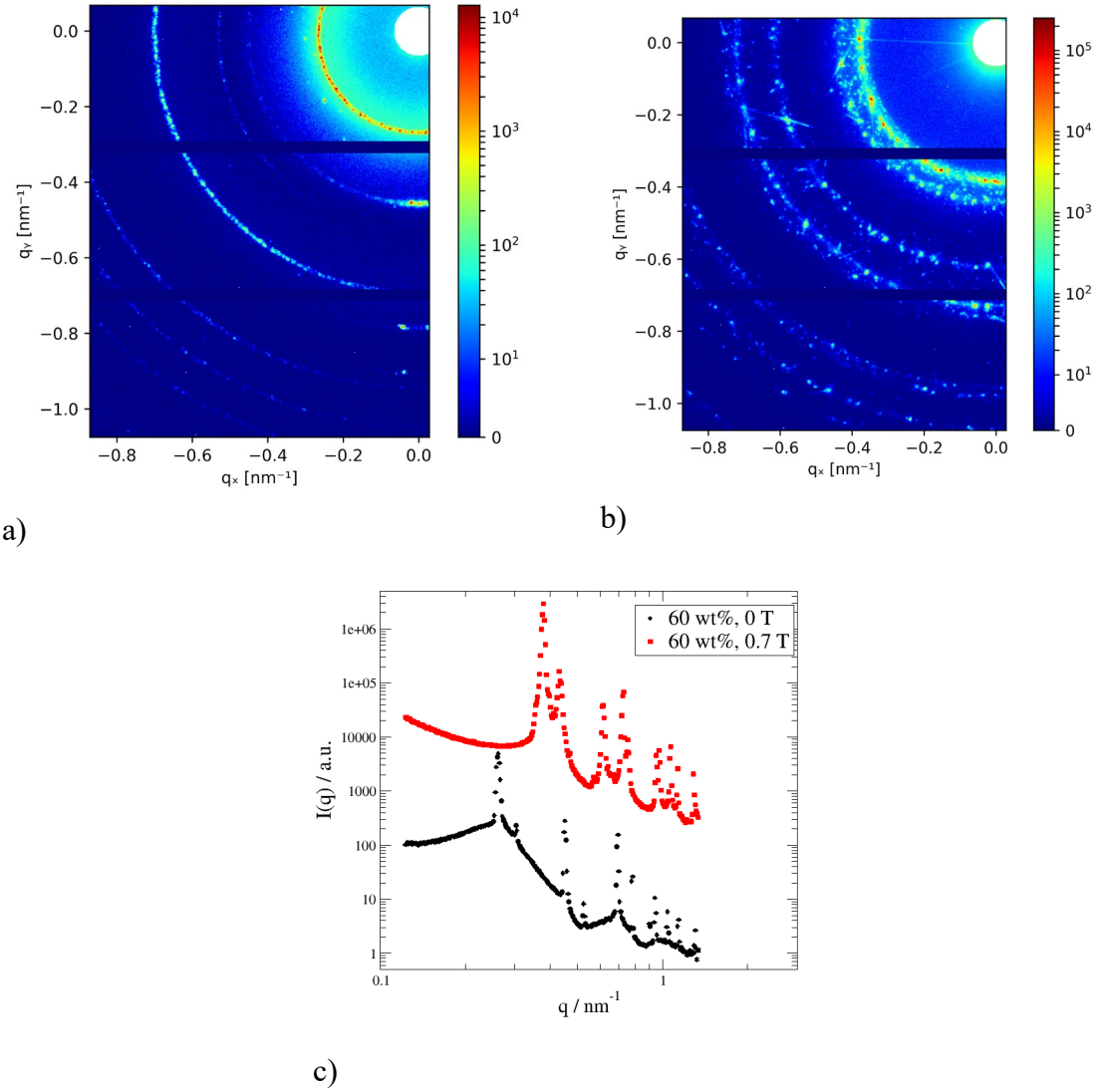

*Figure 5.6 a) 2D SAXS pattern of the nanocomposite at 60 wt% concentration in DEP solvent before the magnetic field b) after the magnetic field and c) the corresponding SAXS curves before (**black curve**) and after (**red curve**) 2 days in the 0.7 Tesla magnet*

When the concentration of functionalized SPIONs reaches 70 wt% the lattice has an FCC structure, which is not perfectly ordered. Scattering curves in this case have wide peaks and additional scattering from non-oriented domains. The same effect is observed for the bulk sample, which doesn't contain any solvent (Figure 5.7 a).

However, the 60 wt% solution of functionalized particles in DEP after being in the magnetic field forms the more ordered FCC lattice. Sharper diffraction peaks of its scattering pattern are successfully overleaped with the FCC lattice fit model and demonstrated the advantage of a solvent for tuning the lattice parameters (Figure 5.7 b).

The lattice parameter a = 28.8 nm of FCC is also lower for the 60 wt% nanocomposites after exposure in the magnetic field than for 70 wt% (a = 37.4 nm) and 100 wt% (a = 34.1 nm) systems. Magnetic field influences interparticle distance in the way that the polymer shells are overlapping as follows from the lattice parameters comparison

(Supporting Information, Table 5-1). Additionally, for the 60 wt% concentrated nanocomposites, the influence of temperature increase on structural changes is demonstrated (Supplementary Information, Figure 5.10). Here temperature parameter doesn't contribute to the structure factor and only local rearrangements are observed at the higher q range.

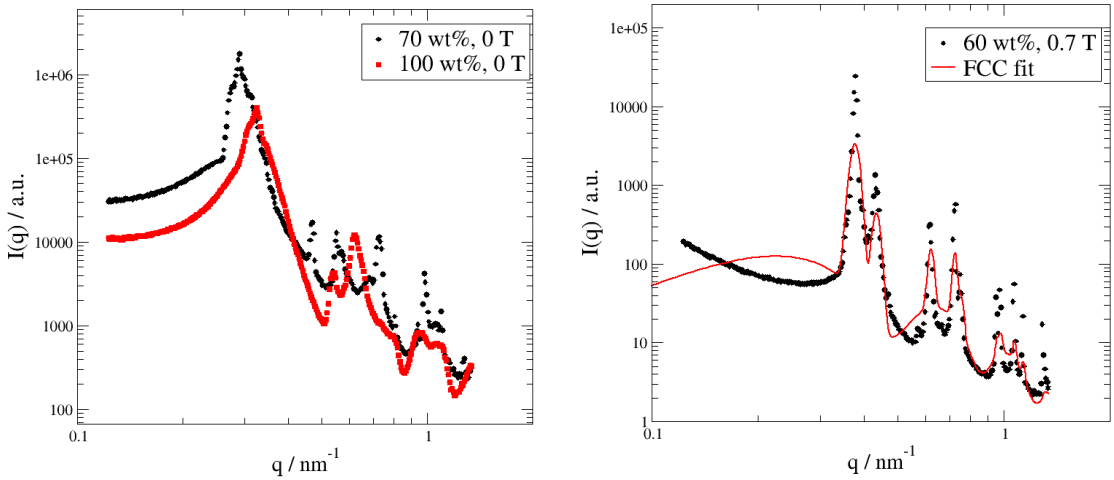

a) b)

Figure 5.7 a) Comparison of FCC lattices formed in bulk and at 70 wt% in the organic solvent, b) FCC fit of 60 wt% nanocomposite in DEP after 2 days in the magnet

For a potential application, the solvent could be evaporated or exchanged for another matrix. For example, in the work of Robbes and colleagues[19,20] maghemite nanoparticles (γ-Fe_2O_3) are poorly grafted with polystyrene (PS) chains and oriented using a magnetic field in a PS matrix. There the structure factor is compared to a model of Percus-Yevick and doesn't show a cubic lattice formation.

Notably, comparable structures formed by polymer-functionalized maghemite nanoparticles in highly-concentrated solutions were reported by Taheri and coauthors[21]. They systematically vary interparticle distance via toluene concentration and attached polymer molecular weights. The same size of nanoparticles (17 nm) grafted within four times longer polymer chains (28 000 g/mol) demonstrate disorder-order transition around 40 wt% concentration to FCC phase and BCC with a further increase of concentration.

Finally, the disorder-order transition in the variable magnetic field up to 2 Tesla was studied by Fu and coauthors[22]. Oleic acid coated 17 nm particles at very low concentrations in toluene (0.05 wt%) were organized directly into FCC lattices under the magnetic field. Contrary to that the self-assembly of functionalized particles in highly-concentrated solutions doesn't happen immediately at 0.7 Tesla which is why samples were annealed for 48 hours.

5.3 Materials and methods

5.3.1 Materials

Diethyl phthalate (Sigma-Aldrich, 99.5 %) solvent was used for sample preparation, Tetrahydrofuran THF (Sigma-Aldrich, ≥99.9%) for particle storage, and Ethanol (VWR Chemicals, ≥99,8%) for precipitation step during the ligand exchange. All solvents were used as received;

Iron oxide nanoparticles: magnetite nanoparticles of 18 nm diameter are synthesized using the thermal decomposition method [23]. THF solvent was evaporated and changed to Diethyl phthalate (DEP);

Grafting polymer: Polystyrene (M_w = 6600 g/mol) was synthesized by living anionic polymerization with *sec*-butyl lithium as an initiator at −70 °C in THF. The polymerization was terminated with CO_2 to obtain a carboxylic acid end group. The hydroxyl end group was subsequently activated by CDI and reacted with PEHA to create a multivalent amine function[13].

5.3.2 Ligand exchange

The ligand exchange consists of two phases. In the first phase, the nanocrystals in the solution were mixed with an excess of the polymer followed by three cycles of quantitative precipitation, centrifugation, and dissolving. The excess polymer was removed in the second phase composed of three cycles of selective precipitation with ethanol, centrifugation, discarding of supernatant, and precipitant dissolving in THF. The whole ligand exchange procedure was carried out as described by Ehlert and coauthors [13].

5.3.3 Sample preparation

Mixtures of functionalized SPIONs at 20-60 wt% concentrations in DEP solvent were prepared in glass vials. As the next step THF solvent was added for obtaining a homogeneous solution. These mixtures were transferred to the borosilicate capillaries of 2 mm diameter and 0.01 mm wall thickness, and a drop of water was added to the top. Capillaries were stored for 7 days at room temperature for the slow evaporation of THF through water and later in a vacuum oven at 60 °C for removing the rest of the additional solvents. The amount of the evaporated THF solvent was controlled with the change of capillary weight.

5.3.4 Transmission electron microscopy (TEM)

TEM measurements were performed using JEOL-F200 Multipurpose Electron Microscope. The standard procedure for sample preparation includes partial drying of diluted nanocrystal solution on a carbon-coated copper grid with the following removal of excess solution. Data evaluation was done in ImageJ software for the determination of average particle radii and size distribution.

5.3.5 SAXS measurements

SAXS experiments were held with the laboratory system "Ganesha-Air" and P03 beamline, DESY[24]. P03 is the microfocus small- and wide-angle X-ray scattering beamline (MiNaXS) at PETRA III. The beam size can be varied between 40 x 20 μm^2 and 10 x 5 μm^2 and the energy range of the beamline is 7 – 21 keV. Samples were measured in borosilicate capillaries (d = 1 mm) with a beam scanning one hundred positions along the capillary. Detector distance was set to 5.6 m, wavelength equaled 1.05 Å.

The laboratory machine has the X-ray source D2-Metalljet (Excillium) with a liquid metal anode operating at 70 kV and 3.57 mA with Ga-Kα radiation (λ = 0.1314 nm) providing a thick beam (< 100 µm) of high brilliance. X-ray optics (Xenocs) provides small and intense beam at the sample position, the beam size is adjusted with two pairs of slits depending on the detector distance. Samples were measured in borosilicate capillaries (d = 2 mm) at room temperature (T = 24 °C). If not stated otherwise data was radially averaged, and normalized to measurement time and transmission without the solvent as background subtracted.

Data analysis: small-angle scattering curves were initially corrected using Jscatter software [25] and fitted with a "polydisperse core-shell sphere" model[26] for the form factor calculation.

5.4 Conclusion

Superparamagnetic iron oxide nanoparticles of 17 nm diameter were grafted with short 6600 g/mol polystyrene chains and studied using the SAXS technique at several concentrations in the organic solvent diethyl phthalate. There were three types of structural states observed: for samples under 50 wt% concentration of nanocomposite - the disordered state, between 50 wt% and 60 wt% the BCC lattice was formed, and above 70 wt% the FCC lattice appeared. Thus, interparticle distance can be controlled not olny via varying a polymer molecular weight but also a solvent amount.

Later the structural changes of nanocomposite solutions were studied under the influence of a magnetic field. Samples in capillaries were placed into the permanent 0.7 Tesla magnet for 48 hours. SAXS patterns of the magnetized samples revealed the disorder-order transition for solutions with a concentration under 50 wt% and BCC to FCC phase transition at 60 wt%. Higher concentrations of nanocomposite already have FCC phase and do not change it in the magnetic field.

The comparison of FCC lattice parameters of the bulk nanocomposite and 60 wt% solution, which was two days in the permanent magnet proves the reduction of interparticle distance by a magnetic field. The lattice parameter of the magnetized sample is 5 nm smaller than for the bulk nanocomposite and slightly bigger (< 1 nm) than for bulk SPIONs stabilized only with oleic acid. In other words, the permanent magnetic field doesn't only initiate the self-assembly but also tunes the parameters of the resultant structure on a sub-nanometer scale.

Indeed, SPION assembly and an assembled structure reconstruction don't happen immediately in the permanent magnetic field for highly-concentrated samples (20-100 wt%). In this work, the time of "annealing" in the magnet is chosen to be 48 hours, which leads to the formation of stable cubic lattices. Nevertheless, there are still several open questions: how does the formed structure depend on the time of magnetization, and if there is a difference in assembly when the direction of the external field changes? These points will be mentioned in detail in Chapter 6.

5.5 Supporting Information

1. **SAXS 2D and 1D plots for 30 wt% and 40 wt% polymer grafted iron oxide nanoparticles in DEP**
2. **Influence of polymer chains and temperature on structural changes in nanocomposite solutions**

1.

Figure 5.8 and Figure 5.9 demonstrate changes in the scattering curves in presence of the magnetic field. With the increase of concentration the structure factor peaks become narrower and shift towards the high q region. Thus, the attractive forces between particles increase and the cubic packing becomes denser.

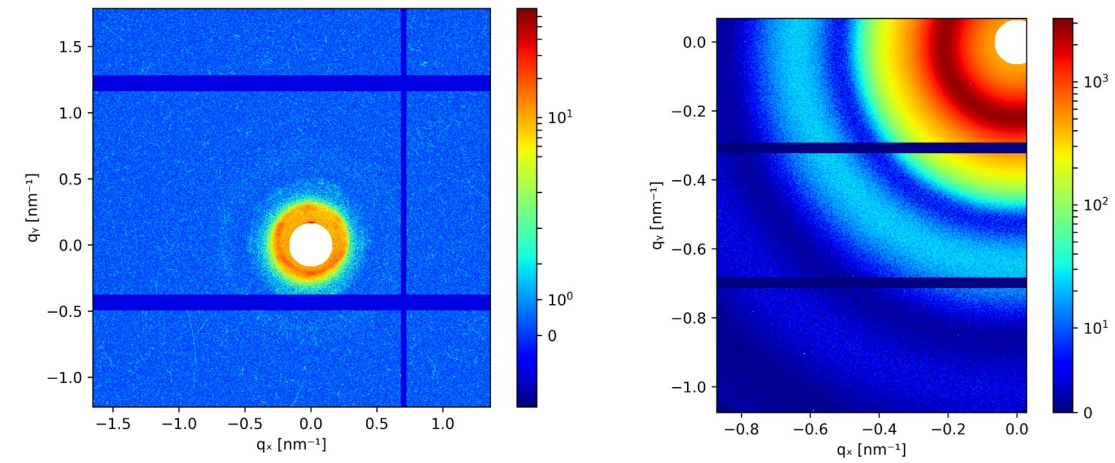

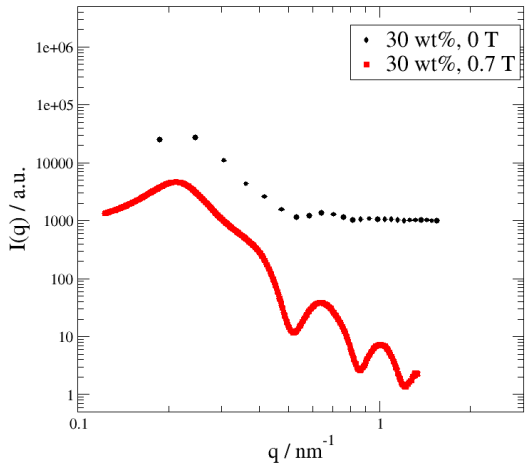

c)

*Figure 5.8 a) 2D SAXS pattern of the nanocomposite at 30 wt% concentration in DEP solvent before the magnetic field b) after the magnetic field and c) the corresponding SAXS curves before (**black curve**) and after (**red curve**) 2 days in the 0.7 Tesla magnet*

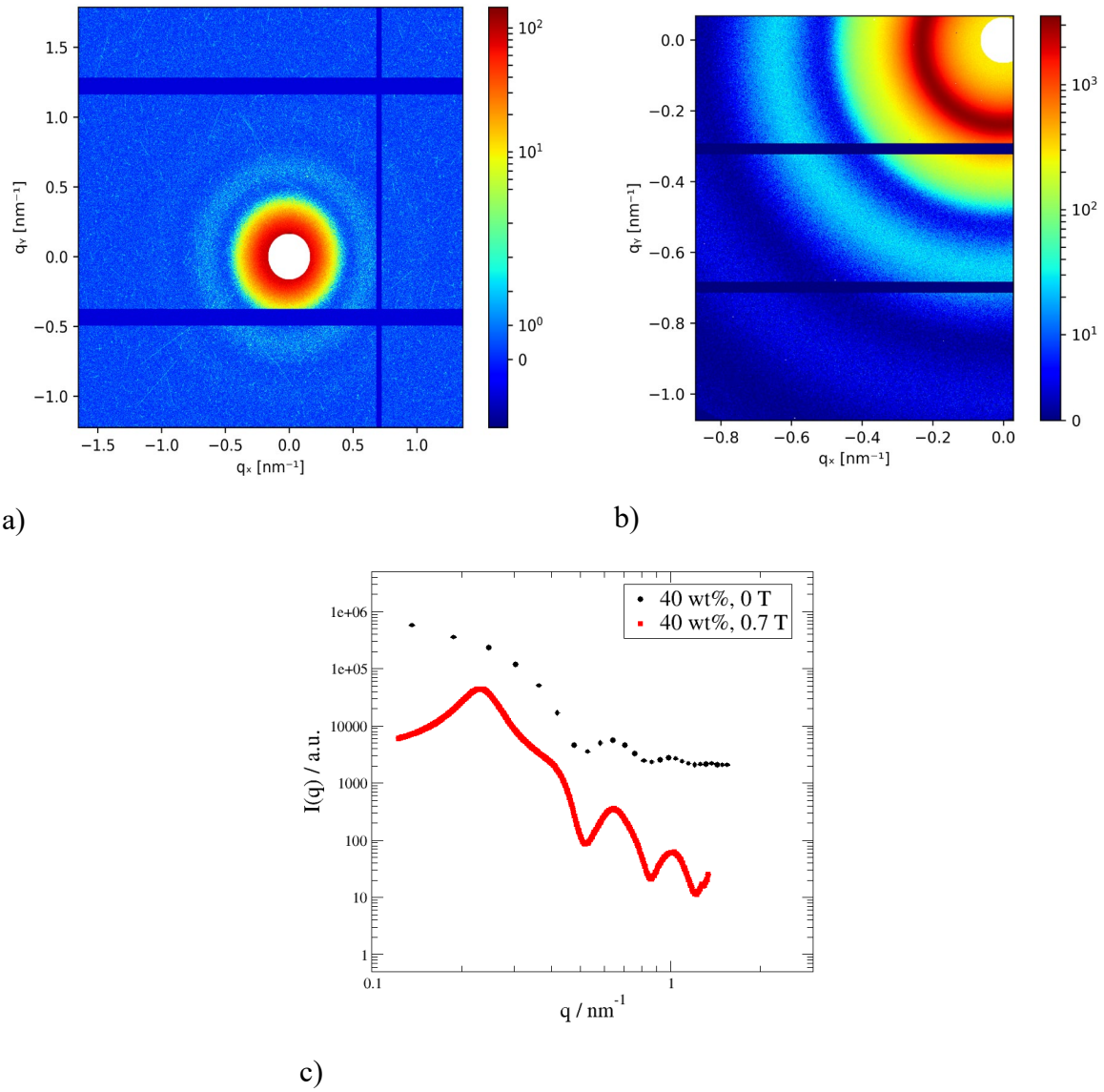

*Figure 5.9 a) 2D SAXS pattern of the nanocomposite at 40 wt% concentration in DEP solvent before the magnetic field b) after the magnetic field and c) the corresponding SAXS curves before (**black curve**) and after (**red curve**) 2 days in the 0.7 Tesla magnet*

2.

Iron oxide nanoparticles, which are stabilized only with the oleic acid surfactant don't aggregate in a large amount of solvent. When the concentration of particles is significantly increased to 60 wt% they assemble into FCC structures with the lattice parameter a = 29.2 nm, which is still larger than the lattice parameter of a bulk sample (Table 5-1). Using another way of external influence on the system – increasing temperature – we underline the role of polymer chains in the nanocomposite. Figure 5.10 *a* demonstrates no change in the assembled structure for particles with oleic acid stabilization, thus interparticle interaction is too strong and doesn't allow external fields like magnetic and temperature to reorient the FCC lattice. For the polymer functionalized magnetite there

are also no significant changes in the structure factor, but the local rearrangements happening during the temperature increase (Figure 5.10 *b*)

Table 5-1 Lattice parameters of FCC and BCC structures forming at high concentrations of nanoparticles in DEP solvent

Surfactant	Concentration, wt%	Lattice parameter a, nm	Schematic interaction
Oleic acid	60	FCC, 29.2	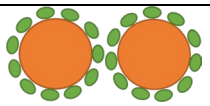
	100	FCC, 28.4	
Polystyrene	60	BCC, 33.94 → FCC, 28.8 in the magnet	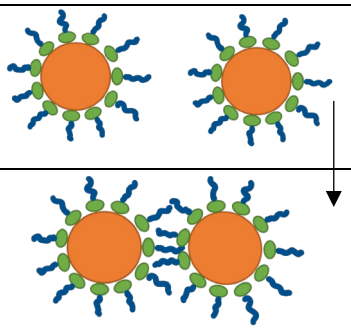
	70	FCC, 37.4	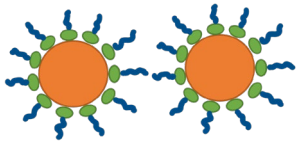
	100	FCC, 34.1	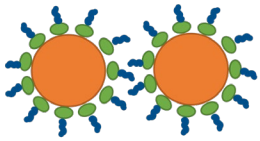

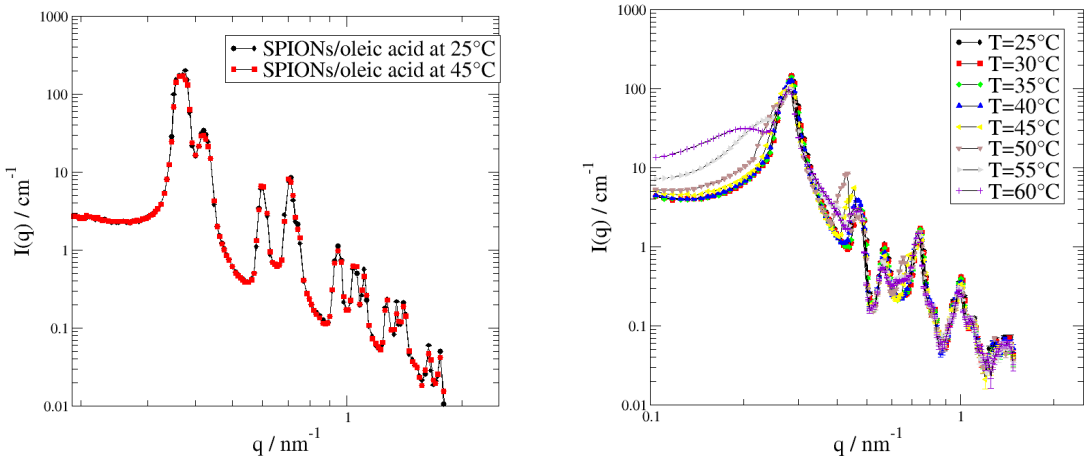

a) b)

*Figure 5.10 SAXS curves of 60 wt% a) oleic acid stabilized magnetite nanoparticles in DEP at **25 °C** and at **45 °C** temperature b) polystyrene functionalized particles in the temperature range from 25 °C to 60 °C. Experimental dots are connected with solid lines for a better visual representation.*

5.6 References

[1] A. Tiwari, M. Michalska-Domanska, S. J. Dhoble, *Functional Materials from Carbon, Inorganic, and Organic Sources* **2023**, 317–365.

[2] Y. Shi, R. Wang, S. Bi, M. Yang, L. Liu, Z. Niu, Y. Shi, L. Liu, R. Wang, S. Bi, M. Yang, Z. Niu, *Adv Funct Mater* **2023**, 2214546.

[3] K. E. Evans, A. Alderson, **n.d.**, DOI 10.1002/(SICI)1521-4095(200005)12:9.

[4] D. J. Siegwart, J. K. Oh, K. Matyjaszewski, *Prog Polym Sci* **2012**, *37*, 18–37.

[5] Q.-Y. Duan, Y.-X. Zhu, B.-H. Shan, Y. Guo, K.-F. Xu, H.-R. Jia, F.-G. Wu, Q.-Y. Duan, B.-H. Shan, Y. Guo, K.-F. Xu, F.-G. Wu, Y.-X. Zhu, H.-R. Jia, *Adv Funct Mater* **2023**, 2213636.

[6] S.-C. Wu, C.-S. Wu, C.-H. Chien, Y.-W. Zhang, C.-X. Yang, C. Liu, M.-H. Li, C.-F. Lin, Y.-H. Wu, B.-H. Lin, Y.-H. Chou, Y.-C. Chang, P. Chen, H.-C. Hsu, S.-C. Wu, C.-S. Wu, Y.-W. Zhang, C.-X. Yang, C. Liu, C.-F. Lin, Y.-H. Chou, P. Chen, H.-C. Hsu, Y.-C. Chang, C.-H. Chien, Y.-H. Wu, B.-H. Lin, *Adv Funct Mater* **2023**, *54561*, 2213427.

[7] C. Liu, T. Li, M. Sun, M. Xie, Y. Zhou, W. Feng, Q. Sun, S.-T. Zhang, S. Xue, W. Yang, C. Liu, T. Li, M. Sun, M. Xie, Y. Zhou, W. Feng, Q. Sun, S. Xue, W. Yang, S.-T. Zhang, *Adv Funct Mater* **2023**, 2215066.

[8] S. Agarwal, A. Greiner, J. H. Wendorff, *Prog Polym Sci* **2013**, *38*, 963–991.

[9] G. Yang, S. J. Park, *Materials 2019, Vol. 12, Page 1177* **2019**, *12*, 1177.

[10] M. Xia, D. Cai, J. Feng, P. Zhao, J. Li, R. Lv, G. Li, L. Yan, W. Huang, Y. Li, Z. Sui, M. Li, H. Wu, Y. Shen, J. Xiao, D. Wang, Q. Chen, M. Xia, D. Cai, J. Feng, P. Zhao, J. Li, R. Lv, G. Li, L. Yan, W. Huang, Y. Shen, J. Xiao, D. Wang, Q. Chen, Y. Li, Z. Sui, M. Li, *Adv Funct Mater* **2023**, 2214813.

[11] L. Zhao, G. Duan, G. Zhang, H. Yang, S. Jiang, S. He, *Nanomaterials 2020, Vol. 10, Page 150* **2020**, *10*, 150.

[12] J. Tani, C. G. Speziale, J. Qiu, *Appl Mech Rev* **1998**, *51*, 505–521.

[13] S. Ehlert, S. M. Taheri, D. Pirner, M. Drechsler, H. W. Schmidt, S. Förster, *ACS Nano* **2014**, *8*, 6114–6122.

[14] X. C. Sun, *http://dx.doi.org/10.1080/00268970210130218* **2009**, *100*, 3059–3063.

[15] O. Petracic, *Superlattices Microstruct* **2010**, *47*, 569–578.

[16] H. Lee, K. Y. Mi, S. Park, S. Moon, J. M. Jung, Y. J. Yong, H. W. Kang, S. Jon, *J Am Chem Soc* **2007**, *129*, 12739–12745.

[17] K. J. Si, Y. Chen, Q. Shi, W. Cheng, *Advanced Science* **2018**, *5*, 1700179.

[18] J. Park, K. An, Y. Hwang, J. E. G. Park, H. J. Noh, J. Y. Kim, J. H. Park, N. M. Hwang, T. Hyeon, *Nat Mater* **2004**, *3*, 891–895.

[19] A.-S. Robbes, F. Cousin, F. Meneau, F. Dalmas, F. Boué, J. Jestin, *Macromolecules* **2011**, *44*, 8858–8865.

[20] S. M. Taheri, S. Fischer, M. Trebbin, S. With, J. H. Schröder, J. Perlich, S. V. Roth, S. Förster, *Soft Matter* **2012**, *8*, 12124–12131.

[21] S. M. Taheri, S. Fischer, S. Förster, *Polymers (Basel)* **2011**, *3*, 662–673.

[22] Z. Fu, Y. Xiao, A. Feoktystov, V. Pipich, M. S. Appavou, Y. Su, E. Feng, W. Jin, T. Brückel, *Nanoscale* **2016**, *8*, 18541–18550.

[23] J. Park, K. An, Y. Hwang, J. E. G. Park, H. J. Noh, J. Y. Kim, J. H. Park, N. M. Hwang, T. Hyeon, *Nature Materials 2004 3:12* **2004**, *3*, 891–895.

[24] A. Buffet, A. Rothkirch, R. Döhrmann, V. Körstgens, M. M. Abul Kashem, J. Perlich, G. Herzog, M. Schwartzkopf, R. Gehrke, P. Müller-Buschbaum, S. v. Roth, *urn:issn:0909-0495* **2012**, *19*, 647–653.

[25] R. Biehl, *PLoS One* **2019**, *14*, DOI 10.1371/JOURNAL.PONE.0218789.

[26] A. Guinier, *Small-Angle Scattering of X-Rays*, Wiley, New York, **1955**.

6 Shearing and magnetic field-induced phase transition in SPIONs complexes

6.1 Abstract

Nowadays an external magnetic field is actively used to target superparamagnetic iron oxide nanoparticles (SPIONs) to the diseased regions[1]. The flow conditions during a transfer affect the behavior and accumulation of magnetic particles. In this work, we study SPIONs self-assembly at shearing and magnetic field conditions using small-angle X-ray scattering. We have chosen 14 nm and 22 nm iron oxide particles grafted with polystyrene chains as a model system and compared the influence of core-shell parameters on the result of nanoparticle assembly in a 0.1 Tesla magnetic field.

Since most of the resultant structures have either FCC or BCC lattice or a mixture of both, we discuss a path of possible alignment and orientation under the shearing conditions and after pre-shearing with a later exposure to the magnetic field. The last configuration is closer to the magnetic targeting method because the magnetic field is also perpendicular to the flow. In most of the cases, we observe a reorientation of the FCC lattice in the magnetic field, not along a reorientation path with a well-defined rotation axis. So for smaller particles with a thinner polymer shell, not well-defined paths, sometimes including twinning are more characteristic, which leads to more complex scattering patterns. For larger particles with a thicker shell, it is favourable to pack into FCC lattices from isotropic state and compact with an increase of magnetization time.

6.2 The FCC-BCC transition and lattice orientation in external fields

Face-centered cubic (FCC) and body-centered cubic (BCC) are two of the most iconic crystal structures. These crystals have different packing, slip systems, ductility, etc. For instance, Figure 6.1 presents FCC and BCC configurations with their lines and planes of the highest particle density.

The packing volume fraction for the two lattices is given by

$$\varphi = \frac{nV}{a^3} \tag{6.1}$$

where n is the number of spheres per unit cell, which for FCC is $n_{FCC} = 4$ and for BCC is $n_{BCC} = 2$. The sphere volume V is given by $V = \frac{4\pi R^3}{3}$, where R is the sphere radius. For an

FCC-BCC transition at a given volume fraction φ and a given sphere radius R, the unit cell dimensions are related by

$$\varphi = \frac{n_{FCC}V}{a_{FCC}^3} = \frac{n_{BCC}V}{a_{BCC}^3} \tag{6.2}$$

such that

$$a_{FCC} = \left(\frac{n_{FCC}}{n_{BCC}}\right)^{1/3} a_{BCC} = 2^{1/3}a_{BCC} \approx 1.26a_{BCC} \tag{6.3}$$

For an FCC lattice, the first reflection is the (hkl) = (111)-peak. It appears at a q-value

$$q_{FCC}^* = \frac{2\pi}{a_{FCC}}\sqrt{h^2+k^2+l^2} = \frac{2\pi}{a_{FCC}}\sqrt{3} \tag{6.4}$$

For a BCC-lattice, the first reflection is the (hkl)=(110)-peak. It appears at a q-value

$$q_{BCC}^* = \frac{2\pi}{a_{BCC}}\sqrt{h^2+k^2+l^2} = \frac{2\pi}{a_{BCC}}\sqrt{2} \tag{6.5}$$

Since $a_{FCC} = 2^{1/3}a_{BCC}$, we have the relation

$$q_{FCC}^* = \frac{2\pi}{a_{FCC}}\sqrt{3} = \frac{2\pi}{2^{1/3}a_{BCC}}\sqrt{3} = \frac{1}{2^{1/3}}\left(\frac{3}{2}\right)^{1/2} q_{BCC}^* \approx 0.97a_{BCC} \tag{6.6}$$

Therefore, for an FCC-BCC phase transition at the same volume fraction, the first-order peaks will have approximately the same position. As an example (see Figure 6.2 a), we calculate the scattering curve for an FCC lattice with a unit cell $a_{FCC} = 30$ nm consisting of spheres with a radius R=6 nm, corresponding to a volume fraction $\varphi = 0.134$. We observe the first reflection at $q_{FCC}^* \approx 0.363$ nm^{-1}. For the same volume fraction, we have a BCC lattice with a unit cell dimension $a_{BCC} = 2^{-1/3}a_{FCC} = 23.8$ nm, and the first reflection at $q_{BCC}^* \approx 0.373$. Therefore, the first reflection for both lattices at the same volume fraction occurs at nearly the same q-value.

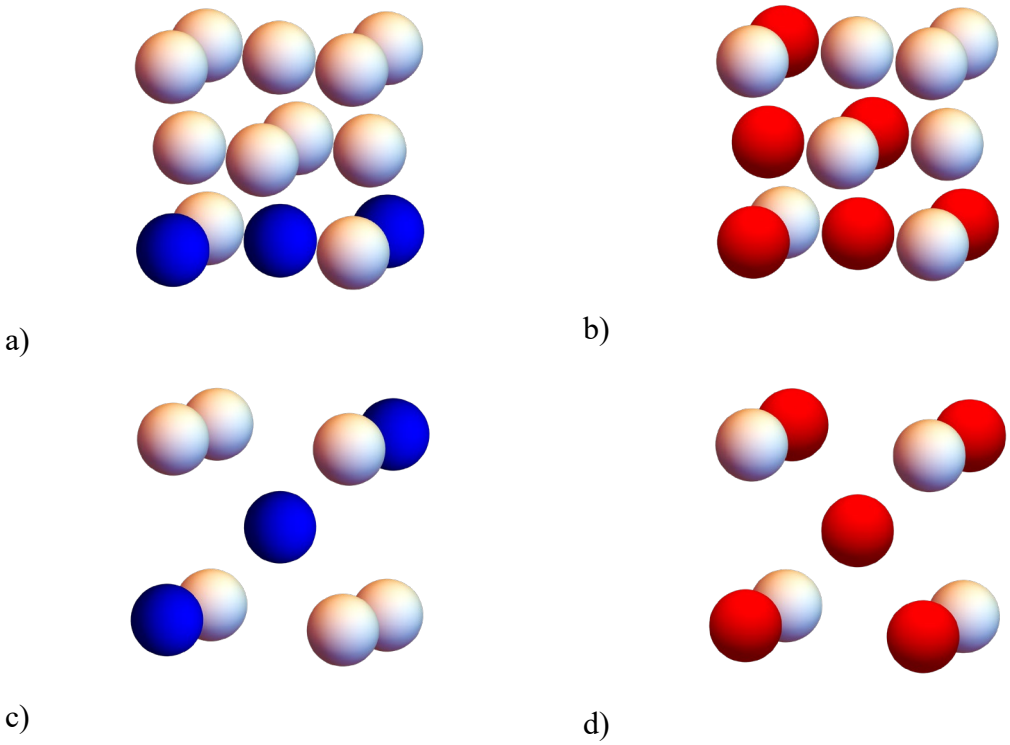

Figure 6.1: The FCC unit cell with a) the line of highest particle density <110> indicated in blue and b) the plane of highest particle density {111} indicated in red. The BCC unit cell with c) the line of highest particle density <111> indicated in blue and d) the plane of highest particle density {110} indicated in red

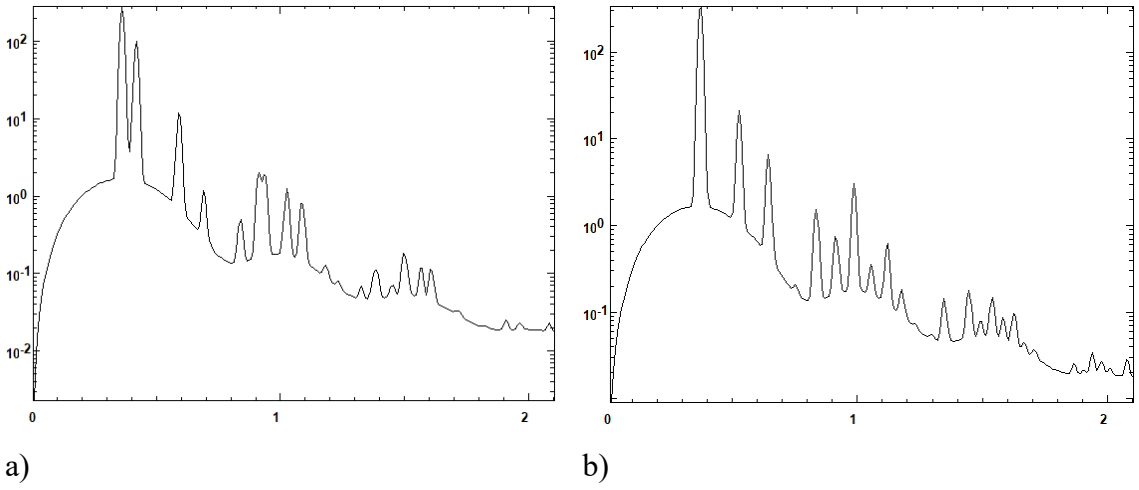

Figure 6.2: Calculated scattering curves for an FCC lattice a) with unit cell dimension $a_{FCC} = 30$ nm and b) a BCC lattice at the same volume fraction and a corresponding unit cell dimension $a_{BCC} = 23.8$ nm. The first reflections nearly occur at the same q-value. A clear signature of the FCC lattice is the proximity of the two first reflections (111, 200)

The principal directions of the shear experiment are shown in Figure 6.3 a. The liquid is confined between the two planes indicated in blue. The liquid is sheared by moving the upper plane to the left, with a fixed lower plane. Therefore, this direction is the flow direction $\boldsymbol{v}$ (1). The direction normal to the planes is parallel to the velocity gradient, and therefore the gradient direction ∇ (2). The direction is perpendicular to $\boldsymbol{v}$ and ∇ is the vorticity direction $\boldsymbol{e}$ (3).



a) b)

Figure 6.3: Scheme of the three principal directions in a) a shear experiment and b) in the magnetic field direction.

For an FCC lattice the line of highest particle density <110> orients parallel to ***v*** (1), and the plane of highest particle density {111} is parallel to the blue planes in Figure 6.3. For a BCC lattice the line of highest particle density <111> orients parallel to ***v*** (1), and the plane of highest particle density {110} is parallel to the blue planes. The respective orientation of the lattices is shown in Figure 6.4.

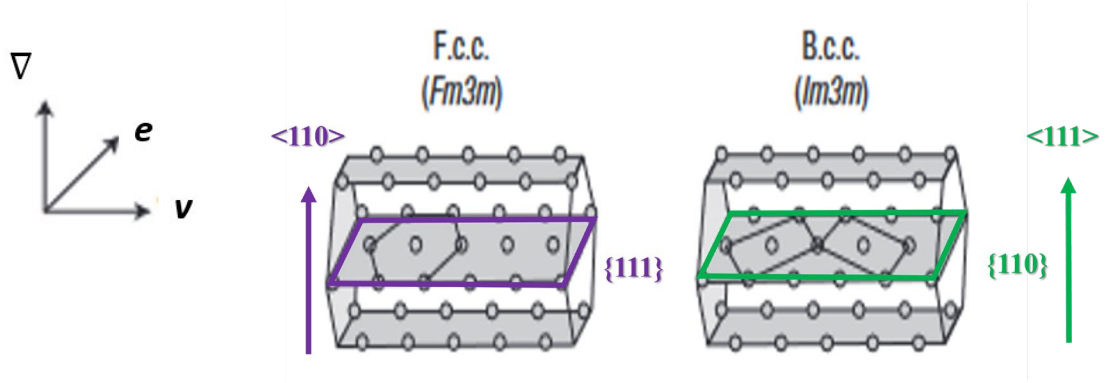

Figure 6.4: Orientations of the FCC- and BCC-lattices under shear. The two twins of the BCC-lattice are indicated. This figure originates from the reference[2] Copyright © 2007, Nature Publishing Group

In the rheo-SAXS experiments, the X-ray beam usually is transecting the liquid normal to the blue planes ('radial' direction), i.e. the beam direction is parallel to the gradient direction ∇. If the flow direction is parallel to the x-direction of the detector, then for an FCC-lattice we observe a scattering pattern with the beam direction parallel to the <111>-direction of the lattice (beam || <111>), the flow direction parallel to the <110>-direction (***v*** || q_x || <110>), and the vorticity direction ***e*** parallel to the <112>-direction ((***e*** || q_y || <112>).

The scattering patterns for an FCC-lattice oriented in a shear direction (equals x-direction) very much depend on the degree of orientational order. For a very high orientational order, only very sharp and crystallographically allowed Bragg reflections are observed as shown in Figure 6.5 a. With decreasing orientational order additional

secondary Bragg-reflections are observed as in Figure 6.5 b, c. For an isotropic sample, only Debye-Scherrer rings are observed. Usually, lyotropic micellar phases exhibit intermediate orientational order, such that the cases in Figure 6.5 b and c are regularly observed. The corresponding real-space image is shown in Figure 6.5 e. An azimuthal plot for the first-order reflections in Figure 6.5 c is shown in Figure 6.5 f, featuring regular angular periods of 60°.

For a BCC-lattice, if the flow direction is parallel to the x-direction of the detector, then we observe a scattering pattern with the beam direction parallel to the <110>-direction of the lattice (beam || <110>), the flow direction parallel to the <112>-direction ($\boldsymbol{v}$ || q_x || <112>), and the vorticity direction $\boldsymbol{e}$ parallel to the <111>-direction (($\boldsymbol{e}$ || q_y || <111>). The scattering patterns for a BCC-lattice oriented in a shear direction (x-direction) also very much depend on the degree of orientational order. For very high orientations, only very sharp and crystallographically allowed Bragg reflections are observed as shown in Figure 6.6 a. With decreasing orientational order additional secondary Bragg-reflections are observed as in Figure 6.6 b and c. For an isotropic sample, only Debye-Scherrer rings are observed. Usually, lyotropic micellar phases exhibit intermediate orientational order, such that the cases in Figure 6.6 c are regularly observed. The corresponding real-space image of one of the two twins is shown in Figure 6.6 e. An azimuthal plot for the first-order reflections in Figure 6.6 c is shown in Figure 6.6 f, featuring irregular angular distances, a typical feature of the BCC lattice.

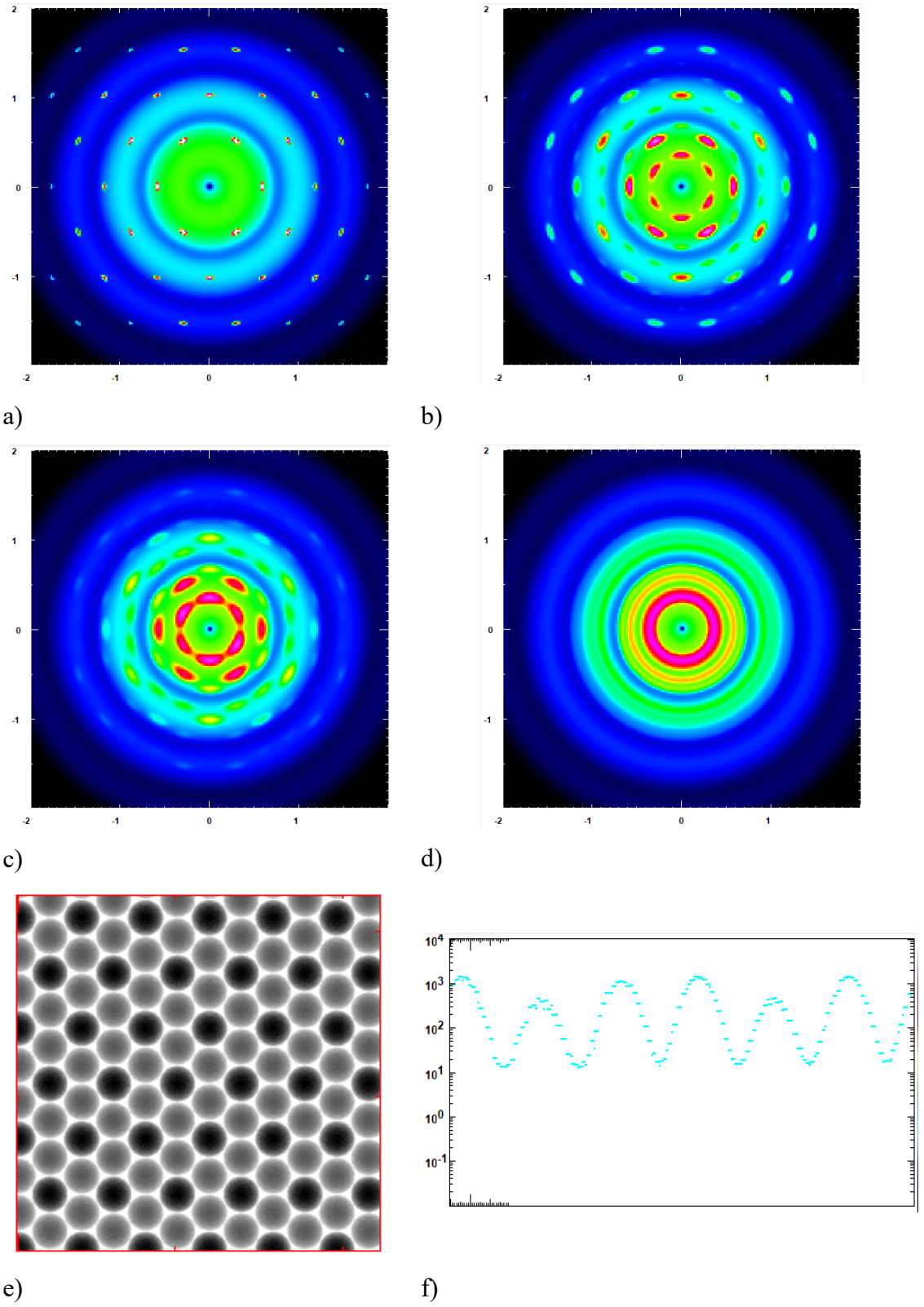

Figure 6.5: Scattering patterns for an FCC lattice assuming the beam-direction parallel to the <111>-direction, the q_x-direction parallel to the <110>-direction, and the q_y-direction parallel to the <112>-direction, corresponding to a shear-direction parallel to the x-direction. The scattering patterns are calculated for a) very high orientational order, b) and c) for intermediate orientational order, and d) for an isotropic case; e) corresponding real-space image, f) an azimuthal plot for the first-order reflections in the image (c).

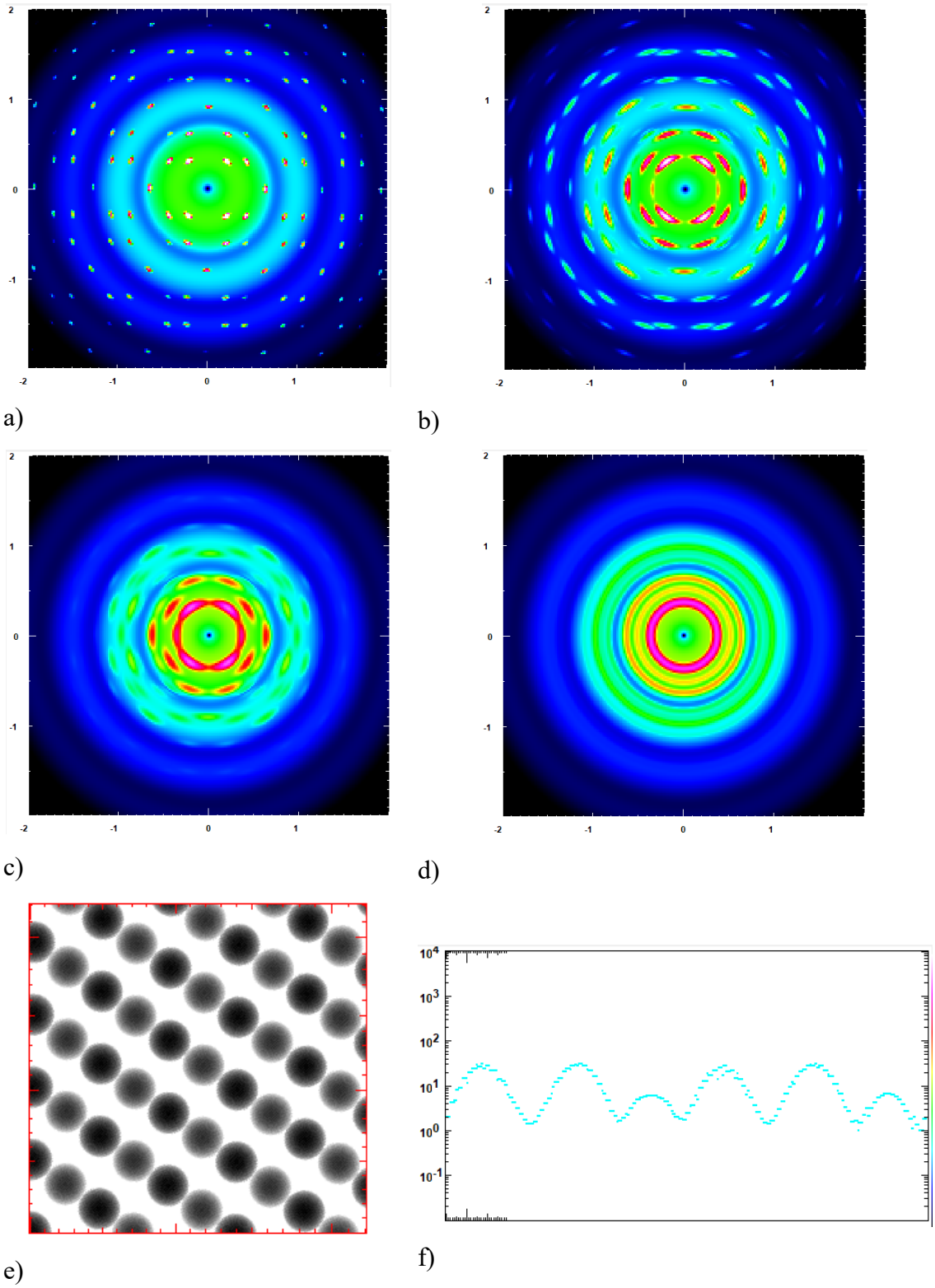

Figure 6.6: Scattering patterns for a BCC lattice assuming the beam-direction parallel to the (110)-direction, the q_x-direction parallel to the (112)-direction, and the q_y-direction parallel to the (111)-direction, corresponding to a shear-direction parallel to the x-direction. The scattering patterns are calculated for a) very high orientational order, b) and c) for intermediate orientational order, and d) for an isotropic case; e) real-space image of one of the two twins, f) an azimuthal plot for the first-order reflections for the image (c).

An FCC-BCC phase coexistence can lead to complex scattering patterns as shown in Figure 6.7 a, where the FCC phase with <111>-direction aligned parallel to the beam

coexists with the BCC phase with the <110>-direction aligned parallel to the beam. As shown in Figure 6.7 b, such scattering patterns are observed experimentally.

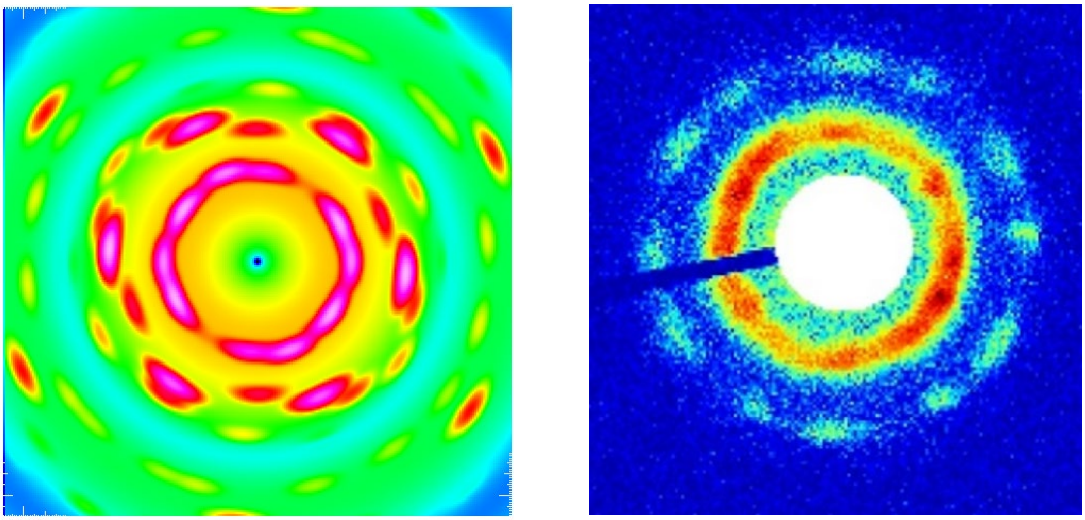

a) b)

Figure 6.7: Scattering patterns for coexisting and epitaxially aligned FCC and BCC phases a) as calculated and b) as observed in a shearing experiment with PI-PS polymer (Chapter 3, Figure 3.9) at, 20wt% in DEP while cooling down to 25°

In a magnetic field, the lines of the highest particle density are aligned in field direction ***B*** (Figure 6.3 b). Since there are no preferred orientations of planes of the highest particle density, a fiber pattern with the fiber direction parallel to the field direction usually results. Therefore, if the beam is parallel to ***B***, for an FCC-lattice the <110>-direction would be parallel to the beam, and a scattering pattern with Debye-Scherrer rings would be expected.

An interesting experiment is to first apply shear to orient the <110>-direction of the FCC-lattice in the shear direction, with the beam parallel to the <111>-direction. The subsequent application of a magnetic field as indicated in Figure 6.8 would tilt the <110>-direction out-of-plane, parallel to the beam. The set of orientations and scattering patterns expected for this path is shown in Figure 6.8. Therefore, after shear the beam would be parallel to the <111>, direction and subsequently will probe the <210> and <310> directions, until the final <110> direction is obtained. The corresponding scattering patterns are shown in Figure 6.8 and exhibit characteristic changes in the central hexagonal arrangement of Bragg peaks. The situation may be complicated by allowing counter-clockwise rotations, slight deviations from this angular path, and twinning. Figure 6.8 e shows the scattering pattern of twins aligned in the <100> direction, which could occur close to the final stage of the reorientation process.

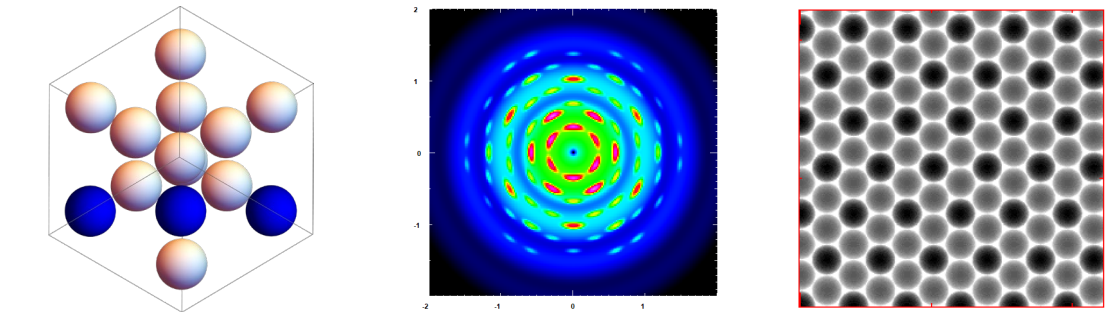

a) (111)

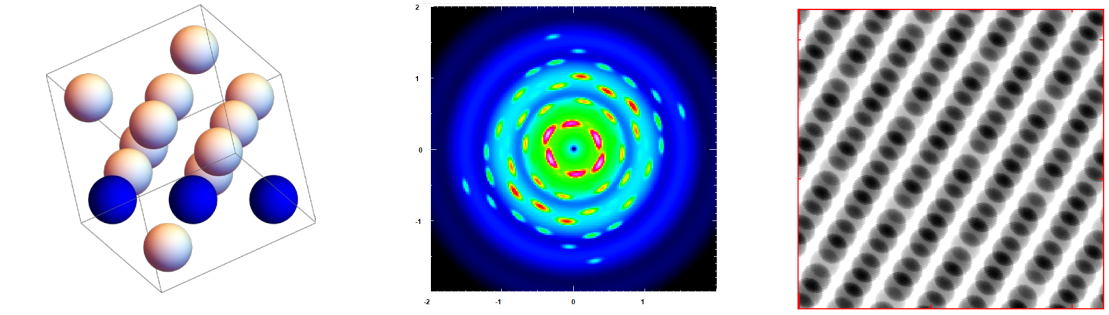

b) (210)

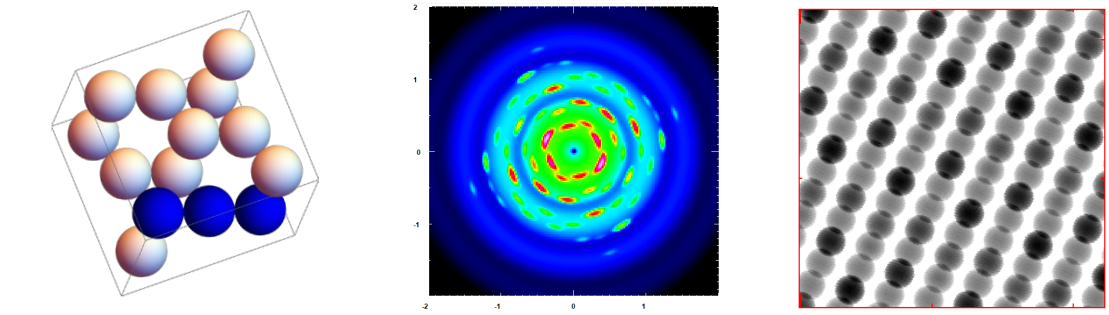

c) (310)

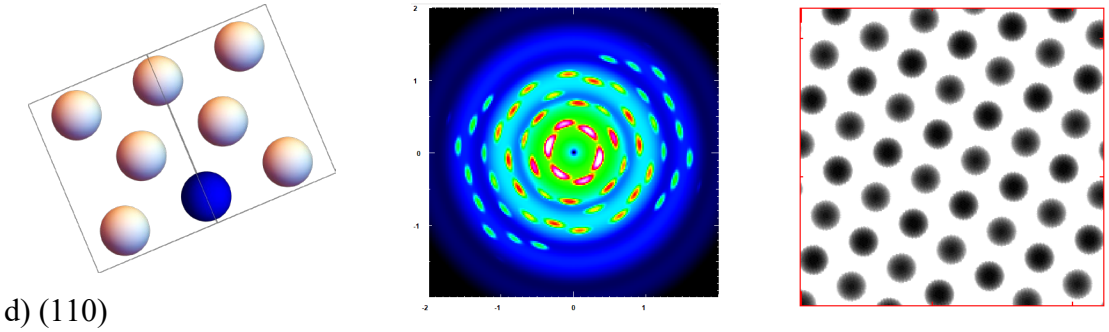

d) (110)

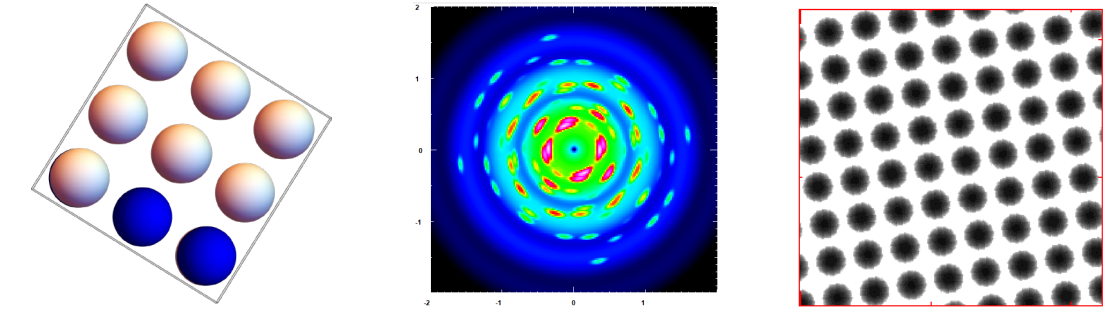

e) (100)

Figure 6.8: a) FCC-lattice viewed in the [111]-direction with the line of highest particle density (110) aligned in the x-direction, as after a shear experiment in the horizontal direction, together with the corresponding scattering pattern and the calculated projection of the lattice. b, c, d) Out-of-plane

reorientation of the line of highest particle density from the horizontal direction into the direction perpendicular to the plane, with the corresponding scattering patterns and calculated projections. Slight deviations of this reorientation path can lead to more complicated projections such as e) the twinned (100)-projection

When performing the shear alignment experiment, we indeed see a reorientation of the FCC-lattice in the magnetic field at different concentrations. We observe that the reorientation process does not progress along a reorientation path with a well-defined rotation axis as indicated in Fig. 6.8. Instead we observe reorientation involving different, not well-defined paths, sometimes involving twinning, leading to a set of complex scattering patterns. Yet, at some stages of the reorientation paths, we observe scattering patterns arising from orientations along the expected orientation path as outlined in Figure 6.8 as shown in Figure 6.9. For example, in addition to the initial <111> shear orientation, we observe the intermediate <210>-orientation, the final <110> orientation, and the <100>-orientation, mostly in twinned states. We note that for the <111> both twins have identical scattering patterns.

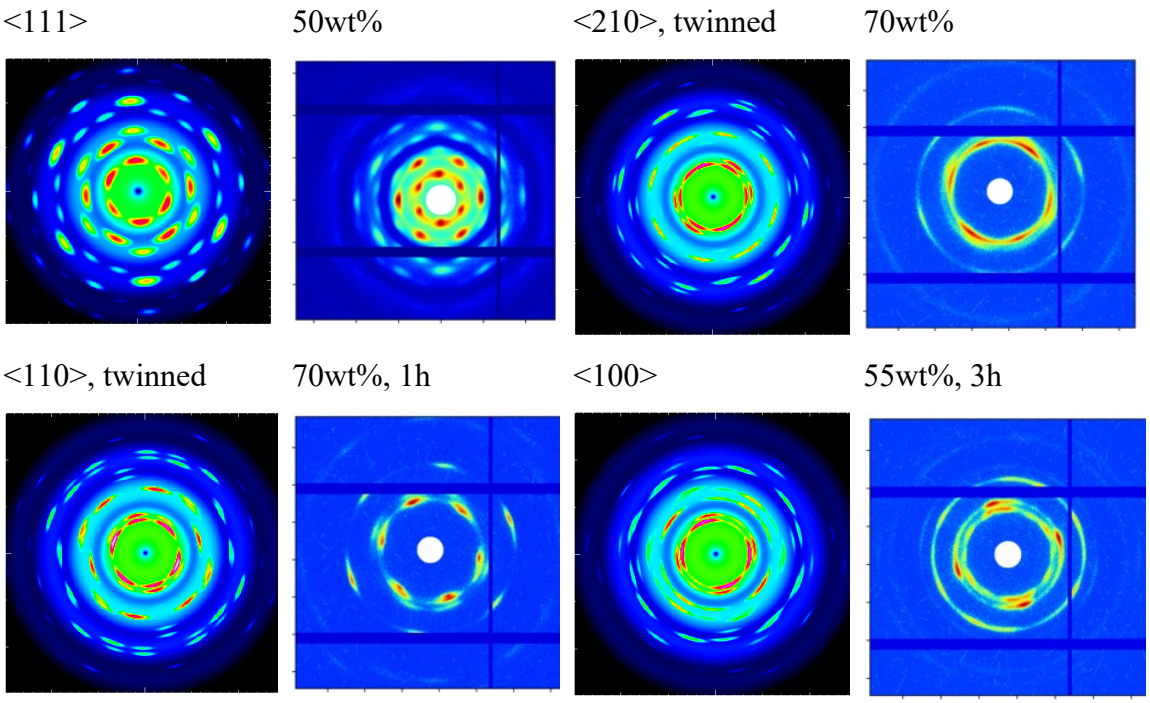

Figure 6.9: Comparison of calculated scattering patterns and measured scattering patterns obtained while reorienting the shear-aligned FCC-lattice in the magnetic field. The measured sample is 14 nm SPIONs grafted with 6 000 g/mol PS.

6.3 Experimental results and discussions

The assembly of systems with a hard core and a soft polystyrene shell was performed in p-Xylene solvent, because of its high boiling point value above 130 °C and low viscosity parameter, which prevents fast solvent evaporation during shearing and simplifies sample preparation. TEM images in Figure 6.10 demonstrate three studied systems, in particular 14 nm SPIONs grafted with short (6 000 g/mol) and long (26 000 g/mol) polystyrene chains, and 22 nm particles with long polymer chains. The presence of polymer controls interparticle distance depending on chain length and makes particles more uniform, which is well-observed from SAXS measurements (Figure 6.10 c). There are bigger particles (D = 22nm) of pebble shape, which are coated with a long polymer and also give many minima on the scattering curve as well as smaller (D = 14 nm) and more uniform particles.

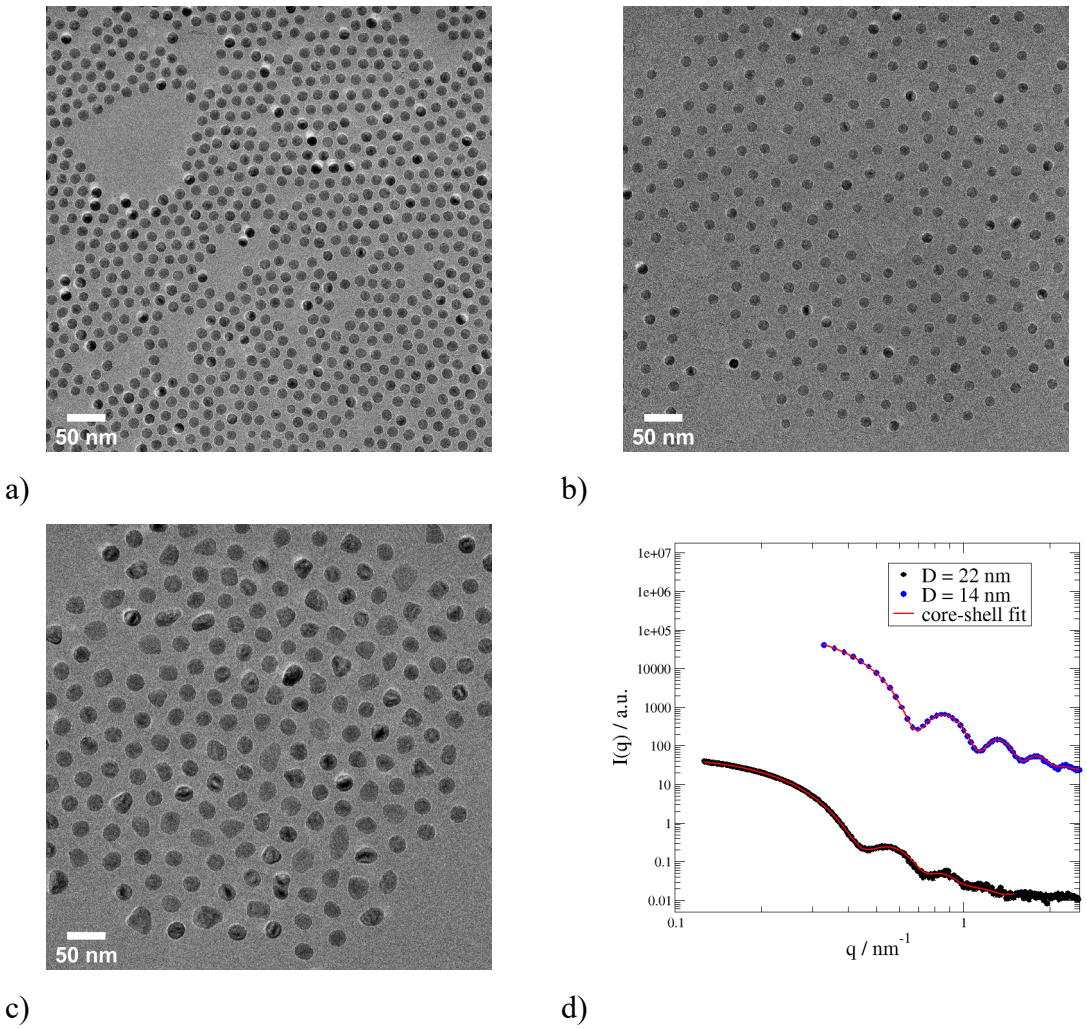

*Figure 6.10: TEM images of iron oxide nanoparticles stabilized with polystyrene chains a) D=14 nm particles and Mw=6 000 g/mol polymer b) D=14 nm particles and Mw=26 000 g/mol polymer c) D=22 nm particles and Mw=26 000 g/mol polymer; d) SAXS curves for 22 nm particles (**black dots**) and 14 nm particles (**blue dots**) stabilized with oleic acid and measured at the diluted state in THF solvent. Scattering curves are fitted with a polydisperse core-shell model (**red line**)*

In the previous chapter, we established that well-ordered structures appear at higher concentrations of nanocomposite in an organic solvent. Therefore, we test the concentration range between 50 wt% and 70 wt% of polymer-grafted iron oxide nanoparticles in p-Xylene.

6.3.1 Influence of shearing external field

Homogeneous mixtures of polymer-grafted SPIONs in the organic solvent were subjected to oscillatory shearing with a constant 8 Hz frequency. Several shearing procedures were tested, including a gradual increase of the strain parameter, long-time shearing at a constant strain of low (1 %), average (60 %), and high (120 %) values, and each of them in a combination with an increasing temperature of the system. As a result, only the sample shearing at high strains above 100 % with the following temperature increase to 60 °C induces structural changes.

For instance, smaller 14 nm iron oxide nanoparticles grafted with shorter polymer chains assemble in hexagonal lattices of long- and short-range order even before shearing, which is shown in the SAXS diffraction pattern (Figure 6.11 a). Shearing at 120 % strain adds to the cubic lattices some twinning effect, which is also well-observed from simulations in <110> direction (Figure 6.11 b). Heating the sample during shearing to 60 °C changes the diffraction pattern in the way that the local order is disappearing and the first scattering ring is shifted towards the high q-range. Moreover, the new state is stable and it can't be changed during cooling the system down to 25 °C (Figure 6.11 c). Meanwhile, the azimuthal position of diffraction spots relative to each other is not changing over the whole experiment significantly, only by 5°. SAXS curves clearly show the difference in the q-position of the first peak and its narrowing at 60 °C temperature (Figure 6.11 d, e). Since the structure factors of fitting functions for FCC and BCC are quite similar due to the common nature of lattices and the initial and resultant scattering patterns are complex, we are stating the overall structure reordering under the shearing and high-temperature conditions.

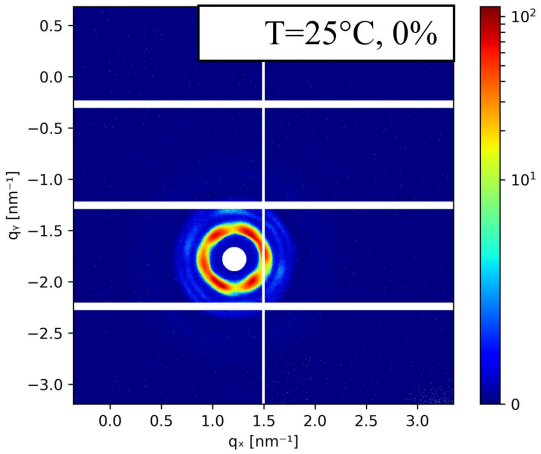
T=25°C, 0%
q_y [nm^{-1}]
q_x [nm^{-1}]
10^2
10^1
0

a)

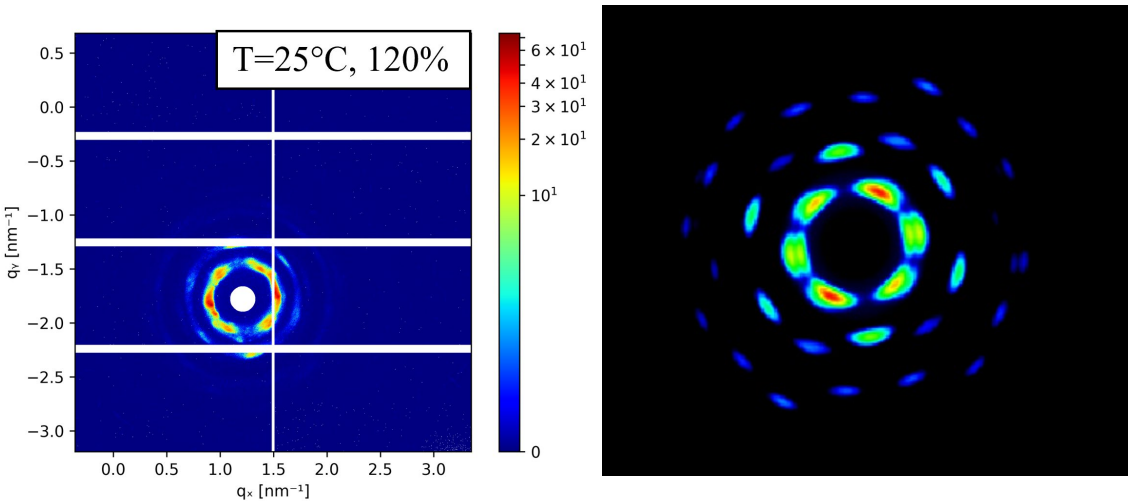
T=25°C, 120%
q_y [nm^{-1}]
q_x [nm^{-1}]
6×10^1
4×10^1
3×10^1
2×10^1
10^1
0

b)

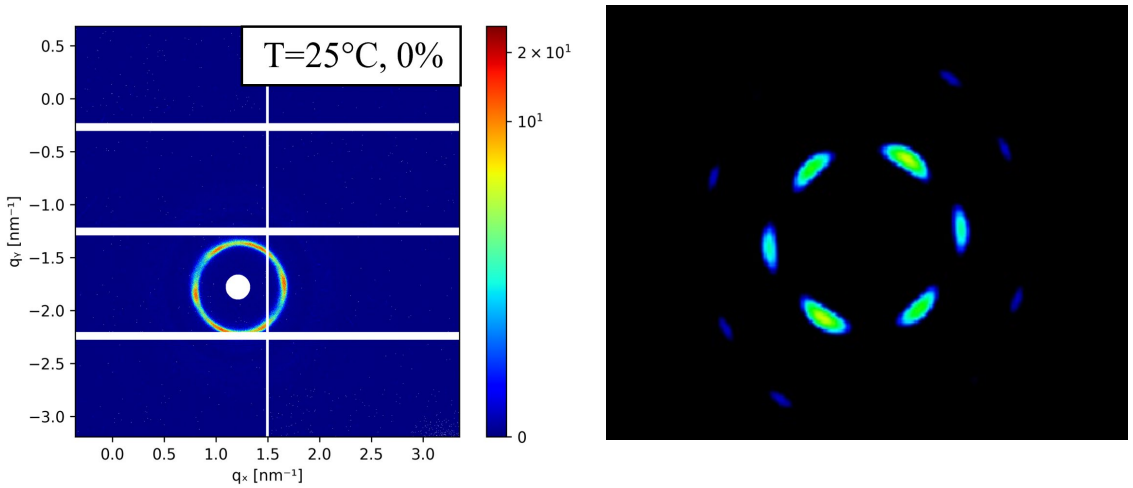
T=25°C, 0%
q_y [nm^{-1}]
q_x [nm^{-1}]
2×10^1
10^1
0

c)

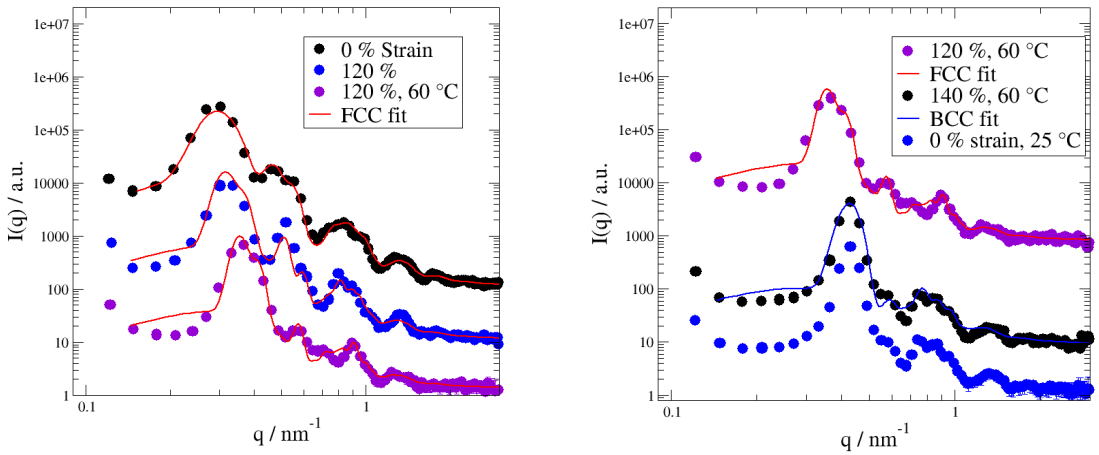

d) e)

*Figure 6.11 SAXS 2D images of 14 nm iron oxide nanoparticles grafted with 6 000 g/mol polystyrene chains at 50 wt% concentration in Xylene solvent a) obtained at room temperature without shearing b) after shearing with 120% strain at 25 °C and the corresponding simulation pattern of <110 > direction c) after shearing with strains up to 140 % and cooling down the system from 60 °C to 25 °C and the corresponding simulation pattern of <110 > direction; radially averaged scattering experimental curves of the changing structure measurements at corresponding shearing and temperature parameters: d) 0 % strain at 25 °C (**black dots**), 120 % strain at 25 °C (**blue dots**), 120 % at 60 °C (**purple dots**) e) 140 % at 60 °C (**black dots**) and 0 % strain at 25 °C (**blue dots**) with additional FCC (**red line**) and BCC (**blue line**) fit curves.*

Similar structural changes happen with the increase of the sample concentration by 10 wt%. In this case, the same tendency is observed: the scattering curve's first peak shifts towards the high q range, where it becomes narrower. It means that the shearing field orients and packs the lattice closer. This effect of packing is even more increased by the temperature field, which again leads to the formation of FCC and BCC mixtures with ordered domains (Figure 6.12 a, c). In comparison to the lower concentration, the 60 wt% sample is too stiff and needs more shearing time for changing the diffraction pattern (Figure 6.12 b).

Larger particles of 22 nm diameter grafted with longer 26 000 g/mol polymer chains have λ parameter 2.6, which makes a difference in the structural behavior of nanocomposite in the organic solvent during shearing and temperature increase. Without external influence, the sample measurements show a homogeneous 2D pattern. After several minutes of shearing FCC diffraction spots appear and later show a change in their orientation. Noteworthy, no significant changes in the first peak position were observed. For the 50 wt% sample FCC lattice is well-oriented in <110> direction at 80% strain and 60 °C temperature (Figure 6.13 a). Further increase in the strain value impairs the orientation of the FCC lattice which is clearly shown in the azimuthal plot in Figure 6.13 b.

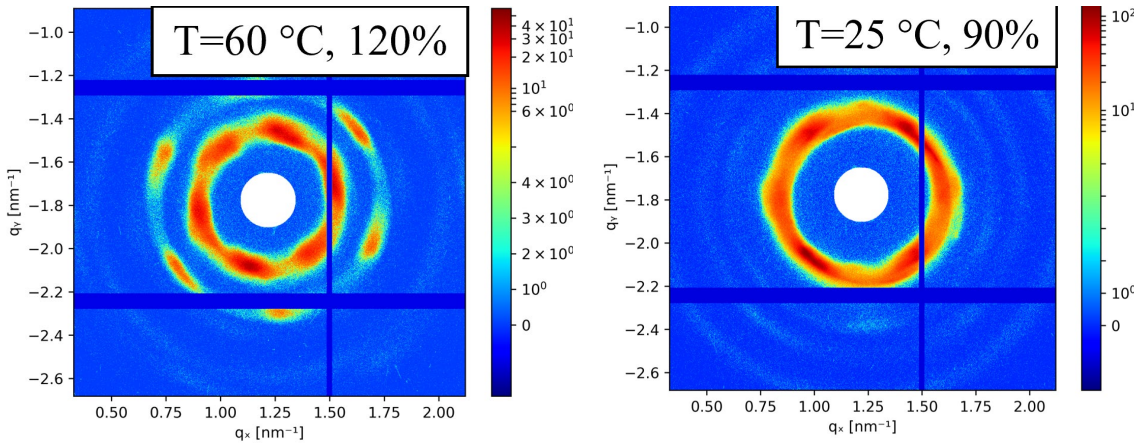

a) b)

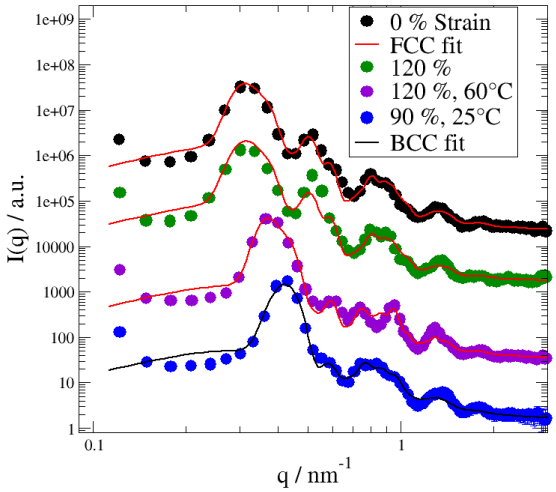

c)

*Figure 6.12 SAXS 2D images of 14 nm iron oxide nanoparticles grafted with 6 000 g/mol polystyrene chains at 60 wt% concentration in Xylene solvent a) obtained during 120 % shearing at 60 °C b) during shearing with 90 % strain and cooling down the system from 60 °C to 25 °C; radially averaged scattering experimental curves of the changing structure measurements at corresponding shearing and temperature parameters: c) 0 % strain at 25 °C (**black dots**), 120 % strain at 25 °C (**green dots**), 120 % at 60 °C (**purple dots**), and 90 % at 25 °C (**blue dots**) with additional FCC (**red line**) and BCC (**black line**) fit curves.*

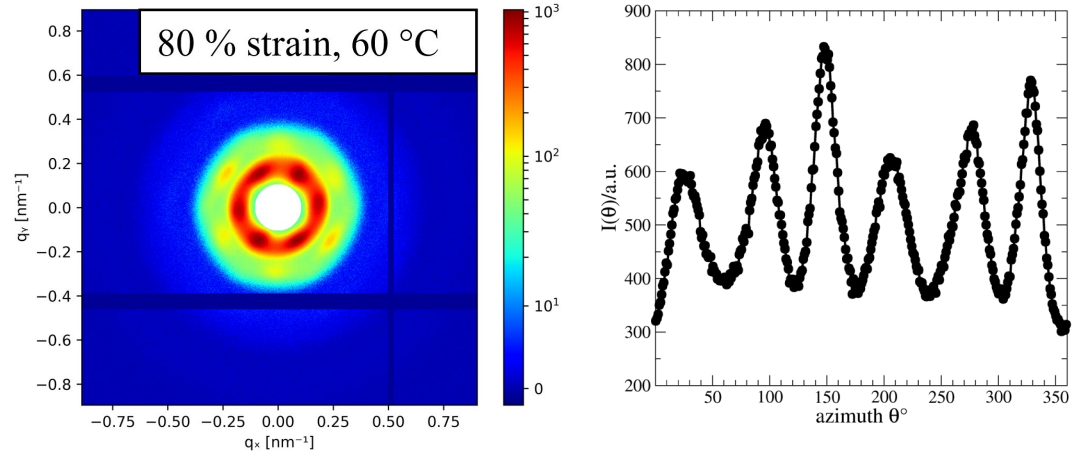

a)

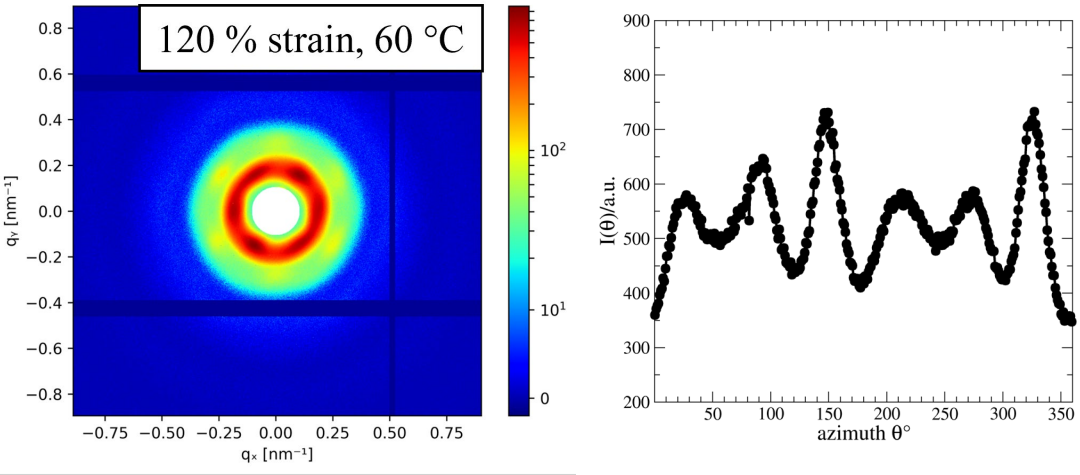

b)

Figure 6.13 SAXS 2D images (left) of 22 nm iron oxide nanoparticles grafted with 26 000 g/mol polystyrene chains at 50 wt% concentration in Xylene solvent and corresponding azimuthal plots of the first scattering ring from the beamstop (right): a) at 80 % strain and 60 °C and b) at 120 % strain and 60 °C

The example of the complete path for a cubic structure orientation under the shearing and temperature fields is shown for the 60 wt% solution in Figure 6.14. The diffraction pattern was homogeneous before shearing and turned to the FCC pattern afterward. Since the sample concentration is 10 wt% higher than in the previous case, a higher strain value is needed for proper orientation of FCC (120 % strain) and more time to lose this orientation (up to 15 minutes). Heating the system to 70 °C doesn't change the overall behavior of the system and could be reduced to 60 °C.

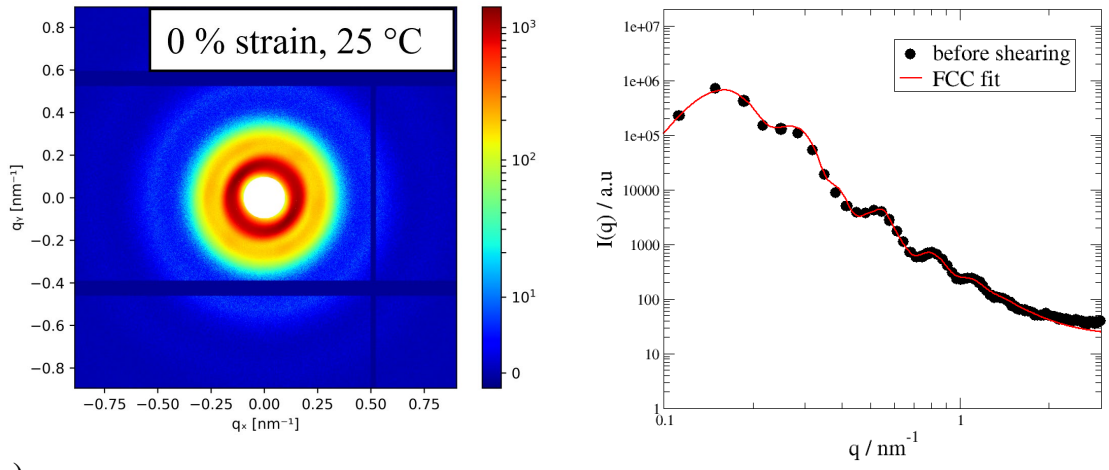
0 % strain, 25 °C
qy [nm⁻¹]
qx [nm⁻¹]
before shearing
FCC fit
I(q) / a.u
q / nm-1

a)

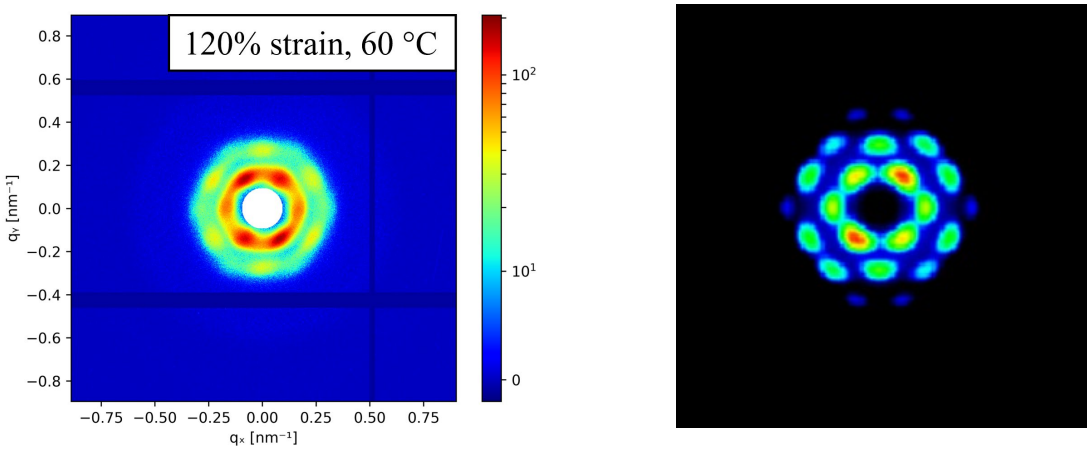
120% strain, 60 °C
qy [nm⁻¹]
qx [nm⁻¹]

b)

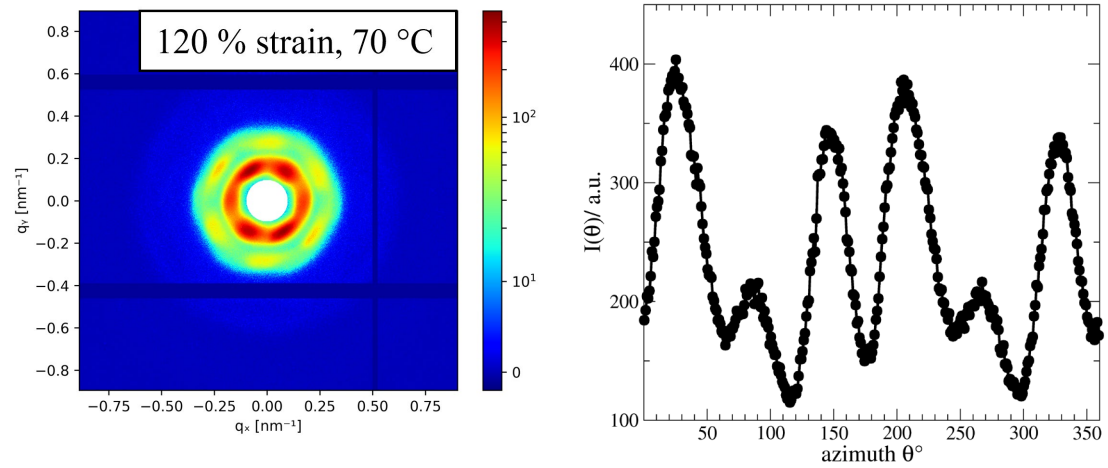
120 % strain, 70 °C
qy [nm⁻¹]
qx [nm⁻¹]
I(θ)/ a.u.
azimuth θ°

c)

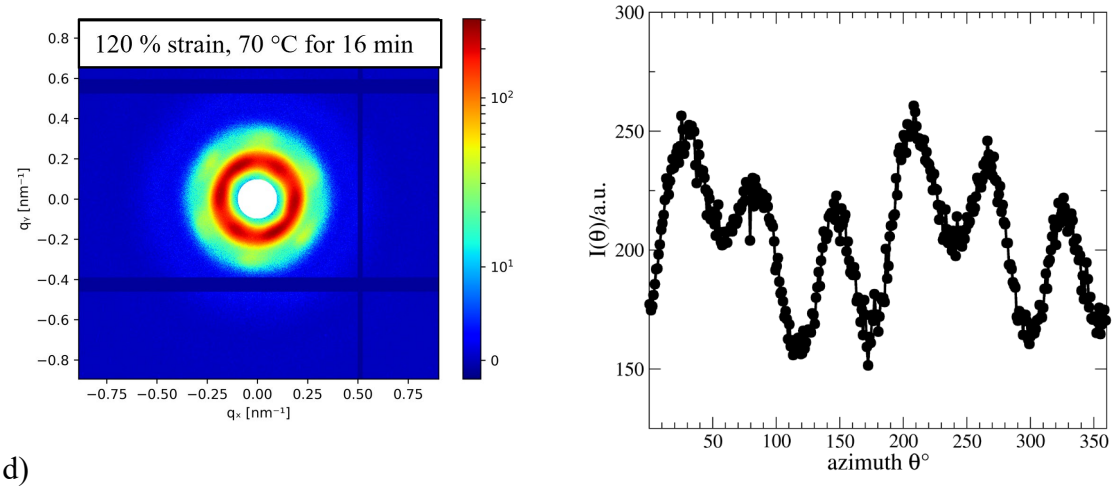

d)

Figure 6.14 SAXS 2D images (left) of 22 nm iron oxide nanoparticles grafted with 26 000 g/mol polystyrene chains at 60 wt% concentration in Xylene solvent and a corresponding radial average plot, simulation or azimuthal plot of the first scattering ring from the beamstop (right) a) at 0 % strain and 25 °C b) at 120% strain and 60 °C c) at 120 % strain and 70 °C, and d) at 120 % strain at 70 °C for 16 more minutes of shearing

Altogether, shearing and heating of the two systems of iron oxide-polymer nanocomposite in the organic solvent leads to the orientation of hexagonal lattices into FCC diffraction pattern in <110> direction. This path for smaller and bigger particles differs because of the length of polymer chains. Since smaller particles are grafted with shorter polymer chains, the interparticle distance is small enough to let them form already pre-oriented lattices, and their domains are completely aligned with shearing at high strains. The bigger 22 nm particles are grafted with longer polymer chains, which provide initially larger distances between cores. Their soft polymer shells are deformed under shearing, which leads to FCC orientation. Three factors, which impact the well-aligned FCC pattern are the value of the shearing strain, shearing time, and a minimum temperature of 60 °C. Exceptional cases, where a self-assembly was not possible are presented in the Supporting Information, Figure 6.20 and Figure 6.21.

Influence of magnetic external field

The <110> direction of the hexagonal lattice is the most common one that can be observed in self-assembled systems using the SAXS method during the shearing of the sample. Contrary to that, a magnetic field application could provide additional directions and alternative ways of assembly, depending on the direction of the field to the sample.

To produce experimental conditions similar to shearing in the Linkam device, where a substance is confined between two planes of tape, studied samples were placed between Kapton tapes also for the experiment in the permanent magnetic field. This way of sample preparation makes possible a preliminary manual shearing of the nanocomposite

and provides a micrometer scale sample thickness, similar to the shearing experiments in the previous paragraph.

Referring back to 14 nm iron oxide nanoparticles grafted with 6 000 g/mol polystyrene chains, we show the influence of 0.1 Tesla magnetic field on their assembly in the organic solvent. Here the direction of the field is perpendicular to the Kapton film (as well as the SAXS beam direction) and therefore to the pre-shearing direction. As follows, poorly-oriented hexagonal lattice domains initially have two favorable directions at the first diffraction ring (Figure 6.15 a); these directions are not favorable anymore after placing the sample for 3 hours into the magnetic field (Figure 6.15 b). There we already observe a formation of the twinned and prevailing BCC lattice in <210> direction with the lattice parameter a = 34 nm.

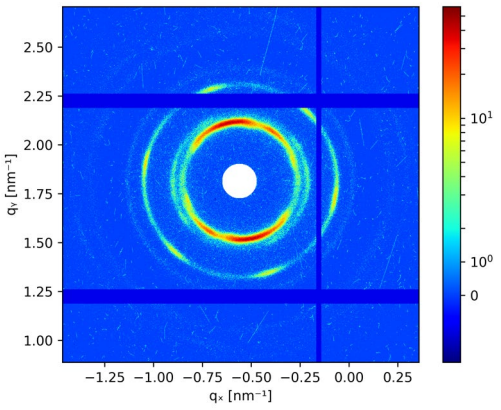

a)

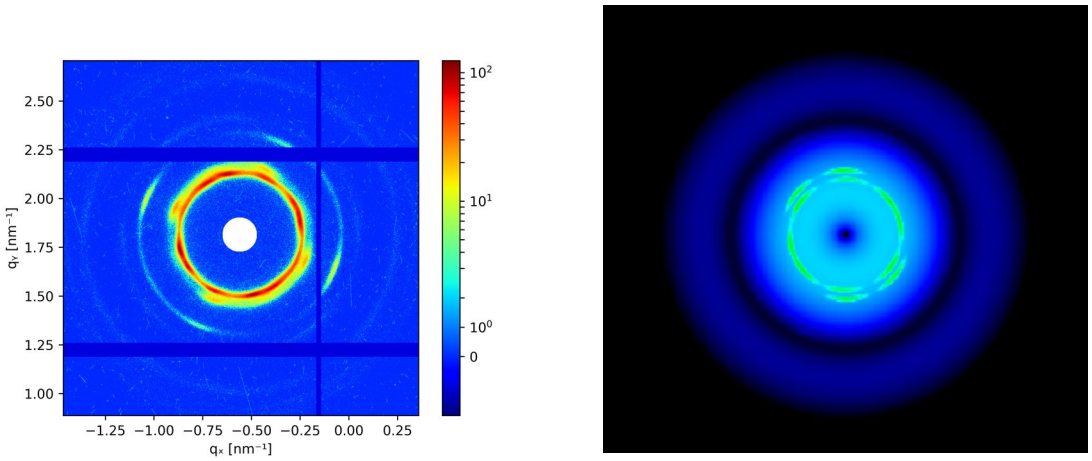

b)

Figure 6.15 2D SAXS images of 14 nm iron oxide nanoparticle with 6 000 g/mol PS at 50 wt% concentration in Xylene a) after pre-shearing b) after 3 hours in 0.1 Tesla magnet and the corresponding simulation of <210> direction for twinned FCC lattice

The influence of time that samples spend in a permanent magnet on the result of self-assembly is well-demonstrated for 55 wt% SPIONs solution. The diffraction pattern of a hexagonal lattice in Figure 6.16 a) turns to the pattern of well-ordered FCC in <111> direction with the lattice parameter a = 37 nm in 1 hour. One more hour in the magnetic field brings changes to the long-range order, which after 3 hours results in reconstruction to <100> direction of FCC (Figure 6.16 c, d).

The time-dependent behavior of magnetization becomes especially important when considering nanoscale and nanosecond timescale magnetization. Instead of simply aligning with an applied field the individual magnetic moments in a material begin to precess around the applied field and come into alignment through relaxation as energy is transferred into the lattice[3].

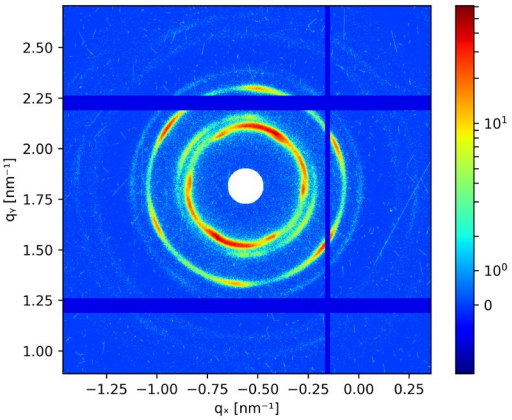

a)

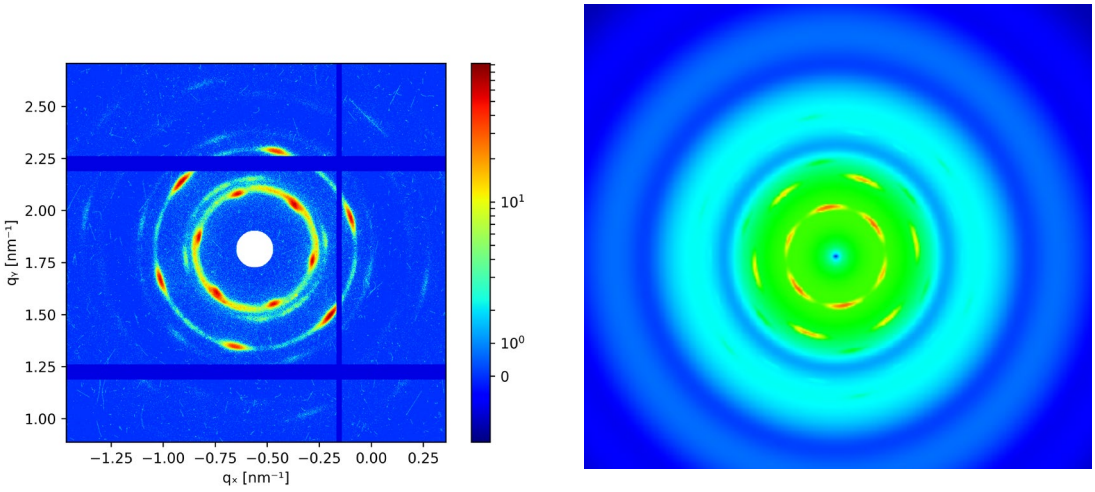

b)

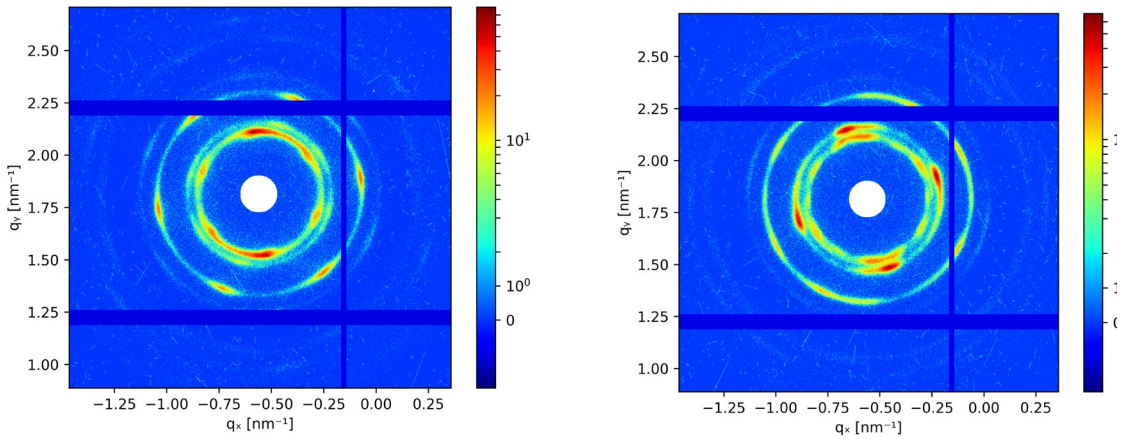

c) d)

Figure 6.16 2D SAXS images of 14 nm iron oxide nanoparticle with 6 000 g/mol PS at 55 wt% concentration in Xylene a) after pre-shearing b) after 1 hour in 0.1 Tesla magnet and the corresponding FCC simulation of <111> direction c) after 2 hours in the magnet d) after 3 hours in the magnet

A stiffer 70wt% sample doesn't show significant changes in the structure after the magnetic field influence (Figure 6.17). Its diffraction pattern only has a different shape of spots, which become slightly elongated after alignment in the field. We assume that this kind of highly-concentrated samples could be reassembled by either a longer exposure in the magnetic field or by increasing the strength of the field. The effect of insufficient magnetic field strength or magnetization time was already significant for 60 wt% SPIONs in Xylene (Supporting Information, Figure 6.22). As an additional factor, the chosen direction of pre-shearing opposes the ordering by the field.

For obtaining a better order of smaller nanoparticles it is relevant to change the orientation of the sample in the magnetic field. Thus, magnetic field lines overlap with the shearing direction and initiate the assembly of FCC lattice on the long-range order (Supporting Information, Figure 6.23).

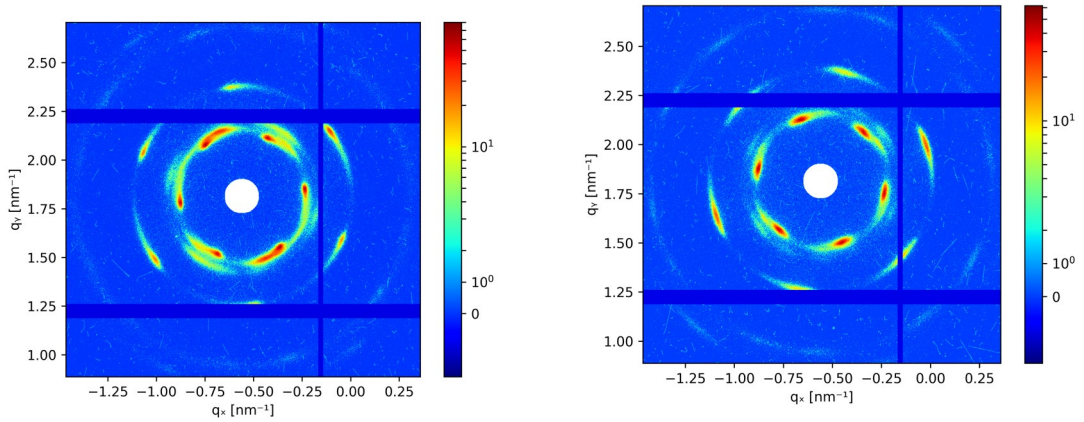

a) b)

Figure 6.17 2D SAXS images of 14 nm iron oxide nanoparticle with 6 000 g/mol PS at 70 wt% concentration in Xylene a) after pre-shearing b) after 3 hours in 0.1 Tesla magnet

Magnetic properties, including the saturation magnetization *Ms*, remanent magnetization *Mr*, and coercivity *Hc*, of Fe_3O_4 NPs are highly influenced by the particle size and domain structure. The saturation magnetization *Ms* increases with increasing particle size, regardless of the crystal structure and particle shape[4].

If we choose bigger particles with longer polymer chains, the result of magnetic field influence will be similar to shearing experiments. The initial state shows an isotropic diffraction pattern which changes to an FCC diffraction pattern after hours in the permanent magnet (Figure 6.18). Here the time parameter only influences the size of the FCC lattice, but the structure and its orientation do not change even after 16 hours. Even though the solution of large particles was pre-sheared the diffraction pattern stayed isotropic. Then during the exposure to the magnetic field, particles could be easily oriented in the preferable for the field <111> direction, which underlines the impact of polymer chain length on the assembly result.

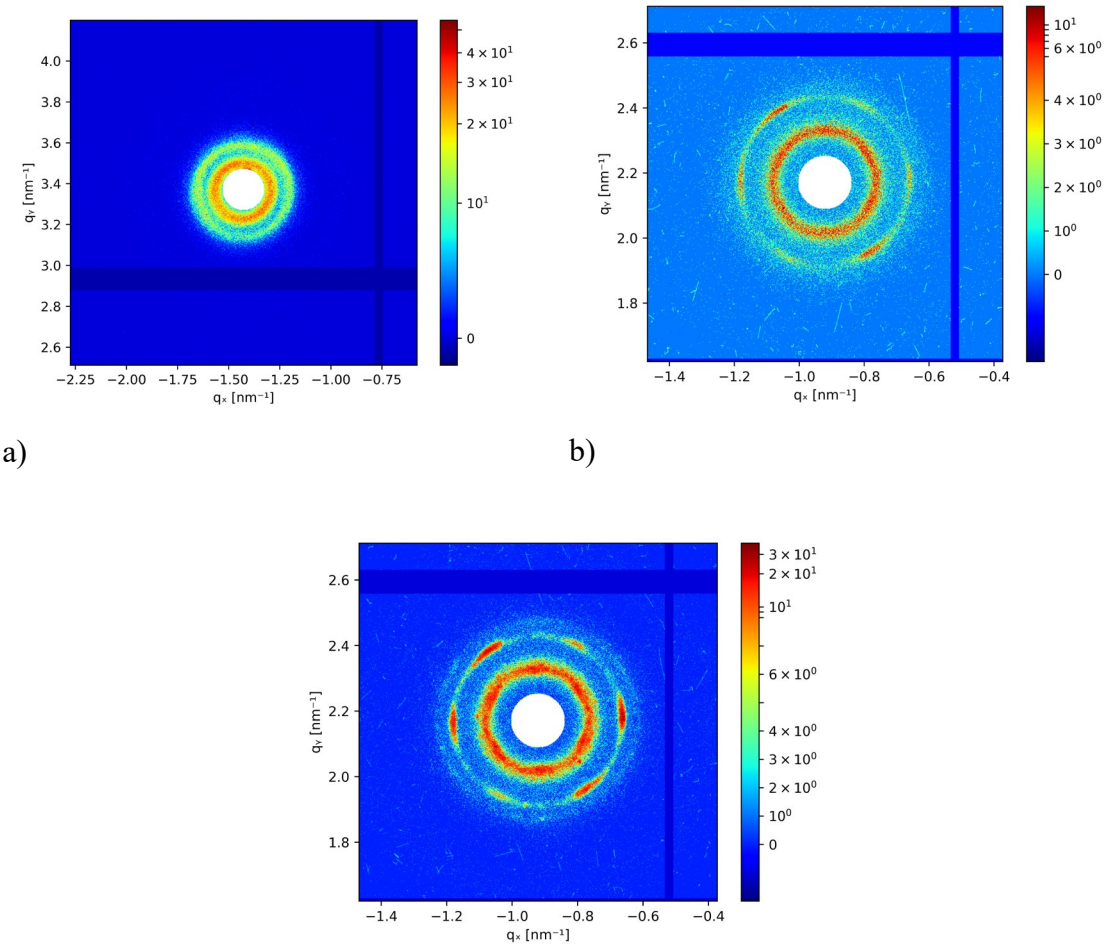

Figure 6.18 2D SAXS images of 22 nm iron oxide nanoparticle with 26 000 g/mol PS at 50 wt% concentration in Xylene a) after pre-shearing b) after 1 hour and c) 16 hours in 0.1 Tesla magnet

The higher concentration of 60 wt% SPIONs demands a longer time for FCC assembly (Figure 6.19). The isotropic pattern changes only after 2 hours and turns to the FCC pattern in <111> direction with lattice parameter a = 72 nm. A further hour of nanoparticle magnetization doesn't lead to any structural changes. The azimuthal plot in Figure 6.19 shows that SPIONs have both short- and long-range order.

To sum up, the permanent magnetic field that is perpendicular to the sample initiates rotations of cubic lattices and their reorientation. For smaller 14 nm particles grafted with short polymer chains, a field-induced assembly leads to complex structures, which depend on magnetization time. For larger 22 nm particles an assembly in the magnetic field starts from the disordered state, in which long polymer chains constrain the interparticle interaction. As a result, well-ordered FCC lattices are formed in <111> direction, which is favored by the field.

The speed of an assembly process depends mainly on the concentration of polymer-covered SPIONs in the organic solvent when other parameters (field intensity, exposure time, and particle type) are fixed.

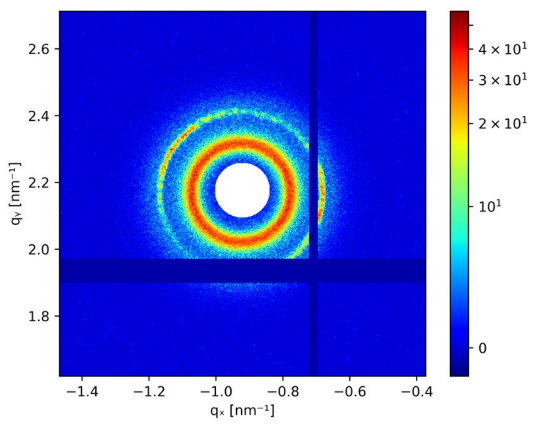

a)

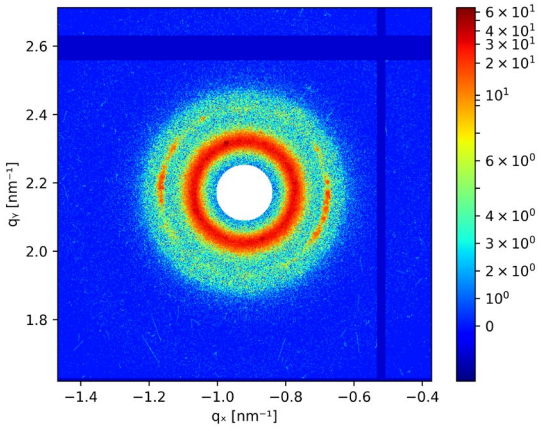

b)

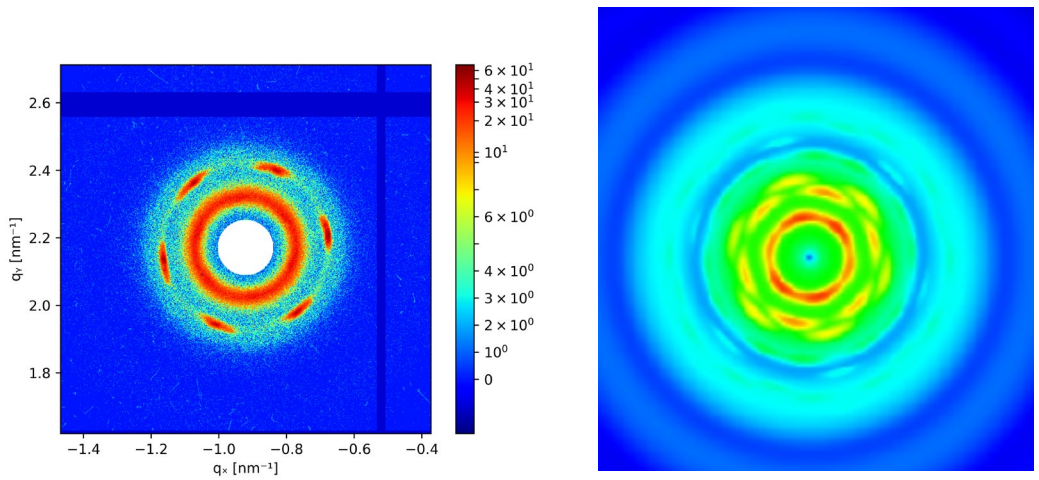

c)

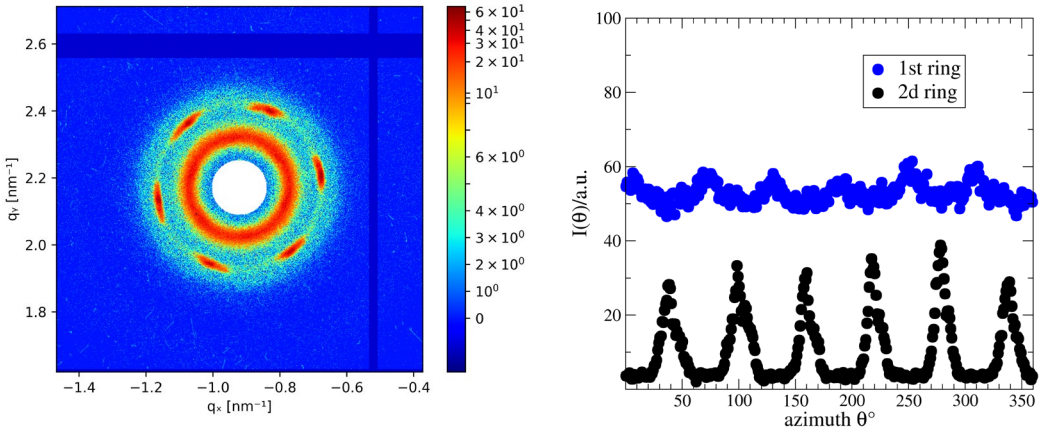

d)

Figure 6.19 2D SAXS images of 22 nm iron oxide nanoparticle with 26 000 g/mol PS at 60 wt% concentration in Xylene a) after pre-shearing b) after 1 hour and c) 2 hours with a corresponding simulation of <111> direction d) 3 hours in 0.1 Tesla magnet with a corresponding azimuthal plot

6.4 Materials and methods

6.4.1 Materials

All solvents were used as received: p-Xylene (Sigma-Aldrich, 99 %) solvent was used for sample preparation, Tetrahydrofuran THF (Sigma-Aldrich, ≥99.9%) for particle storage, and Ethanol (VWR Chemicals, ≥99,8%) for precipitation step during the ligand exchange. *Iron oxide nanoparticles:* magnetite nanoparticles of 14 nm and 22 nm diameter were synthesized using the thermal decomposition method [5]. THF solvent was evaporated and changed p-Xylene;
Polymer grafting: Polystyrene (M_w = 6600 g/mol and M_w = 26000 g/mol) was synthesized by living anionic polymerization with *sec*-butyl lithium as an initiator at −70 °C in THF. The polymerization was terminated with CO_2 to obtain a carboxylic acid end group. The hydroxyl end group was subsequently activated by CDI and reacted with PEHA to create a multivalent amine function[6]. The ligand exchange procedure was carried out as described by Ehlert and coauthors [6].

6.4.2 Sample preparation

Mixtures of functionalized SPIONs at 40-70 wt% concentrations in the p-Xylene solvent were prepared in glass vials. Polymer-grafted particles were mixed with the solvent and centrifuged for 10 minutes at 3000*g until a homogeneous state.

6.4.3 Transmission electron microscopy (TEM)

TEM measurements were performed using JEOL-F200 Multipurpose Electron Microscope. The standard procedure for sample preparation includes partial drying of diluted nanocrystal solution on a carbon-coated copper grid with the following removal of excess solution. Data evaluation was done in ImageJ software for the determination of average particle radii and size distribution.

6.4.4 SAXS measurements

The laboratory machine "Ganesha-Air" has the X-ray source D2-Metalljet (Excillium) with a liquid metal anode operating at 70 kV and 3.57 mA with Ga-Kα radiation (λ = 0.1314 nm) providing a thick beam (< 100 μm) of high brilliance. X-ray optics (Xenocs) provides small and intense beam at the sample position, the beam size is adjusted with two pairs of slits depending on the detector distance.

Samples were measured in two different ways. The first one is using the shearing device Linkam CSS450. Various shearing procedures were applied at a fixed 8 Hz frequency, and the maximum shearing strain and temperature reached 140% and 70 °C respectively. The second way is measuring Kapton films (1.5 cm^2) with samples at room temperature (T = 24 °C) after they were exposed to a magnetic field. For that films were placed between two pieces of ferrite magnet so that the magnetic field intensity equaled 0.1 Tesla.

If not stated otherwise data was radially averaged, and normalized to measurement time and transmission with the solvent as background subtracted.

Data analysis: small-angle scattering curves were initially corrected using Jscatter software [7] and fitted with a "polydisperse core-shell sphere" model[8] for the form factor calculation. 2D SAXS patterns were analyzed and fitted in Scatter software[9].

6.5 Conclusion

The complexity of the FCC-BCC phase transition, which appears because of the influence of external fields has been discussed in detail. The difference in scattering patterns for FCC and BCC lattices was shown depending on the degree of orientational order. Also, the coexistence of these two phases was demonstrated experimentally and proved by simulation of the resultant structure. We discuss a path of possible lattice alignment under the shearing conditions and after pre-shearing with later exposure to the magnetic field.

Later we provide experimental results for solutions of superparamagnetic iron oxide nanoparticles grafted with polymer chains in an organic solvent, which were assembled in external fields. The first type of experiment considered shearing the nanocomposite complexes of 40 wt% - 70 wt% concentrations at high strains and temperatures reaching 70 °C. The second type included their alignment in the 0.1 Tesla magnetic field after pre-shearing along <111> direction. As a result, we indeed see a reorientation of the FCC lattice in the magnetic field, and this process does not progress along a reorientation path with a well-defined rotation axis in most cases. Instead, it involves other, not well-defined paths, sometimes including twinning, which leads to a set of complex scattering patterns.

A significant role in obtaining well-oriented cubic structures plays parameters of particle size, polymer length, and sample concentration.

Smaller 14 nm particles with short polymer chains 6 000 g/mol are not far apart and already form pre-oriented lattices before shearing, while their domains are completely aligned at high strain conditions. The bigger 22 nm particles are grafted with longer 26 000 g/mol polymer chains, and therefore, they have thicker shells. For them, both external fields induce the assembly of FCC lattice from an isotropic state. An additional essential parameter is the temperature of shearing 60°C, at which an internal reconstruction starts. The process of FCC reorientation is irreversible, which means that the obtained order is not influenced by temperature reduction to 25 °C.

We define the nanocomposite concentration range 50-60 wt% in p-Xylene, in which it is possible to regularly obtain an anisotropic pattern and easily change it in external fields. Finally, the time of magnetization is crucial for the nanoparticle assembly, which was proved by the comparison of the diffraction pattern after each hour they were exposed to the magnetic field. For smaller particles it assumes progressing rotation, change of the orientation direction, and building of complex structures via twinning. On the opposite, bigger particles' diffraction pattern changes only concerning the width of diffraction spots

and the lattice parameter size, meaning a closer packing with the increase of magnetization time.

6.6 Supporting Information

1. **Parameters of nanocomposite solution, which restrict a structural order in external fields**
2. **The destructive influence of magnetic field at high concentrations**
3. **Structural changes in the magnetic field depending on the sample orientation**

Parameters of nanocomposite solution, which restrict a structural order in external fields

The following samples were not presented before because external fields don't play an important role in their self-assembly.

Firstly, smaller 14 nm particles with long 26 000 g/mol polymer chains give a homogeneous 2D pattern that can't be changed using shearing and increasing the temperature. Meanwhile, only a slight interparticle distance decrease is observed on radially averaged data plots (Figure 6.20).

Secondly, larger 22 nm particles with long polymer chains have a minimal concentration in an organic solvent, which is crucial for their self-assembly, so that at 40 wt% concentration a cubic lattice orientation is no more possible to be formed (Figure 6.21). Shearing at 30 % strain brings the first SAXS pattern changes - the second scattering ring appears. Further shearing and temperature manipulations don't influence the structure.

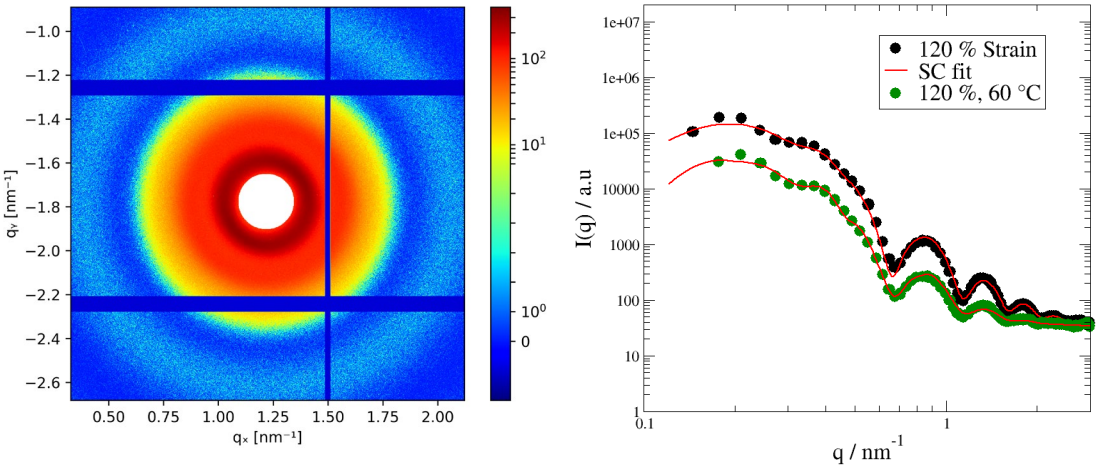

*Figure 6.20 SAXS 2D images (left) of 14 nm iron oxide nanoparticles grafted with 26 000 g/mol polystyrene chains at 60 wt% concentration in Xylene solvent at 120 % strain and 60 °C, and corresponding radial average plots (right) for 120% strain at 25 °C (**black dots**), for 120 % strain at 60 °C, which are fitted with the simple cubic SC model (**red line**)*

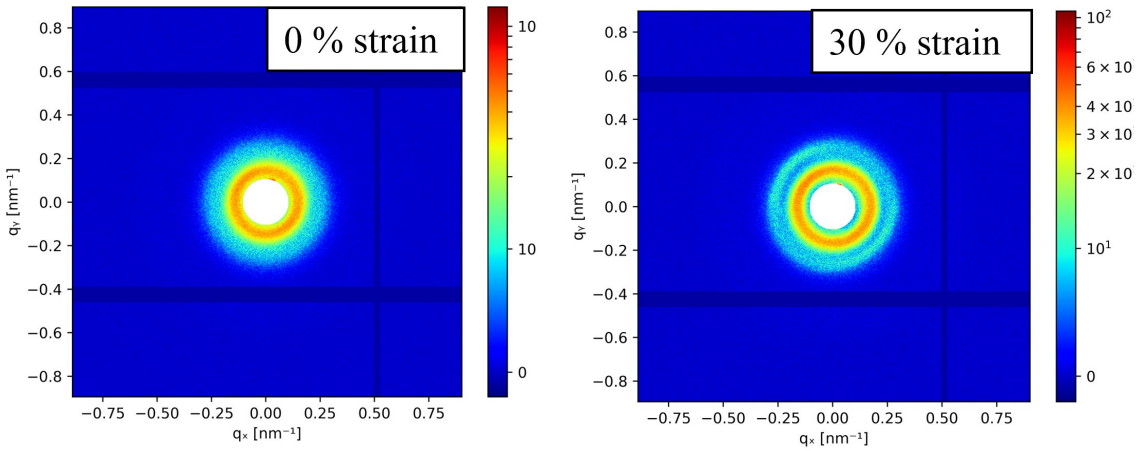

Figure 6.21 SAXS 2D images (left) of 24 nm iron oxide nanoparticles grafted with 26 000 g/mol polystyrene chains at 40 wt% concentration in Xylene solvent before shearing and after applying 30 % strain at 25 °C

The destructive influence of magnetic field at high concentrations

For highly-concentrated mixtures of polymer-grafted 14 nm SPIONs, there is a limit of concentration, at which the magnetic field is capable of cubic lattice rotations. In Figure 6.22 the sample at 60 wt% has an initial hexagonal diffraction pattern with "bright" long-range order, which got significant defects after 3 hours under a magnetic field. It probably happens because the orientation of lattices, which were ordered during pre-shearing is not favorable for the chosen direction of the magnetic field (lines of the magnetic field are perpendicular to the sample).

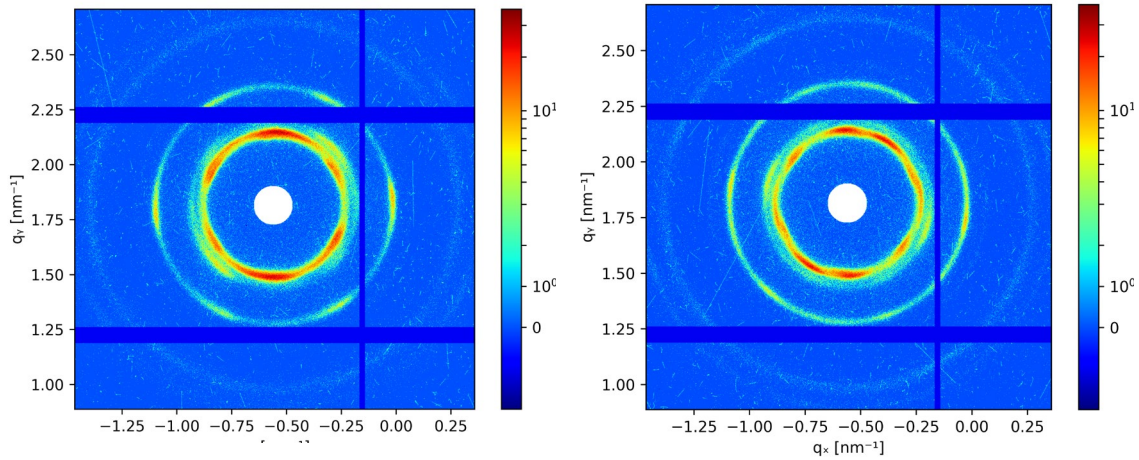

a) b)

Figure 6.22 2D SAXS images of 14 nm iron oxide nanoparticle with 6 000 g/mol PS at 60 wt% concentration in Xylene a) after pre-shearing b) after 3 hours in 0.1 Tesla magnet

Structural changes in the magnetic field depending on the sample orientation

Change in the magnetic field direction enables lattice rotation also for highly concentrated systems (Figure 6.23). Since the magnetic field is parallel to the sample and therefore, it overlaps with the pre-shearing direction, a twinned hexagonal pattern of well-ordered domains is obtained.

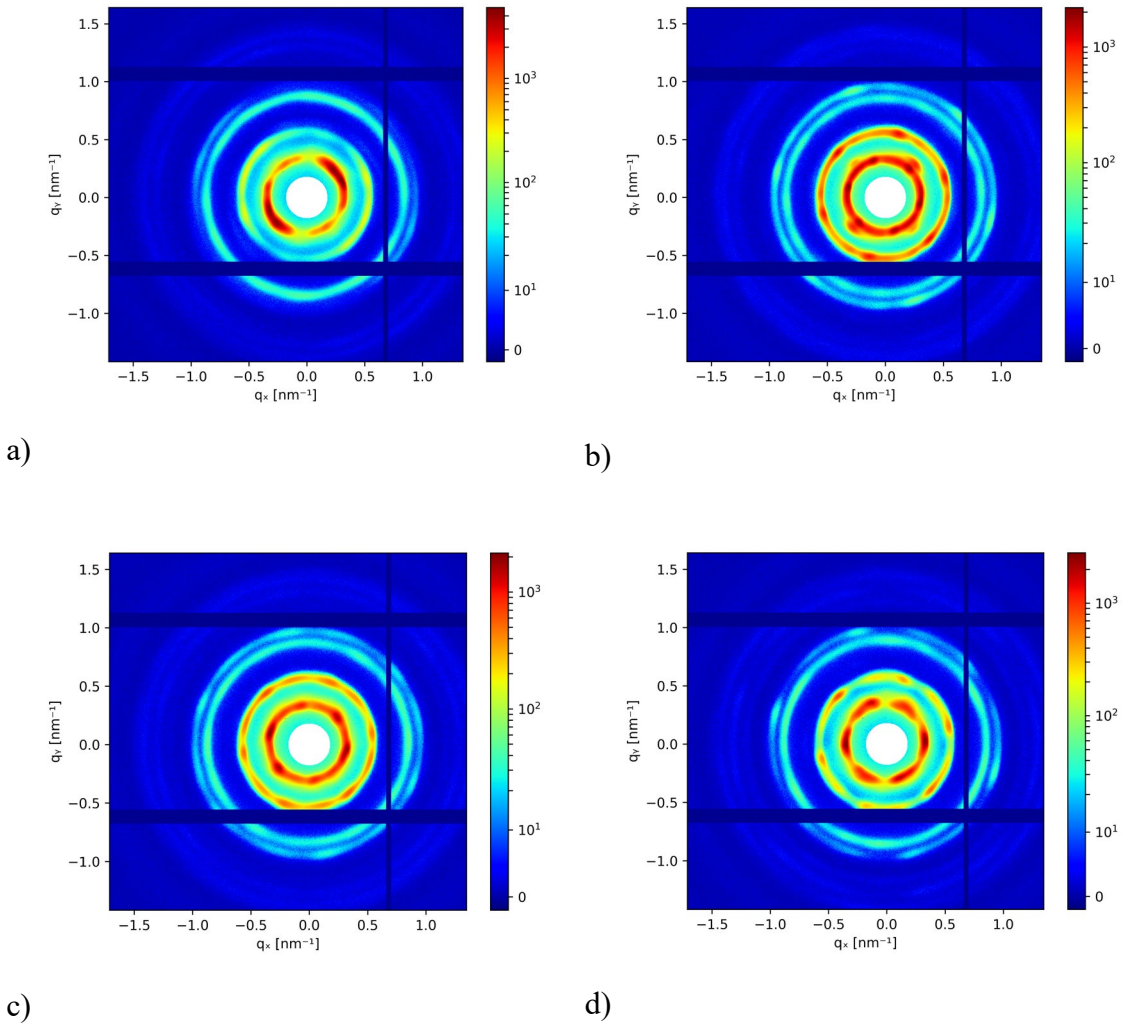

Figure 6.23 SAXS 2D images of 14 nm iron oxide nanoparticles grafted with 6 000 g/mol polystyrene chains at 60 wt% concentration in Xylene solvent: a) pre-sheared, b) exposed for an hour, c) 4 hours, d) 5 hours to the magnetic field that is oriented along the film with a sample (parallel)

6.7 References

[1] A. Janikowska, J. Matuszak, S. Lyer, E. Schreiber, H. Unterweger, J. Zaloga, J. Groll, C. Alexiou, I. Cicha, *Springer* **2017**, *7*, DOI 10.1038/srep42314.

[2] S. Förster, A. Timmann, C. Schellbach, A. Frömsdorf, A. Kornowski, H. Weller, S. V. Roth, P. Lindner, *Nature Materials 2007 6:11* **2007**, *6*, 888–893.

[3] J. Stöhr, H. C. Siegmann, *Magnetism: From Fundamentals to Nanoscale Dynamics* **2006**, *152*, 1–822.

[4] Q. Li, C. W. Kartikowati, S. Horie, T. Ogi, T. Iwaki, K. Okuyama, *Scientific Reports 2017 7:1* **2017**, *7*, 1–7.

[5] J. Park, K. An, Y. Hwang, J. E. G. Park, H. J. Noh, J. Y. Kim, J. H. Park, N. M. Hwang, T. Hyeon, *Nature Materials 2004 3:12* **2004**, *3*, 891–895.

[6] S. Ehlert, S. M. Taheri, D. Pirner, M. Drechsler, H. W. Schmidt, S. Förster, *ACS Nano* **2014**, *8*, 6114–6122.

[7] R. Biehl, *PLoS One* **2019**, *14*, DOI 10.1371/JOURNAL.PONE.0218789.

[8] A. Guinier, *Small-Angle Scattering of X-Rays*, Wiley, New York, **1955**.

[9] S. Förster, L. Apostol, W. Bras, *urn:issn:0021-8898* **2010**, *43*, 639–646.

Conclusion and Outlook

In this thesis, mechanisms and pathways of core-shell nanoparticle self-assembly in organic solvents were studied in shearing and magnetic fields. Two types of systems, with soft and hard cores, were analyzed and compared to their locations in the phase diagram depending on the core-shell ratio and core volume fraction. Typically observed structures were FCC and BCC lattices, as well as the A15 Frank-Kasper phase and Q12 quasicrystalline phase.

The wide application of nanosystems[1] demands precise control over size, composition, and structural parameters. While a soft core's size can be tuned by changing the length of polymer chains, for a hard inorganic core it depends on the availability of particle sizes. For iron oxide nanoparticles obtained with the thermal decomposition method, it is challenging to reach larger diameters of spherical, monocrystalline particles. Therefore, its synthesis was performed in several ways for obtaining gram-scale amounts of superparamagnetic spherical particles in an optimal size range.

The first type of system had both a soft core and shell. The ratio of core and shell radii to the core radius is the essential parameter λ, which plays an important role in the formation of a resultant structure, as well as the core volume fraction φ_{core}. Based on these two parameters, a phase diagram of possible structures (obtained from molecular dynamic simulations) could successfully fit the experimental results of $C_{16}E_{20}$ (Brij 58) polymer-water solutions. A concentration range of 49-58 wt% of hydrated diblock oligomer enables the formation of the A15 Frank-Kasper phase, which was thoroughly studied at various shearing and temperature conditions for determining experimental parameters of the reproducible transitions between FCC, BCC, A15, and H1 phases. The brightest result was a successful ordering of the A15 phase on the long-range distance, meaning that the SAXS diffraction pattern has completely reproduced calculations of oriented A15 domains in <110> direction. Additionally, the influence of polymer distribution on the formation of lyotropic liquid crystal phases (LLC) was analyzed. A homemade sample of improved quality formed an equal A15 phase, which in comparison to an industrial sample could not be oriented. One of the challenges, which has appeared during the shearing experiments was the solvent evaporation after a certain time. Since an increase in temperature is an essential thermodynamic parameter, it could enable additional phase transition paths, if the issue of water evaporation was solved. It demands future studies of alternative high-boiling point solvents and suitable concentrations, in which polymer still forms core-shell micelles.

A notable feature of the A15 phase is its neighborhood with a quasicrystal phase (QC) in the phase diagram. Highly important for fundamental research, quasicrystals are ordered, but aperiodic structures due to the lack of translational symmetry. They are more common for solid-state materials, nevertheless, these structures also appear in soft matter[2,3]. For instance, polyisoprene-polystyrene block copolymers (PI-PS) in mixtures with an organic solvent form QCs under shearing with high 80% strain and 60 °C [4]. Thus, applying previously gained knowledge about the soft core-shell polymer system of PI-PS, a test of a new cuette-type shearing device was performed. In this case, the λ parameter was varied not only via shearing but also via temperature. This possibility comes from the DEP solvent property to change its solubility with temperature and as a consequence, change the core-shell ratio. During the experiments, the cuette-type geometry of the sample holder prevented a lack of material on the SAXS beam path, which usually happens due to the decrease of a gel's viscosity with heating. As a result, PI-PS block copolymers demonstrated structural stability and reproducibility of self-assembly properties. Moreover, changing temperature along with the shearing led to the reduction of structural defects and either building or destruction of well-ordered FCC lattices. The cuette cup also allowed studying of structures from two different directions (radial and tangential), although results in the tangential direction were not constantly reproducible. This technique should be still improved by developing a proper centering of the oscillating rod to guarantee an even sample distribution. Furthermore, having access to strains up to 500 % enables perspective studies of any stiff, highly-concentrated samples.

In the second part of the thesis, core-shell systems with hard inorganic core and soft polymer shells were studied. For the core, which should not be deformed under shearing, inorganic particles of iron oxide were chosen. Since superparamagnetic nanoparticles intend to self-assemble in external fields, it makes the system particularly attractive. Nowadays there are already several established applications of such nanostructures for biomedicine, electronics, and industrial production of composite materials and oil [5–10]. It demands well-established production processes for obtaining big amounts of monodisperse, uniform, monocrystalline nanoparticles of various sizes. Among different synthesis routes, thermal precursor decomposition methods are the most versatile. Its kinetic mechanism has non-classical nucleation and growth paths involving amorphous precursor phases and aggregative growth steps [11]. Based on this knowledge, a range of different thermal decomposition routes was systematically examined to find an optimal way to a reproducible size control over relevant nanoparticle diameters. SAXS and TEM

methods were used for the characterization of the nanoparticle shape and size distribution. Thus, it was demonstrated that a thermal pretreatment of the iron oxide precursor is essential to achieve reproducible size control. Furthermore, each solvent (1-octadecene, trioctylamine, docosane) provides access to a temperature range between 300 – 370 °C, within which the variation of temperature, heating rate, or precursor concentration allows to reproducibly control the nanoparticle size on a nanometer scale. Finally, the synthesis of monocrystalline superparamagnetic iron oxide nanoparticles was performed in a size range of 5 – 24 nm. In this step, further studies of nanoparticle growth kinetic are necessary for expanding the range of particle sizes, while saving a desired shape, size distribution, and structural composition. For that, the annealing time during a synthesis should be carefully considered, since it is the time of particle growth as well. Also, other high boiling point solvents could be tested for opening a new possible size range. Noteworthy, particles lose their ideal spherical shape above 24 nm diameter, which is critical for certain applications. Nevertheless, it doesn't affect the self-assembly if the surfactant's chains of a sufficient length make the surface even.

Particularly the self-assembly of polymer-grafted SPIONs was the next object of study. Polystyrene chains (6 000 g/mol) were transferred to the 17 nm nanoparticles using the ligand exchange method[12], which resulted in a sufficient grafting density for an equal interparticle distance. Nanocomposite mixtures with DEP organic solvent demonstrated self-assembly at concentrations above 50 wt%: between 50 wt% and 60 wt%, the BCC lattice was formed, whereas the FCC lattice appeared above 70 wt%. In this way, only the solvent amount influences the result and the possibility of the assembly itself. After storing particles for 48 hours in the permanent 0.7 Tesla magnet, several phase transitions were observed. For instance, a disorder-order transition for solutions with a concentration below 50 wt%, as well as a BCC to FCC phase transition at 60 wt%. Higher concentrations of nanocomposite demonstrated a decrease in the lattice parameter, which signalized the FCC phase packing in the magnetic field. An interesting BCC to FCC phase transition was detected during SAXS measurements at the synchrotron source, which supplies a thin beam and allows to obtain the sharp peaks of scattering curves. Typical for this kind of BCC-FCC phase transition is a shift of scattering curves towards a high q-range. Indeed, structural changes in the permanent magnetic field do not happen immediately for highly-concentrated samples (20-100 wt%). In the above-described experiment, the exposure time in the magnet was chosen to be 48 hours, which leads to the formation of stable cubic lattices. Thus, the dependence of the formed structure on the time of magnetization was not considered yet.

Finally, a path of possible FCC and BCC lattice alignment in external fields was discussed in detail. Experimental results of FCC-BCC phase coexistence were in good agreement with simulated diffraction patterns. For obtaining SAXS data of self-assembled nanoparticles, two methods of external influence were applied: shearing and pre-shearing with later exposure to the magnetic field. In the first case, nanocomposite complexes (14 nm grafted with 6k PS and 22 nm grafted with 26k PS in p-Xylene) of 40 wt% - 70 wt% concentrations were sheared at high strains and temperatures reaching 70 °C. The second case included their alignment in the 0.1 Tesla magnetic field after pre-shearing along <110> direction. Both methods induce the reorientation of the FCC lattice in the magnetic field, which does not progress along a well-defined rotation axis in most cases and leads to a set of complex scattering patterns. A significant role in obtaining well-oriented cubic structures play parameters of particle size, polymer length, and sample concentration. To illustrate, smaller 14 nm particles with short polymer chains already form pre-oriented lattices before shearing, and their domains are aligning at high strains. By way of contrast, the bigger 22 nm particles have a thicker polymer shell and consequently, both assemble into FCC lattices from an isotropic state in both external fields. An additional essential parameter is the temperature of shearing 60 °C, at which an internal reconstruction starts. The process of FCC reorientation is irreversible and is not influenced by temperature reduction to 25 °C. Also, the time of magnetization is crucial for nanoparticle assembly, which was proven during time-resolved measurements. For smaller particles, progressing rotation was observed, change of the orientation direction, and building of complex structures via twinning. On the opposite, changes in bigger particles' diffraction patterns signalize only further FCC packing. The next perspective study on highly-concentrated, polymer-grafted SPION solutions would be changing the field gradient, and its direction and varying a range of the system parameters like core-shell ratio, polymer type, and solvent. For using SPIONs complexes in medicine, e. g. in drug delivery[5] or as a contrast agent[7], the solvent should be exchanged for a non-toxic one, which can change the result of the assembly and demand additional research.

6.8 References

[1] J. Tani, C. G. Speziale, J. Qiu, *Appl Mech Rev* **1998**, *51*, 505–521.

[2] S. Fischer, A. Exner, K. Zielske, J. Perlich, S. Deloudi, W. Steurer, P. Lindner, S. Förstere, *Proc Natl Acad Sci U S A* **2011**, *108*, DOI 10.1073/pnas.1008695108.

[3] K. Yue, M. Huang, R. L. Marson, J. Hec, J. Huang, Z. Zhou, J. Wang, C. Liu, X. Yan, K. Wu, Z. Guo, H. Liu, W. Zhang, P. Ni, C. Wesdemiotis, W. Bin Zhang, S. C. Glotzer, S. Z. D. Cheng, *Proc Natl Acad Sci U S A* **2016**, *113*, DOI 10.1073/pnas.1609422113.

[4] T. Jurczyk, S. F. Förster, W. Richtering, **2021**, DOI 10.18154/RWTH-2021-11518.

[5] A. Janikowska, J. Matuszak, S. Lyer, E. Schreiber, H. Unterweger, J. Zaloga, J. Groll, C. Alexiou, I. Cicha, *Springer* **2017**, *7*, DOI 10.1038/srep42314.

[6] T. L. Hennig, H. Unterweger, S. Lyer, C. Alexiou, I. Cicha, *Molecules* **2019**, *24*, 2588.

[7] J. Yan, S. Li, F. Cartieri, Z. Wang, T. K. Hitchens, J. Leonardo, S. E. Averick, K. Matyjaszewski, *ACS Appl Mater Interfaces* **2018**, *10*, 21901–21908.

[8] Ş. Yılmaz, A. Zengin, Y. Akbulut, T. Şahan, *Environmental Science and Pollution Research* **2019**, *26*, 20454–20468.

[9] A. S. Kamzin, I. M. Obaidat, V. S. Kozlov, E. V. Voronina, V. Narayanaswamy, I. A. Al-Omari, *Physics of the Solid State 2021* **2021**, *2021*, 1–10.

[10] M. Rajnak, M. Timko, P. Kopcansky, K. Paulovicova, J. Tothova, J. Kurimsky, B. Dolnik, R. Cimbala, M. V. Avdeev, V. I. Petrenko, A. Feoktystov, *J Magn Magn Mater* **2017**, *431*, 99–102.

[11] V. Leffler, S. Ehlert, B. Förster, M. Dulle, S. Förster, *ACS Nano* **2021**, *15*, 840–856.

[12] S. Ehlert, S. M. Taheri, D. Pirner, M. Drechsler, H. W. Schmidt, S. Förster, *ACS Nano* **2014**, *8*, 6114–6122.

Acknowledgements

I would like to acknowledge all colleagues, with whom I had ever a chance to work. Thank you very much for sharing your scientific experience and contributing to this project.
Additionally, I would like to express my sincerest gratitude towards:

- Prof. Dr. Stephan Förster for supervising my PhD project and for his brilliant ideas
- Prof. Dr. Walter Richtering for the co-supervision of this thesis
- My scientific advisors Dr. Margarita Kruteva and Dr. Martin Dulle for their support, introduction to SAXS, highly valuable advices and reading of this work
- Dr. Ralf Biehl for his willingness to help and for the professional Python troubleshooting
- Dr. Jurgen Allgaier, Dr. Kuno Schwärzer, Dr. Lisa Fruhner and Dr. Sascha Ehlert for the time they invested into synthesis of my samples
- Dr. Aakash Sharma and Dr. Jörg Stellbrink for the passionate introduction to rheology
- Dr. Andrei Chumakov for his enthusiasm and help with synchrotron measurements
- Dr. Tobias Jurczyk for sharing his gained knowledge of shearing nanocomposites
- Technician group of JCNS, system administrators and secretariat for making my working routine comfortable
- The whole PhD/PostDoc team for the lunches we spent together, for a unique multicultural atmosphere, enormous amount of group activities and positive vibes
- Nils Beckmann and Igor Graf von Westarp for their time, effort and high attention to my work

Finally, a huge thank to my previous mentors, supervisors and family, who taught me, inspired me, and invested in me.

Curriculum Vitae

Personal details

Name:	Vladislava Fokina
Date of birth:	21.11.1995
Place of birth:	Tver, Russia

Education

2019 – 2024	*PhD Physical Chemistry* Jülich Centre for Neutron Science (JCNS-1), Forschungszentrum Jülich GmbH & Institute of Physical Chemistry, RWTH Aachen
2017 - 2019	*Nuclear physics* Dubna State University
2013 - 2017	*Applied physics* Tver State University
2002 - 2013	School №29, Tver